

# **Application of spaceborne geodetic sensors for hydrology**

Von der Fakultät Luft- und Raumfahrttechnik und Geodäsie  
der Universität Stuttgart  
zur Erlangung der Würde eines Doktor-Ingenieurs (Dr.-Ing.)  
genehmigte Abhandlung

Vorgelegt von  
**Mohammad Javad Tourian**  
aus Teheran

Hauptberichter: Prof. Dr.-Ing. Nico Sneeuw  
Mitberichter: Prof. Dr. rer. nat. Dr.-Ing. András Bárdossy

Tag der mündlichen Prüfung: 25. Oktober 2013

Geodätisches Institut der Universität Stuttgart

2013





**Application of spaceborne geodetic sensors  
for hydrology**

Von der Fakultät Luft- und Raumfahrttechnik und Geodäsie  
der Universität Stuttgart  
zur Erlangung der Würde eines  
Doktors der Ingenieurwissenschaften (Dr.-Ing.)  
genehmigte Abhandlung

Vorgelegt von  
**Mohammad Javad Tourian**

aus Teheran

**München 2013**

---

Verlag der Bayerischen Akademie der Wissenschaften  
in Kommission beim Verlag C. H. Beck

Adresse der Deutschen Geodätischen Kommission:



Deutsche Geodätische Kommission

Alfons-Goppel-Straße 11 • D – 80 539 München

Telefon +49 – 89 – 23 031 1113 • Telefax +49 – 89 – 23 031 - 1283 / - 1100

e-mail [hornik@dgfi.badw.de](mailto:hornik@dgfi.badw.de) • <http://www.dgk.badw.de>

Hauptberichter: Prof. Dr.-Ing. Nico Sneeuw

Mitberichter: Prof. Dr. rer. nat. Dr.-Ing. András Bárdossy

Tag der mündlichen Prüfung: 25.10.2013

Diese Dissertation ist auch auf dem Dokumentenserver der Universität Stuttgart veröffentlicht

<<http://elib.uni-stuttgart.de/opus/doku/e-diss.php>>

---

© 2013 Deutsche Geodätische Kommission, München

Alle Rechte vorbehalten. Ohne Genehmigung der Herausgeber ist es auch nicht gestattet,  
die Veröffentlichung oder Teile daraus auf photomechanischem Wege (Photokopie, Mikrokopie) zu vervielfältigen.

# Acknowledgement

I would like to express my genuine thanks to my supervisor, Prof. Dr.-Ing. Nico Sneeuw for his smart guidance, warm encouragements and helpful comments. He sharpened my mind towards a clear and scientific way of thinking and developing new ideas. For all of this I owe him more than I can describe.

I am also grateful to Dr. rer.nat. Johannes Rieger for his great efforts to open the doors of understanding of the hydrology. I appreciate all his contributions of time, ideas and comments to make a productive and stimulating working experience.

My deep gratitude goes to Prof. Dr. rer.nat. Dr.-Ing. András Bárdossy for giving me the opportunity of working in his department. His precious comments have opened new doors for research possibilities, from which my thesis benefited tremendously.

My research tasks have been mainly defined within the *Direct Water Balance* project, which was funded by Deutsche Forschungsgemeinschaft (DFG) in the framework of Special Priority Program Mass Transport and Mass Distribution in the System Earth. I would like to acknowledge all of my colleagues in this project, who provided a great team work atmosphere. My special thanks go to Balaji Devaraju for his help, support and his permanent positive attitude of collaboration. I would like to also appreciate Christof Lorenz for his immense support and consultation.

I also greatly appreciate all of my colleagues at the Institute of Geodesy and the Institute for Modelling Hydraulic and Environmental Systems for their help, feedback and emergency assistance. Above and beyond all the colleagues, I would like to additionally highlight my deep thanks to my friend Henning Lebrenz for his support and time to discuss about more important issues than science.

I would like to also thank the following data providers for making the data available: GRACE – CSR, GFZ, JPL, and ITG; discharge data – GRDC, USGS, USACE, ORE HYBAM, ArcticRIMS project, Water Survey Canada and Australian Government National Water Commission; precipitation data – GPCC, CRU, GPCP and data from the University of Delaware; evapotranspiration data – GLEAM, GLDAS, ECMWF, MERRA, MERRA Land.

My acknowledgments would not be complete without giving thanks to my lovely parents and my supportive brothers Majid and Sajjad. I am so much grateful for their loving support and admiration over the years. Last, but certainly not least, my tremendous and deep thanks are extended to my love, my wife Parisa, without whom I could not have completed this journey. Her patient, support and unwavering belief in me were the main source of confidence and motivation to complete this thesis.



## Preface

There are a number of figures and tables contained in this dissertation that have been previously published, whereby I was author for such publications. I have received significant support from co-authors (from previous published works) in terms of feedback regarding figures and tables produced; however, all such figures and tables are my original work. As well, all permissions have been obtained from co-authors so that figures and tables can be reproduced within the body of this thesis. Lastly, all such figures and tables are appropriately referenced when they are reproduced from another published source.



## Abstract

How much freshwater do we have on land? How is the freshwater cycle changing with time? Actually, we can not properly answer these questions as our knowledge of the spatial and temporal dynamics of the hydrological cycle is limited. The lack of knowledge is mainly induced by shortage of observational evidence, which motivates the objective of this study: the monitoring of the hydrological cycle using spaceborne geodetic sensors. Among the current space geodetic sensors, GRACE and satellite altimetry are the two active mission concepts, that can capture part of the hydrological cycle. However, monitoring the hydrological cycle using these two sensors is challenging.

Satellite altimetry is investigated as an independent spaceborne sensor that provides the water level and discharge time series. An algorithm is developed to improve the quality of water level time series over inland water surfaces. This algorithm particularly deals with the challenges of resolution and uncertainty of altimetry. The obtained altimetric water level time series is validated against *in situ* measurements showing about 10% improvement in accuracy of the time series. Moreover, this study proposes an algorithm to reduce the random noise from pre-retracked data. The algorithm combines the results of different retrackers and provides water level time series with reduced noise level. The validation shows a significant reduction of noise level and a clear improvement in correlation with *in situ* measurements.

Moreover, this study proposes a statistical approach based on quantile functions to infer a functional relationship between altimetric water level and *in situ* river discharge without the need for synchronous data sets. This method is based on a scatter diagram of quantile functions, in which the probability-coordinate is eliminated. In contrast, the conventional methods for simultaneous measurements operate directly on time series and eliminate the time-coordinate. The results show that the proposed methodology provides the same range of error as the common conventional empirical method. The good performance of the statistical approach supports the usage of altimetry to salvage pre-satellite altimetry discharge data and turn them into active use for the satellite altimetry time frame. In addition, a stochastic process model is implemented to (i) deal with the data outages in altimetric discharge, (ii) provide a scheme for data assimilation and (iii) smooth the discharge estimation. The model benefits from the cyclostationary behaviour of the discharge and is combined with the estimated discharge from altimetry and available *in situ* measurements to form a linear dynamic system. The dynamic system is solved using the Kalman filter, that provides an unbiased discharge with minimum variance. The error level of the results is comparable to the empirical approach.

In this study, the utility of GRACE data as sensor of hydrological water storage changes is shown to be limited by the following challenges: consistency, resolution, separability and uncertainty. The challenge of inconsistency is addressed by developing two filters for hydrological and hydro-meteorological water storage changes, which lead to a better correlation with GRACE mass storage changes. The challenges of separability and resolution are not specifically investigated in this study, yet their consequences, which appear in different forms of uncertainties is investigated.

To deal with the GRACE uncertainties, an algorithm is developed to detect outliers in monthly solutions. The outliers have been corrected by replacing them by an inter-annual monthly mean of the respective month. The results conclude that outlier identification and correction must be performed before further assimilation of GRACE products into hydrological or hydro-meteorological analysis. Further, a long-range correlation has been identified as another source of uncertainty in GRACE monthly solutions. EOF analysis is employed to identify the zonal behaviour of the GRACE  $C_{20}$  errors as the responsible source for the long-range correlation. It is considered as an error source because its residual contains tidal aliasing errors instead of white noise. Therefore, to reduce the uncertainties in GRACE monthly solutions, tidal aliasing errors are also investigated. Primary and secondary tidal aliasing errors of main tidal constituents, S1, S2, P1, K1, K2, M2, O2, O1 and Q1 are identified in GRACE monthly solutions. The effect of tidal aliasing error is estimated using a least squares Fourier analysis indicating errors up to 22 mm over the globe.

In general, after dealing with GRACE's challenges and achieving a data set without outliers, long-range correlation and tidal aliasing errors, the noise level of GRACE is quantified. The quantification shows a variation between 2–20 mm/month over different parts of the globe, with higher values over tropical and boreal regions. The results specifically confirm that small catchments in the tropics contain more noise contamination. It is also shown that a lower noise level of a catchment does not necessarily lead to a better correlation of GRACE with hydro-meteorological signal.

Finally, the joint performance of spaceborne geodetic sensors for estimating the actual evapotranspiration  $ET_a$  is assessed. There, two approaches are introduced to estimate  $ET_a$  using the results of GRACE and satellite altimetry. The results of both approaches are compared with different models and their ensemble mean. All in all, given the obtained relative discrepancy, the methods seem to be a viable way for determining  $ET_a$  for most non-desert catchments containing hot and warm summers.

## Zusammenfassung

Wie viel Süßwasser haben wir auf dem den Kontinenten? Wie ändert sich der Wasserkreislauf mit der Zeit? Eigentlich können wir diese Fragen nicht richtig beantworten, da unser Wissen über die räumliche und zeitliche Dynamik des hydrologischen Zyklus begrenzt ist. Die mangelnden Kenntnisse werden vor allem durch den Mangel an Beobachtungen verursacht. Aus diesem Grund stellt sich diese Arbeit zum Ziel, den Wasserkreislauf mit satellitengestützten geodätischen Sensoren zu überwachen. Unter den aktuellen geodätischen Sensoren gelten GRACE und Satellitenaltimetrie als zwei aktive Missionen, die Teile des hydrologischen Kreislaufs erfassen können. Allerdings stellt die Überwachung des Wasserkreislaufs mit diesen zwei Sensoren eine Herausforderung dar.

Es wird in dieser Arbeit untersucht, inwieweit Satellitenaltimetrie als unabhängiger Sensor der Wasserstand und Abflusszeitreihen bereitstellen kann. Daher wurde ein Algorithmus entwickelt, um die Qualität von Wasserstandszeitreihen zu verbessern. Vor allem befasst sich dieser Algorithmus mit den Herausforderungen der Auflösung und Unsicherheit der Altimetrie. Die erhaltenen altimetrischen Wasserstandszeitreihen wurden gegenüber in-situ-Messungen validiert und zeigen eine Genauigkeitsverbesserung von ca. 10% der Zeitreihen. Darüber hinaus schlägt diese Arbeit einen Algorithmus vor, um das Rauschen der *pre-retracked* Daten zu reduzieren. Der Algorithmus kombiniert die Ergebnisse der verschiedenen *retrackers* und liefert Wasserstandszeitreihen mit reduziertem Rauschpegel. Die Validierung zeigt außer einer signifikanten Reduktion des Rauschpegels eine deutliche Verbesserung der Korrelation in den in situ Messungen.

Außerdem schlägt diese Studie einen statistischen Ansatz vor, der sich auf sogenannten Quantil-Funktionen basiert, um eine funktionale Beziehung zwischen altimetrischem Wasserstand und der in-situ Abflussmenge abzuleiten, ohne dass dafür synchrone Daten verfügbar sein müssen. Dieses Verfahren basiert sich auf einem Streudiagramm der Quantil-Funktionen, so dass die Wahrscheinlichkeit-Koordinate eliminiert wird. Dagegen arbeiten die herkömmlichen Verfahren für gleichzeitige Messungen direkt auf die Zeitreihen und beseitigen die Zeit-Koordinate. Die Ergebnisse zeigen, dass die vorgeschlagene Methode ein ähnliches Fehlerniveau wie konventionelle empirischen Methoden liefert. Die gute Leistung des statistischen Ansatzes erlaubt die Benutzung von alten Abflussdaten und rettet diese sozusagen in den Zeitraum der Satellitenaltimetrie hinüber. Darüber hinaus ist ein stochastisches Prozessmodell implementiert um (i) sich mit den Daten lücken im altimetrischen Abfluss zu befassen, (ii) eine Methodik für die Datenassimilation bereitzustellen und (iii) die Abflussschätzung zu glätten. Zusammen mit den altimetrisch geschätzten Abflüssen und den vorhandenen in-situ-Daten bildet das Prozessmodell ein dynamisches System. Das dynamische System wurde mit dem Kalman-Filter gelöst, welches einen Unverzerrten Abfluss mit minimaler Varianz ergibt. Die Fehler der Kalman-Filterlösung sind dem RMSE von empirischen und statistischen Ansätzen vergleichbar.

In dieser Arbeit wird die Nutzbarkeit von GRACE-Daten als Sensor für die hydrologische Wasserspeicheränderung durchgeführt. Sie wird durch folgende Herausforderungen begrenzt: Konsistenz, Auflösung, Trennbarkeit und Unsicherheit. Die Herausforderung der Inkonsistenz wird durch die Entwick-

lung von zwei Filtern für hydrologische und hydro-meteorologischen Wasserspeicheränderungen ange- sprochen, die zu einer besseren Korrelation mit GRACE Massenspeicheränderungen führt. Die Her- ausforderungen der Trennbarkeit und Auflösung sind nicht speziell in dieser Studie untersucht worden. Allerdings würden deren Wirkungen, die in verschiedenen Formen erscheinen untersucht.

Um mit den GRACE-Unsicherheiten umzugehen, wird ein Algorithmus entwickelt zur Ausreißererkennung. Die Ausreißer werden so korrigiert, dass sie durch einen mehr-jährlichen Monatsmittelwert des jeweiligen Monats ersetzt sind. Es ergibt sich, dass die Ausreißeridentifikation und -korrektur vor einer weiteren Assimilation von GRACE-Produkte in hydrologische oder hydro-meteorologische Analysen durchgeführt werden sollen. Zusätzlich ist eine weiträumige Korrelation als eine weitere Quelle der GRACE-Unsicherheit in monatlichen Daten identifiziert worden. Die EOF-Analyse wird verwendet, um das zonale Verhalten vom GRACE  $C_{20}$ -Fehler als die verantwortliche Quelle für die großräumige Korrelation zu identifizieren. Dieses wird als eine Fehlerquelle betrachtet, weil sein Residuum Gezeiten- Aliasing-Fehler anstatt weißes Rauschen enthält. Um die Unsicherheiten bei GRACE monatlichen Lösun- gen zu reduzieren, werden die Gezeiten-Aliasing-Fehler untersucht. Primäre und sekundäre Gezeiten- Aliasing-Fehler von Haupt-tiden, S1, S2, P1, K1, K2, M2, O2, O1 und Q1 sind in GRACE Monatsdaten identifiziert worden. Die Auswirkung der Gezeiten-Aliasing-Fehler wird mit der kleinsten Quadrate Fourier-Analyse geschätzt, welche global eine Größenordnung von bis zu 22 mm erreicht.

Nach Auserreißereliminierung, Beseitigung der großräumigen Korrelation und Reduktion der Gezeiten- Aliasingfehler kann schließlich das Rauschniveau von GRACE qualifiziert werden. Es zeigt sich eine Variation zwischen 2–20 mm/Monat über verschiedene Teile der Welt, mit höheren Werten über tropische und boreale Regionen. Die Ergebnisse bestätigen, dass die kleinen Einzugsgebieten in den Tropen mehr Rauschen enthalten. Es ist auch gezeigt, dass ein niedriger Rauschpegel von einem Einzugsge- biet nicht unbedingt zu einer besseren Korrelation von GRACE mit dem hydro-meteorologischen Signal führt.

Schließlich wird die Leistung der satellitengestützten geodätischen Sensoren zum Schätzen der tatsäch- lichen Verdunstung  $ET_a$  beurteilt. Es werden zwei Ansätze vorgestellt, um die Verdunstung unter Ver- wendung der Ergebnisse der GRACE und Satellitenaltimetrie zu schätzen. Die Ergebnisse der beiden Ansätze werden mit verschiedenen Modellen und ihrem Ensemble Mittelwert verglichen. Alles in allem zeigen die erhaltenen relativen Abweichungen, dass die Methoden für die meisten nicht-ariden Einzugs- gebieten mit heißen und warmen Sommern ein gangbarer Weg zur Bestimmung von  $ET_a$  sind.

# Contents

|  |           |
|--|-----------|
| <b>1 Introduction</b>  | <b>7</b>  |
| 1.1 Monitoring the hydrological cycle by spaceborne geodetic sensors . . . . . | 10        |
| 1.2 Challenges . . . . .   | 13        |
| 1.2.1 Precipitation . . . . .  | 13        |
| 1.2.2 Discharge . . . . .  | 14        |
| 1.2.3 Changes in the water storage . . . . .                                   | 17        |
| 1.2.4 Moisture flux divergence ( $\nabla \cdot \vec{Q}$ ) . . . . .            | 20        |
| 1.2.5 Actual evapotranspiration ( $ET_a$ ) . . . . .                           | 21        |
| 1.3 Objective . . . . .  | 21        |
| 1.4 Outline of the thesis . . . . .  | 23        |
| <b>2 Monitoring inland water level variations by satellite altimetry</b>       | <b>25</b> |
| 2.1 Principle of measurement . . . . .   | 25        |
| 2.2 Controls of resolution . . . . .   | 28        |
| 2.2.1 Footprint size . . . . .   | 28        |
| 2.2.2 Footprint location and the off-nadir effect . . . . .                    | 31        |
| 2.3 Controls on uncertainty . . . . .  | 32        |
| 2.3.1 Outlier elimination . . . . .  | 34        |
| 2.3.2 Off-nadir correction . . . . .   | 35        |
| 2.3.3 Random noise reduction . . . . .   | 36        |
| 2.3.3.1 Excluding noisy waveforms . . . . .                                    | 39        |
| 2.3.3.2 Unsupervised classification of waveforms . . . . .                     | 43        |
| 2.4 Random noise reduction on retracked data . . . . .                         | 50        |
| 2.4.1 Validation of the combination approach . . . . .                         | 54        |
| <b>3 River discharge from satellite altimetry</b>                              | <b>57</b> |
| 3.1 Controls on consistency problem . . . . .                                  | 58        |
| 3.1.1 Consistency check for rivers in group 1 . . . . .                        | 61        |
| 3.1.2 Consistency check for rivers in group 2 . . . . .                        | 62        |
| 3.2 Modeling the rating curve . . . . .  | 64        |
| 3.2.1 Modeling the rating curve for rivers in group 1 . . . . .                | 64        |
| 3.2.2 Modeling the rating curve for rivers in group 2 . . . . .                | 65        |

|          |   |            |
|----------|---|------------|
| 3.3      | River discharge estimation . . . . .  | 70         |
| 3.4      | Validation of statistical approach . . . . .                                      | 72         |
| 3.5      | Stochastic process model and Kalman filtering . . . . .                           | 78         |
| 3.5.1    | Validation of estimated discharge using Kalman filter . . . . .                   | 84         |
| <b>4</b> | <b>Water storage changes by GRACE</b>   | <b>87</b>  |
| 4.1      | Consistency challenge . . . . .   | 88         |
| 4.2      | Challenge of resolution . . . . .   | 93         |
| 4.3      | Challenge of separability . . . . .   | 93         |
| 4.4      | Challenge of uncertainty . . . . .  | 94         |
| 4.4.1    | Outlier identification algorithm . . . . .  | 95         |
| 4.4.2    | Long-range correlations . . . . .   | 102        |
| 4.4.3    | Tidal aliasing error . . . . .  | 111        |
| 4.4.3.1  | Removing the effect of tidal aliasing error . . . . .                             | 114        |
| 4.4.3.2  | Impacts of removing tidal aliasing errors . . . . .                               | 120        |
| 4.5      | Noise level of GRACE . . . . .  | 126        |
| <b>5</b> | <b>Estimation of actual evapotranspiration using space-borne geodetic sensors</b> | <b>129</b> |
| 5.1      | $ET_a$ from GRACE and hydro-meteorological approaches . . . . .                   | 130        |
| 5.2      | $ET_a$ from GRACE-altimetry approach . . . . .                                    | 137        |
| <b>6</b> | <b>Summary, conclusion and recommendation</b>                                     | <b>139</b> |
| 6.1      | Summary and conclusion . . . . .  | 139        |
| 6.2      | Perspective of future work . . . . .  | 145        |
| <b>A</b> | <b>Waveform retracking algorithms</b>   | <b>169</b> |
| A.1      | Fitting algorithm $\beta$ -parameter retracking . . . . .                         | 169        |
| A.2      | The Off Center Of Gravity (OCOG) retracker . . . . .                              | 171        |
| A.3      | Threshold retracker . . . . .   | 172        |
| A.4      | Surface/volume scattering retracking . . . . .                                    | 173        |

# Chapter 1

## Introduction

For a long time, geodesy and the representation of the Earth had been confined to classical geodetic networks and using ordinary geodetic instruments e.g. theodolites and gravimeters. In the early 20<sup>th</sup> century, geodesy was way beyond the measurement capabilities of the day with the goal of improving the accuracy of measurements. A few years later after improving the measurements technology, theory needed to be improved again. Hence, the goal of geodesy was understood to be increasing the resolution of the grid networks in the scope of sub-disciplines: horizontal control, vertical control and physical geodesy (Barlier and Lefebvre, 2001; Sneeuw, 2000). Along with achieving these goals in the mid 20<sup>th</sup> century, the missing link for monitoring the Earth was realized as homogeneous networks on a continental scale. The NAD datum (North American Datum) and the ED50 datum (European datum) are examples of efforts for tackling the missing link by homogenizing the local geodetic networks. However, these efforts seemed to be time consuming and unaffordable as the networks had to be created by manual surveying of the entire continent. For homogenizing the networks, a tall fixed reference target that is visible over large distances could have solved many of problems. However, visibility of the target is only possible, when the target is big enough to be captured through optical techniques. In astro-geodesy since beginning of the 19<sup>th</sup> century the Moon and the stars are regarded as geometric targets for the study of the Earth. For instance, *Laplace* in the year 1802 used nodal motion of the Moon to determine the flattening of the Earth (Seeber, 2003). With the advance of technology, the geometrical approach in astro-geodesy was accelerated. Efforts like the development of dual rate Moon position camera by Markowitz (1954) provided room for geodetic studies and operational purposes. The geometrical methods were followed and further developed by other researchers, which ushered in satellite geodesy and led to need for having artificial satellites. However, the primary questions about the artificial satellite were: what should and can be monitored by an artificial satellite? How to use measurements for Earth studies?

An orbiting artificial satellite, that is visible by optical techniques from long distances was one of the initial ideas. With this approach, artificial satellite could serve as 1) high target reference point, 2) proof mass in gravitational field, 3) gyroscope for inertial orientation and/or 4) a platform for observation. However, such approach was obviously limited as the magnitude of a moving target is a function of many limiting factors e.g. energy consumption, atmospheric friction, etc. Therefore, other methods had

to be found instead of optical methods such as communication between the satellite and ground stations through radio signals.

Finally all the notions and ideas were realised by launching the *Sputnik 1* on October 4, 1957. The launch was a turning point in political, military, technological, and scientific developments (Launius, 2009). Particularly, *Sputnik 1* helped to identify the upper atmospheric layers's density through measuring the satellite's orbital changes (Krassovsk, 1959). In the year after, the launch of *Explorer 1* and *Sputnik 2* helped to determine the Earth flattening more accurately (Seeber, 2003). The development of satellites moved fast and in a functional way, such that with improving the representation of the Earth further developments were demanded. The demand of having a positioning system led to the launch of *Transit* satellite in 1960, which was designed to provide accurate location information by being located in a orbit with an altitude of 1100km. The demand of determining the leading spherical harmonic coefficients of the geopotential field led to the launch of the first dedicated geodetic satellite *ANNA-1B* in October 1962 (Burkard, 1983). *ANNA-1B* was one of the first active satellites as it was emitting very bright flashes of light for being captured by ground stations. Shortly after, the first two GEOS satellites (launched in 1965 and 1968) were developed under the Explorer program (Douglas et al., 1974). They consisted of a number of optical and wireless systems for accurate tracking, and laser reflectors. As active satellites, they were an evolution of the *ANNA-1B* and could send out short series of six to seven flashes at times when they could be optically observed from Earth.

By increasing the number of launched satellites, the community came to realize the need for a world geodetic system. World Geodetic System (WGS) 60, 66, 72 and 84 are samples of geodetic systems, which were established through a worldwide triangulation on the observations of satellites (Badekas, 1969; Burkard, 1983). A very high altitude satellite positioning system could have led to a more precise positioning of satellites. Therefore, the Global Positioning System (GPS) project was developed in 1973 to overcome the limitations of previous navigation systems and positioning the low orbit satellites. It became fully operational in 1994 (Aeronautics & Space Engineering Board, 1995).

After launching GPS satellites and serving them as space-based reference points, satellite geodesy entered into the geo-dynamics and earthquake studies (Segall and Davis, 1997). Using the precise positioning of GPS, other artificial satellites could be considered as accurate sensors. Especially non-active geodetic satellites could sense the gravity field and help to determine its parameters. On the other hand, active geodetic satellites could be designed as sensors to monitor the changes over the globe by sensing the varying parameters e.g. sea or inland water level.

In general, assuming the satellites as sensors conducted the application of satellite geodesy for other sciences like oceanography and hydrology. In oceanographic application, active satellites like satellite altimetry particularly help to estimate and monitor the ocean circulation, sea level variations due to the global warming and tides. Satellite altimetry measures height by estimating the time taken by a radar pulse to travel from the satellite antenna to the surface and back to the satellite receiver. These measurements are combined with precise satellite location data yielding surface water heights (Fu and Cazenave, 2001). Since satellite altimetry monitors the surface water heights, it can also contribute to

hydrological studies (Calmant and Seyler, 2006). The hydrological application of satellite altimetry has been mainly explored after TOPEX/Poseidon and ERS-1/ENVISAT began to operate.

TOPEX/Poseidon is the first dual frequency (Ku and C band) radar altimeter space mission designed to accurately measure global ocean topography. TOPEX/Poseidon satellite was launched on August 10, 1992, on a near circular orbit with  $\beta/\alpha = 127/10$  (Fu et al., 1994). The repeat cycle is 10 nodal days, which corresponds to 9.915 solar days. The orbit inclination is  $66^\circ$  which enables the observation of the ocean within corresponding latitude bounds (Zieger et al., 1991). TOPEX/Poseidon's successor mission, Jason-1, was launched in 2001 to continue the on-going measurements of sea surface topography. At the same time, TOPEX/Poseidon and Jason-1 were placed in the same orbit forming a so called tandem phase, in which they were separated by only about 70 seconds. The tandem phase lasted about 7 months and on August 2002 TOPEX/Poseidon was moved into an orbit with the same ground tracks, though shifted by half a track spacing (Haines et al., 2010).

ENVISAT was launched in March 2002 as a successor of ERS-1 and ERS-2 by the European Space Agency (ESA) (Frappart et al., 2006a). During March 2002–October 2010, it flew on a sun-synchronous orbit at an altitude of 790km. The orbit had an inclination of  $98.5^\circ$  that leads to a global coverage of the Earth between latitudes of  $\pm 81.5^\circ$  (da Silva et al., 2010). The  $\beta/\alpha = 501/35$  leads to ca. 80km inter-track distance at the equator, i.e. less than TOPEX/Poseidon's spacing of 311km. In October 2010 the satellite moved to lower orbit to ensure an additional 3 years lifespan. However, the end of the mission was formally announced in May 2012 after loss of contact in April 2012. ENVISAT carried an array of Earth observation instruments that gather information about the earth (land, water, ice, and atmosphere) using a variety of measurement principles. Radar Altimeter 2 (RA-2) was one of these instruments. It was a dual-frequency nadir pointing radar operating in the Ku (13.575 GHz) and S (3.2 GHz) bands.

Apart from altimetry satellites, other missions with different measurement concepts also pave the way of using artificial satellite for oceanographic and hydrological application. Gravity Recovery and Climate Experiment (GRACE), Gravity Field and Steady-State Ocean Circulation Explorer (GOCE) are two examples of those missions.

The GRACE satellites, a joint mission of NASA (National Aeronautics and Space Administration) and DLR (German Aerospace Center), were launched in March 2002 (Tapley et al., 2004). These two satellites were placed in the same orbit, separated by ca. 220km. The mission provides a direct measure of monthly water storage changes by estimating the relative motion of the mass center of the two satellites, which is measured with an highly accurate inter-satellite K-band microwave link. The use of GRACE gravity data allows to determine continental water storage changes and to close the water budget on short time scales for the first time (Rodell and Famiglietti, 1999; Dickey et al., 1999; Rieger and Guntner, 2005).

GOCE was launched on March 2009 on a sun-synchronous, near-circular, low-Earth orbit with altitude of 260km and inclination of  $96.7^\circ$  (Drinkwater et al., 2003). It carries a highly sensitive gravity gradiometer to detect fine density differences in the crust and oceans of the Earth. Particularly, the direction and speed

of geostrophic ocean currents can be estimated by combining the gravity data of GOCE with estimation of sea surface height derived from satellite altimeters.

The aforementioned missions promote a number of novel approaches in oceanography, geophysics, hydrology and hydro-meteorological sciences. Among these sciences, in hydrology there is a pressing need for more observational evidence. This necessity arises from the evident limited knowledge of the spatial and temporal dynamics of the surface freshwater variations and discharges (Alsdorf et al., 2002). The questions like: How much freshwater do we have on land? How is it changing with time? can not be answered properly. The estimation of freshwater on surface, ground, snow or soil moisture are confined to rough estimates based on ad hoc assumptions. At the surface, knowledge about water surface height variation and bathymetry of rivers and lakes are limited. The depth of soil moisture is not really known in global scale. Rain gauge measurements do not provide reasonable areal representation of input to hydrological cycle. The global publicly available discharge database is declining steadily over the past few years. Therefore, this study is focused into the monitoring of the hydrological cycle by spaceborne geodetic sensors.

## 1.1 Monitoring the hydrological cycle by spaceborne geodetic sensors

The most fundamental principle of hydrology is the hydrological cycle. The hydrological cycle represents the way in which the water evaporates by solar energy from the oceans and the land surface and is carried over the earth in atmospheric circulation as water vapor. It precipitates again as rain or snow and intercepted by vegetation and trees, which provide runoff on the land surface and storage changes within. Gravity causes the infiltration of the surface runoff into soils and recharges groundwater. The water then discharges into streams and ultimately flows out into the ocean from which it will evaporate once again (Maidment, 1993). Figure 1.1 illustrates schematically the hydrological cycle.

The endless hydrological cycle proceeds in the absence or presence of human activity, but increasing amounts of CO<sub>2</sub> and other greenhouse in the earth's atmosphere, related to human activities, lead to global warming. The current global warming compels change in the speed of hydrological cycle process. Many scientists believe that a speeding up of the hydrological cycle may lead to more extreme weather conditions on parts of the earth, which affects human's life. (Hendriks, 2010). To that end, monitoring the hydrological cycle is crucial to human life. As discussed before, knowledge of the spatial and temporal dynamics of hydrological cycle is limited (Alsdorf et al., 2002). Measuring the hydrological cycle components is the starting point of study on hydrological cycle and overcoming the limitations. Therefore, it is needed to quantitatively describe the hydrological cycle. Water balance equations define the hydrological cycle in quantitative terms. In general, in any river basin the amount of water entering and leaving would lead to a change in the storage,  $\Delta S$ , which can be formulated as

$$\text{inflow} - \text{outflow} = \Delta S . \quad (1.1)$$

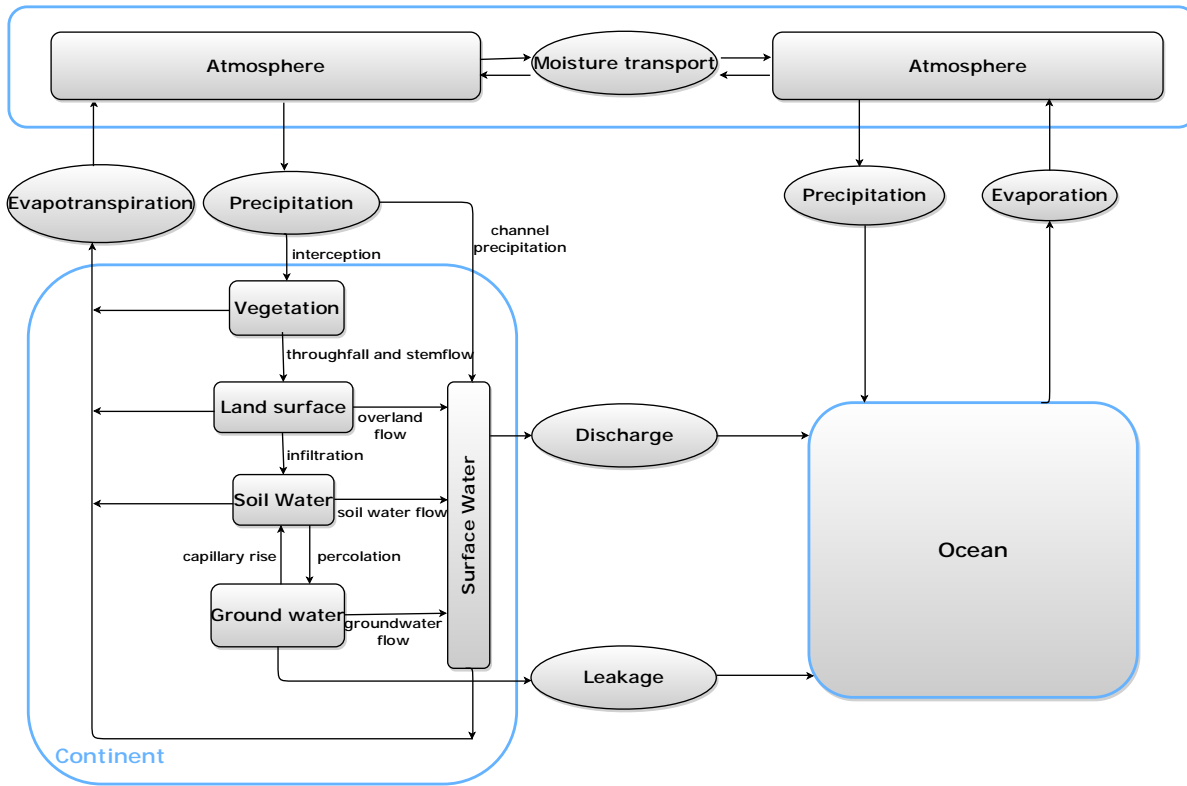


**Figure 1.1:** Schematic illustration of the hydrological cycle, in which the ovals represent input or output processes

Given a certain time period  $\Delta t$  for occurring the inflow, outflow and change in the storage, the equation is

$$\frac{\text{inflow}}{\Delta t} - \frac{\text{outflow}}{\Delta t} = \frac{\Delta S}{\Delta t} . \quad (1.2)$$

Over a river basin, inflow/ $\Delta t$  is precipitation  $P$  and the outflow/ $\Delta t$  can be assumed as summation of evapotranspiration  $ET_a$  and river discharge  $R$  ( $ET_a + R$ ). Evapotranspiration itself consists of two process of evaporation and transpiration. The term transpiration refers to a portion of the water that is absorbed by plant roots and eventually discharged back into the atmosphere. Since the equation (1.2) is also valid instantaneously and is true for very small  $\Delta t$ , the  $\Delta S/\Delta t$  can be turned to  $dS/dt$ , which describes the changes in the water storage within the  $dt$ . Therefore, for river basins the water balance equation can be written as

$$P - ET_a - R = \frac{dS}{dt} , \quad (1.3)$$

On the other hand, for large river basins and at monthly to seasonal time scales, the spatially averaged water budget of the atmosphere can be approximately assumed as precipitation minus evapotranspiration (Fersch, 2011)

$$\frac{dW}{dt} - \nabla \cdot \vec{Q} = P - ET_a . \quad (1.4)$$

The  $dW/dt$  is the variation of atmospheric water storage. Due to low average residence time of water vapor in the atmosphere, ca. 9 days (Hendriks, 2010), it can be neglected for the monthly time scale.  $\nabla \cdot \vec{Q}$  denotes the divergence of moisture flux, which is linked to the vertical exchange terms of the terrestrial water balance. By neglecting the  $dW/dt$  and substituting the term  $\nabla \cdot \vec{Q}$  in the equation (1.3), the water balance equation can be rewritten as

$$-\nabla \cdot \vec{Q} - R = \frac{dS}{dt} . \quad (1.5)$$

It is important to note that due to existence of the river discharge parameter, both balance equations (1.3) and (1.5) are only valid over sub-/catchments and not over degree cells. Although equations (1.3) and (1.5) allow us to quantify the hydrological cycle, lack of observations prevent solving and closing the equations for many river basins. Despite the lack of observations, within current hydrological studies, modeling the hydrological interactions using few measurements of hydrological components is one of major approaches for quantification of hydrological cycle. However, comparison between different models and gauged observation reveals large model error, sometimes greater than 100% (Alsdorf and Lettenmaier, 2003). Particularly, a large difference between models underlines the necessity of *in situ* measurements for improving and validating the models. However, this becomes increasingly problematic as the worldwide number of gauging stations has been decreasing since the 1970s (Milzow et al., 2011; Fekete and Vörösmarty, 2007), which emphasizes the demand for independent sensors like spaceborne geodetic sensors for observing the hydrological interactions. Nevertheless the way in which these sensors observe the hydrological interactions should be extensively scrutinized. Figure 1.2 demonstrates the range of temporal and spatial scales of the hydrological cycle. The range of temporal and spatial resolution of measurements by current space geodetic sensors GRACE, GOCE and satellite altimetry have been also specified. The range of measurements has specifically been depicted over different compartments of active hydrological cycle i.e. surface water, soil moisture and ground water. GRACE senses the changes in the gravity field at a spatial resolution of ca. 400 km and at monthly time scale (Tapley et al., 2004). It measures the sum of all mass effects within the hydrosphere-cryosphere; it cannot distinguish between the different sources of mass variations. Satellite altimetry provides observations of the surface water at the temporal resolution of 10 and 35 days (depending on mission) and spatial resolution of ca. 1 km along track and 80–400 km between tracks. Geodetic sensors like GOCE, CHAMP (not shown in the figure) are not able to capture the hydrological cycle as they measure the static part of the gravity field.

As depicted in Figure 1.2, current spaceborne geodetic sensors are not able to capture the fast phenomena of the hydrological cycle. Precipitation and evapotranspiration are the hydrological interactions that mainly belong to the fast branch, as they vary significantly within a day. On the other hand, interception, streamflow, infiltration, percolation, capillary rise, groundwater flow, leakage and discharge all occur on much longer time scales, which can be partially monitored by GRACE and satellite altimetry.

The hydrological interactions and components within different parts of the hydrological cycle should be investigated in terms of observability by any of the mentioned geodetic sensors. Apart from that, the data availability of each component and demand for an independent sensor from space should be also

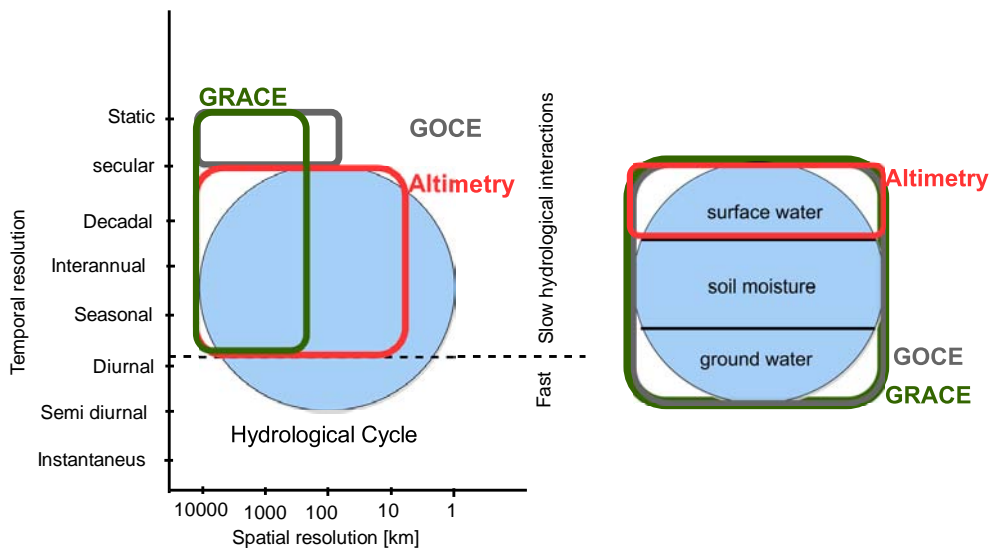


**Figure 1.2:** Spatial and temporal scales of hydrological cycle within different soil compartments and capability of monitoring by spaceborne geodetic sensors of GRACE, GOCE and satellite altimetry

investigated. These issues are defined as challenges of this study, which will be discussed in the next section.

## 1.2 Challenges

A general overview of monitoring the hydrological cycle by spaceborne geodetic sensors has been given in the previous section. This section discusses about data situation and need for measurement by spaceborne geodetic sensors for four major hydrological interactions of precipitation, discharge, changes in the water storage and actual evapotranspiration. Moreover, the data situation of the hydro-meteorological component of moisture flux's divergence will be also studied.

### 1.2.1 Precipitation

Precipitation, one of the fast hydrological interactions, is traditionally measured using various types of rain gauges such as the non-recording cylindrical container, the recording weighing, float, and tipping-bucket type. In the recent past, precipitation is also measured with weather radar and weather satellites. Generally, due to adequate amounts of sensors, global gridded precipitation data is available from different data providers e.g. Climatic Research Unit (CRU), Global Precipitation Climatology Center (GPCC), Global Precipitation Climatology Project (GPCP), Tropical Rainfall Measuring Mission (TRMM) by NASA and University of Delaware. Some of the data centers provide gridded data in mm/day or mm/month only over the continents and some also provide the data over the oceans.

Although precipitation is measured more regularly, its large systematic and random errors are well known, which often arise with large uncertainties from the use of imperfect gauging techniques (Fekete et al., 2004). In fact, the main concern regarding the precipitation data is the quality of the data rather than the data availability (Habib et al., 2001). The quality of the gridded precipitation fields depends primarily on the number of active gauges and their spatial distribution (Lorenz and Kunstmann, 2012). As an example, Figure 1.3 shows aggregated precipitation time series over the Amazon basin for the time period of 1986–2002 from four different products (see equation (1.7) for aggregation). Visual inspection reveals that GPCP is mostly overestimated. The overestimation of GPCP can be quantified by the mean annual amount of precipitation for the time period of 1986–2002 (Table 1.1). The average values of mean annual precipitation of the 255 largest basins from different products express a good agreement between the GPCC, CRU and Uni Delaware data and overestimation of GPCP.

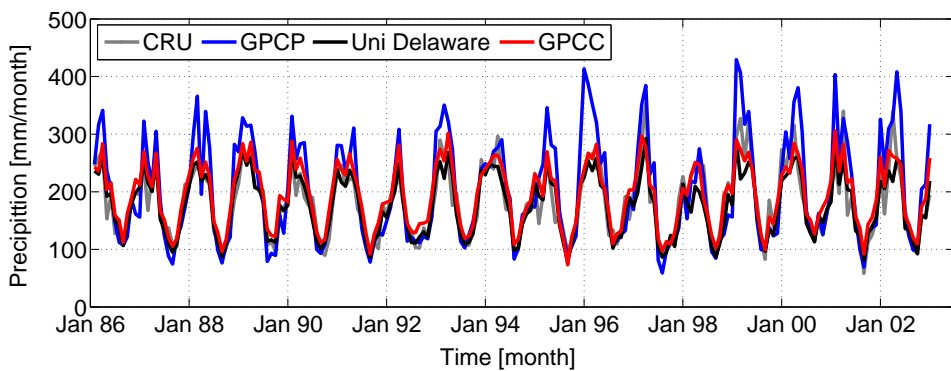


**Figure 1.3:** Comparison of different precipitation products for the Amazon catchment

**Table 1.1:** Mean annual precipitation of different products averaged over all catchments

| Product     | Average |
|-------------|---------|
| CRU         | 746.7   |
| GPCC        | 750.5   |
| GPCP        | 863.7   |
| UniDelaware | 738.1   |

Since current geodetic sensors do not cover fast variations of the hydrological cycle, the contribution of spaceborne geodetic sensors for measuring precipitation is limited. In this study, precipitation from GPCC is chosen for further analysis as it provides more consistent water storage changes with GRACE and hydro-meteorological signals (Rieger et al., 2012).

### 1.2.2 Discharge

River discharge plays an important role in hydrological studies, being an output from hydrological models and input to many hydrological interactions. River discharge can not be measured directly and it

is calculated from the average stream velocity and cross-sectional area of river. The data is available from different sources: Global Runoff Data Center (GRDC), ArcticRIMS project, water survey Canada, United States Geological Survey (USGS), United States Army Corps of Engineers (USACE), ORE HYBAM project, department of water, land and biodiversity conservation by the government of Australia and the department of water affairs and forestry by the Republic of South Africa. However, due to several reasons like changing data policy, financial constraints and declining *in situ* measurement, the publicly available database is limited in spatial and temporal coverage and has been on the decline, lately. This decline is highlighted in Figure 1.4, in which the number of available stations with discharge data declines by the time. A full range of data for the period of 1980–2010 is only available for 47 out of the 255

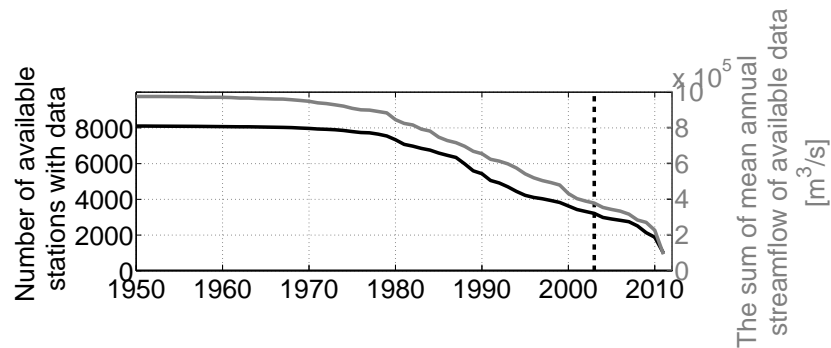


**Figure 1.4:** Evolution of available stations with discharge data according to GRDC database together with the sum of mean annual streamflow of available data. Among the 8424 stations around the world only 3323 gauging stations are available after launching of ENVISAT and GRACE (dashed line)

largest catchments including dischargeless basins (Figure 1.5). However, their spatial distribution covers the main climatic zones comprising northern tundra, moderate, semi-arid, arid and tropical catchments (Figure 1.6).

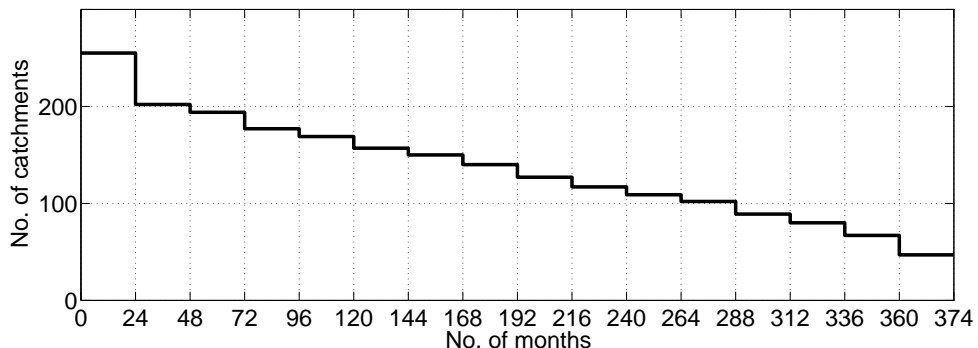


**Figure 1.5:** Number of catchments with area larger than  $30\,000\text{ km}^2$  with discharge data covering different time periods within the period of 1980–2010

In general, since the global publicly available discharge database is declining steadily over the past few years, the current and future river discharge data situation is not satisfactory. Hence, the demand of using independent sensors and algorithm to obtain river discharge seems to be urgent.

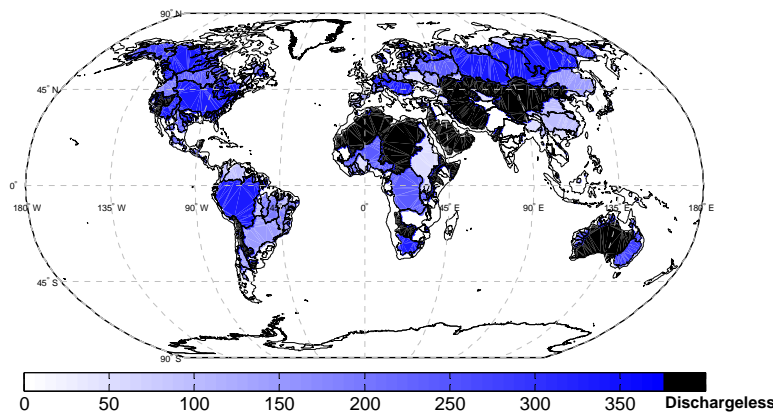


**Figure 1.6:** Spatial distribution for number of available months within the period of 1980–2010 for catchment with area larger than  $30\,000\text{ km}^2$

As river discharge is a relatively slow hydrological process occurring at the surface water layer, it can be captured by satellite altimetry. The intersection of a satellite track with a water body can be defined as a *virtual station*. Fundamentally, a satellite altimeter measures surface water height. The measured height can be turned into a discharge value through functional relation. The river discharge at the selected gauges is typically determined from an empirical functional relation between water level estimated by satellite altimetry at a virtual station close to discharge gauging station and measured discharges at the gauge (Zakharova et al., 2006). This relation, referred to as a *rating curve*, is specific to each gauging station. This conventional method needs simultaneous measurements of water level from altimetry and *in situ* discharge measurements. Such a methodology brings certain challenges

- **Uncertainty:** satellite altimetry was originally designed for oceans and due to various disturbing effects like size of inland water bodies, vegetation canopy and neighboring topography, the quality of measurements over the inland waters is generally poor.
- **Consistency:** satellite altimetry provides only 10 (TOPEX/Poseidon) and 35 (ENVISAT) days interval time series and discharge measurements are often available in daily or monthly time scales. These 10/35 days values do not lead to daily or monthly time series, as altimetry provides snapshot measurements of water level. Moreover, the conventional technique for extracting river discharge is limited by the availability of *in situ* discharge measurements simultaneous with altimetry data. In case of using ENVISAT altimetry, simultaneous measurements mean that discharge data should be available after the year 2003. This becomes a serious restriction as GRDC database provides discharge data after 2003 for only 40% of stations cf. Figure 1.4.
- **Resolution:** the inter-track distance of altimetry ground track at the equator is approximately 80 and 311km for ENVISAT and TOPEX/Poseidon, respectively. Thus, missing some of the inland water bodies and rivers by altimetry is inevitable. Moreover, the along track distance of 20 Hz altimetry is ca. 370m, which might lead to very few measurements over narrow rivers. Besides

that, the temporal resolution of 10 or 35 days time interval of altimetry does not allow to study very dynamic rivers.

In fact, each of these mentioned challenges are linked to each other. The inappropriate spatial and temporal resolution brings inconsistency and uncertainty. Moreover, the inherent uncertainty of satellite altimetry leads to more inconsistency of water level from altimetry and *in situ* discharge measurements (Figure 1.7).

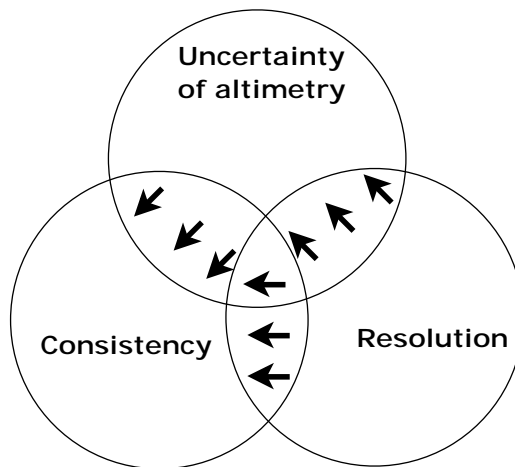


**Figure 1.7:** Challenges of deriving river discharge from satellite altimetry

The limitations due to the spatial or temporal resolution can not be completely tackled as they are driven by orbit configuration. However, uncertainty and inconsistency due to choosing inappropriate virtual station can be avoided by careful investigation on location of altimetry footprint and illuminated topography. Furthermore, the inherent uncertainty of measurements can be reduced using post-processing refinements. For the consistency problem, a comprehensive investigation is demanded to avoid miss-modeling of the rating curve.

### 1.2.3 Changes in the water storage

For a long time, a direct observation of the water storage components e.g. snow, ice, surface water, soil, un/saturated underground storages was not possible on large spatial scales (Rodell and Famiglietti, 1999). Measurements of water storage changes by measurements of changes in groundwater levels and in soil water saturation are not reliable due to the insufficiently known storage coefficients and the inadequate density of monitoring points on large spatial scales (Strassberg et al., 2007; Yeh et al., 2006; Rodell et al., 2006; Rieger et al., 2012). Therefore, hydrologists were not able to close the water balance on monthly or seasonal time scales. Only at long time scales, the assumption that long-term average of storage change are negligible would allow a closure of the water balance. For describing the short time scales,

hydrological or atmospheric models have been used, for which the relevant processes and water transfer between the different storage components are integrated (Döll et al., 2003; Rodell et al., 2004a).

Since March 2002, the indirect monthly snapshots of the Earth's gravity field by GRACE allows to determine continental water storage changes and to close the water budget on short time scales (Tapley et al., 2004). It provides detailed measurements of Earth's gravity field, provided in form of spherical harmonic coefficients  $C_{lm}$  and  $S_{lm}$ , which are available from different sources: GeoForschungsZentrum (GFZ), Germany, Jet Propulsion Laboratory (JPL), USA, Center for Space Research (CSR), University of Texas at Austin (Bettadpur, 2007), ITG from University of Bonn (ITG-GRACE, 2010). Within the current GRACE data processing paradigm, data centers attempt to eliminate as much time-variable gravity field signal as possible originating from the GRACE data by applying models of known signal, e.g. tides or atmospheric pressure (Flechtner et al., 2006). Practically, it can be assumed that, GRACE is able to detect those short time scale mass variations on the Earth's surface, which occur only in a thin layer close to the Earth's surface (Wahr et al., 1998). By this consideration, surface mass changes can be transformed to geoid changes and vice versa. Moreover, by assuming that this thin layer consists of water, the surface mass density can be converted into water height which is commonly denoted as *equivalent water height*. Following Wahr et al. (1998), equivalent water height  $M(\theta, \lambda; t)$  is expressed as

$$M(\theta, \lambda; t) = \frac{R\rho_{\text{ave}}}{3\rho_w} \sum_{l=0}^{\infty} \frac{2l+1}{1+k_l} \sum_{m=0}^l P_{lm}(\cos \theta) \times [\Delta C_{lm}(t) \cos m\lambda + \Delta S_{lm}(t) \sin m\lambda] \quad (1.6)$$

where  $\rho_{\text{ave}}$  is the average density of the Earth ( $5515 \text{ kg/m}^3$ ),  $\rho_w$  is the average density of water ( $\rho_w = 1000 \text{ kg/m}^3$ ),  $R$  is the radius of Earth (6378.137 km),  $k_l$  is the Love number,  $P_{lm}$  are normalized associated Legendre functions of degree  $l$  and order  $m$ ,  $\Delta C_{lm}$  and  $\Delta S_{lm}$  are normalized spherical harmonic coefficients after subtracting the temporal mean. This temporal mean is practically estimated over mission duration, which might not represent the real long-term mean. Therefore, one can argue that GRACE is not a reliable sensor for study on climate change. Over a catchment, the estimated equivalent water height,  $M(\theta, \lambda; t)$  is aggregated via area weighted averaging

$$M(\chi; t) \approx \sum_{i=1}^p M(\theta_i, \lambda_i; t) \frac{A_i}{A_\chi} , \quad (1.7)$$

where  $\chi$  is the catchment index,  $p$  are the number of pixels associated with the catchment  $\chi$ ,  $A_i$  is the area of the cell  $i$  in the catchment  $\chi$ , and  $A_\chi$  is the total area of the catchment. Figure 1.8 shows the spatial distribution of  $M$  for a selected month (October 2010) over the globe and aggregated over the catchments. The derivative of aggregated equivalent water heights over individual catchments, hereafter  $dM/dt$ , would ideally be equal to the changes in the respective water storage  $dS/dt$ . Using equations (1.3) and (1.5), the following triangle can be formed, that is valid over each river basin

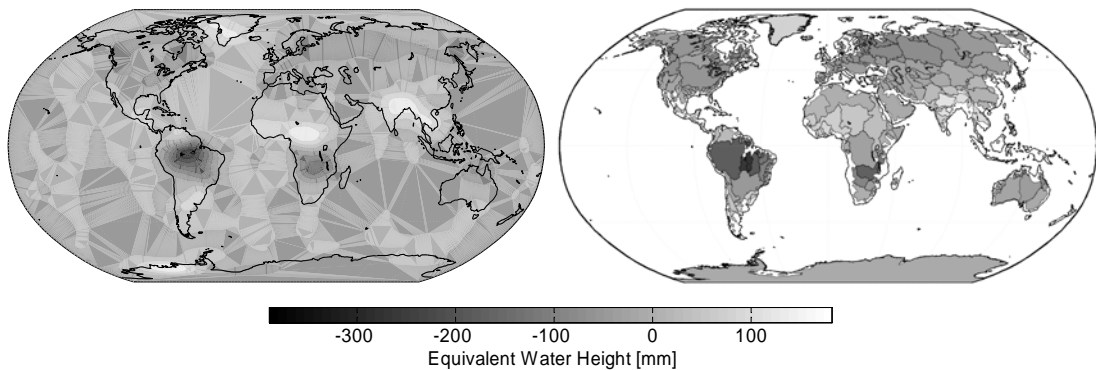


**Figure 1.8:** GRACE release 5 data from GFZ data centre. The left panel shows the grid-based equivalent height,  $M(\theta, \lambda; t)$ , for October 2010 and the right panel shows the aggregated equivalent water height,  $M(\chi)$ , for October 2010 over catchments.

$$\begin{array}{ccc}
 & \frac{dM}{dt} & \\
 \swarrow & & \searrow \\
 \frac{dS}{dt} = (P - R - ET_a) & \longleftrightarrow & \frac{dS}{dt} = -\nabla \cdot \vec{Q} - R
 \end{array} \quad (1.8)$$

In spite of the clear relationship between GRACE, hydrological and hydro-meteorological water storage changes, closing the continental water balance seems to be difficult. Actually, the resulting equivalent water heights are the de-aliased GRACE solutions, for which the de-aliasing models are used to eliminate the effect of known tidal and geophysical signals (Flechtner, 2007). Clearly, any uncertainty in the de-aliasing models shows up in the GRACE solutions. These uncertainties subsequently might lead to an erroneous hydrological interpretation, which limit the utility of GRACE as a reliable hydrological sensor for most basins (Swenson and Wahr, 2003; Velicogna et al., 2001; Han et al., 2004). In general, the utility of GRACE data for hydrological water storage changes is limited by following challenges:

- **Uncertainty:** the errors in de-aliasing models, intrinsic instrumental error (accelerometer, GPS positions of GRACE, etc.), errors emanating from the different stages of data processing (precise orbit determination, lack of proper error propagation, etc.), invisibility of the degree 1 term in GRACE are sources for uncertainties in GRACE data. The uncertainties in GRACE will appear in different forms e.g. outliers and North-South streaks.
- **Resolution:** the 400 km spatial resolution of GRACE limits its application for small basins, where closing continental water balance is hindered by erroneous signals.
- **Separability:** GRACE measures the integrated water storage variations in all storage components on the continents including atmosphere. In order to achieve continental water storage changes, different sources of water storage changes like atmospheric and non-tidal oceanic variations should be estimated and excluded from the GRACE observation, which is a challenging task (Flechtner

et al., 2006). Separability also becomes critical in the evaluation of GRACE data against model based or *in situ* measurements of water storage changes, since models and *in situ* measurements often represent individual parts of storage components (Güntner, 2008).

- **Consistency:** The de-aliasing procedure is very sensitive to the consistency of models and GRACE observation. Therefore, any inconsistency might lead to uncertainty in monthly solutions. Besides that, during the evaluation of GRACE, consistencies of GRACE measurements and hydrological and hydro-meteorological signals are also very important. In fact, the numerical limitations to achieve comparable variation with hydrological or hydro-meteorological signals from those by GRACE lead to inconsistency.

Similar to the challenges for river discharge, these challenges are also linked to each other (Figure 1.9). The inappropriate temporal and spatial resolutions of GRACE cause an uncertainty in the data and affect the consistency of the de-aliasing models with the observations. Accordingly, the uncertainty in GRACE data brings a certain inconsistency with hydrological water storage changes. Also, the inconsistency between the known signal and the observations leads to a mis-modeling within the separation, which provides the uncertainty in the data.

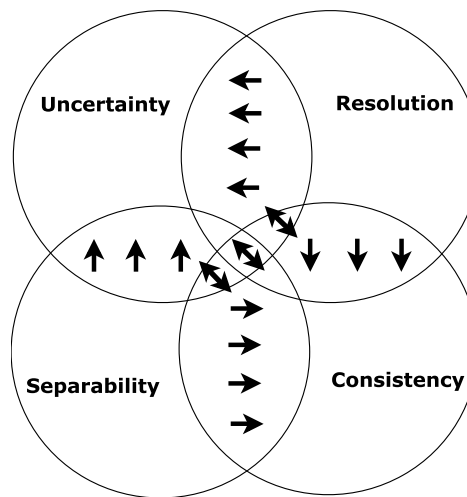


**Figure 1.9:** Challenges of utility of GRACE signals as representative of hydrological water storage changes

#### 1.2.4 Moisture flux divergence ( $\nabla \cdot \vec{Q}$ )

The divergence of moisture flux,  $\nabla \cdot \vec{Q}$ , is linked to the vertical fluxes of the terrestrial water balance. It is estimated through vertical integral of moisture divergence. It is a function of air pressure  $p$  [Pa],

gravitational acceleration  $g$  [m/s<sup>2</sup>], horizontal wind vector  $\vec{v}_h$  [m/s] and specific humidity  $q$  [kg/kg] at different levels from zero pressure to surface pressure  $p_{sfc}$  (Fersch, 2011):

$$\nabla \cdot \vec{Q} = \frac{1}{g} \cdot \nabla \int_{p=0}^{p=p_{sfc}} \vec{v}_h q dp \quad (1.9)$$

$\nabla \cdot \vec{Q}$  is available from different sources: ERA-INTERIM data from the European Centre for Medium-Range Weather Forecasts (ECMWF), MERRA data from NASA (Hirschi et al., 2005) and NNRP1 and NNRP2 data from National Centers for Environmental Prediction / National Center for Atmospheric Research (NCEP / NCAR). For the rest of this study, the net balance of moisture flux data is used from ERA-INTERIM as it leads to optimally consistent water storage changes (Rieger et al., 2012).

### 1.2.5 Actual evapotranspiration ( $ET_a$ )

Actual evapotranspiration is integral to studies of hydrological cycle, yet its quantification and determination is difficult (Rodell et al., 2004a). It is determined over land surface by soil humidity, plant specific maximum evapotranspiration, atmospheric conditions and net radiation (Maidment, 1993; Chow, 1964). A precise point-wise measurement of  $ET_a$  at the gauges seems to be difficult, as it is regulated by complicated factors. In order to estimate or model the evapotranspiration, different methodologies based on water balance methods, water vapor stream methods and energy balance methods are employed. The results of previous studies indicate that the different  $ET_a$  models vary among themselves in the range of 30 % (PILPS, 1996; Gates, 1997).

With the advent of GRACE, a new option can be offered for estimation of actual evapotranspiration. Over a river basin and on a monthly time scale, actual evapotranspiration can be indirectly determined by use of GRACE, precipitation and river discharge data

$$ET_a = P - R - \frac{dM}{dt} \quad . \quad (1.10)$$

Alternatively, it is also possible to use the other part of triangle (1.9) and derive  $ET_a$  as

$$ET_a = P + \nabla \cdot \vec{Q} \quad . \quad (1.11)$$

## 1.3 Objective

The main objective of this study is to monitor the hydrological cycle using spaceborne geodetic sensors. As discussed before, the current sensors capture part of the hydrological cycle, namely the main hydrological processes with certain limitations. Therefore, this study is confined to investigate monitoring the main processes, for which the only spaceborne geodetic sensors of GRACE and satellite altimetry can be

used. Table 1.2 summarizes the data situation, capability of geodetic sensors and their challenges for monitoring the main hydrological processes.

**Table 1.2: Monitoring the hydrological cycle by spaceborne geodetic sensors: capabilities, challenges and possibilities**

|                             | Precipitation                 | River discharge   | Water storage changes  | Moisture flux                 | Actual evapotranspiration                            |
|-----------------------------|-------------------------------|---|--|-------------------------------|--|
| <i>in situ</i>              | ✓                             | ✓(partially)  | ✗  | ✗                             | ✗  |
| Model                       | ✓                             | ✓   | ✓  | ✓                             | ✓  |
| Spaceborne geodetic sensors | ✗                             | Satellite Altimetry   | GRACE  | ✗                             | ✗  |
| Challenges                  | –                             | uncertainty consistency resolution                                    | uncertainty separability resolution consistency  | –                             | –  |
| <b>Task/Role</b>            | use for evaluation & analysis | <b>Developing algorithms to derive river discharge from altimetry</b> | <b>Addressing the challenges to derive meaningful <math>dM/dt</math> for hydrology</b> | use for evaluation & analysis | <b>determination &amp; assessment of limitations</b> |

Due to aforementioned challenges and capabilities, following tasks are defined to be addressed for achieving the main goal of this study:

1. Achieving inland water level time series from satellite altimetry, for which the challenges of uncertainty and resolution of satellite altimetry need to be addressed.
2. Obtaining an algorithm to derive river discharge from satellite altimetry. In order to achieve this goal, first the level of consistency between available river discharge *in situ* measurements and water level from satellite altimetry should be investigated. Subsequently, an appropriate model should be developed to derive river discharge from satellite altimetry.
3. Developing an algorithm to reduce the noise level of GRACE and achieve hydrologically meaningful time series for water storage changes over river basins. For this goal, the challenges of uncertainty and inconsistency of GRACE should be specifically targeted.
4. Assessing the limitations of actual evapotranspiration estimation from water balance equation.  $ET_a$  can be determined by  $dM/dt$  from GRACE, river discharge from altimetry and precipitation from available data sets, yet the limitations of this methodology should be scrutinized.

## 1.4 Outline of the thesis

In this thesis each of the aforementioned tasks for achieving the main goal of the study will be investigated in one separate chapter. Chapter 2 deals with achieving an acceptable time series for inland water level from satellite altimetry by post-processing investigations. Especially, the chapter addresses the challenges of uncertainty and resolution of satellite altimetry. In Chapter 3, an algorithm will be developed to derive river discharge from satellite altimetry. There, the problem of inconsistency between available river discharge *in situ* measurements and water level from satellite altimetry will be tackled. Moreover, a statistical modeling approach using quantile functions will be proposed to create the rating curve without the requirement of simultaneous measurements. Further, Chapter 4 deals with developing algorithms to reduce the noise level of GRACE. The challenges of uncertainty and inconsistency will be extensively targeted. In this study the estimation of river discharge from altimetry and water storage change from GRACE will be considered arbitrary. It should be mentioned that neither is prerequisite material for the other; therefore, they may be studied in either order, or independently, for that matter. The resulting discharge from altimetry and water storage change from GRACE will be used in Chapter 5 for actual evapotranspiration estimation. There, the limitations of estimation of actual evapotranspiration from water balance equation and spaceborne geodetic sensors will be addressed. Finally, summary and conclusion are provided in Chapter 6.



## Chapter 2

# Monitoring inland water level variations by satellite altimetry

Over the past two decades, satellite altimetry has been used as a monitoring tool for inland water surfaces and hydrological cycle (Alsdorf and Lettenmaier, 2003; Calmant and Seyler, 2006; Papa et al., 2006; Crétaux and Birkett, 2006; Papa et al., 2010; Berry et al., 2005). Particularly, monitoring the water levels in large rivers and lakes was aim of researches since launch of TOPEX/Poseidon and ENVISAT missions (Birkett, 1995; Cazenave et al., 1997; Stanev et al., 2004; Frappart et al., 2006a, 2008; Crétaux et al., 2011). In the recent past, estimating river discharge from satellite altimetry was also studied by many researches (Kouraev et al., 2004; Zakharova et al., 2006; Leon et al., 2006; Coe and Brikett, 2004; Papa et al., 2010).

Inspired by the proven capability of satellite altimetry for monitoring part of the hydrological cycle and lack of *in situ* measurements for river discharge, in this chapter achieving river water level time series from altimetry data is investigated. The river water level time series will be employed as input to establish the rating curve and derive river discharge. However, as discussed in Chapter 1, inherent uncertainty of altimetry and resolution are the obstacles for obtaining an appropriate time series of river water level. Tackling the uncertainty and resolution problems need certain post-processing considerations on the altimetry data, which will be discussed in detail in this chapter. First, the measurement principle of satellite altimetry will be explained.

### 2.1 Principle of measurement

The antenna of satellite altimeter continuously emits pulses of electromagnetic energy ( $0 < t < t_0$ ), that propagate in a spherical wavefront. The wavefront faces and illuminates the nearest surface directly under the satellite around the nadir at  $t = t_0$  (Figure 2.1). From  $t_0$  onwards, the altimeter receives the return of the reflected signal. The area of interaction between pulse and surface grows through reaching the wavefront at surfaces further from nadir, thus illuminated area extends to form a disc (for flat surfaces). During  $t_0 < t < t_1$ , backscattered power reaches the altimeter from illuminated area within the disc. The

received power at the altimeter forms an ascending part (leading edge) of the altimeter waveform. As the trailing edge of the pulse reaches the surface, the illuminated area forms an annular ring of increasing diameter and narrowing width. The maximum power on the waveform occurs at the time of transition to an annular ring ( $t = t_1$ ). Thereafter  $t > t_1$ , due to limitation of antenna beam width and fewer proper reflected facets, the backscattered power begins to decline. Over the pulse duration, the received power is recorded and a waveform with a rapidly rising leading edge and long decay of the trailing edge is constructed accordingly (Figure 2.1). Practically, the constructed waveform contains noise belonging to

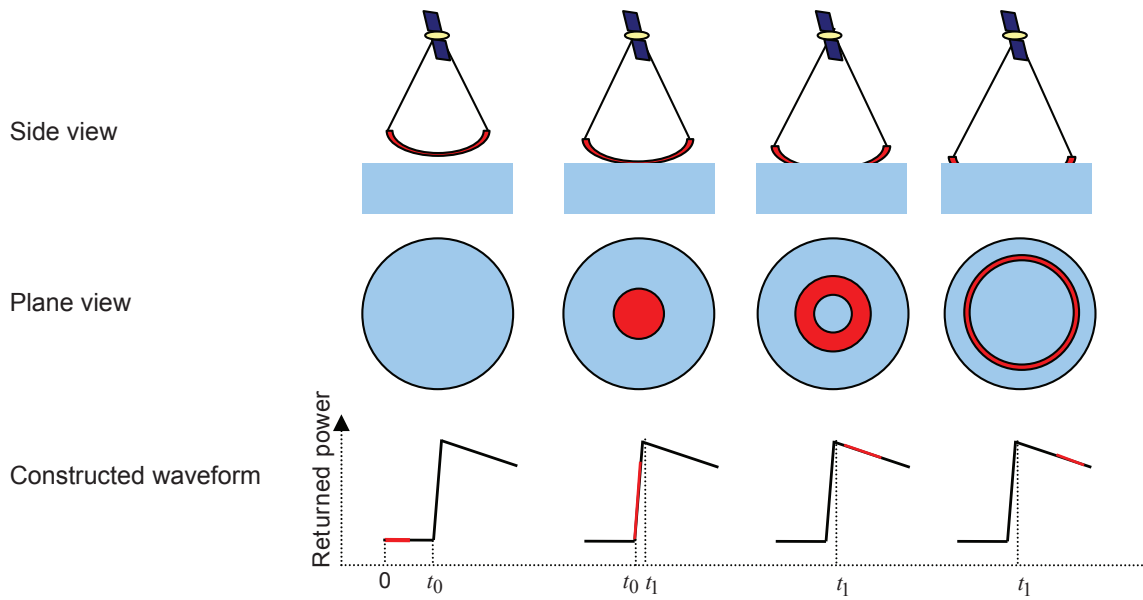


**Figure 2.1:** Interaction of a pulse and scattering surface, and the procedure of constructing the returned waveform

the received power. In order to reduce the noise level in waveform, the received power from subsequent pulses are averaged and a mean waveform is constructed (Quarry et al., 2001). This averaged returned waveform is a time series of the mean returned power recorded by a satellite altimeter which consists mainly of three parts (Brown, 1977; Hayne et al., 1994; Chelton et al., 2001)(Figure 2.2):

- **The thermal noise:** The altimeter sometimes generates noise power before the first return of a signal from the scattering surfaces. It imposes a constant power level to the return waveform.
- **The leading edge:** This part is the main part of waveform which contains the maximum return power from the scattering surfaces. The information about the Surface Wave Height (SWH) and range between the satellite altimeter and the mean sea surface at the nadir can be extracted from the leading edge.
- **The trailing edge:** As the return power from the scattering surface is decaying, the trailing edge of waveform is constructed. It can be approximated by a straight line whose slope depends on the altimeter antenna pattern and the off-nadir angle (Chelton et al., 2001).

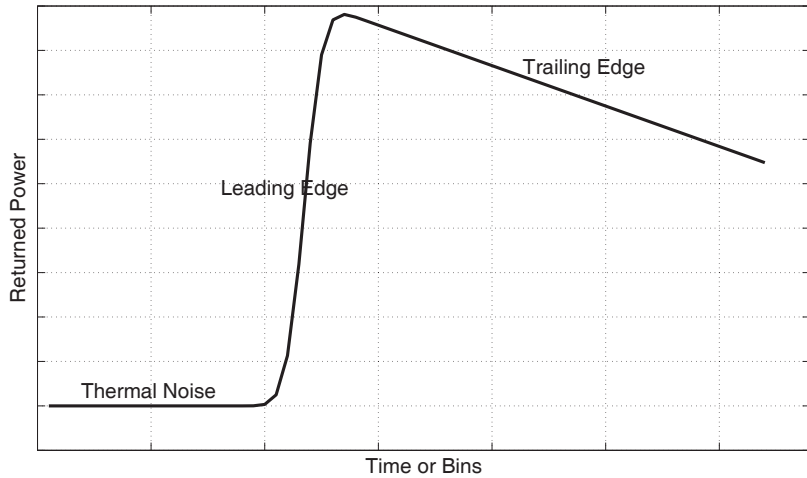


**Figure 2.2:** Schematic altimeter mean return waveform over ocean surface

In general, the waveform contains information about the range to the nadir, reflectivity and the large-scale roughness of the scattering surfaces (Deng, 2003). The range to the nadir is computed on the on-board tracker by estimating the time taken by the radar pulse to travel from the satellite antenna to the surface and back to the satellite receiver (Fu and Cazenave, 2001; Frappart et al., 2006a). This travel time represents the time that the midpoint of the pulse needs to return from water surface at nadir. Therefore, the on-board tracker estimates the time by identifying the mid-point on the leading edge of the waveform (Lee, 2008). This is done by continuously adjusting the range window by the on-board tracker to keep the leading edge of the waveform at a specified position at the centre of the range window, the so-called *tracking point* (Deng, 2003). The tracking point is in the range bins 24.5 for TOPEX/Poseidon and 32.5 for ENVISAT, which is designed before the launch of satellite. Thus, the on-board tracker seeks for the half-power point on the leading edge of the waveform to determine its offset to the tracking point and realign subsequent waveforms (Chelton et al., 2001). Identifying the half-power point on the leading edge of an ideal waveform is easily performed by the on-board tracker. However, the waveforms over inland water bodies do not represent an ideal shape and often show noisy leading and trailing edge, which leads the on-board tracker to provide an erroneous range. Figure 2.3 shows 25 randomly selected TOPEX/Poseidon waveforms over Lake Balaton (Hungary), which represent waveforms with noisy leading and trailing edge, multi peaks, quasi-specular and quasi-Brown waveforms.

The estimated ranges from the waveforms are then combined with precise satellite location data to yield surface water heights (Fu and Cazenave, 2001). In spite of noisy waveforms and consequently erroneous surface water heights over inland water bodies, the noise level can be reduced by controlling the sources of generating noise in altimetry. As discussed in Chapter 1, control on resolution and uncertainty of satellite altimetry will lead to reducing the noise in surface water height's time series.

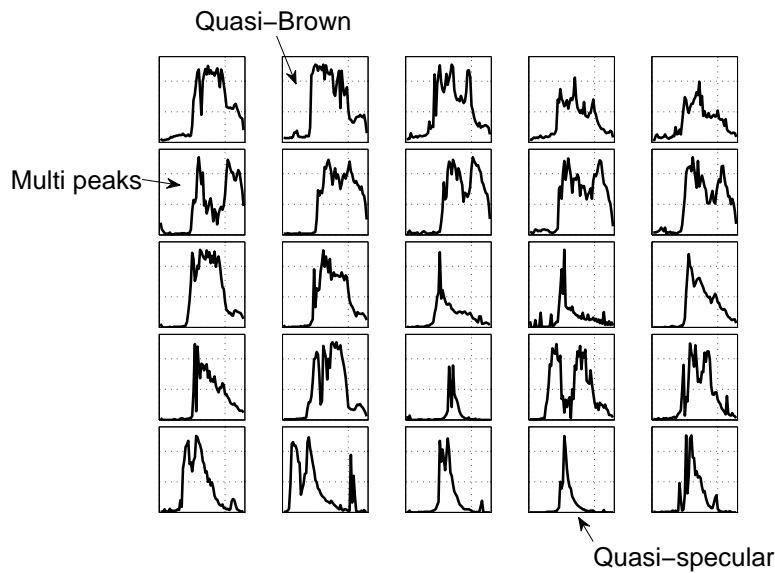


**Figure 2.3:** 25 randomly selected TOPEX/Poseidon waveforms over Lake Balaton showing various shapes of waveforms, a sample from each type of waveform is shown

## 2.2 Controls of resolution

In fact, neither spatial nor temporal resolution of altimetry data can be improved, as they depend on the orbit configuration of satellite. The only room for controlling the resolution of altimetry to avoid uncertainty and inconsistency is controlling the size and location of virtual station. The size of virtual station is important to investigate, as within a certain radius around the virtual station, successive altimeter measurements at each pass of satellite form the time series of different geophysical measurements. Therefore, by defining a meaningful radius and center for circle of virtual station, the contaminated measurements from non-water surfaces can be avoided. However, this control requires study of the size and location of altimetry footprint.

### 2.2.1 Footprint size

As shown in Figure 2.1 a single transmitted pulse forms a circular footprint at nadir. Nevertheless, as altimeter transmits bursts of pulses every ca. 50ms and the obtained individual waveforms are averaged to reduce the noise, the footprint is not circular anymore. In oceanographic application the altimeter data is averaged over a time period of about 1 s (Chelton et al., 2001). Given the ground speed of satellite of 5.9 and 6.6 km/s for orbit heights of 1336 and 785 km, respectively, the 1 Hz waveform belongs to an oval footprint with length of ca. 8.5 km (Figure 2.4) (Fu and Cazenave, 2001). The center of the oval footprint is defined as the sub-satellite point along the ground track. Figure 2.5 shows schematically the oval footprint and subsatellite points of TOPEX/Poseidon's ground track over Balaton Lake. For a narrow lake like Balaton, given the ca. 7km width at the crossing location of satellite, at most two centers of the

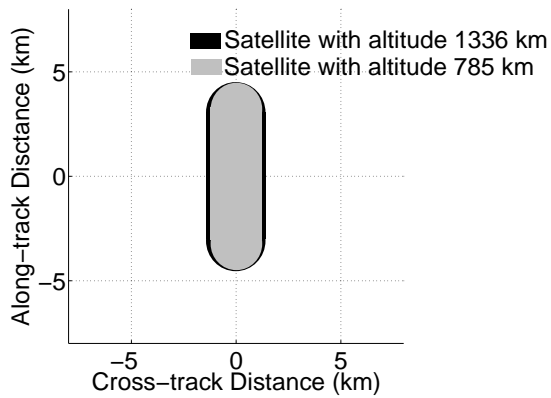


**Figure 2.4:** The oval footprint characteristics for flat area belong to 1 s averages of altimetry at nadir (Fu and Cazenave, 2001)

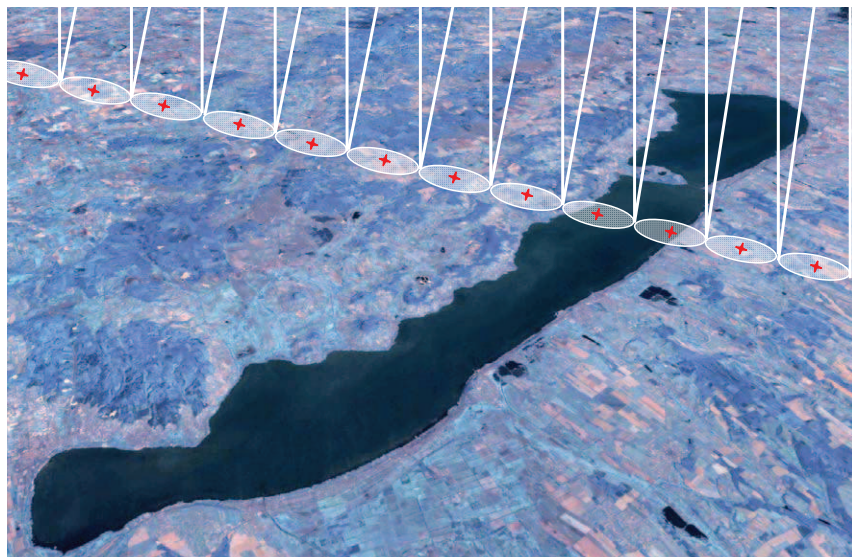


**Figure 2.5:** Schematic oval footprint and sub-satellite point, Lake Balaton (Hungary), TOPEX/Poseidon

oval footprints in each pass belong to the water body of the lake. In addition, in most of the passes, the oval footprints covers both the land and water surfaces. This situation is almost valid for all inland water bodies with narrow width e.g. rivers and small lakes. Therefore, for inland water application of satellite altimetry a finer resolution is needed.

Altimeters from different missions and different altimeters follow different strategies to end up with the average altimeter returned waveform. For instance, TOPEX emits a burst of 228 Ku band pulses in each 53 ms interval and receives the returned echoes in 128 bins of width 3.125 ns (Quartly et al., 2001). This on-board 128 bins waveform is averaged in multiples of 1, 2 and 4 to form the 64 bins waveform (Table 2.1) (Hayne et al., 1994). Poseidon altimeter emits 1700 pulses per second and averages them in groups of 86 pulses every 53 ms. The waveform is sampled in 64 bins of width 3.125 ns with the tracking point at bin 31.5 (Quartly et al., 2001).

**Table 2.1:** TOPEX telemetry sample to waveform sample relationship (Hayne et al., 1994)

| 128 bins waveform | 64 bins waveform | method           | sampling rate |
|-------------------|------------------|------------------|---------------|
| 1-16              | 1-8              | averaged by two  | 6.25 ns       |
| 17-48             | 9-40             | transcribe       | 3.125 ns      |
| 49-64             | 41-48            | averaged by two  | 6.25 ns       |
| 65-128            | 49-64            | averaged by four | 12.5 ns       |

In addition to 1 Hz data, different altimeters also provide 10 / 18 / 20 Hz data of range measurements, precise satellite locations, additional information of tracker data, instrumental corrections, corresponding geophysical corrections and flags. The 10 / 18 / 20 Hz data can provide a finer resolution to study inland water bodies. For 10 Hz measurements of TOPEX/Poseidon, the along-track distance of measurements is ca. 700m and 18 Hz measurements of ENVISAT are measured every ca. 370m in along-track direction. Figure 2.6 shows the 10 waveforms from 10 Hz data that belong to an oval footprint over Balaton Lake. The measurements from water body and land area are distinguishable as the first 5 waveforms show quasi-specular shape which is the typical waveform pattern over deep and calm waters (Berry et al., 2000). It is clear that, when the satellite approaches the coast, the waveforms become more noisy (Figure 2.6). Practically, there is no direct mathematical or analytical relationship between the shape of the waveforms and topography of sub-satellite point. In fact, various shapes of waveforms occur due to the effect of topography, vegetation canopy and water height. Therefore, the radius of virtual station should be defined carefully to assign water reflected measurements only and avoid contamination of neighboring topography. For instance, for the case of Figure 2.6, the size of the virtual station should be defined, in a way that only the first 5 waveforms are considered for constructing water level time series.

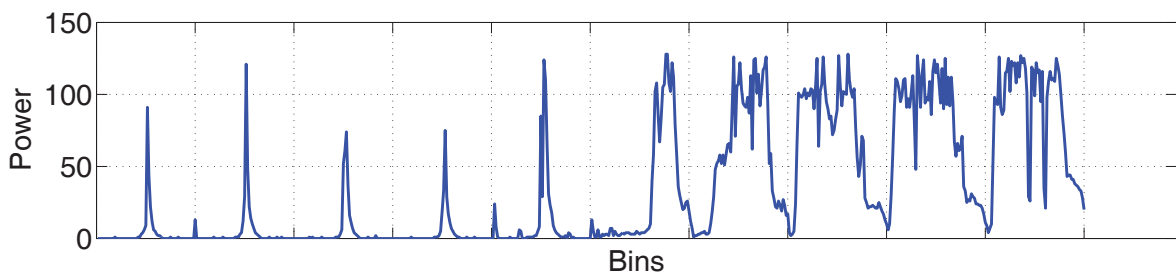


**Figure 2.6:** 10 Hz waveforms of altimetry over Balaton Lake belonging to cycle 25 of TOPEX/Poseidon . Each of these waveform have a circular footprint, which form an oval footprint all together

Moreover, the inside situation of water body and its neighboring topography plays an important role for defining the radius of virtual station. In essence, the inside situation seems to be problematic in three cases: 1) existing temporary islands of braided rivers within the range of virtual station 2) frozen and snow covered water body and 3) water bodies with vegetation canopy. For instance, the width of the Brahmaputra river at the crossing location of ENVISAT altimetry at  $\phi = 25.73^\circ \lambda = 89.76^\circ$  is ca. 10 km, but only a 4 km diameter can be defined for virtual station to avoid contamination of measurements by existence of temporary islands in the middle of the braided river (Figure 2.7).



**Figure 2.7:** Google Earth imagery over Brahmaputra River at the location of a virtual station. The river width at the altimeter crossing is ca. 10km, however, due to the existence of temporary islands in the braided river the radius of virtual station is defined as 2 km.

### 2.2.2 Footprint location and the off-nadir effect

As satellite altimetry is a nadir measuring technique, the location of a footprint is supposed to be at the nadir of the satellite. However, over inland waters the nadir mis-pointing of the satellite's antenna seems to happen very often (da Silva et al., 2010) especially in ERS and ENVISAT measurements. It can occur over all kinds of water bodies, e.g. lakes, very large and narrow river segments. The nadir mis-pointing occurs differently over narrow and large water bodies. Over narrow water bodies, the echo bounces back off the water body before and after passing right over it, which leads to a parabolic shape of water height. This effect is schematically illustrated in the Figure 2.8(a), where the altimetry profile is affected by off-nadir measurement at a crossing with the water body. On the other hand, over large lakes and rivers, one single mis-pointing in the middle of the water body leads to forming a V-shaped water level profile, which is shown schematically in Figure 2.8(b). Two real examples of off-nadir effect over Don River (Russia) and HongZe Lake (China) from measurements of ENVISAT and TOPEX/Poseidon are shown in figures 2.9 and 2.10, respectively.

In general, the off-nadir effect over narrow water bodies, as shown in Figure 2.9(d), brings the opportunity of having more data, as the antenna locks over the water body before and after the nadir. Therefore, the estimated water height can be corrected and used for making the water level time series. However, for assuming the off-nadir measurements, the neighboring topography plays an important role. Thus, for a narrow water body with heterogeneous neighboring topography, off-nadir measurements appear to be contaminated and not useful for building the water level time series. As an example, ENVISAT altimetry data over narrow rivers of Don at  $\varphi = 47.50$  &  $\lambda = 40.56$  and Vistula at  $\varphi = 40.56$  &  $\lambda = 18.84$  are influenced by off-nadir measurements. However, in Vistula River off-nadir measurements are contaminated by heterogeneous topography around the river water body. There, using off-nadir measurements and correcting them results in generating an erroneous water level time series. For such a case, in order to achieve an acceptable time series and preventing contribution of the noisy off-nadir measurements, the virtual station should be narrowed instead of off-nadir correction. This is not the case for the Don River

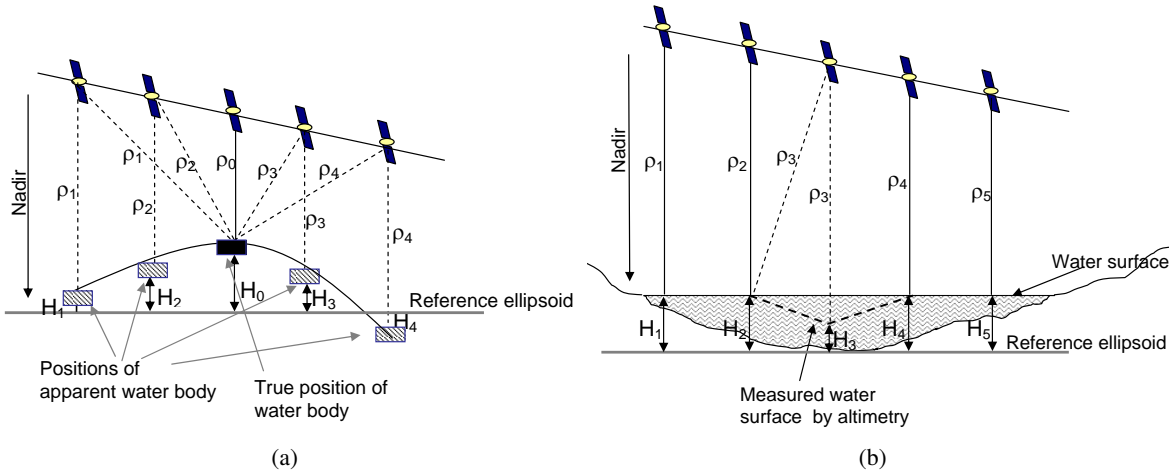


**Figure 2.8:** a) 5 schematic snapshots of satellite altimetry, before, at and after zenith location of water body. The satellite captures the water body before arriving at the zenith and measures  $\rho_1$  and  $\rho_2$  as range, which leads to providing  $H_1$  and  $H_2$  as water level.  $H_3$  and  $H_4$  are estimated as water level by measuring  $\rho_3$  and  $\rho_4$  after passing the zenith.  $H_1$ ,  $H_2$ ,  $H_0$ ,  $H_3$  and  $H_4$  form a parabolic water level profile.  
b) Passing of the satellite over a large water body with 5 snapshots of measurements. One single mis-pointing of the satellite in the middle of the water body causes a V-shaped water level profile. The off-nadir range of  $\rho_3$  leads to estimating a low water heights in the middle of the water body.

as the neighboring topography around the virtual station is smooth, which allows to use the off-nadir measurements.

On the other hand, the deteriorated V-shaped profiles due to the off-nadir measurements over large water bodies, shown in Figure 2.10(b), only provide more uncertainty and the effect should be eliminated from the data.

As a result, the nominal location is matched with the real measured location when off-nadir angle of satellite is zero. Therefore, the off-nadir effect of satellite altimetry has to be investigated and corrected for inland water studies.

## 2.3 Controls on uncertainty

The uncertainty in the altimetry originates from geophysical and instrumental disturbing sources. Geophysical disturbing sources can be introduced as

- Neighboring topography and heterogeneity of reflecting surface
- Islands within the virtual station
- Frozen and snow covered water body

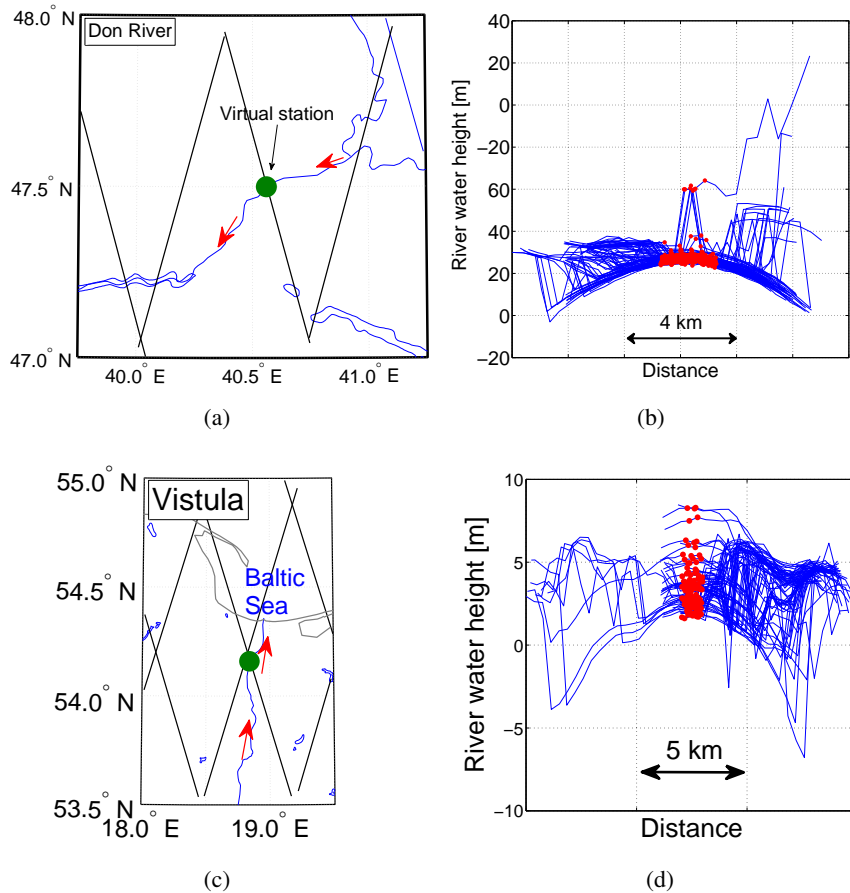


**Figure 2.9:** (a) and (c) The Don River in Russia and Vistula River in Poland and ground tracks of ENVISAT with virtual station. The width of river at this location for both rivers is ca. 300 m. (b) and (d) Along track profiles for different cycles of ENVISAT over the Don and Vistula rivers, respectively. Red dots represent the nadir measurements within the radius of virtual station.

- Vegetation canopy
- Atmospheric delayed propagation: ionospheric, wet and dry tropospheric
- Vertical crustal motions: Earth and polar tides.

Among the aforementioned disturbing sources, the atmospheric delayed propagation and vertical crustal motion can be referred to as systematic uncertainties, which are relatively well modeled by known algorithms and external auxiliary sensors and data. For instance, ionospheric correction is estimated by combining radar altimeter measurements acquired at two separate frequencies (C-band and Ku-band for TOPEX/Poseidon, Ku-band and S-band for ENVISAT). Wet tropospheric correction is calculated from radiometer measurements and/or meteorological models. Geophysical Data Records (GDRs) provide these two systematic sources. The uncertainties driven by disturbing sources of neighboring topography, temporary islands within the virtual station, frozen and snow covered water body and vegetation canopy will appear as outliers and random noise in the altimetry data.

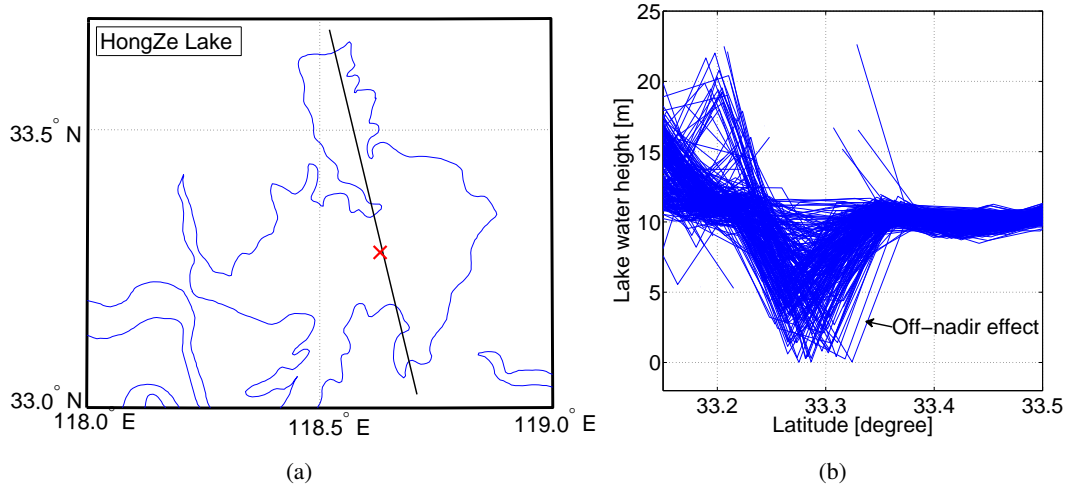


**Figure 2.10:** (a) HongZe Lake in China and ground track of TOPEX/Poseidon, the marked place in the middle of the lake shows the position of occurrence of the two successive off-nadir measurements (b) Latitudinal along track profile for different cycles of TOPEX/Poseidon

On the other hand, the following instrumental errors are known to be the main instrumental disturbing sources (Fu and Cazenave, 2001)

- Oscillator drift error
- Doppler shift effect
- Tracker response error
- Nadir mis-pointing

for which the corrections are already implemented in the GDR except for nadir mis-pointing error. As discussed in Section 2.2.2, the nadir mis-pointing of the satellite will appear as parabolic form over narrow water bodies and V-shaped form over large water bodies, which should be corrected in both cases. Moreover, as discussed in 2.1 the on-board range estimation algorithm is designed to deal with ideal shape of waveforms. This limits the application of altimetry over inland waters, for which the obtained waveforms often do not follow the ideal shape. Therefore, the range estimation by on-board tracker contains random noise, which should be reduced.

As a conclusion, the uncertainty in the altimetry data appear in three known forms of 1) outliers, 2) off-nadir measurements and 3) random noises. Here, the algorithms to correct these major forms of uncertainties are developed and discussed.

### 2.3.1 Outlier elimination

A simple outlier detection algorithm can be developed based on the data snooping method, which searches for the observation in which the maximum gross error has been made during measurement

(Baarda, 1968). Since the distribution of residuals is typically normal, the data snooping procedure is done on the residual water level (Tourian et al., 2011). In order to estimate water level residuals a model representing the inter-annual monthly mean is defined to be excluded from the water level time series  $H(t)$

$$\bar{H}(t) = a_0 + a_1(t) + \sum_{i=2}^3 a_i \cos(\omega_i t) + b_i \sin(\omega_i t) \quad (2.1)$$

where  $\omega$  is the angular frequency for annual ( $\omega_2$ ) and semi-annual ( $\omega_3$ ) variation and  $a_0, a_1, a_i$  and  $b_i$  are the unknown coefficients of the model. A least squares estimation is performed to achieve the unknown coefficients. Then the water level residual is computed by:

$$r(t) = H(t) - \bar{H}(t), \quad (2.2)$$

which comprises the inter-annual variabilities and error. By defining a suitable confidence level ( $\alpha$ ), the appropriate critical value ( $k_{\alpha/2}$ ) is attained under the null hypothesis that no outlier exists in the time series. In this study 95% is chosen for  $\alpha$ , which corresponds to critical value of 1.96 for normal distribution. Therefore, the null hypothesis will be accepted if:

$$-k_{\alpha/2} < \frac{r(t)}{\sigma} < k_{\alpha/2}, \quad (2.3)$$

where the  $\sigma$  is the standard deviation of the computed residual. By rejecting or accepting the null hypothesis, outliers are identified iteratively (Figure 2.11). If the null hypothesis is rejected, the detected outlier is removed and a new  $\sigma$  is computed and snooping procedure will be iterated.

### 2.3.2 Off-nadir correction

In this study, the off-nadir effects over narrow water bodies are corrected via fitting a degree 2 polynomial to the along-track profile of 20Hz water level measurements within the radius of the virtual station. Similar to the algorithm by da Silva et al. (2010), at each cycle, the maximum water level of the fitted polynomial on the along-track profile is assumed to be the nominal water level at nadir  $H_0$ . Then the difference between the along-track profile and the fitted polynomial is computed as the residual profile. The off-nadir corrected profile is then obtained by summing up the  $H_0$  and the computed residual profile (Figure 2.12).

It should be noted that the correction algorithm should only be performed within the radius of the virtual station (red dots in Figure 2.9(d)) instead of fitting the polynomials along all available observations. This specially helps to avoid noisy water level values contaminated by the neighboring topography. Figure 2.13 illustrates the along-track profiles of 20Hz water level measurements over the Don River before and after off-nadir correction. It can be seen that, the parabolic form of the along-track profiles are vanished after off-nadir correction.

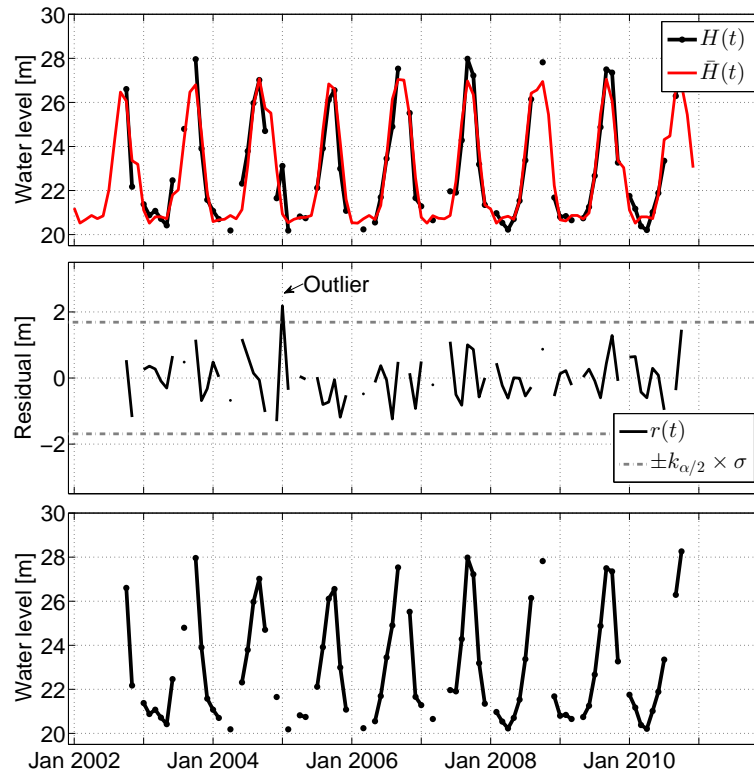


**Figure 2.11:** Top panel) water level time series,  $H(t)$ , and the modeled inter-annual monthly mean over Niger river. Middle panel) the computed water level residual together with the confidence intervals. Bottom panel) outlier corrected water level time series over Niger River

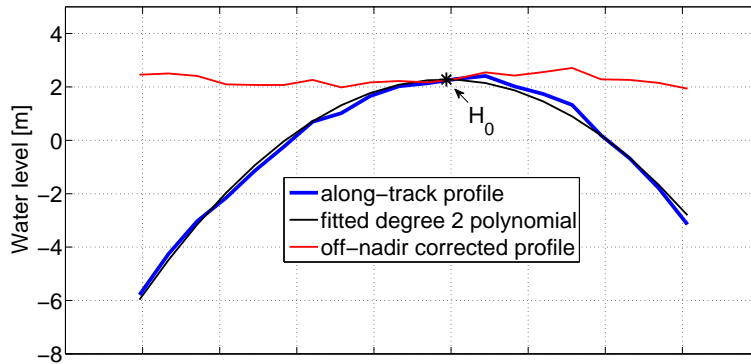


**Figure 2.12:** A sample of off-nadir affected along-track water level profile from 20Hz measurements over the Don River together with fitted degree two polynomial and the corrected profile

### 2.3.3 Random noise reduction

After identifying and eliminating the outliers and taking the effect of off-nadir measurement into account, the remaining uncertainty can be assumed to be random noise. A common approach to deal with random noise in altimetry data over non-ocean surfaces is waveform retracking (Rodriguez and Martin, 1994; Deng and Featherstone, 2006; Gommenginger et al., 2011). Retracking is a procedure in which the al-

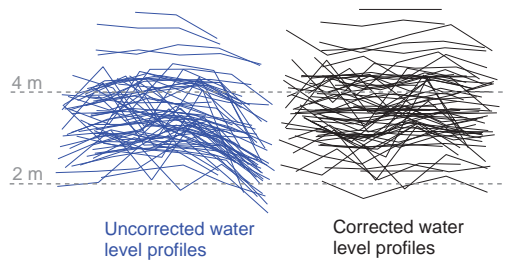


**Figure 2.13:** Water level profiles over Don River belong to different passes over the time before (left) and after (right) off-nadir correction

timeter waveform is post-processed to improve the estimation of parameters given by GDRs (Lee, 2008). The main outcome of this post-processing procedure is correction of estimated range by the on-board tracker.

As discussed before, over non-ocean surfaces, the on-board satellite altimeter tracker has poor capability to track the rapid changes of the surface topography. This leads to the offset between the mid-point of the leading edge of the waveform and the pre-designed, known, fixed, instrument-independent position on the leading edge of the waveform, the so-called tracking gate<sup>1</sup> (Figure 2.14). In the altimeter, this offset represents the error in the range measurements and waveform retracking stands for determination of the offset by certain algorithm (Figure 2.14). This offset can be transformed into the range by

$$\Delta R = \text{Offset} \times \tau \times \frac{c}{2}, \quad (2.4)$$

where  $\tau$  is the sampling rate (for TOPEX/Poseidon it is 3.125 nsec see table 2.1) and  $c$  is the light speed.

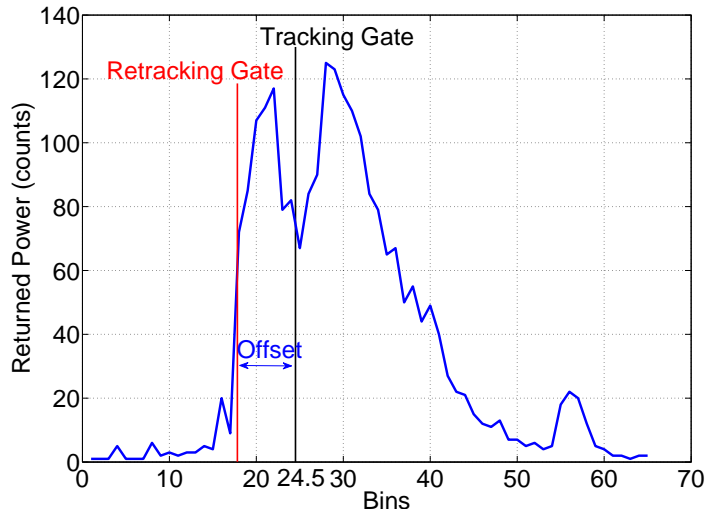


**Figure 2.14:** The concept of waveform retracking

<sup>1</sup>A gate consists of averages of neighboring waveforms

Several non-linear range estimation algorithms have been developed over non-ocean surfaces since 1983, e.g. the  $5\beta$  parameter retracking algorithm (Martin et al., 1983), the threshold method (Wingham et al., 1986) and the surface/volume scattering-retracking algorithm (Davis, 1993). In general, the retracking algorithms over non-ocean surfaces can be categorized into four classes:

1. Fitting algorithm:  $5\beta$  or  $9\beta$ -parameters retracking
2. The Off Centre Of Gravity (OCOG) technique
3. Threshold retracking
4. Surface/volume scattering retracking

which are explained in detail in Appendix A. Practically, each of the aforementioned retracking algorithms has its highest performance on a specified shape of waveform (Deng and Featherstone, 2006). For instance, fitting algorithms are appropriate methods for quasi-Brown model waveforms and are not applicable on a quasi specular waveform. OCOG retracking method is sensitive to the noise in the trailing edge, that deteriorates the estimation of center of mass of the waveforms. Threshold retracking seems to be applicable to any kind of waveform with a clear leading edge by seeking a percentage of maximum occurred power in the leading edge. Figure 2.15 visually highlights the performance of each retracking method for two sample waveforms over Balaton Lake. As depicted in the figure, for the waveform with quasi-Brown model,  $5\beta$  retracking shows better result in comparison with OCOG and threshold retracking. Due to the noisy trailing edge of waveform the Center Of Gravity (COG), width and amplitude computed by OCOG retracking method are deteriorated. As the amplitude for threshold retracking is derived from OCOG method, the result of threshold retracking method is also not satisfactory. On the other hand, for a quasi-specular waveform, both the threshold and OCOG retracking methods show same result while the  $5\beta$  retracking fails.

Therefore, before starting the waveform retracking, different shapes of waveforms should be distinguished and carefully classified. In fact, the aim of the waveform classification procedure is splitting or classifying automatically each data set into different consistent groups. This basically can be done in the setting of supervised classification, corresponding to situations when the different groups of waveforms are identified before the beginning of the classification. However, as waveforms show totally different patterns over different inland water bodies (Figure 2.3), identifying the groups of waveforms might lead to neglecting a group of unexpected waveforms. Therefore, an unsupervised classification with good performance can extract any of existing consistent waveforms as a separate group.

The unsupervised classification has been widely studied in the statistical literature for finite-dimensional data e. g. (Anderberg, 1973; Hartigan, 1975). In this context, nonparametric density estimates have been often used for the unsupervised classification (Anderberg, 1973; Hartigan, 1975; Dabo-Niang et al., 2007). In these methods, the mean, median or mode of the data are used for deriving the heterogeneity of data and classifying it into consistent groups (Dabo-Niang et al., 2007). The drawback of such algorithms is the sensitivity of them to noise in the data. In other words, for classifying waveforms, a

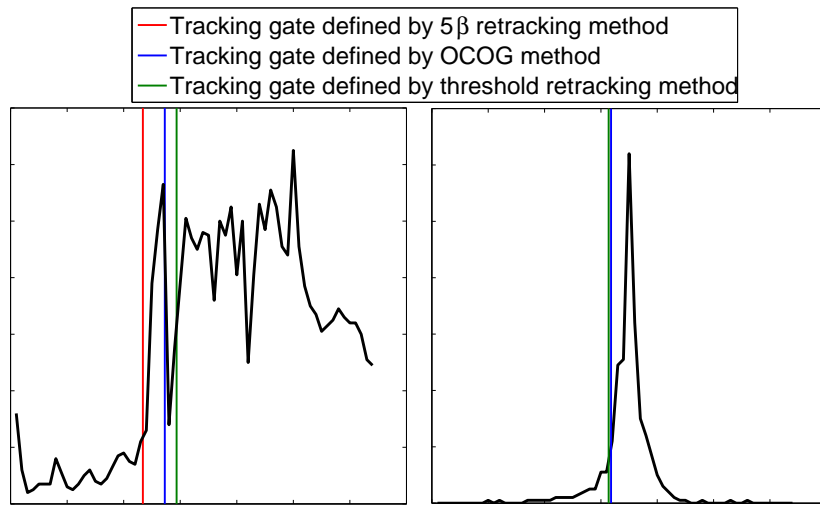


**Figure 2.15:** Two sample waveform from group 1 and 2 of Balaton Lake and the defined tracking gate from different retracking methods. For the waveform with quasi-Brown shape, the  $5\beta$  retracking method leads to a tracking gate at the leading edge, while it is not the case for OCOG and threshold retracking method.

noisy waveform deteriorates the nonparametric density estimates of the data and that would lead to a non-represented mean, median or modal waveforms, which ultimately cause an erroneous classification. Therefore, before performing an unsupervised classification, a step of excluding the noisy waveforms from the data set is required.

### 2.3.3.1 Excluding noisy waveforms

A noisy waveform is defined here as a waveform with noisy leading edge, in which defining the half power of leading edge is cumbersome. In order to exclude the noisy waveforms, an algorithm is developed in which a  $5\beta$  parameters curve is fitted to the waveforms (Figure 2.16). In this algorithm the noise level of each waveform is assessed by computing a *dissimilarity value* between the waveform and  $5\beta$  fitted curve i.e. the residual after fitting. Therefore, the goodness of fit plays an important role for defining the dissimilarity value. To achieve the best fit, an empirical approach is employed to derive the parameters of  $5\beta$  algorithm.

In this approach, the thermal noise level,  $\beta_1$ , of the return waveform is estimated using the averaging of the power of initial bins of waveform. However, for some waveforms it's better to assume 0 value for  $\beta_1$ , for which the thermal noise show a large variation.  $\beta_2$  is the return maximum amplitude and most challenging parameter to define.

As the waveforms over the inland water bodies show noisy behaviour, defining the maximum amplitude of the waveform should be carefully done. For that, here a three bins moving average of the waveform is computed to reduce the level of noise in the waveform. In fact, a bin in the waveform can be assumed as a maximum value when its derivative shows change in the sign from bin before to bin after. Therefore,

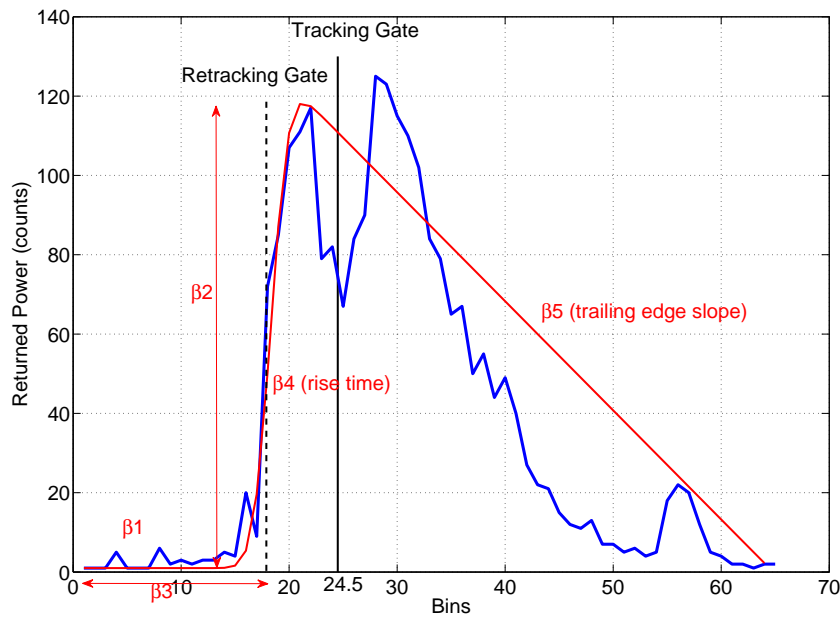


**Figure 2.16:**  $5\beta$  parameter model fitting algorithm, where  $\beta_1$  is the thermal noise level of the return waveform,  $\beta_2$  is the return signal amplitude,  $\beta_3$  is the mid-point on the leading edge of the waveform,  $\beta_4$  is the return waveform rise time and  $\beta_5$  is slope of the trailing edge

from the moving averaged waveform, the corresponding derivative is computed. Among the extrema, the one with maximum change in the sign is chosen. Subsequently, an array of extrema five bins before and after the chosen bin are generated. The maximum power from the generated array is introduced as  $\beta_2$  (Figure 2.17). Afterwards,  $\beta_3$  is arbitrarily defined as the bin that is located three bins before the maximum power occurs. As  $\beta_4$  represents the rise time of the leading edge in the waveform, the common practical value of 1.3 is used for  $\beta_4$  (Anzenhofer et al., 1999). Finally,  $\beta_5$  is determined via computing the slope of the line between the defined maximum power to the last bin's power (diagram in Figure 2.19).

After defining the parameters, a curve using the  $5\beta$  algorithm is fitted to the waveform. The fitted curve can be compared with the waveform to obtain a dissimilarity value and assess the noise level. However, as waveforms over inland water often contain noisy leading and trailing edges, it can be expected that a non-representative  $\beta_3$  leads to a curve with offset in the position of leading edge. The offset can be quantified by cross correlating the fitted curve with the waveform. The cross correlation function helps to identify the lag with maximum correlation between two curves. Therefore, by shifting the fitted waveform in the length of the lag with maximum correlation, ( $-1$  in Figure 2.18), it is expected to fit the  $5\beta$  parameters curve (red curve in Figure 2.18) to the waveform with minimum possible discrepancy.

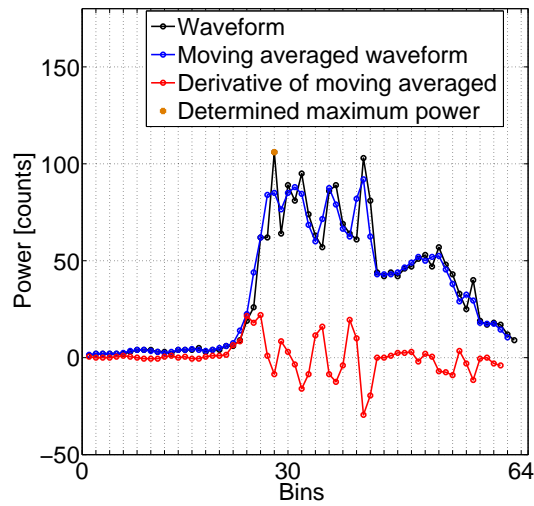


**Figure 2.17:** A sample waveform belongs to cycle 32 at  $\varphi = 46.84^\circ, \lambda = 17.82^\circ$  over Lake Balaton with its moving average and derivative

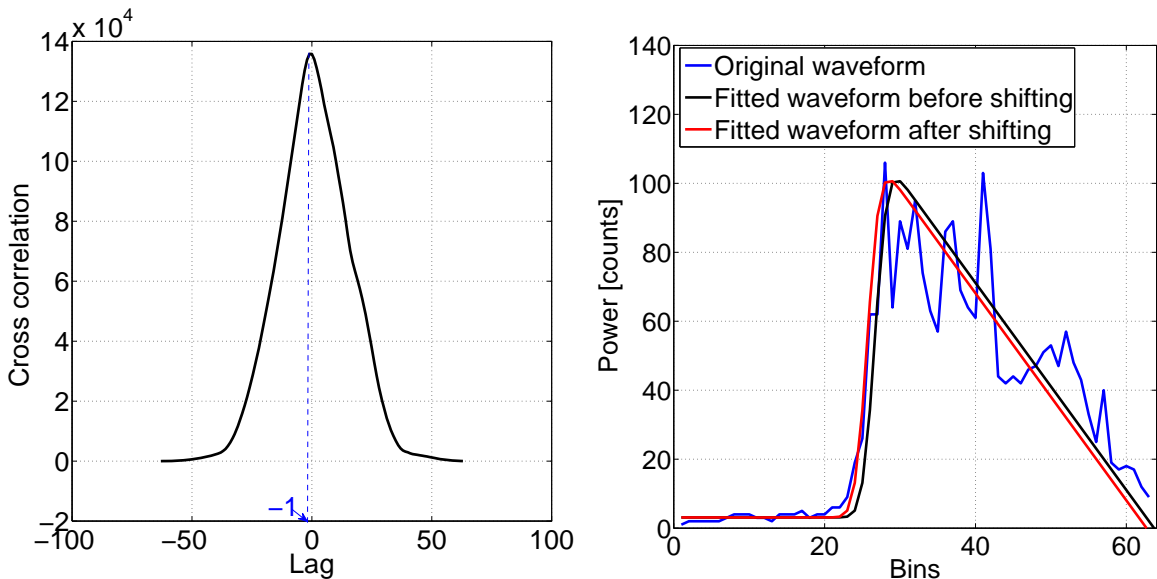


**Figure 2.18:** Left) cross correlation of fitted waveform using  $5\beta$  parameter algorithm and the original waveform, which shows its maximum value at lag = -1 Right) A sample of original waveform together with the fitted waveform by  $5\beta$  parameter algorithm (black) and shifted fitting waveform due to the obtained lag from cross correlation

Afterwards, a function is defined to assess the noise level of a waveform, from which the dissimilarity of leading edges of the waveform and fitted curve is computed

$$diss = \frac{\sum_{i=k_1}^{k_n} (W_i - Y_i)^2}{\rho} \quad (2.5)$$

where  $W_i$  is the original waveform,  $Y_i$  is the fitted curve,  $k_1$  and  $k_n$  are the bins where the leading edge starts and ends, respectively.  $\rho$  denotes the correlation coefficient of waveform and fitted curve within the leading edge ( $k_1-k_n$ ). A noisy leading edge will give rise to low correlation coefficient  $\rho$  and, hence, lead to a high dissimilarity value. Figure 2.19 represents the developed algorithm of detecting the noisy waveform. The higher the dissimilarity value, the less similar the leading edge of the waveform and fitted

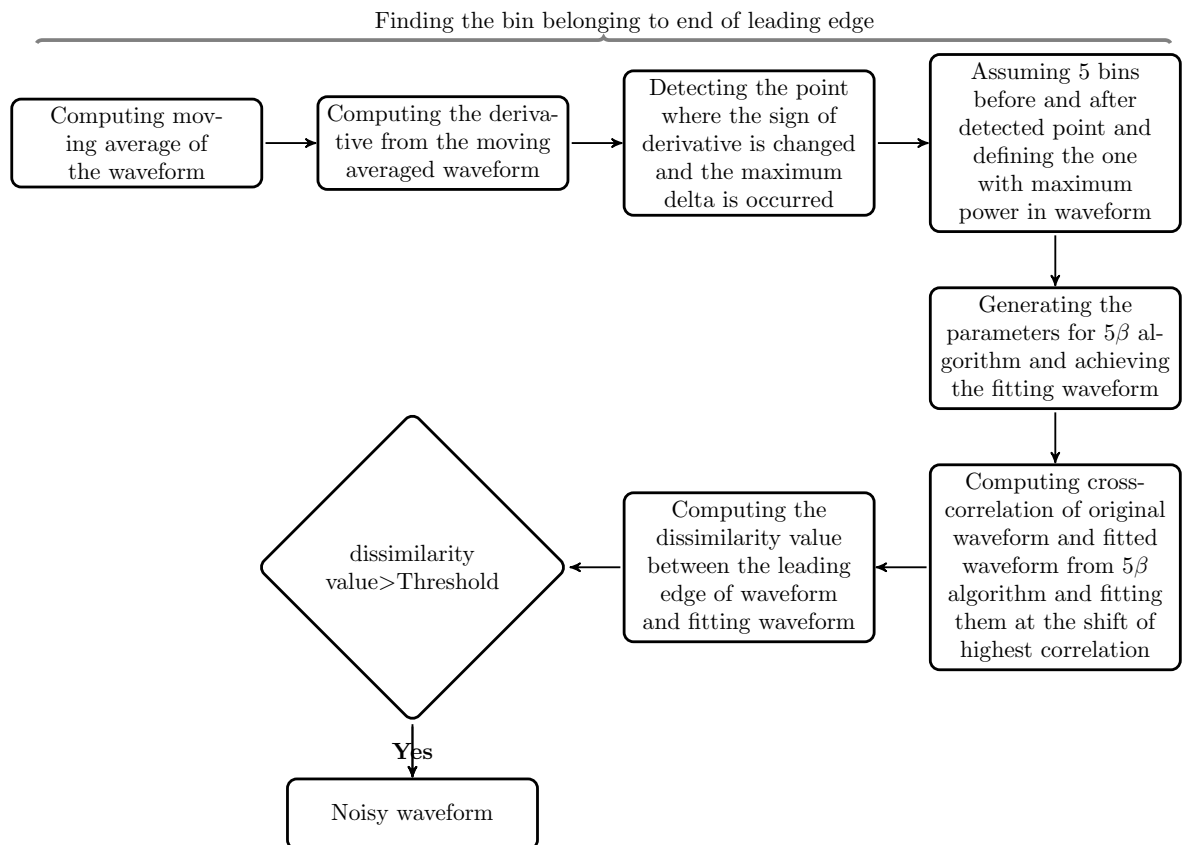


**Figure 2.19:** Diagram of detecting the noisy waveforms using the defined dissimilarity function of original and fitted waveform within the leading edge

curve. Figure 2.20 shows a set of waveforms over Urmia Lake with the computed dissimilarity value for each, in which the high dissimilarity values are assigned to the noisy waveforms, indeed.

By a practical assessment on the shape of waveforms and their dissimilarity values, 60 is defined as a threshold for dissimilarity value of the noisy waveforms. All the waveforms with dissimilarity value greater than 60 are assumed to be noisy and removed from the data set. After removing the noisy waveforms, the obtained data sets can be now used for unsupervised classification and further investigations.

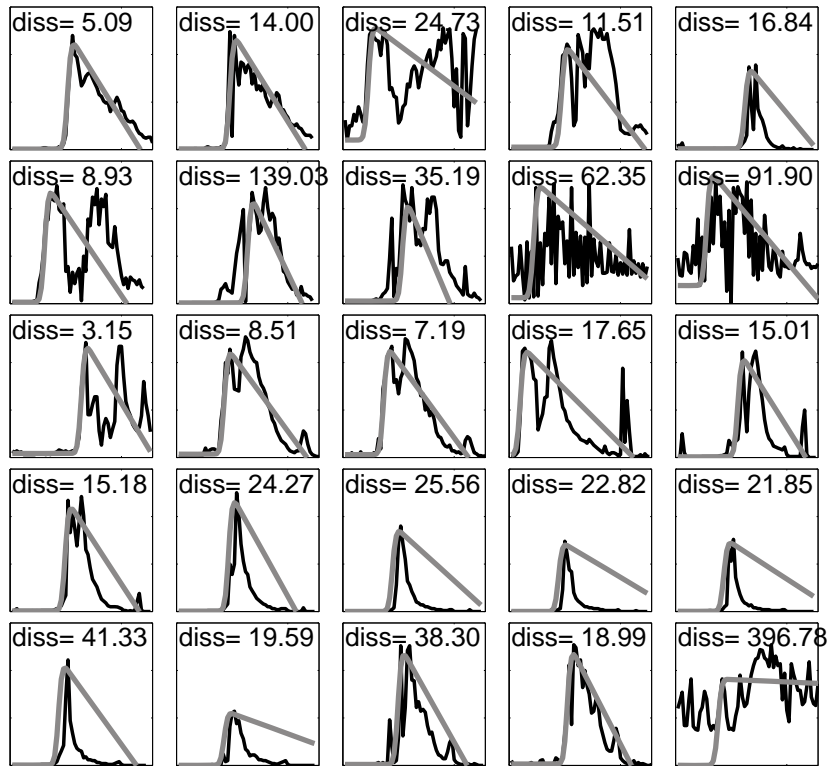


**Figure 2.20:** 25 randomly selected waveforms over Balaton Lake. The estimated dissimilarity between the leading edge of original and fitted waveforms reveals the level of noise in each waveform

### 2.3.3.2 Unsupervised classification of waveforms

A nonparametric density estimate of the data set reveals the level of heterogeneity of the data set. In case of a non-heterogeneous waveform data set with no horizontal shift between the leading edges of waveforms, the mean waveform represents the central representation of the data set. Practically, some of the waveforms are similar to each other, even when their leading edges occur in different bins. These waveforms should be classified in a same group and retracked with the same method as they indicate similar behaviour. However, as the leading edge may occur at different bins, the mean waveform can not represent the center of the data set. This can also be demonstrated by histograms of values belonging to different waveforms of a data set at different bins. Figure 2.21 shows the histogram of returned power at different bins for the waveforms of TOPEX/Poseidon over Balaton Lake. The not normally distributed histograms at different bins expresses that the mean value of returned power at each bin does not lead to a central waveform. Moreover, the median or mode of the values at different bins also do not describe the central value of each bin. This occurs due to the fact that the distributions of returned power at different bins are different, sometimes exponentially distributed like bin 52 and sometimes close to an equal distribution like bin 37, which again can be explained by the existence of a horizontal shift in the waveforms. Therefore, the median or the modal waveform should be redefined in which the horizontal shift of waveforms are considered for the estimation of proximity of waveforms. A proximity function

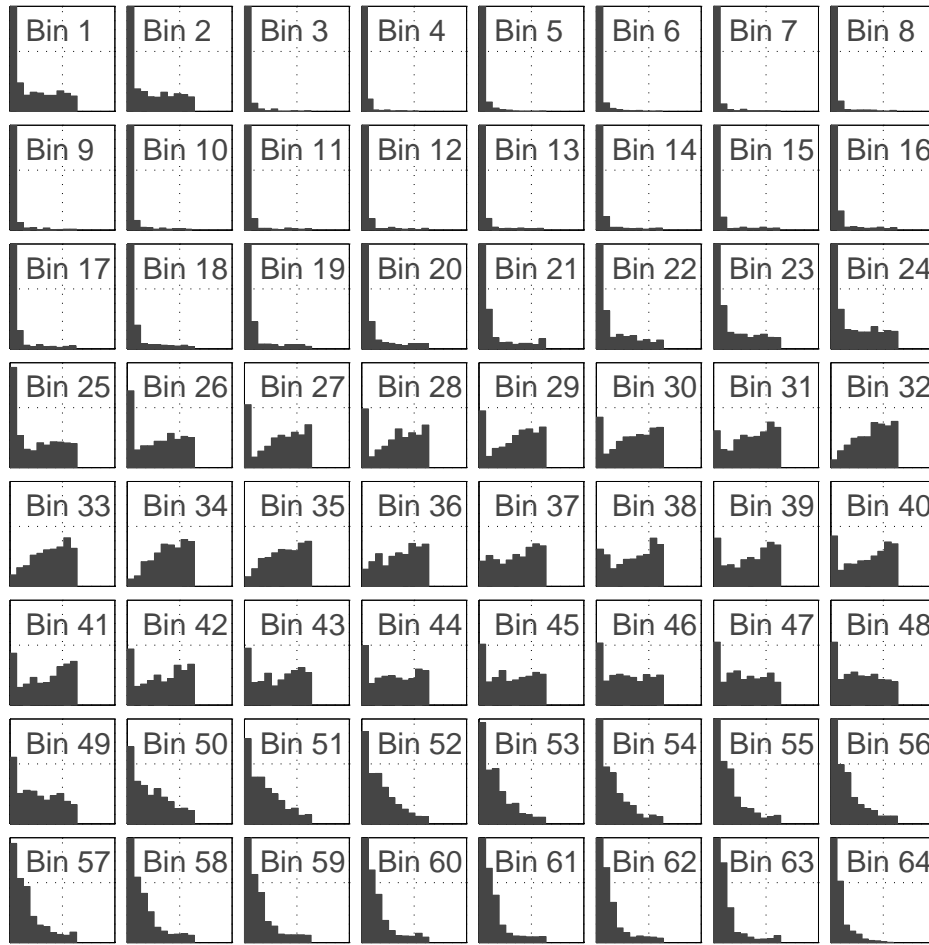


**Figure 2.21:** Histograms of returned power of waveforms of TOPEX/Poseidon over Lake Balaton at different bins

between two waveforms  $W_1$  and  $W_2$  that is invariant under translation is defined as (Dabo-Niang et al., 2007)

$$d(W_1, W_2) = \min_{\alpha \in (-\alpha_0, +\alpha_0)} \frac{1}{b-a-2|\alpha|} \int_{a+|\alpha|}^{b-|\alpha|} (W_1(t+\alpha) - W_2(t-\alpha))^2 dt \quad (2.6)$$

where  $(a, b) = (1, 64)$  is the range of each waveform. The parameter  $\alpha$  helps to shift the waveforms and compute the difference between shifted waveforms. As the leading edge could occur within the bins 9–40 (see Table 2.1), a choice of  $\alpha = 40 - 9 = 31$  leads to considering all possible horizontal shifts. Among the estimated differences for different shifted waveforms, the minimum value is introduced as the proximity value of two waveforms. By introducing such proximity function, the median waveform that is most similar to all other waveforms can be chosen as (Dabo-Niang et al., 2007)

$$W_{\text{median}} = \arg \min_{j=1,2,\dots,N} \sum_{i=1}^N d(W_i, W_j) , \quad (2.7)$$

where  $N$  indicates the number of waveforms in the data set. Subsequently, the modal waveform can be defined as the waveform with the maximum local probability. This definition can be translated mathematically as follow (Dabo-Niang et al., 2007)

$$W_{\text{modal}} = \arg \max_{j=1,2,\dots,N} \sum_{i=1}^N 1_{B(W_j,h)}(W_i) \quad (2.8)$$

where  $B(W, h)$  is a ball with radius  $h$  centered at  $W$ . This means that  $B(W_{\text{modal}}, h)$  determines an area, where the sample of waveforms is the most dense. In other words,  $B(W_{\text{modal}}, h)$  contains the largest number of waveforms among all the balls of radius  $h$ . As all of the  $W_i$ s lying to  $B(W_j, h)$  should play the same role for computing the modal waveform, an indicator function of  $1_{B(W_j,h)}$  is implemented in the equation (2.8). However, such an indicator function brings a huge border effect. In order to reduce this border effect, Dabo-Niang et al. (2007) proposed using a kernel smoothing function. The indicator has been replaced with an asymmetrical kernel function  $K$ , which is a positive decreasing function on the positive real line  $[0, \infty]$ . Therefore, equation (2.8) can be replaced by:

$$W_{\text{modal}} = \arg \max_{j=1,2,\dots,N} \sum_{i=1}^N K\left(\frac{d(W_i, W_j)}{h}\right) \quad (2.9)$$

In fact,  $K$  is a smoothing function that acts as a weight function, that can be assumed as follow

$$K(u) = \frac{3}{2}(1-u^2)1_{(0,1)}(u) \quad (2.10)$$

The indicator function  $1_{(0,1)}$  is 1, if  $u \in (0, 1)$  otherwise it is assigned 0, which leads to  $K(u) = 0$ . The shape of  $K \in (0, 1)$  has been shown in Figure 2.22.

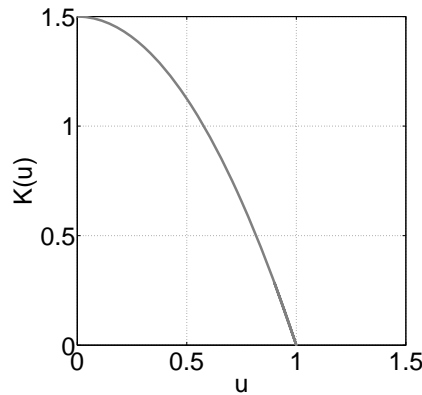


**Figure 2.22:** Smoothing Kernel function  $K$ , proposed by Dabo-Niang et al. (2007) for satellite altimetry waveforms

Practically, for each waveform in the set of waveforms  $S$ , the term  $\sum_{i=1}^n K\left(\frac{d(W_i, W_j)}{h}\right)$  can be interpreted as a ball with radius  $h$ , centered at the waveform, which allows to define the modal waveform by finding its

maximum value. Hence, the radius of the ball should be carefully determined. The balls can be converted to ball probabilities by dividing the above term by the number of waveforms  $N$

$$P_W(h) = \frac{1}{N} \sum_{i=1}^N K\left(\frac{d(W_i, W)}{h}\right) \quad (2.11)$$

For each fixed value of  $h$ ,  $N$  ball probabilities of  $P_W$  are defined which make a set of independent realizations of the same real random variable with density function  $d_{S,h}$ . This density function can be estimated through the one-dimensional smoothing technique. In this study, the density estimate  $\hat{d}_{S,h}$  has been obtained by Gaussian kernel density estimation. Among all  $h$  values, we are looking for the  $\hat{h}$  that is most accurate for discovering heterogeneity in the set of waveforms. The entropy of  $\hat{d}_{S,h}$  was suggested as a useful index for measuring the homogeneity of each density estimate by Dabo-Niang et al. (2007). So,

$$\hat{h}_S = \arg \min_h \int \hat{d}_{S,h}(t) \log \hat{d}_{S,h}(t) dt \quad (2.12)$$

defines the most accurate bandwidth for detecting difference structures in the waveforms  $S$ . The corresponding density estimate is  $\hat{d}_{S,\hat{h}_S}(\cdot)$  hereafter  $\hat{d}_S(\cdot)$ . Figure 2.23 depicts an example of computed entropy for TOPEX/Poseidon waveforms over Lake Balaton.

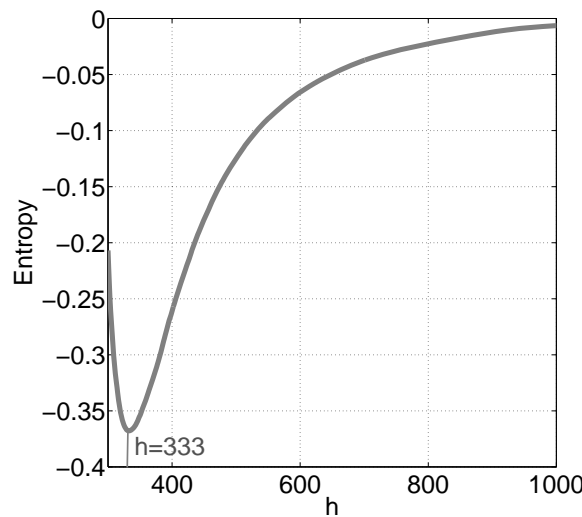


**Figure 2.23:** The estimated entropy for a range of bandwidth (300–1000) for TOPEX/Poseidon waveforms over lake Balaton

Subsequently, the modal waveform is defined as the waveform with maximum number of waveforms in its ball with radius  $\hat{h}_S$ . In case of a homogeneous data set both the mean and the median waveforms are useful to achieve centrality for the data, but the modal waveform is applicable for detecting any structural differences between data sets. This fact can be used for classification purpose to find some differences between modal  $W_{\text{modal}}$  and  $W_{\text{median}}$  or  $W_{\text{mean}}$  waveforms. The heterogeneity index can be defined as

$$HI(S) = \frac{d(W_{\text{modal}}, W_{\text{median}})}{d(W_{\text{median}}, 0) + d(W_{\text{modal}}, 0)} \quad (2.13)$$

where due to the existence of horizontal shift in the waveforms,  $W_{\text{median}}$  has been chosen rather than  $W_{\text{mean}}$ . Figure 2.24 shows the mean, median and modal waveform of a set of 1124 waveforms from TOPEX/Poseidon over Lake Urmia with  $HI$  index of 1.04.

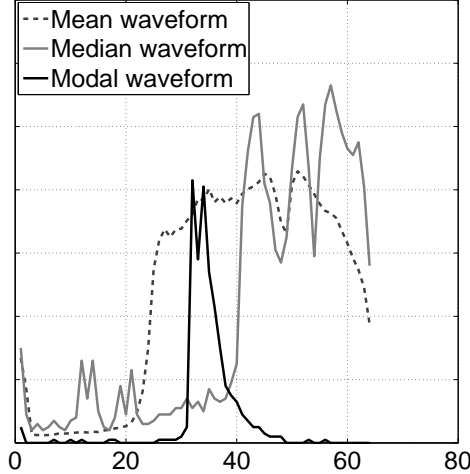


**Figure 2.24:** Mean, median and modal waveforms over the TOPEX/Poseidon waveforms of Urmia Lake with  $HI$  index of 1.04. Median waveform belongs to cycle 83 at  $\varphi = 37.1^\circ$  and  $\lambda = 45.41^\circ$  and modal waveform belonging to the cycle 188  $\varphi = 37.20^\circ$  and  $\lambda = 45.42^\circ$

An unsupervised classification procedure should be able to construct a possible splitting of  $S$  into  $G$  appropriate fixed groups  $S_1, \dots, S_G$ . The accuracy of splitting is addressed by comparing the heterogeneity index of the initial sample  $S$  and each  $S_1, \dots, S_G$

$$SHI(S; S_1, \dots, S_G) = \frac{1}{N} \sum_{k=1}^G N(S_k) HI(S_k) \quad (2.14)$$

where the  $N(S_k)$  is the number of waveforms in group  $k$ . The estimated heterogeneity index of each group  $SHI$  is then used to compute the splitting score

$$SC = SC(S; S_1, \dots, S_G) = \frac{HI(S) - SHI(S; S_1, \dots, S_G)}{HI(S)} \quad (2.15)$$

The number of groups is determined by the number  $G$  of peaks of  $\hat{d}_S(\cdot)$ . To classify  $S$  into groups

$$S = \bigcup_{k=1}^{k=G} S_k \quad \text{where } S_k = \{W \in S, p_{k-1} < \hat{p}_W(\hat{h}_S) < p_k\} \quad (2.16)$$

in which  $p_0 = 0$  and  $p_G = 1$ . In fact, after classification of  $S$  into  $S_1, \dots, S_G$  the splitting score is computed and compared with a predefined threshold,  $\tau$ , to accept or reject the process of classification. Figure 2.25 shows the obtained groups from TOPEX/Poseidon waveforms over Lake Urmia, which are classified into two major groups of quasi-Brown and quasi-specular waveforms. The corresponding splitting score

for classification is 0.83, which meets the criterion for classification as  $\tau = 0.05$  was chosen as the threshold (Dabo-Niang et al., 2007).

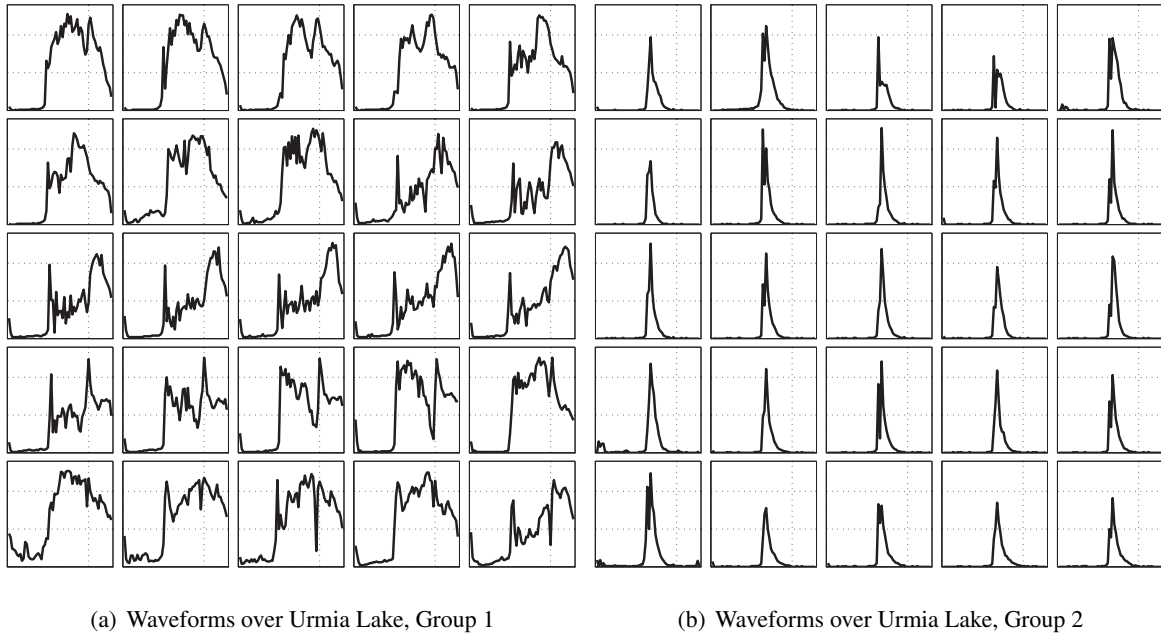


**Figure 2.25:** Result of unsupervised classification over TOPEX/Poseidon waveforms over Urmia Lake. The group 1 shows quasi-Brown waveforms and group 2 contains quasi-specular waveforms

The heterogeneity index of each group helps to assess the need for further classification of the obtained groups. For instance, the low *HI* values of 0.16 and 0.19 for groups 1 and 2 of waveforms over Lake Urmia, respectively, express the homogeneity of the groups and no need for further classification.

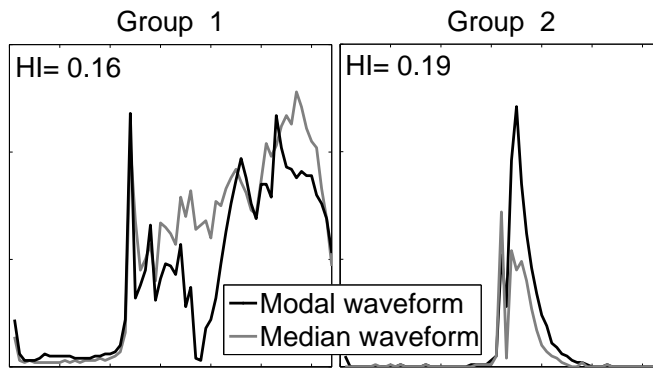


**Figure 2.26:** Modal and median waveforms of obtained groups over Urmia lakes. The computed Heterogeneity index for each group directly influenced by difference between the modal and median waveforms, which represents the heterogeneity of data set

After classifying the waveforms, an appropriate retracking method should be performed for each class to achieve water level time series with minimum possible error. Different combination of retracking

**Table 2.2:** Selected virtual stations and in situ gauge over the Lake Urmia for validation

| Station           | Lon.   | Lat.   |
|-------------------|--------|--------|
| Virtual station 1 | 37.21° | 45.43° |
| Virtual station 2 | 37.29° | 45.48° |
| Virtual station 3 | 37.51° | 45.62° |
| in situ gauge     | 37.59° | 45.26° |

algorithms over the obtained groups can be sought to assess the performance of retracking methods. Here, four scenarios are designed for retracking

- First scenario: retracking the quasi-Brown waveforms e.g. group 1 with  $5\beta$  fitting algorithm and retracking the quasi-specular waveforms e.g. group 2 using the threshold retracking method with different thresholds of 20%, 30%, 40% and 50%
- Second scenario: employing the threshold retracking method with different thresholds of 20%, 30%, 40% and 50% for all the waveforms in both groups
- Third scenario: retracking the the quasi-Brown waveforms with  $5\beta$  fitting algorithm and performing the OCOG retracking method for quasi-specular waveforms
- Fourth scenario: retracking all waveforms using only the OCOG retracking method

The aforementioned scenarios are employed for the classified waveforms of three virtual stations over Lake Urmia (Table 2.2). By subtracting the *in situ* water level measurements from the time series before and after retracking the residual values are obtained. The mean and RMS values of residual represent the bias and level of noise for the time series. The results are summarized in Table 2.3, where the residual of original water level time series of data set 1 over Urmia Lake have a RMS value of 0.63 m and mean value of 0.13 m.

By performing the scenario 1, the RMS and mean values decrease to 0.57 m and 0.07 m, respectively. This means that the retracking procedure successfully but not spectacularly decreases the error level of time series. However, using threshold retracking for all the waveforms in both groups (scenario 2) the error level of Lake Level Height (LLH) time series increases to 0.73 m, which again emphasizes the importance of primary step of classification before retracking. Scenario 3 and 4 cause a huge increase in the error of water level time series of 2.03 m and 2.85 m, respectively. This occurs due to the noisy trailing edge of waveforms, which spoil the employed OCOG retracking method in scenario 3 and 4. The results came to same conclusion for data sets 2 and 3, where the scenario 3 leads to decrease the bias and noise level of residual for water level time series (Table 2.3). Figure 2.27 shows the water level time series of Urmia Lake at the virtual station 3 before and after retracking using scenario 1. Again, the high noise and bias level of residual in scenario 2 and 4 together with low noise and bias level of residual in scenario 1 emphasizes the necessity of classification of the waveforms before retracking.

**Table 2.3:** Results of retracking of waveforms belonging to virtual stations 1, 2 and 3 over Urmia Lake using different scenarios

| Virtual station |      | Before retracking | After retracking, scenario |              |              |              |       |       |       |       |       |       |
|-----------------|------|-------------------|----------------------------|--------------|--------------|--------------|-------|-------|-------|-------|-------|-------|
|                 |      |                   | 1                          |              |              |              |       | 2     |       |       |       |       |
|                 |      |                   | 20%                        | 30%          | 40%          | 50%          |       | 20%   | 30%   | 40%   | 50%   |       |
| 1               | RMS  | 0.63              | 0.57                       | 0.57         | <b>0.57</b>  | <b>0.57</b>  | 0.61  | 0.61  | 0.65  | 0.73  | 2.03  | 2.85  |
|                 | Mean | 0.13              | 0.08                       | 0.08         | <b>0.07</b>  | <b>0.07</b>  | -0.04 | -0.14 | -0.24 | -0.39 | 0.54  | -0.13 |
| 2               | RMS  | 0.81              | <b>0.72</b>                | <b>0.72</b>  | <b>0.72</b>  | <b>0.72</b>  | 0.76  | 0.78  | 0.83  | 0.88  | 1.69  | 3.27  |
|                 | Mean | 0.04              | <b>0</b>                   | <b>0</b>     | <b>0</b>     | <b>0</b>     | -0.13 | -0.22 | -0.33 | -0.48 | 0.43  | 0.09  |
| 3               | RMS  | 0.63              | <b>0.59</b>                | <b>0.59</b>  | <b>0.59</b>  | <b>0.59</b>  | 0.69  | 0.68  | 0.67  | 0.63  | 0.60  | 1.5   |
|                 | Mean | -0.14             | <b>-0.12</b>               | <b>-0.12</b> | <b>-0.12</b> | <b>-0.12</b> | -0.58 | -0.47 | -0.67 | -0.63 | -0.12 | -0.97 |

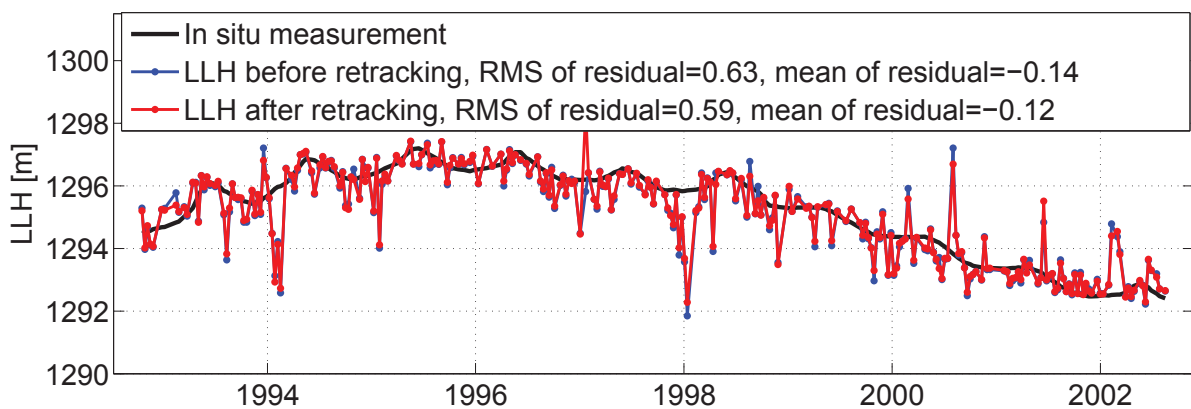


**Figure 2.27:** Water level time series of Urmia Lake at the virtual station 3 before and after retracking using scenario 1

## 2.4 Random noise reduction on retracked data

As discussed before, the on-board altimeter often uses a standard algorithm tuned for ocean surfaces to estimate the range from the waveforms (Marth et al., 1993; Quartly et al., 2001). Nevertheless, ENVISAT employs four retracking algorithms of *Ocean* (Brown, 1977), *Ice-1* (Wingham et al., 1986), *Ice-2* (Legrésy and Rémy, 1997) and *SeaIce* (Laxon, 1994) to obtain ranges compatible with different surfaces. This compatibility is assured if the returned waveforms from a surface follow an expected shape, for which the retracker is designed. *Ocean* and *Ice-2* retrackers are based on the Brown model (Brown, 1977), *Ice-1* retracker is based on OCOG scheme and *SeaIce* retracker uses the threshold to calculate the tracker offset (Frappart et al., 2004). However, the heterogeneity of waveforms over inland water bodies has been identified in this study, leading to uncertainty of each retracker's estimation. Frappart et al. (2006b) reported that, among these algorithms, *Ice-1* and *Ice-2* show better performance over continental water bodies. However, previous studies demonstrated different performance of the four retrackers over different water bodies (da Silva et al., 2010; Frappart et al., 2006b). Therefore, the noise level of each retracker should be investigated serving as a way to achieve a better estimation.

In order to assess the noise level, water level time series derived with each retracker can be compared to each other. 20Hz measurements of water level are compared after applying geophysical corrections. Each retracker provides an along-track profile of water level variation within the range of the virtual station. Although all the profiles from different retrackers are derived from the same measurement and waveforms, they show distinct behaviour (Figure 2.28 left). Assuming that the range of virtual station is correctly determined, statistical characteristics of each profile can represent the performance of each retracker in each pass. Particularly, as the ground velocity of ENVISAT is ca. 6.6km/s, the observed water level from a river or lake with narrow width should not vary too much. Therefore, a water profile with smaller standard deviation should be closer to the ground truth. Standard deviations ( $\sigma_t$ ) of water levels profiles also allow to interpret retrackers' error level. The estimated mean values of profiles are then considered as estimated water level from each retracker. Figure 2.28 (top) shows the mean profiles from different retrackers over Niger River. The estimated  $\sigma_t$  values of each retracker over time are shown in Figure 2.28 (bottom). The lower the  $\sigma_t$ , the smaller the error of estimated water level by that specific retracker.

The average value  $\bar{\sigma}$  of each retrackers  $\sigma_t$  over time, represents the general error level of each retracker. Practically, it is expected that the average error  $\bar{\sigma}$  of each retracker represents the capability of the retracker algorithms over the virtual station as it is estimated through the variation of water level within the virtual station. Table 2.4 summarizes the estimated  $\bar{\sigma}$  values from different retrackers for the Amazon, Amur, Brahmaputra, Congo, Danube, Don, Mekong, Niger, Ob, Mississippi and Vistula rivers. These case studies are chosen as they have different characteristics, which brings the opportunity of a comprehensive investigation. The Amazon, Amur, Ob, Danube, Congo, Mississippi, Mekong, Niger and Brahmaputra are broad enough to be captured by altimetry, while the Don and Vistula are narrow rivers with width of 0.3 km (Table 2.4). The Ob River is located in the boreal region, which is mostly covered with snow and ice. The Amazon, Congo and Niger flow in the tropics, where high water levels occur during the wet season. As indicated in the Table 2.4, the  $\bar{\sigma}$  values of ocean retracker as a standard retracker of ENVISAT represent the maximum error for most of the rivers. However, the retracker with minimum error is different for different rivers: *Ice-1* for the Amazon, Amur, Brahmaputra, Mississippi and Vistula, *Ice-2* for Danube, *SeaIce* for Don, Mekong, Congo and Niger and *Ocean* for Ob.

Although the results demonstrate that employing different algorithms than the standard *ocean* retracker leads to noise reduction, it can not be concluded that one given retracker performs best. Hence, an algorithm should be sought to combine the results of the different retrackers in order to reduce noise level. In fact, measurements from different retrackers can be combined as they are originally from the same waveforms.

The algorithm for the combination of retrackers implements the following criterion: over each pass/time pick up the water level from the retracker with the lower  $\sigma_t$  and assign it to the water level time series / River Surface Height (RSH). In case the minimum  $\sigma_t > 1$  m, however, the algorithm chooses the median of *Ice-1* retracker's for RSH.

**Table 2.4:** Virtual Stations over different rivers with their characteristics together with estimated average error  $\bar{\sigma}$  of each retracker for the obtained water level time series

| Name        | virtual station |            |                   |     | River width [km] | average error $\bar{\sigma}$ of |             |             |             |
|-------------|-----------------|------------|-------------------|-----|------------------|---------------------------------|-------------|-------------|-------------|
|             | Lat. [deg]      | Lon. [deg] | Track Radius [km] |     |                  | Ocean                           | Ice-1       | Ice-2       | SeaIce      |
| Amazon      | -1.89           | -55.59     | 153               | 1.5 | 3.7              | 0.60                            | <b>0.48</b> | 1.50        | 1.23        |
| Amur        | 50.50           | 137.04     | 332               | 1.0 | 2.0              | 2.34                            | <b>0.22</b> | 0.35        | 0.22        |
| Brahmaputra | 25.73           | 89.76      | 398               | 2.0 | 10               | 1.77                            | <b>0.17</b> | 0.25        | 0.24        |
| Congo       | -4.31           | 15.45      | 72                | 2.0 | 5.0              | 4.32                            | 0.41        | 0.61        | <b>0.29</b> |
| Danube      | 45.25           | 28.54      | 7                 | 0.7 | 1.5              | 5.05                            | 0.58        | <b>0.33</b> | 0.86        |
| Don         | 47.50           | 40.56      | 414               | 0.5 | 0.3              | 10.81                           | 1.01        | 0.53        | <b>0.47</b> |
| Mekong      | 13.78           | 105.97     | 433               | 0.7 | 1.4              | 0.36                            | 0.33        | 0.39        | <b>0.32</b> |
| Mississippi | 32.34           | -90.92     | 491               | 0.7 | 1.2              | 1.94                            | <b>0.35</b> | 0.82        | 0.47        |
| Niger       | 7.85            | 6.91       | 351               | 0.8 | 1.6              | 0.33                            | 0.23        | 0.22        | <b>0.19</b> |
| Ob          | 65.13           | 65.28      | 6                 | 1.0 | 2.3              | <b>0.39</b>                     | 0.41        | 0.85        | 0.51        |
| Vistula     | 54.16           | 18.84      | 472               | 0.3 | 0.3              | 0.44                            | <b>0.08</b> | 0.09        | <b>0.08</b> |

By employing this criterion, it is expected to achieve water level time series with decreased noise level in comparison to the water level time series from the retrackers. Figure 2.28 (middle) illustrates the obtained RSH time series over Niger River with total  $\bar{\sigma} = 0.15$  m, that indicates a 0.02 m reduction in noise level comparing to the *SeaIce* retracker. Table 2.5 shows the estimated  $\bar{\sigma}$  values from different retrackers again

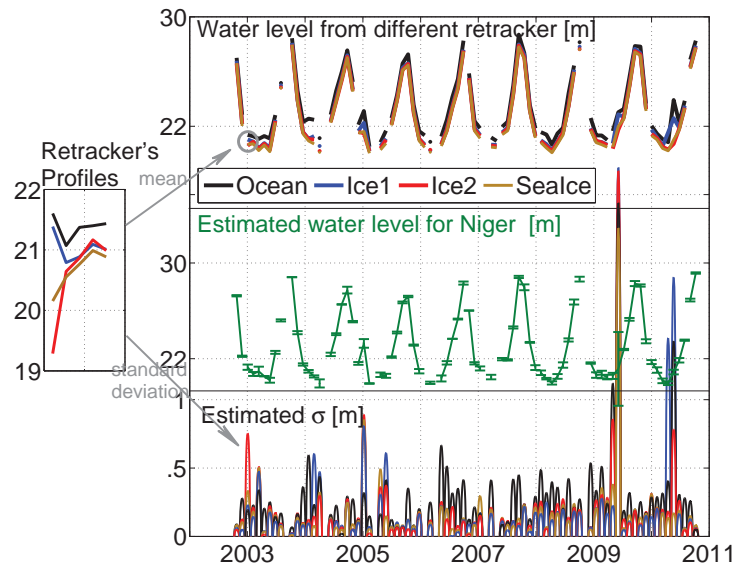


**Figure 2.28:** Left: along-track profiles of water level within the virtual station of Niger River around January 2003. Right: Top) Water level time series for Niger River after geophysical and outlier corrections from different retrackers. Middle) The estimated water level time series over Niger River using combination of time series from different retrackers and choosing the measurement with minimum error at each time. Bottom) Computed standard deviation of each retracker's measurements which represent each retracker's error over time

together with the  $\bar{\sigma}$  of RSH of different rivers. As expected the  $\bar{\sigma}$  values of the combination approach (for RSH) are less than  $\bar{\sigma}$  for retracking methods. The  $\bar{\sigma}$  values of ocean retracker as a standard retracker of ENVISAT represent the maximum error for most of the rivers. The estimated  $\bar{\sigma}$  of different retrackers for Don River before and after off-nadir correction emphasizes the necessity of this correction. Also, the  $\bar{\sigma}$  of water level time series after outlier correction always show lower value, which highlights the effect of outlier correction.

**Table 2.5:** Estimated average error  $\bar{\sigma}$  of each retracker together with the estimated error for the obtained water level time series before and after outlier correction for different rivers

| Name                 | Ocean | Ice-1 | Ice-2 | SeaIce | RSH  | RSH <sub>oc</sub> |
|----------------------|-------|-------|-------|--------|------|-------------------|
| Amazon               | 0.60  | 0.48  | 1.50  | 1.23   | 0.42 | <b>0.39</b>       |
| Amur                 | 2.34  | 0.22  | 0.35  | 0.22   | 0.16 | <b>0.15</b>       |
| Brahmaputra          | 1.77  | 0.17  | 0.25  | 0.24   | 0.17 | <b>0.15</b>       |
| Congo                | 4.32  | 0.41  | 0.61  | 0.29   | 0.27 | <b>0.26</b>       |
| Danube               | 5.05  | 0.58  | 0.33  | 0.86   | 0.28 | <b>0.27</b>       |
| Don                  | 10.81 | 1.01  | 0.53  | 0.47   | 0.57 | 0.46              |
| Don <sub>nadir</sub> | 5.24  | 0.31  | 0.21  | 0.19   | 0.10 | <b>0.09</b>       |
| Mekong               | 0.36  | 0.33  | 0.39  | 0.32   | 0.28 | <b>0.27</b>       |
| Mississippi          | 1.94  | 0.35  | 0.82  | 0.47   | 0.29 | <b>0.28</b>       |
| Niger                | 0.33  | 0.23  | 0.22  | 0.19   | 0.17 | <b>0.15</b>       |
| Ob                   | 0.39  | 0.41  | 0.85  | 0.51   | 0.20 | <b>0.19</b>       |
| Vistula              | 0.44  | 0.08  | 0.09  | 0.08   | 0.07 | <b>0.05</b>       |

RSH<sub>oc</sub>: Obtained water level time series after outlier correction

Don<sub>nadir</sub>: Don River after off-nadir correction

It should be noted that, results in Table 2.5 are achieved without taking any systematic discrepancy i.e. biases, if any, between retrackers into account. It is known from previous studies over the ocean that different retrackers are potentially affected by biases. This happens as different retrackers treat noises at different parts of the waveform differently. For instance, OCOG based retrackers are more sensitive to the noises of the trailing edge, while threshold based retrackers are not influenced by noises of the trailing edge and are more sensitive to the noise at the leading edge (see Figure 2.15).

In fact, biases between retrackers is a function of both methodology and shape of the waveforms. Therefore, for inland water application of altimetry, the provided bias computed over ocean does not lead to a meaningful result. This can be also inferred from the reported biases from previous studies over different water bodies, where negligible bias between *Ice-1* and *Ice-2* over Amazon has been reported by da Silva et al. (2010) and Crétaux et al. (2009) achieved 24 cm of bias over Lake Issykkul for these two retrackers. Moreover, Calmant et al. (2012) investigated the bias of *Ice-1* retracker over the Amazon River using GPS analysis for thirty-nine gauges. Interestingly, they found different bias values for the thirty-nine gauges varying between 0.7 to 1.5 m. This discussion leads to a conclusion that the bias of a retracker, if any, over inland water bodies relies more on the shape of the waveforms rather than the methodology. In addition the shape of waveforms over certain virtual station do not follow similar behaviour. The shape varies

due to effect of wind, vegetation canopy, water level and neighboring topography. In fact, the mentioned effects change over different seasons and climate conditions, which leads to changing waveform shape of the and different discrepancies (i.e. bias) between retrackers in each pass. This is also highlighted in Figure 2.29, where 20 Hz water level variations over the virtual station of Obidos at the Amazon River show positive bias between *ocean* and *Ice-1* retrackers in November 2003, while it reveals a negative bias in November 2005.

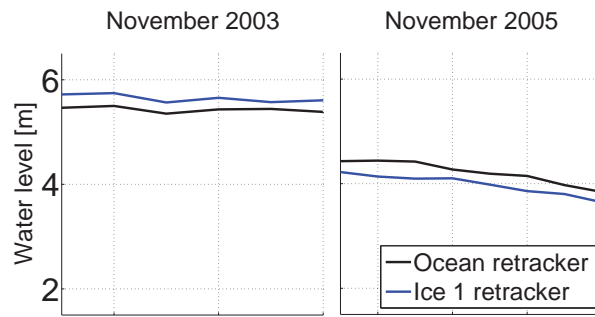


**Figure 2.29:** Water level variations over Obidos virtual station at Amazon River belonging to *Ocean* and *Ice-1* retrackers for November 2003 and 2005

A possible solution to remove any bias between retrackers is performing the investigation at the waveform level and over each pass, individually. In such investigation one can classify the waveforms of each pass into classes with similar sensitivity to the algorithm of retracking and find out the biases of them. However, even without dealing with any systematic discrepancy the results of the combination approach emphasize the necessity of combining retrackers instead of using one of them for reducing the random noise in the time series.

#### 2.4.1 Validation of the combination approach

The combination approach approach can be validated against available *in situ* measurements of water level at a gauge close to the virtual station. Among the virtual stations in the Table 2.4, the *in situ* water level measurements are only available for the Amazon, Congo and Mississippi. The daily *in situ* water level time series of the Amazon River at Obidos with  $\varphi = -1.94^\circ$ ,  $\lambda = -55.5^\circ$ , Congo River at Congo à Beach Brazzaville with  $\varphi = -4.31^\circ$ ,  $\lambda = 15.45^\circ$  and Mississippi River at Vicksburg with  $\varphi = 32.34^\circ$ ,  $\lambda = -90.92^\circ$  are used for validation. The gauges are located in distances of 10km, 17km and 5km from the virtual stations of the Amazon, Congo and Mississippi, respectively. Since the bias between *in situ* and altimetric water level time series does not play a role in this discussion, it is removed via the difference of average values of both time series. Figure 2.30 shows water level time series from different retracking methods , combination approach and *in situ* measurements over the aforementioned locations.

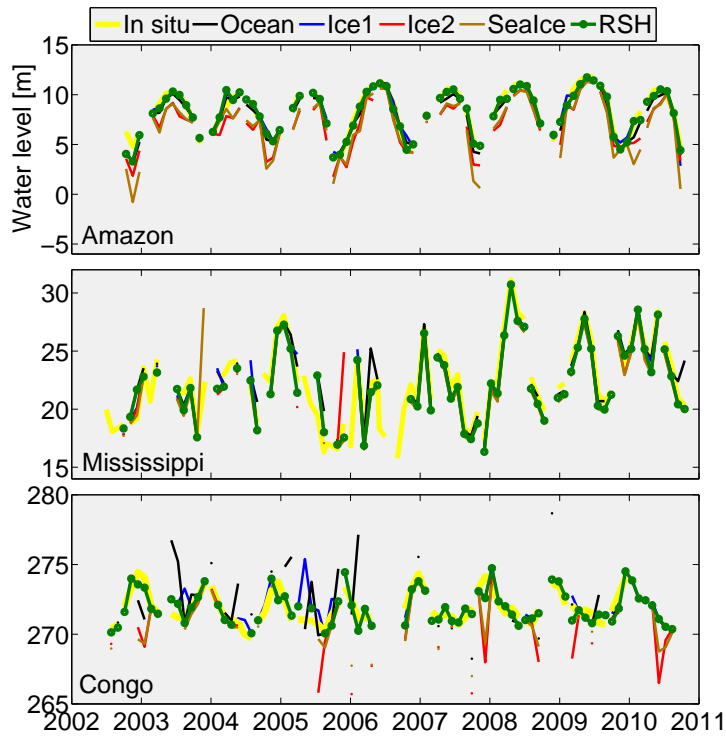


**Figure 2.30:** Top) Water level time series from different retracking methods, combination approach and the *in situ* measurements for Amazon River at Obidos. Middle) Mississippi River at Vicksburg. Bottom) Congo River at Congo à Beach Brazzaville

The RSH time series from the combination approach show maximum correlations with *in situ* measurements for all three cases (Table 2.6). The error of estimated water level is obtained by subtracting each time series from the *in situ* time series. The residual of time series for the combination approach also indicate the minimum standard deviation ( $\sigma$ ) of 0.44 m, 0.62 m and 0.82 m for the Amazon, Congo and Mississippi, respectively. This supports the idea of combining different retrackers to generate the water level time series for a virtual station, instead of using one of the retrackers. However, as the combination approach uses the values from different retrackers, the contribution of each retracker for creating the RSH should be assessed. Table 2.6 lists the computed correlation, residual  $\sigma$  of water level time series from different retracker and combination approach and contribution of each retracker to RSH for the Amazon, Mississippi and Congo rivers. For the Amazon, the obtained RSH from the combination approach contains 76 epochs: 27% (20 epochs) from *Ocean* retracker, 69% (53 epochs) from *Ice-1* retracker and 4% (3 epochs) from *SeaIce* retracker. *Ice-2* retracker does not contribute to the estimated RSH for Amazon. The contribution of *Ice-1* retracker is also high for the Mississippi, where the obtained RSH from the combined approach contains 73 epochs: 14% (10 epochs) from *Ocean* retracker, 64% (47 epochs) from *Ice-1* retracker, 11% (8 epochs) from *Ice-2* retracker and 11% (8 epochs) from *SeaIce* retracker. The result in Table 2.6 show that the *Ice-1* retracker contributes the most to RSH for all three cases. This was already expected as in previous studies *Ice-1* retracker was introduced as the best retracker for inland water studies (Frappart et al., 2006a) and also can be seen in the Table 2.6. All in all, the results of

**Table 2.6:** Correlation and  $\sigma$  of residual of obtained water level time series from different retracking methods and the combination approach with in situ measurements together with percentage of contribution of different retrackers for creating RSH for three virtual stations in Amazon, Congo and Mississippi rivers

|                          | Ocean Ice-1 | Ice-2 | SeaIce | RSH  |             |
|--------------------------|-------------|-------|--------|------|-------------|
| <b>Amazon</b>            |             |       |        |      |             |
| Correlation              | 0.97        | 0.96  | 0.92   | 0.89 | <b>0.98</b> |
| $\sigma$ of error<br>[m] | 0.54        | 0.58  | 0.89   | 1.29 | <b>0.44</b> |
| Contribution<br>to RSH   | 27%         | 69%   | 0%     | 4%   | –           |
| <b>Congo</b>             |             |       |        |      |             |
| Correlation              | 0.30        | 0.77  | 0.39   | 0.46 | <b>0.85</b> |
| $\sigma$ of error<br>[m] | 2.21        | 0.80  | 2.05   | 1.54 | <b>0.62</b> |
| Contribution<br>to RSH   | 7%          | 77%   | 5%     | 11%  | –           |
| <b>Mississippi</b>       |             |       |        |      |             |
| Correlation              | 0.93        | 0.95  | 0.94   | 0.94 | <b>0.97</b> |
| $\sigma$ of error<br>[m] | 1.14        | 0.89  | 1.06   | 1.10 | <b>0.82</b> |
| Contribution<br>to RSH   | 14%         | 64%   | 11%    | 11%  | –           |

validation emphasize the necessity of combining retrackers instead of using one of them for reducing the random noise in the time series.

# Chapter 3

## River discharge from satellite altimetry

Satellite altimetry has been introduced in Chapter 1 as an alternative sensor for the indirect estimation of river discharge. The indirect methodology conventionally is based on finding a functional relationship (rating curve) between water level estimated by satellite altimetry at a virtual station close to the discharge gauging station, upstream or downstream, and measured discharges at the gauge. It is known that this technique has certain limitations, which will be addressed in this chapter.

On the one hand, this technique is limited by the availability of *in situ* discharge measurements simultaneous with altimetry data. In case of using ENVISAT altimetry, simultaneous measurements mean that the discharge data should be available after the year 2003. This becomes a serious restriction as among the 8424 recorded gauging stations in GRDC database, only 40% of stations provide discharge data after 2003 (Figure 1.4). On the other hand, the location of the altimetry footprint can also limit the usage of the technique. It becomes critical in two ways, one being a footprint dissimilar with gauge in terms of geomorphology (Papa et al., 2010) and the other is the low quality water level time series by altimetry driven by an inappropriate location of footprint. Figure 3.1 depicts the discharge gauges, the crossing tracks of ENVISAT and the chosen virtual stations for those rivers that have been investigated in Chapter 2.

If *in situ* discharge measurements and high quality water level time series from altimetry are available, the performance of the methodology is restricted by sampling problems (Papa et al., 2012). In other words, establishing the rating curve is possible if the measurements of water level from altimetry and of *in situ* discharge are consistent in statistical sense. This consistency is challenging as satellite altimetry provides only 10 or 35 days interval time series and discharge measurements are often available in daily or monthly time-scales.

The challenges of uncertainty and resolution of altimetry have been investigated in Chapter 2, where different algorithms have been developed and employed to control the uncertainty and resolution problems. In this chapter the problem of inconsistency of time series, which directly affects constructing the rating curve, is targeted. Then, a statistical modeling approach is investigated to create the rating curve without the requirement of simultaneous measurements . Finally, the problems of river discharge estimation using the established rating curves will be discussed and possible solutions will be investigated.

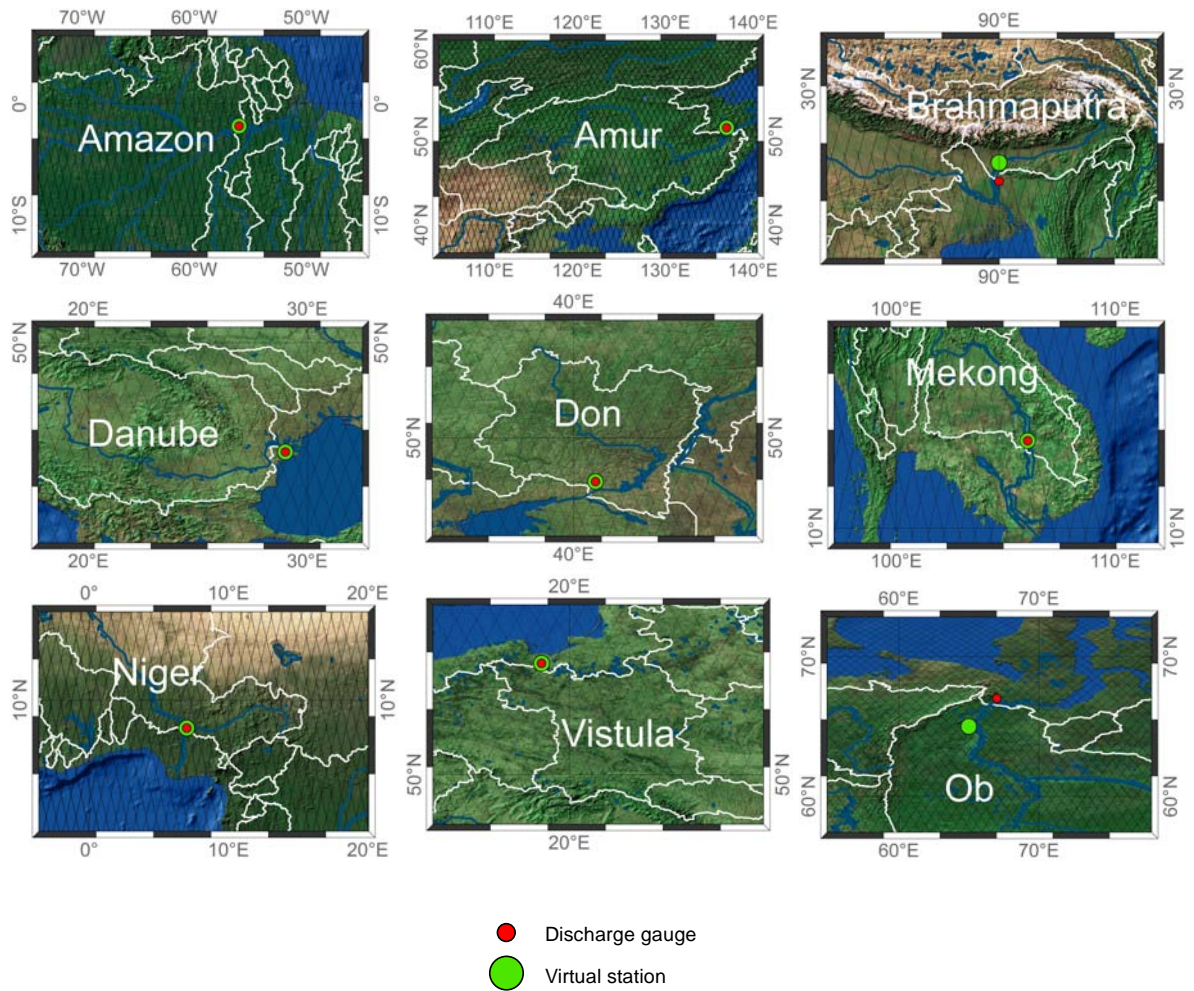


**Figure 3.1:** The discharge gauging stations of and the crossing tracks of ENVISAT for different rivers. The virtual stations of Amazon, Amur, Brahmaputra, Danube, Mekong, Vistula and Ob are defined upstream of discharge gauge and downstream for Niger and Don

### 3.1 Controls on consistency problem

In order to construct a rating curve from the relationship of the water level and discharge, corresponding time series are needed. River discharge measurements at different gauges are typically available in daily or monthly time scale, often containing missing values in the order of a month to years. On the other hand, water level time series belonging to a virtual station of altimetry close to the gauge is available every 10 or 35 days (depending on the mission). Figure 3.2 shows the daily *in situ* discharge measurements together with the water level time series from ENVISAT. Daily discharge values are not available over Dec. 2002 and early 2003, while water level time series are missing before Oct. 2002. Moreover, being just a snapshot, altimetry provides neither daily nor monthly sampling. In general, from the data availability and situation, the sources of inconsistency are distinguished as

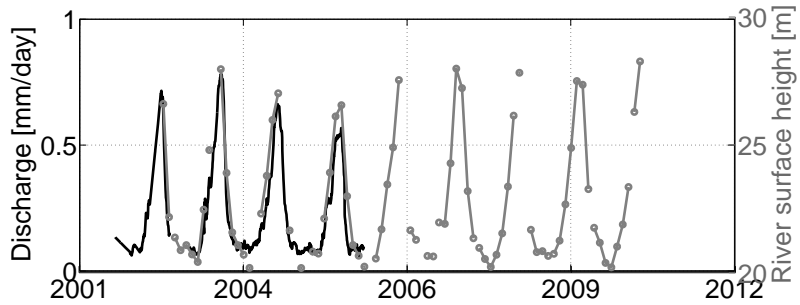


**Figure 3.2:** Time series of daily discharge measurements at a gauge that is located over Niger River at  $\varphi = 7.80^\circ$  and  $\lambda = 6.76^\circ$  together with the river surface height time series from ENVISAT belonging to the virtual station 10km upstream at  $\varphi = 7.85^\circ$  and  $\lambda = 6.91^\circ$

- Data availability
- Temporal resolution

**Data availability** In terms of data availability, rivers are categorized into three groups

Group 1: Rivers with available discharge measurements synchronous with the time period of altimetry e.g. the Amazon, Niger, Danube, Amur and Ob.

Group 2: Rivers whose available discharge measurements are not synchronous with altimetry e.g. the Mekong, Brahmaputra, Don and Vistula.

Group 3: Rivers with no available discharge measurements at all e.g. the Nile and Parana rivers

Practically, it is not possible to establish a rating curve for rivers in group 3 as discharge measurements are not available. Moreover, for establishing the rating curve, rivers in group 1 and 2 should be treated differently. However, for both groups the estimation of river discharge using the corresponding rating curves is only possible at the times of altimetry. Hence, it is important to study the temporal resolution of satellite altimetry.

**Temporal resolution** As 35-day sampling of altimetry is sufficiently close to a month, it is more convenient to turn the snapshot measurements into monthly discharge. This raises two important questions:

1. Which time resolution of discharge corresponds better to water level from altimetry for creating a functional relationship? daily discharge at the day of altimetry considered as monthly value (hereafter quasi-monthly) or true monthly discharge? For the former, the daily discharge at the day of altimetry is multiplied by the number of days of that month. For the latter, all daily values at the month of altimetry are aggregated (Figure 3.3).
2. Is the statistical distribution of the observed discharge at the times of altimetry measurements consistent with the statistical distribution of the complete discharge dataset?

The first question concerns the dynamic behaviour of the river, where in case of stationary flows monthly and quasi-monthly discharge will be similar. They will be dissimilar in highly fluctuating rivers with narrow width. The example of Figure 3.3 shows a difference of monthly and quasi-monthly discharge. Figure 3.4 shows the comparison of monthly and quasi-monthly discharge measurements for the Danube and Niger rivers, that overall represent similar behaviour with deviations up to ca. 20%.

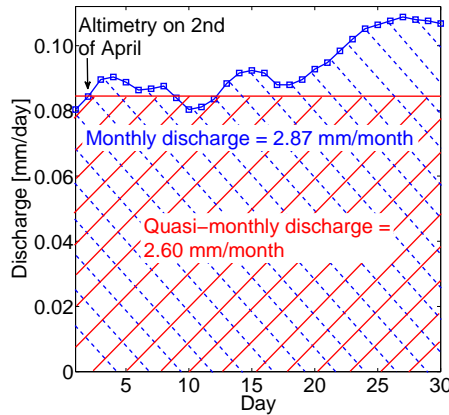


**Figure 3.3:** Daily discharge of Niger River in April 2004. ENVISAT flies over virtual station of Niger River on April 2, 2004. The quasi-monthly discharge for April 2004 is  $0.086\text{ mm/day} \times 30 = 2.60\text{ mm/month}$  and the monthly discharge is  $2.87\text{ mm/month}$ .

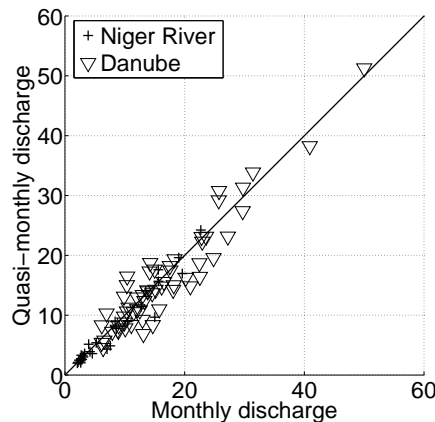


**Figure 3.4:** Scatter plot of quasi-monthly discharge versus the true monthly discharge value of Niger and Danube rivers for 2002–2012

The second question expresses the performance of the rating curve. If the statistical distribution of the observed discharge at the times of altimetry measurements does not represent the statistical distribution of discharge, the derived rating curve would not be able to model every possible value of discharge within the range of distribution. Answering this question also justifies the ability of altimetry to map extreme values.

In order to compare the distribution of both sets of data, the corresponding empirical Cumulative Distribution Function (CDF) of monthly and quasi-monthly values are compared. The statistical comparison of distributions have been done using the Kolmogorov-Smirnov (K-S) test, which is a nonparametric test for the equality of one-dimensional probability distributions from two samples (Massey, 1951). The null hypothesis of this test is that the samples are drawn from the same distribution. Therefore, the K-S statistic quantifies a distance between the empirical distribution functions of two samples to assess the similarity of the distributions. A smaller test statistic implies a stronger similarity. The more similar distributions of monthly or daily discharge within the time period of altimetry with the whole distribution of monthly or daily discharge, the better the model can extract river discharge. The test statistic can also be employed as a tool to answer the first question where the lower test statistic would lead to a choice between quasi-monthly or monthly discharge for building the rating curve. However, addressing the mentioned questions and building the rating curve should be dealt with differently for rivers in group 1 and 2.

### 3.1.1 Consistency check for rivers in group 1

In order to investigate the boundary condition of constructing rating curves for rivers in group 1, the rivers Amazon, Niger, Danube, Amur and Ob have been chosen. Table 3.1 lists the location of discharge gauging stations, the time period of the available discharge data and the distance of the gauging station to the defined virtual stations (Table 2.4) of these five rivers (cf. Figure 3.1).

**Table 3.1:** Discharge gauging stations of five rivers in group 1 with the time period of available discharge measurements for each and their distance to the close by virtual stations. + means that the virtual station is located upstream and – stands for downstream.

|        | Area<br>[km <sup>2</sup> ] | Lat.<br>[deg] | Lon.<br>[deg] | Period    | Distance to<br>virtual station<br>[km] |
|--------|----------------------------|---------------|---------------|-----------|--|
| Amazon | 4672 876                   | -1.94         | -55.51        | 1927–2010 | +10                                    |
| Amur   | 1949 471                   | 50.63         | 137.12        | 1940–2004 | +14                                    |
| Danube | 771 277                    | 45.21         | 28.71         | 1931–2008 | +13                                    |
| Niger  | 2100 508                   | 7.80          | 6.76          | 1970–2006 | -17.6                                  |
| Ob     | 2926 321                   | 66.57         | 66.53         | 1954–2009 | +170                                   |

As for rivers in this group discharge measurements are available during the time period of altimetry, the two raised questions can be answered by performing the K-S test over the monthly and daily discharge at the time of ENVISAT measurements and the whole available discharge data. The critical value for  $\alpha = 0.05$  is given by (Kececioglu, 1993)

$$K = 1.36 \sqrt{\frac{n_1 + n_2}{n_1 n_2}}, \quad (3.1)$$

**Table 3.2:** Kolmogorov-Smirnov test statistics with significance level of 0.05 for the comparison of distribution of two sets of data: monthly/daily discharge at the time of altimetry and whole monthly/daily discharge of rivers in group 1

| River  | Monthly     |      | Daily       |      |
|--------|-------------|------|-------------|------|
|        | D           | K    | D           | K    |
| Amazon | 0.09        | 0.14 | <b>0.08</b> | 0.16 |
| Niger  | <b>0.18</b> | 0.21 | 0.20        | 0.24 |
| Danube | <b>0.06</b> | 0.16 | 0.08        | 0.17 |
| Amur   | <b>0.18</b> | 0.25 | 0.29        | 0.31 |
| Ob     | 0.06        | 0.15 | <b>0.05</b> | 0.17 |

where  $n_1$  and  $n_2$  are the sample sizes of datasets. Figure 3.5 shows the obtained CDF and the results of K-S test at a significance level of 0.05 over the Niger River. The null hypothesis for all the chosen rivers

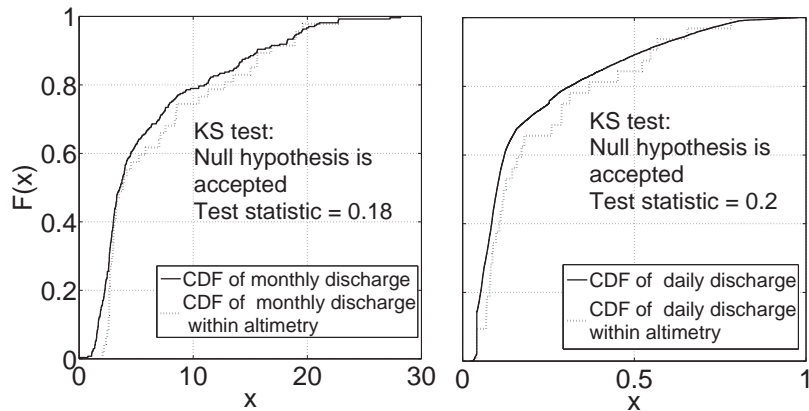


**Figure 3.5:** Comparison of empirical cumulative distribution functions of whole available monthly (left) / daily (right) discharge and monthly/daily discharge at the time of altimetry and the results of K-S test with significance level of 0.05.

in group 1 is accepted, which means that the obtained test statistics  $D$  is lower than the critical value  $K$  (Table 3.2). For the Amazon and Ob the statistics from the daily discharge indicate higher similarity whereas the Niger, Danube and Amur are statistically closer to discharge. However, as the test statistics for both monthly and daily discharge data are very close to each other, they will both be used for further investigations.

### 3.1.2 Consistency check for rivers in group 2

In order to study the problems of constructing rating curves for rivers in group 2, the rivers Mekong, Brahmaputra, Don and Vistula have been selected. The location of the discharge gauging station, time period of available discharge data and the distance of gauging station to the defined virtual stations (Table 2.4) are shown in Table 3.3 (cf. Figure 3.1). Synchronous measurements of discharge and altimetry are not available for rivers in group 2. Therefore, the aforementioned questions should be answered

**Table 3.3:** Discharge gauging stations of group 2 rivers with the time period of available discharge and their distance to the virtual stations

|             | Area<br>[km <sup>2</sup> ] | Lat.<br>[deg] | Lon.<br>[deg] | Period    | Distance to<br>virtual station<br>[km] |
|-------------|----------------------------|---------------|---------------|-----------|--|
| Brahmaputra | 521 828                    | 25.18         | 89.67         | 1985–1992 | +61                                    |
| Don         | 378 180                    | 47.54         | 40.64         | 1952–1995 | -8                                     |
| Mekong      | 640 708                    | 13.53         | 105.94        | 1960–1994 | +32                                    |
| Vistula     | 186 147                    | 54.10         | 18.80         | 1900–1994 | -8                                     |

**Table 3.4:** Kolmogorov-Smirnov test statistics with significance level of 0.05 for the comparison of distribution of two sets of data: arbitrary daily discharge at the time of altimetry and whole daily discharge

| River       | Daily |      |
|-------------|-------|------|
|             | D     | K    |
| Mekong      | 0.03  | 0.15 |
| Brahmaputra | 0.05  | 0.21 |
| Don         | 0.02  | 0.15 |

differently. A randomly selected measurement epoch with 35-day interval is assumed as representative of the time of altimetry measurements within the available discharge time period. Then the daily discharge measurements at the considered time are compared using K-S test with the whole daily discharge. The arbitrary epochs are moved day by day 34 times within the period of available measurements to cover all the possible cases. The test statistics for all 34 cases are then averaged and nominated as the test statistic  $D$  of daily discharge (Table 3.4). As size of samples remain constant for all 34 cases, the critical value  $K$  of all 34 cases are the same (Table 3.4). The null hypothesis implying the samples are drawn from the same distribution for the rivers of Mekong, Brahmaputra and Don for all 34 cases are accepted at the 0.05 significance level. Daily discharge data is not available for Vistula River.

Following the same procedure for monthly discharge leads to very small test statistics, as the monthly discharge at arbitrary epochs and whole monthly available discharge show very similar distributions. Therefore, answering the question 2 relies more on the daily discharge measurements and their distribution. The obtained low statistics imply that the distribution of every 35 days sampled discharge data is similar to the distribution of all available discharge data. This similarity allows us to establish a rating curve from the available measurements. On the other hand, question 1 can not be specifically addressed as there is no real epoch of ENVISAT altimetry within the available discharge data. Hence, both monthly and daily discharge are investigated to construct the rating curve.

**Table 3.5:** Computed Pearson's correlation (corr.) and rank correlation (rank corr.) coefficient of simultaneous measurements of quasi-monthly/monthly discharge with water level from altimetry for the selected rivers in group 1

| River  |            | Monthly | Quasi-monthly |
|--------|------------|---------|---------------|
| Amazon | Corr.      | 0.94    | 0.95          |
|        | Rank Corr. | 0.96    | 0.97          |
| Niger  | Corr.      | 0.95    | 0.96          |
|        | Rank Corr. | 0.90    | 0.90          |
| Danube | Corr.      | 0.83    | 0.86          |
|        | Rank Corr. | 0.86    | 0.87          |
| Amur   | Corr.      | 0.94    | 0.96          |
|        | Rank Corr. | 0.88    | 0.94          |
| Ob     | Corr.      | 0.82    | 0.85          |
|        | Rank Corr. | 0.79    | 0.83          |

## 3.2 Modeling the rating curve

After verifying the consistency between the water level and river discharge time series, the corresponding rating curve can be modeled. However, as the river discharge data base is not simultaneously available with altimetry for river in group 2, the rating curves for rivers in group 1 and 2 should be constructed differently. For rivers in group 1, the empirical rating curve, which was also used by previous studies, e.g. (Kouraev et al., 2004; Zakharova et al., 2006; Leon et al., 2006; Coe and Brikett, 2004; Papa et al., 2010), can be established via simultaneous measured monthly or quasi-monthly discharge data and the water level from altimetry. On the other hand, for rivers in group 2, the empirical rating curve can not be established and an alternative approach must be sought.

### 3.2.1 Modeling the rating curve for rivers in group 1

The rating curve can be constructed by fitting an empirical relationship between synchronous measurements of water level and monthly or quasi-monthly discharge. In order to investigate the possible existing relationship, dependence of two sets is estimated by computing the Pearson's correlation (standard correlation) and rank correlation. The correlation of two sets reveals a linear dependency whereas the rank correlation measures the extent of monotonic relationship in general. Table 3.5 shows the estimated correlation and rank correlation coefficients between the water level from altimetry and monthly and quasi-monthly discharge in the chosen rivers in group 1. All the water level from altimetry in the Amazon, Niger, Danube, Amur and Ob rivers show high correlations and rank correlations with measured discharge.

The high correlation and rank correlation values in Table 3.5 express a high monotonic dependency between the data sets plus a weak non-linearity. This motivated the study to attempt to establish an empirical model between discharge and water level from altimetry and use it as an empirical rating curve for virtual stations. Therefore, the measured monthly and quasi-monthly discharge are mapped against the water level from altimetry to establish the empirical rating curve. All the rivers under study have shown quadratic relationship between discharge and water level (cf. Figure 3.6). Least squares estimation has been employed to fit a quadratic line to the scattered points.

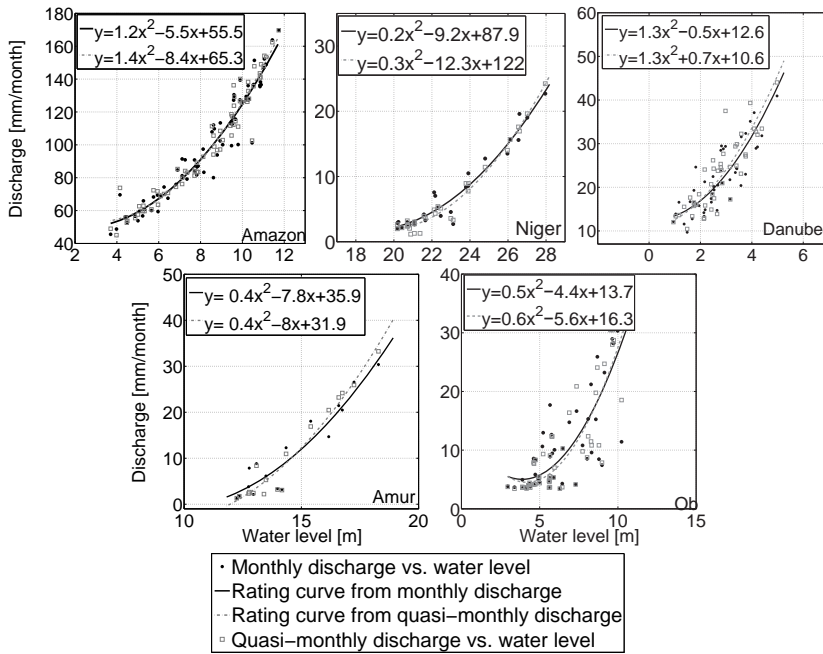


**Figure 3.6:** Scatter plot of simultaneous measurements of discharge versus water level from altimetry with the fitted quadratic empirical rating curve models for the quasi-monthly and monthly discharge data of rivers in group 1

### 3.2.2 Modeling the rating curve for rivers in group 2

As shown in Section 3.1.1 discharge measurements and water level from a nearby altimetry footprint are monotonically dependent. In general, the high correlation and rank correlation coefficients in Table 3.5 express the highly monotonic dependency between the data sets. In fact, the monotonic relation between water level and discharge with positive rank correlation indicates that the function to derive discharge from water level is a non-decreasing function. This characteristic justifies a statistical approach, based on quantile function mapping.

The quantile function, denoted by  $Q(p)$ , provides a way of describing the distribution of a data set (Gilchrist, 2000). The quantile functions for data sets of water level from altimetry,  $Q_W(p)$ , and discharge from *in situ* measurements,  $Q_R(p)$ , are

$$Q_R(p) = \inf\{X_R \in R : p \leq F(X_R)\} \quad (3.2)$$

$$Q_W(p) = \inf\{X_W \in R : p \leq F(X_W)\} \quad (3.3)$$

where  $X_R$  and  $X_W$  refer to the discharge and water level values and  $F(\cdot)$  represents the cumulative distribution function. The quantile function specifies, for a given probability  $0 < p < 1$ , the maximum value which the  $X_R$  or  $X_W$  can attain with that probability.

In order to derive discharge from satellite altimetry, the function  $T(\cdot)$ , referred to as a rating curve, should be modeled, which explains the relationship of water level and discharge

$$X_R = T(X_W) , \quad (3.4)$$

As it has been demonstrated that the function  $T(\cdot)$  is a non-decreasing function, the Q-transformation rule (Gilchrist, 2000) holds since a non-decreasing function  $T(\cdot)$  of a non-decreasing function (quantile function) must itself be non-decreasing. Therefore, quantile functions of both data can be used instead of the data itself to achieve the functional relationship of water level and discharge,  $T(\cdot)$  (Tourian et al., 2013):

$$Q_R = T(Q_W) . \quad (3.5)$$

This particularly helps to achieve the relationship between water level and discharge without the need for simultaneous measurements.

An empirical approach is used to obtain the quantile function of water level and discharge. For that, both the monthly values of water level and the measured discharge are sorted, ascendingly. The rank of each data set is normalized to emulate a range of probability between 0 and 1 using Weibull plotting position:

$$p_i = \frac{k_i}{N+1} \quad (3.6)$$

where  $k_i$  is the rank of the sorted values,  $N$  is the number of measurements and  $p_i$  is the probability of water level or discharge data. The sorted values of water level and discharge measurements versus their corresponding probability form the empirical quantile function cf. Figure 3.7 (middle).

The quantile function particularly provides information on the probability that a particular flow or water level was exceeded over the available period. This can also be viewed as the complement of the cumulative distribution function (CDF) of the considered discharge or water level variations. Therefore, a direct connection between the quantile functions at the corresponding probability represents a relationship between discharge and water level, which can be referred to as a *statistical* relationship. In principle, the obtained relationship can be used as look-up table implying the desired rating curve. However, as this

study aims to compare the statistical and empirical rating curves, a similar way of approximation for both is needed. In general, the rating curve can be approximated with different numerical and physically based methods like polynomial regression, power type equation, etc. In this study the simple quadratic estimation is used for modeling the rating curve. Thus, the statistical rating curve is achieved by fitting a quadratic curve over the obtained statistical relationship. Figure 3.7 shows the empirical quantile functions for water level and monthly discharge for the Mekong river and the resulting statistical discharge-water level relationship, that leads to a statistical rating curve for the virtual station on the Mekong River by fitting a quadratic curve. In fact, the rating curve is constructed here by eliminating the probability-coordinate  $p$ , whereas for the empirical approach conventionally time-coordinate  $t$  is eliminated. Moreover, the similar quantile functions of river discharge, belonging to the time periods of 1960–1970 and 1991–1994, we gain confidence that a quantile function represents a time invariant estimation for a given probability.

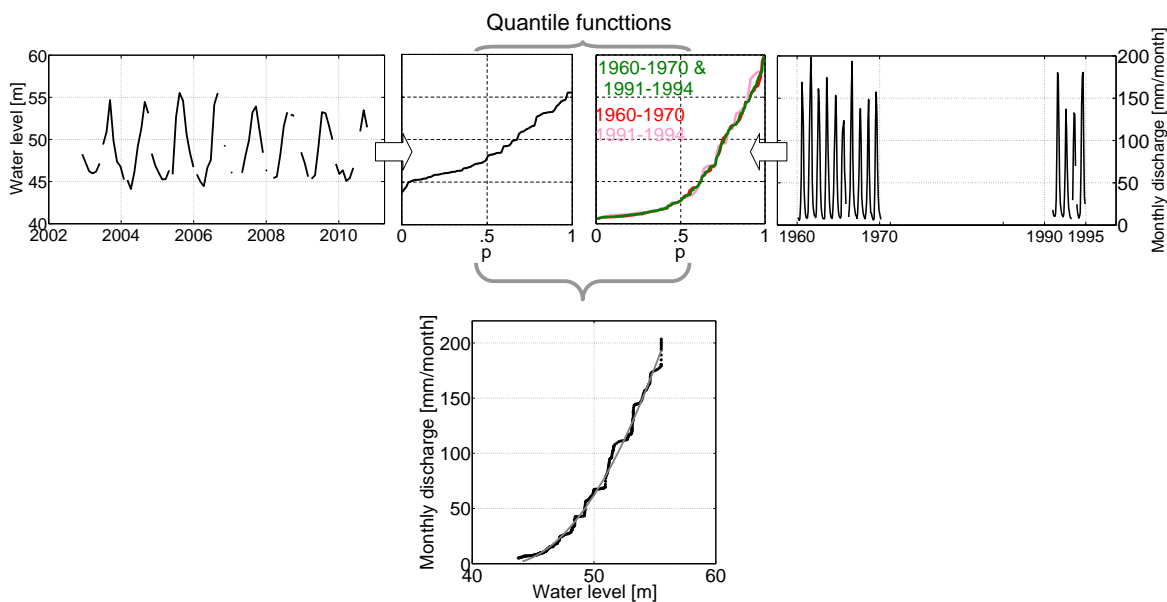


**Figure 3.7:** Estimated water level from satellite altimetry and available discharge for the Mekong River are transferred to quantile functions. From the corresponding probabilities the scatter plot of discharge versus water level is constructed. A smoothed rating curve is then obtained by fitting a quadratic curve to the scatter. Note the dissimilar time axes of the two datasets (top).

A similar approach can be used to derive the rating curve from daily discharge data. To this aim, daily discharge values are converted to quasi-monthly discharge and a corresponding quantile function is achieved. A careful comparison of the quantile functions from monthly and quasi-monthly discharge data reveals that the extreme daily values can overestimate the quantile function belonging to monthly discharge. As an example, Figure 3.8 shows the different behaviour between the quantile functions from monthly and quasi-monthly discharge due to the existence of extreme values in daily discharge data.

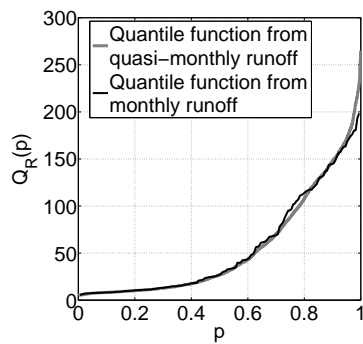


**Figure 3.8:** Quantile functions from monthly and quasi-monthly discharge of the Mekong River

In fact, a extreme value refers to extreme deviations from the median of probability distribution. In this case an extreme quasi-monthly discharge can be derived from an extreme daily discharge value, which does not follow the true monthly discharge's distribution. A method is here employed to deal with the effect of extreme daily value in quantile function of monthly discharge data in the following way. The daily discharge values within each year are converted to quasi-monthly discharge and used to form the quantile functions individually for each year. The number of available daily discharge measurements in a year is used as a weight for that year. Then the weighted median of quantile functions of different years is calculated (Tourian et al., 2013). This allows an estimation of a quantile functions that is insensitive to quasi-monthly values (Figure 3.9), which is then used to directly connect its probabilities to the probabilities of the quantile function from water levels and establish the statistical rating curve.

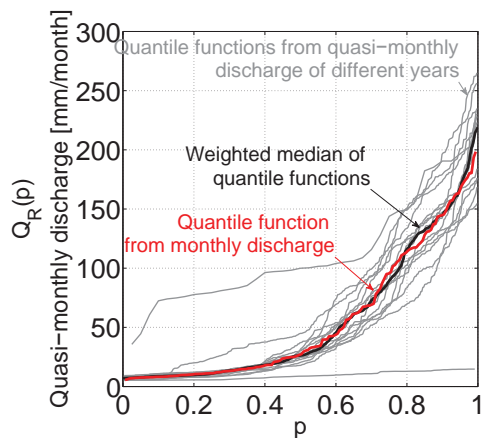


**Figure 3.9:** Quantile functions from quasi-monthly discharge of the Mekong River constructed for each year separately (gray). The weighted median of all years (black) is comparable to the depicted quantile function from monthly discharge (red)

The proposed methodology is employed for the chosen rivers in group 2 to obtain the statistical rating curve for monthly and quasi-monthly discharge (Figure 3.10). As expected, the rating curves show a non-decreasing behaviour except for the rating curve from the quasi-monthly data of the Don River.

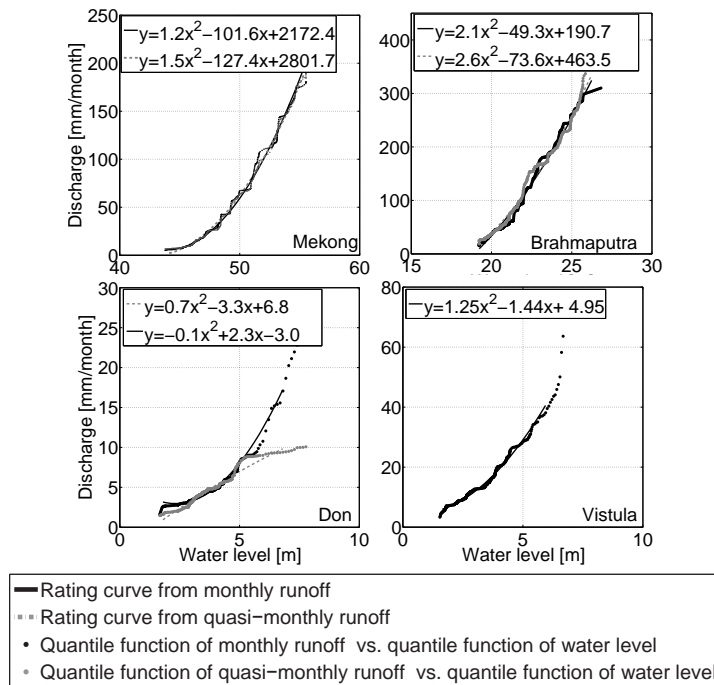


**Figure 3.10:** Scatter plots of discharge versus the water levels from altimetry for rivers in group 2, produced from the respective quantile functions. The fitted quadratic models represent the obtained statistical rating curve for monthly and quasi-monthly discharge

For this group, verifying the rating curves is not possible as there is no simultaneous water level and discharge data for rivers in group 2. However, *in situ* discharge measurements are available for rivers in group 1 within the time period of altimetry. Thus the statistical rating curve for rivers in group 1 can be established. The proposed statistical rating curve can be validated against the conventional empirical approach. Figure 3.11 shows the result of such validation, in which empirical rating curves together with the statistical one for monthly and quasi-monthly discharge data over rivers in group 1 are demonstrated.

Both methods lead to very similar rating curves for the virtual stations of the Amazon, Danube and Ob. For the Niger River, the both types of rating curves do follow the same pattern, yet with a distinctive bias between curves, cf. 1.2 mm/month. On the other hand, the empirical and statistical rating curves are not consistent with each other for the virtual station of Amur River. The non-similarity for Niger and Amur can be explained by the difference of quantile functions of discharge data consisting of discharge values at the time of altimetry and quantile function of whole available discharge data. Actually, these differences could have been expected as the K-S test statistics from the consistency check in Table 3.2 show higher values for the Amur and Niger compared to the Amazon, Danube and Ob.

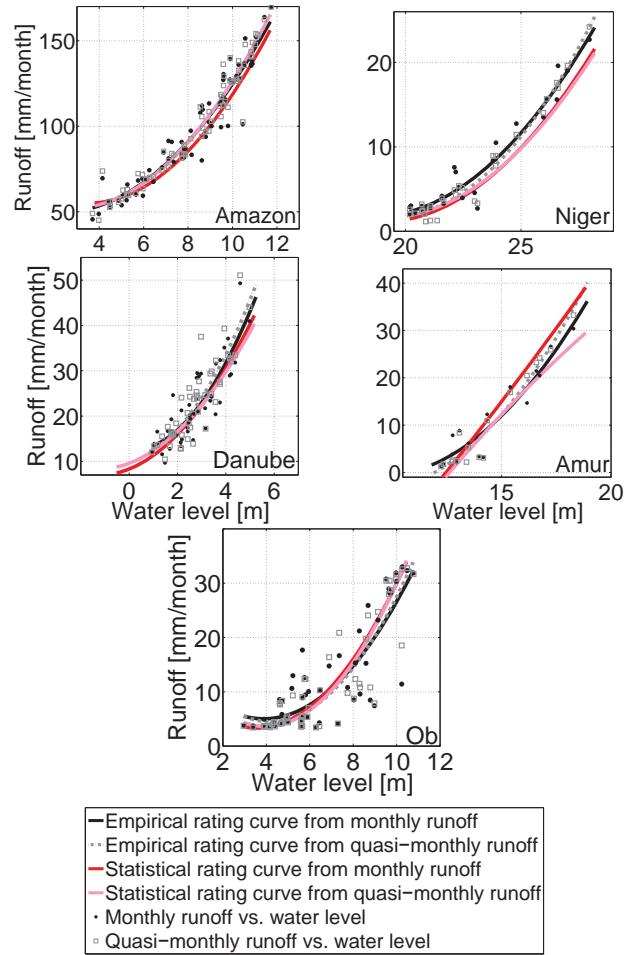


**Figure 3.11:** Scatter plot of simultaneous measurements of discharge versus water level from altimetry with the fitted quadratic empirical rating curve models for the quasi-monthly and monthly discharge data of rivers in group 1

### 3.3 River discharge estimation

River discharge can be estimated through the obtained rating curves for virtual stations and available water level values from altimetry at the virtual station. For group 1 the estimated discharge can be compared with available measured discharge to address the error budget of estimation or goodness of modeling. However, this would not thoroughly verify the method as the measured discharge is also used for modeling the rating curve. The estimated discharge shows a good agreement with measured discharge, yet with some distinct unexpected fluctuations (e.g. March 2004 in Amazon, Jan. 2005 on the Niger) which are generated by noisy altimetry. Residuals are computed by subtracting the estimated monthly and quasi-monthly discharge from those measured. The computed RMS of residuals (RMSE) provides information on the error of estimation and the error budget can be then calculated by (Getirana and Peters-Lidard, 2012)

$$\text{error} = \frac{\text{RMSE}}{\max. - \min.} \quad (3.7)$$

Error budgets of ca. 8%, 7%, 10%, 10% and 17% are achieved for the Amazon, Niger, Danube, Amur and Ob, respectively (Figure 3.12). The obtained errors of 9.1 and 8.3 mm/month of Amazon River,

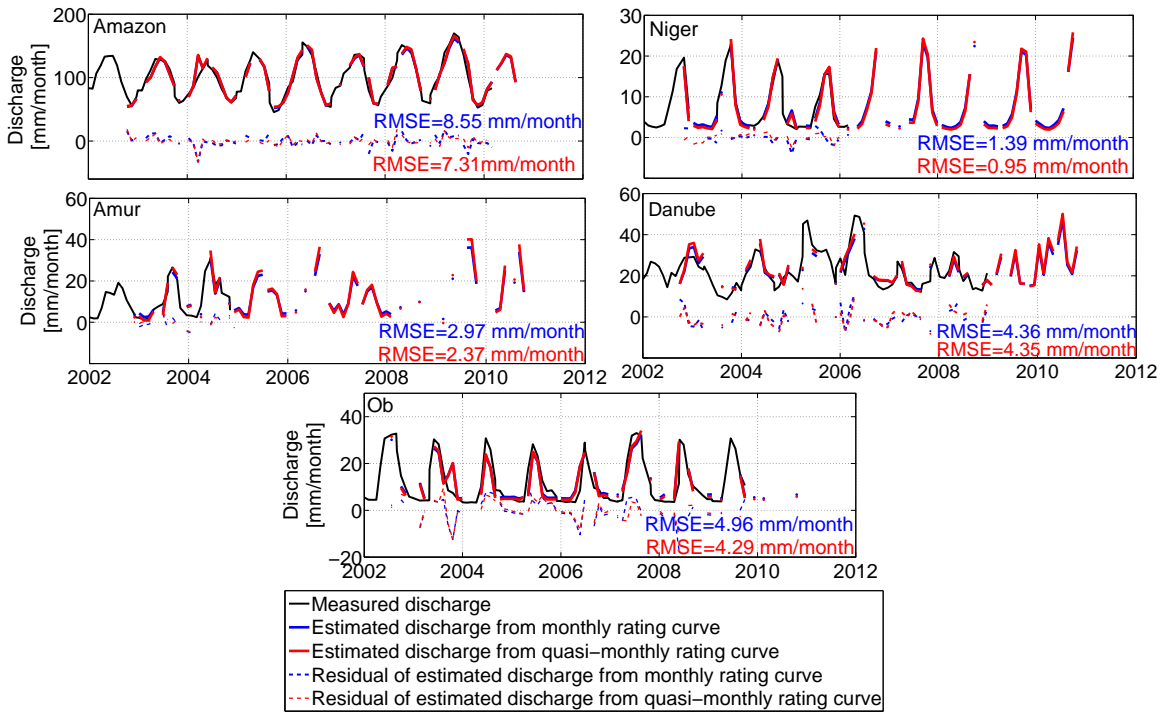


**Figure 3.12:** Estimated discharge from the empirical rating curves of simultaneous measurements of discharge and water level from altimetry for rivers in group I together with the achieved residual by subtracting the estimated discharge from the in situ measurements. The computed RMSE values in mm/month represent the error of estimation

which leads to 8% accuracy are relatively high as the proper conditions for measuring water height by satellite altimetry are available. This particularly can be explained by an outlier from altimetry in March 2004 that produces ca. 20 mm/month error. On the other hand, high RMSE values for Ob and Danube are not influenced by a single outlier. In this case, poor modeling of the rating curve seems to be responsible. This was already expected as water level and available *in situ* discharge measurements show low correlations (Table 3.5). Thus, having a water level time series with acceptable accuracy does not guarantee achieving a good estimation for river discharge.

Comparing the obtained RMSE values for estimated discharge using the proposed statistical approach with the estimated discharge using empirical approach reveals a similar range of error budget for both methods (Table 3.6). The comparable RMSE values in Table 3.6 specially express that the statistical approach provides similar performance, despite using quantile functions of data instead of data itself.

Although the different estimated discharge from both approaches show similar error budget, a scatter plot of estimated discharge using the empirical and statistical approaches reveals the non linear behaviour of estimated discharge for the Danube and Amur rivers (Figure 3.13). This might occur due to the change in discharge behaviour over the years for these rivers. In fact, when discharge variation changes over

**Table 3.6:** Computed RMSE of estimated discharge from empirical and statistical approach in mm/month for rivers in group 1

| River  |               | Empirical | Statistical | Error %     |
|--------|---------------|-----------|-------------|-------------|
| Amazon | monthly       | 8.5       | 9.1         | $\sim 8\%$  |
|        | quasi-monthly | 7.3       | 8.3         |             |
| Niger  | monthly       | 1.4       | 1.6         | $\sim 7\%$  |
|        | quasi-monthly | 0.9       | 1.3         |             |
| Danube | monthly       | 4.3       | 4.4         | $\sim 10\%$ |
|        | quasi-monthly | 4.3       | 4.6         |             |
| Amur   | monthly       | 2.9       | 3.5         | $\sim 10\%$ |
|        | quasi-monthly | 2.4       | 3.1         |             |
| Ob     | monthly       | 4.9       | 5.1         | $\sim 17\%$ |
|        | quasi-monthly | 4.3       | 4.3         |             |

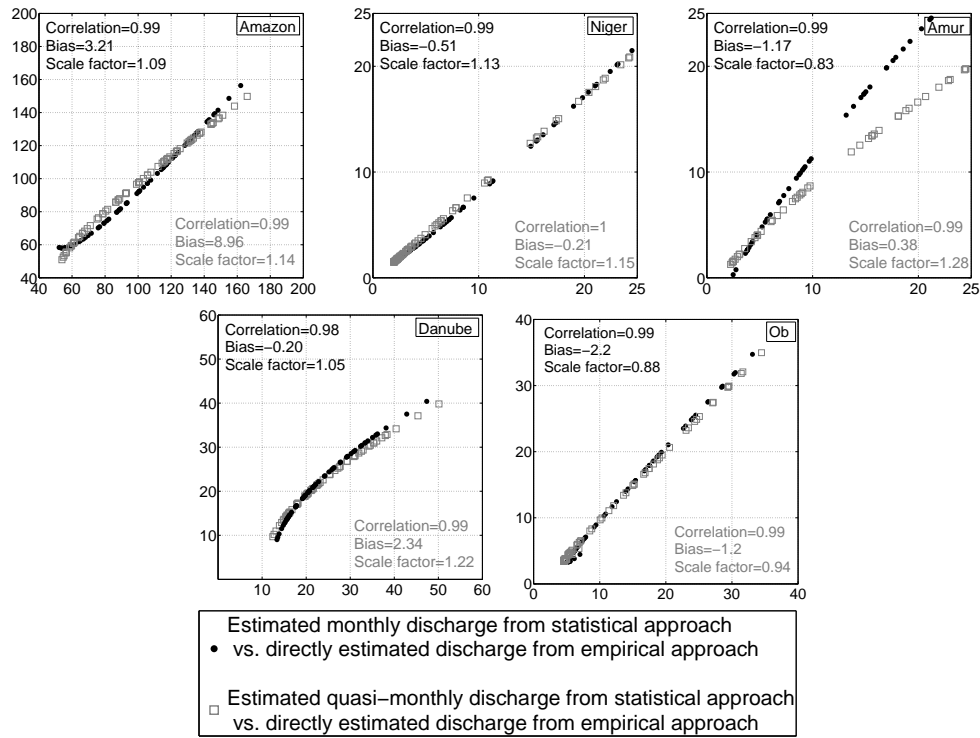
the time the obtained statistical rating curves and empirical rating curves are not correspondent. On the other hand, linear scatter plot indicates similar rating curves, which are produced by similar discharge variations. This means that the discharge behaviour has been stationary over the time for the Amazon, Niger and Ob rivers over last years. The high diversion of scatters for Amur reveals the dissimilar rating curves and consequently various discharge estimation. Table 3.7 shows statistical comparison of discharge time series from empirical and statistical approaches for rivers in group 1.

Figure 3.14 shows the estimated discharge for the selected rivers in group 2. As *in situ* discharge measurements are not available for rivers in group 2, verification and validation of estimated discharge is not possible. However, as an internal comparison, discharge estimations from quasi-monthly and monthly discharge data are compared to each other and RMSE of 2.3, 1.7 and 1.2 mm/month are achieved for the Mekong, Brahmaputra and Don, respectively. These RMSE values correspond to an error of 1%, 1% and 8%. Without daily discharge data the inter-comparison for Vistula is not available.

### 3.4 Validation of statistical approach

Note that in the previous verification of discharge estimation from the statistical approach against the one from the empirical approach, simultaneous data was used in the construction of the statistical discharge data set. Nevertheless, the proposed methodology should be validated against *in situ* measurements, when the ground truth is not used for modeling. Therefore, in this section a leave-out validation is performed and the results are discussed.

Moreover, it has been emphasized that the proposed methodology is mainly developed for the rivers with no available *in situ* measurements after launch of satellite altimetry. For such rivers, as the *in situ* discharge data is not available, it is common in the hydrological community to employ the available



**Figure 3.13:** Scatter plots of estimated discharge from the statistical method versus estimated discharge from the empirical method of constructed rating curves. The statistical characteristics of scattered points represent the similarity of estimations

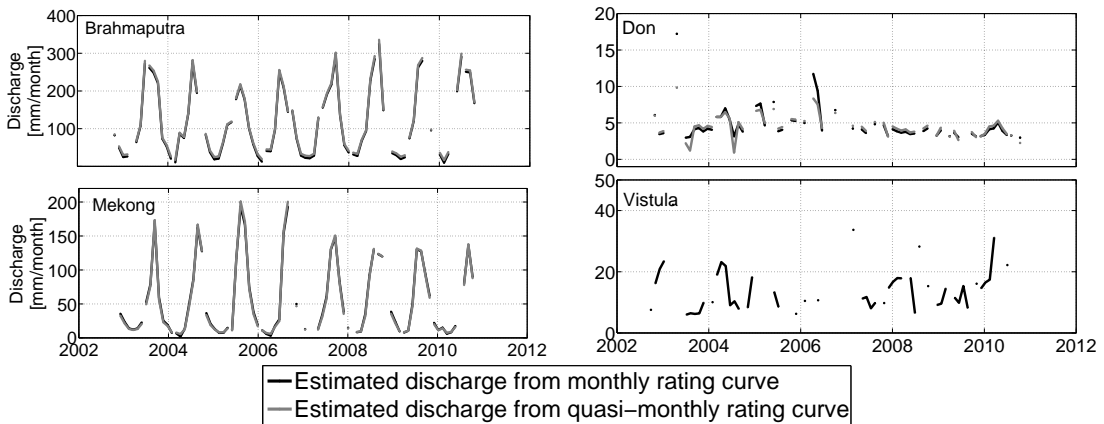


**Figure 3.14:** Estimated discharge in mm/month from the statistical rating curves obtained from the statistical method of performing rating curves out of asynchronous measurements of water level and discharge for different rivers in group 2. Inter-comparison of monthly and quasi-monthly discharge leads to RMSE of 2.3, 1.7 and 1.2 mm/month for the Mekong, Brahmaputra and Don, which correspond to 1%, 1% and 8% error, respectively

annual cycle (monthly mean) of discharge for study of hydrological interactions in the monthly time scale. Therefore, it is important to find out whether the estimated discharge is better than the monthly mean of discharge.

**Table 3.7:** Statistical comparison of discharge time series from empirical and statistical approach for the selected rivers in group 1

| River  |               | Correlation | Bias       | Scale factor |
|--------|---------------|-------------|------------|--------------|
|        |               | [ ]         | [mm/month] | [ ]          |
| Amazon | monthly       | 0.99        | 3.2        | 1.09         |
|        | quasi-monthly | 0.99        | 8.9        | 1.14         |
| Niger  | monthly       | 0.99        | -0.5       | 1.13         |
|        | quasi-monthly | 1.00        | -0.2       | 1.15         |
| Danube | monthly       | 0.98        | -0.2       | 1.05         |
|        | quasi-monthly | 0.99        | 2.3        | 1.22         |
| Amur   | monthly       | 0.99        | -1.2       | 0.83         |
|        | quasi-monthly | 0.99        | 0.4        | 1.28         |
| Ob     | monthly       | 0.99        | -2.2       | 0.88         |
|        | quasi-monthly | 0.99        | -1.2       | 0.94         |

**Leave-out validation against in situ measurements** In order to validate the statistical approach for estimation of discharge, a modified discharge data set is produced by excluding the data within the time period of altimetry for group 1 rivers. The quantile functions are then constructed from the modified discharge data and directly connected to the quantile function of water level to establish the statistical rating curves for each river. Using the available altimetry data and the achieved rating curves, discharge values are estimated for rivers in group 1. Figure 3.15 shows the estimated discharge using the statistical approach for rivers in group 1, for which the discharge at time of altimetry has not been used for modeling the rating curve. The validation is then conducted by comparing the the estimated discharge with *in situ* measurement. Table 3.8 shows the computed RMSE values and error budgets of estimation for both monthly and quasi-monthly data for different rivers.

The estimated RMSE values imply the same range of error as indicated in Table 3.6. For all the rivers, the estimated errors are only slightly worse in case of using modified discharge data. The maximum degradation happened in the estimation of quasi-monthly discharge for Ob River, where the estimated RMSE increases from 4.3 mm/month to 4.9 mm/month. The results show that the modified data follow the same statistical properties as the whole data set, which also points at homogeneity and stationarity of the data. Overall, the statistical approach seems to perform well.

**Altimetric discharge or annual cycle?** Given the relative error levels implied by the new discharge estimation methodology, the question seems to be justified, whether the whole effort of saving heritage discharge data into the satellite altimetry era was worth it. However, the hydrological community commonly calculates the mean monthly discharge from heritage discharge data and employs it as representative of measured data (Maidment, 1993). The question, therefore, is: Is the estimation of discharge by altimetry better than the mean annual cycle? Hence, the estimated discharge should be also compared with the annual cycle (monthly mean). In other words, by estimating the discharge using altimetry it is

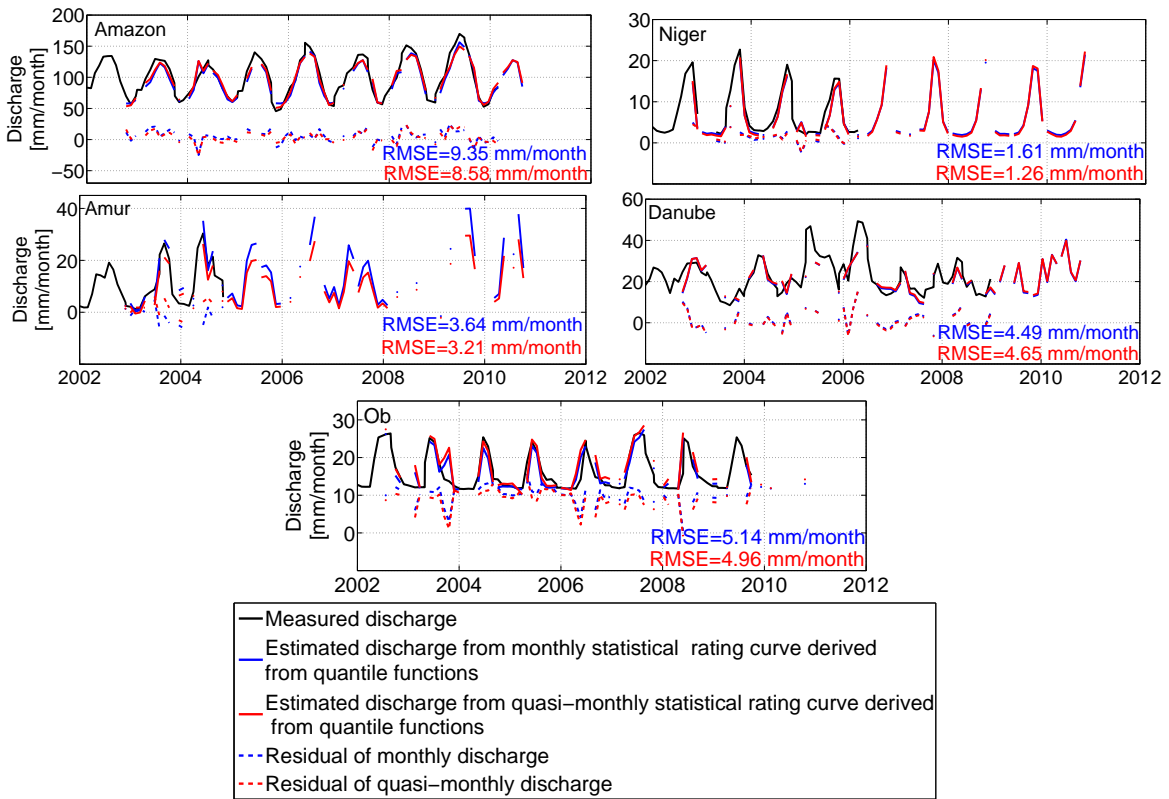


**Figure 3.15:** Estimated discharge from the rating curves obtained from the statistical methods of performing rating curve for rivers in group 1. Residuals are achieved by subtracting the estimated discharge from the in situ measurements discharge. The computed RMSE values in mm/month reveals the performance of statistical approach for constructing the rating curve

expected to have better estimation than the annual cycle, that is often used by hydrologists for modeling purposes.

In fact, a good estimation should bring extra discharge information beyond the annual cycle. Therefore, a test is performed for rivers in group 1, in which *in situ* measurements that belong to a given year are excluded and then the annual cycle is computed. The computed annual cycle is then compared with estimated discharge from altimetry using the statistical approach and with the *in situ* data that was left out.

This comparison is performed by computing the difference between altimetric  $X_{\text{alt}}$  and observed discharge  $X_{\text{ins}}$  and the difference between the computed mean annual cycle  $\bar{X}_{\text{ins}}$  for discharge and the observed discharge:

$$v_{\text{alt}} = X_{\text{alt}} - X_{\text{ins}} \quad (3.8)$$

$$v_{\text{mean}} = \bar{X}_{\text{ins}} - X_{\text{ins}} \quad (3.9)$$

**Table 3.8:** Computed RMSE values for estimated river discharge from empirical and statistical approach in mm/month for rivers in group I

| River  |               | RMSE Error % |       |
|--------|---------------|--------------|-------|
| Amazon | monthly       | 9.3          | ~ 8%  |
|        | quasi-monthly | 8.6          |       |
| Niger  | monthly       | 1.6          | ~ 7%  |
|        | quasi-monthly | 1.3          |       |
| Danube | monthly       | 4.5          | ~ 10% |
|        | quasi-monthly | 4.6          |       |
| Amur   | monthly       | 3.6          | ~ 10% |
|        | quasi-monthly | 3.2          |       |
| Ob     | monthly       | 5.1          | ~ 17% |
|        | quasi-monthly | 4.9          |       |

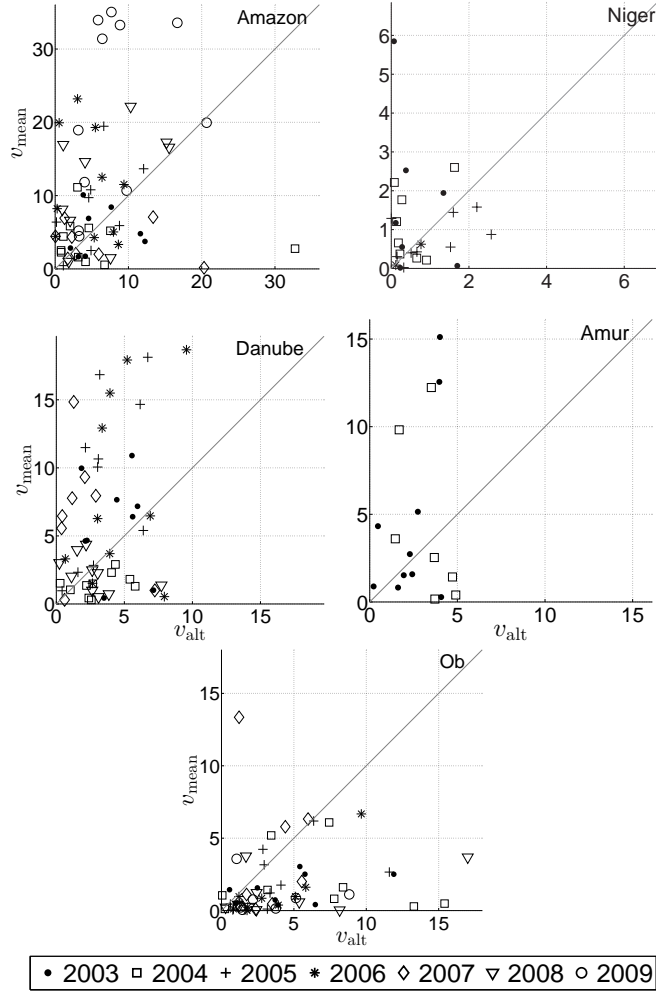
where  $\bar{X}_{\text{ins}}$  for the  $j^{\text{th}}$  month of the  $i^{\text{th}}$  year as

$$\bar{X}_{\text{ins}}(t_j) = \frac{1}{N} \sum_{i=1}^N X_{\text{ins}}(t_{i,j}) \quad , \quad (3.10)$$

where  $N$  is referring to the number of available years. If the residual values from altimetry  $v_{\text{alt}}$  are smaller than residual values from the mean annual cycle  $v_{\text{mean}}$ , it means that the estimation of discharge by altimetry provides information on the discharge variation better than the annual cycle. Here, the annual cycle is computed by excluding each year in the available data individually. Then residual values from altimetry and residual values from the mean annual cycle are compared for different rivers in group 1 (Figure 3.16). The scatter of Amazon, Danube and Amur lies predominantly to the left (Figure 3.16). Thus the altimetric discharge at selected gauges of the Amazon, Danube and Amur are closer to observed discharge, which means that the altimetric discharge performs better than the mean annual cycle for most of the months. Although the estimated RMSE for discharge at the selected gauge of the Niger River is low (Table 3.8), the scatter plot in Figure 3.16 expresses that for some months the mean annual cycle provides a better estimation. Unlike the Niger, estimated discharge at the gauge in the Danube River provides better estimation than the mean annual cycle for most of the months, while the estimated error is relatively high (~ 10%).

On the other hand, the scatter plot of the Ob River in Figure 3.16 indicates that the estimation of altimetric discharge does not bring extra information. This finding correlates with the high error range of ~ 17%. The scatter plot shows that, for the selected gauge at the Ob River, for many months over different years it is better to derive discharge from the annual cycle instead of using the water level from the chosen virtual station. This can be explained by the existence of ice on the Ob River during the winter period and erroneous measurements by satellite altimetry. Moreover, the large distance between the virtual station and gauge can be also the reason for unsatisfactory result of altimetric discharge. In addition, according to Kouraev et al. (2004), for Ob at Salekhard (the selected gauge at this study) there exists at

least 2 rating curves: flood rising and flood falling. However, in this study one unique rating curve has been built, which could lead to very high errors.



$v_{\text{mean}}$ : Monthly mean of discharge - observed discharge  
 $v_{\text{alt}}$ : Altimetric discharge - observed discharge

**Figure 3.16:** Comparison of estimated discharge by altimetry and the annual cycle computed by excluding data of different years. Residuals are obtained by subtracting the observed discharge from altimetry discharge and the annual cycle, respectively.

All in all, river discharge can be estimated from satellite altimetry using the proposed statistical approach at an accuracy level that is relevant to hydrology if

1. the altimetric water level is derived with sufficient quality
2. altimetry can appropriately sample the river's water level variations
3. the distance between virtual station and gauge is small enough to be geomorphologically similar
4. the river discharge is stationary (does not show significant trend or variation)

5. the heritage discharge data is lengthy enough to be statistically representative

Although the proposed method helps to salvage pre-satellite altimetry data and turn them into active use for the satellite altimetry time frame, the altimetric discharge estimation suffers from:

- data outages in ca. 25% of the time (figures 3.12 and 3.14)
- noisy altimetric water level causing an incorrect estimation of discharge.

In fact missing values in altimetry lead to a gap in the estimation of discharge. On the other hand, any noisy altimetry can cause an incorrect estimation of discharge. Therefore, it would be desirable to have an algorithm that covers the missing values and combines all available measurements with their uncertainties to provide an acceptable estimation.

### 3.5 Stochastic process model and Kalman filtering

Inspired by the aforementioned problems of altimetric discharge, this section aims to develop a desirable algorithm that

- deals with the data outages
- provides a scheme for data assimilation
- smooths the discharge estimation

Here, an algorithm will be investigated to use stochastic process model for discharge and combine it with available measurements. A stochastic process model for discharge can be designed to benefit from the cyclostationarity of discharge. Given  $X_t$ , the discharge time series, which is a cyclostationary signal, the residual can be computed by (for  $\bar{X}_t$  see 3.10)

$$r_t = X_t - \bar{X}_t \quad (3.11)$$

In general, it can be assumed that the residual from time  $t - 1$  to  $t$  does not change drastically. Given such assumption, a linear process model can be written as

$$r_t = Ar_{t-1} + e, \quad (3.12)$$

where,

$$E\{r_t\} = 0. \quad (3.13)$$

In the above linear process model the process dynamics  $A$  is unknown and is not accessible. Therefore an approximation of process dynamic  $\hat{A}$  should be considered. This approximation is a linear estimator of the state  $r_t$  given  $r_{t-1}$  (Gelb, 1974):

$$\hat{r}_t = \hat{A}r_{t-1}. \quad (3.14)$$

Consequently, the process/estimation error can be quantified as,

$$e = \hat{r}_t - r_t \quad \text{with} \quad C\{e\} = E\{ee^T\}, \quad (3.15)$$

and the minimum variance occurs when:

$$\text{tr}[C\{e\}] = \min . \quad (3.16)$$

Since the equation (3.13) is valid for all  $A$ , the expectation can be justified (Moritz, 1989; Kurtenbach, 2011):

$$E\{\hat{r}_t\} = E\{\hat{A}r_{t-1}\} = \hat{A}E\{r_{t-1}\} = 0 = E\{r_t\} . \quad (3.17)$$

In order to determine the minimum variance estimator, first the outer product of the error vector from equation (3.15) is calculated:

$$ee^T = (\hat{r}_t - r_t)(\hat{r}_t - r_t)^T . \quad (3.18)$$

Then by substituting  $\hat{r}_t$  from (3.14) and multiplying the terms,

$$ee^T = (\hat{r}_t - r_t)(\hat{r}_t - r_t)^T \quad (3.19)$$

$$= (\hat{A}r_{t-1} - r_t)(\hat{A}r_{t-1} - r_t)^T \quad (3.20)$$

$$= \hat{A}r_{t-1}r_{t-1}^T\hat{A}^T - r_tr_{t-1}^T - \hat{A}r_{t-1}r_t^T + r_tr_t^T . \quad (3.21)$$

On the other hand, auto-covariance and cross covariance are defined as:

$$\text{Auto-covariance: } \Sigma = C\{r_t\} = E\{r_t r_t^T\} \quad (3.22)$$

$$\text{Cross-covariance: } \Sigma_\Delta = C\{r_t, r_{t-1}\} = E\{r_t r_{t-1}^T\} \quad (3.23)$$

The error covariance matrix is thus:

$$C\{e\} = E\{ee^T\} = \hat{A}\Sigma\hat{A}^T - \Sigma_\Delta\hat{A}^T - \hat{A}\Sigma_\Delta^T + \Sigma , \quad (3.24)$$

which can be rearranged into:

$$C\{e\} = \Sigma - \Sigma_\Delta\Sigma^{-1}\Sigma_\Delta^T + (\hat{A} - \Sigma_\Delta\Sigma^{-1})\Sigma(\hat{A} - \Sigma_\Delta\Sigma^{-1})^T . \quad (3.25)$$

The first term is stationary

$$\Sigma - \Sigma_\Delta\Sigma^{-1}\Sigma_\Delta^T = c, \quad (3.26)$$

and for the second term, since it is a quadratic form in  $\hat{A}$ , it is always the case that

$$(A - \Sigma_\Delta\Sigma^{-1})\Sigma(A - \Sigma_\Delta\Sigma^{-1})^T \geq 0 . \quad (3.27)$$

**Table 3.9:** Calculated auto-covariance  $\Sigma$ , cross-covariance  $\Sigma_\Delta$ , scalar value of  $\hat{A}$  and  $C\{e\}$  from the monthly residual of discharge of rivers under study

| River       | $\Sigma$ | $\Sigma_\Delta$ | $\hat{A}$ | $C\{e\}$<br>[mm/month] |
|-------------|----------|-----------------|-----------|------------------------|
| Amazon      | 159.9    | 141.9           | 0.88      | 33.9                   |
| Amur        | 30.7     | 19.4            | 0.63      | 18.3                   |
| Brahmaputra | 845.9    | 595.4           | 0.70      | 426.9                  |
| Danube      | 37.4     | 25.5            | 0.68      | 20.0                   |
| Don         | 5.4      | 3.67            | 0.68      | 2.9                    |
| Mekong      | 243.1    | 120.8           | 0.49      | 183.1                  |
| Niger       | 6.5      | 4.1             | 0.63      | 3.9                    |
| Ob          | 11.2     | 5.8             | 0.51      | 8.2                    |
| Vistula     | 45.8     | 21.2            | 0.46      | 35.9                   |

It can be inferred that the error covariance matrix is minimum, if the second term disappears, which leads to the definition of

$$\hat{A} = \Sigma_\Delta \Sigma^{-1}, \quad (3.28)$$

and a covariance matrix of for process noise:

$$C\{e\} = \Sigma - \Sigma_\Delta \Sigma^{-1} \Sigma_\Delta^T. \quad (3.29)$$

As in this study the stochastic process model is performed on the one-dimensional discharge time series, the auto-covariance and the cross covariance are not matrix and can be computed by

$$\Sigma = C\{r_t\} = E\{r_t r_t^T\} = M\{r_t^T r_t\} = \frac{1}{N}\{r_t^T r_t\} \quad (3.30)$$

$$\Sigma_\Delta = C\{r_t, r_{t-1}\} = E\{r_t r_{t-1}^T\} = M\{r_{t-1}^T r_t\} = \frac{1}{N-1}\{r_{t-1}^T r_t\} \quad (3.31)$$

Hence,  $\hat{A}$  and  $C\{e\}$  are not matrices and they are scalar values. Table 3.9 shows the computed  $\Sigma$ ,  $\Sigma_\Delta$ , scalar values of  $\hat{A}$  and process error  $C\{e\}$  for the chosen rivers in group 1 and 2. The higher the  $\hat{A}$  the closer the discharge residual behaviour to stationary. This means that the residual time series of discharge for Amazon behave more stationary in comparison to other rivers. Moreover, the higher the amplitude of the residual the higher the process model error level  $C\{e\}$ .

After defining the unknown term  $\hat{A}$ , the stochastic process model for discharge as a cyclostationary signal will be developed by substituting (3.12) in (3.11):

$$\begin{aligned} (X_t - \bar{X}_t) &= \hat{A}(X_{t-1} - \bar{X}_{t-1}) + e \\ (X_t - \bar{X}_t) &= \hat{A}X_{t-1} - \hat{A}\bar{X}_{t-1} + e \\ X_t &= \hat{A}X_{t-1} - \hat{A}\bar{X}_{t-1} + \bar{X}_t + e \end{aligned} \quad (3.32)$$

which can be rewritten in the form of

$$X_t = \hat{A}X_{t-1} + BU_{t-1} + e, \quad (3.33)$$

where,

$$B = \begin{bmatrix} -\hat{A} & I \end{bmatrix} \quad \& \quad U_{t-1} = \begin{bmatrix} \bar{X}_{t-1} \\ \bar{X}_t \end{bmatrix}. \quad (3.34)$$

The form obtained in (3.33) is the stochastic process model of discharge that will be estimated at  $t$  by having: the discharge at  $t-1$ , auto-covariance, cross-covariance and monthly mean of discharge. Auto-covariance, cross-covariance and monthly mean are computed using the available measured discharge which can belong to any time period.

For the observation model, available observations of discharge from *in situ* or satellite altimetry allow to control and improve the discharge estimation of the stochastic process model. In fact, the stochastic process model provides discharge estimation without data outages while the observations are not available for all months. The linear observations equation reads:

$$Z_t = HX_t + v_t \quad \text{with} \quad v_t \sim \mathcal{N}(0, Qx_t), \quad (3.35)$$

where  $Z_t$  denotes the available *in situ* measurements of discharge  $R_{\text{ins},t}$  together with the estimated discharge by the rating curves from satellite altimetry  $R_{\text{alt},t}$ :

$$Z_t = \begin{bmatrix} R_{\text{alt},t} \\ R_{\text{ins},t} \end{bmatrix}, \quad (3.36)$$

So that the design matrix is populated with unit matrices:

$$H = \begin{bmatrix} I \\ I \end{bmatrix}. \quad (3.37)$$

The estimated error,  $\sigma_t$ , of water level from satellite altimetry at each time is propagated into the rating curve model to achieve the corresponding error for estimated discharge from altimetry,  $\sigma_{\text{alt},t}$ . This estimated error can be assigned to the  $Qx_t$  matrix which contains the covariance information of observations at each time  $t$ :

$$Qx_t = \begin{bmatrix} \sigma_{\text{alt},t}^2 & 0 \\ 0 & \sigma_{\text{ins},t}^2 \end{bmatrix} \quad (3.38)$$

where  $\sigma_{\text{ins},t}$  provides uncertainties for available *in situ* measurements of discharge, and the observations from different sources are assumed to be uncorrelated. As there is no information about the uncertainties

of *in situ* discharge measurements and also as the *in situ* measurements are assumed to be the ground truth, the  $\sigma_{\text{ins},t}$  is supposed to be 0. So,

$$Qx_t = \begin{bmatrix} \sigma_{\text{alt},t}^2 & 0 \\ 0 & 0 \end{bmatrix} \quad (3.39)$$

It should be mentioned that, a typical 10–20% of uncertainty can be assumed for  $\sigma_{\text{ins},t}$ , which might provide a more realistic estimation, yet with discrepancy from *in situ* measurements. In this study, as the only benchmark for evaluating the results is the *in situ* measurements, the discrepancy is not desirable and avoided.

The process model (3.33) and observation model (3.35) are independent. In fact, together they form a linear dynamic system. The state  $X_t$  will be estimated using the information from the process model and the observations. This estimation should be unbiased and have minimum variance. A widely used algorithm for solving this system is the Kalman filter (Gelb, 1974).

The Kalman filter is a recursive estimation algorithm in which the state of a dynamic system optimally estimated from noisy observations using least squares. Kalman (1960) formulated the eponymous Kalman filter algorithm for discrete time systems first, which was followed by Kalman and Bucy (1961) who extended it for continuous time systems.

In this study the dynamic system comprising (3.33) and (3.35) is solved by Kalman filtering. Figures 3.17 and 3.18 show the result of the Kalman filter estimates for rivers in group 1 and 2, respectively. As indicated in Figure 3.17, estimated discharge using Kalman filter follows the available observations and in case of a gap in observation it goes back to the stochastic model, which fills the gap via the cyclostationary mean and process model. As the uncertainty of *in situ* measurements is assumed to be 0, the estimated discharge by Kalman filter fits exactly to the available values from *in situ* measurements. This means that, the estimated discharge is the same as *in situ* measurements and in case of unavailability of *in situ* observations it relies on process model and estimated discharge by altimetry. In the case of unavailability of both, it proceeds with cyclostationary mean (monthly mean) of discharge and updated covariance information at each time. This helps to cope with months of problematic altimetry in the Amazon (March 2004) and Niger (Jan. 2005) rivers. However, estimated discharge by Kalman filter in Ob River again expresses the problem of modeling the rating curve.

As shown in Figure 3.18, the estimated discharge using Kalman filter for rivers in group 2 also follows the observation and it proceeds with cyclostationary behavior with updated covariance information at each time when no observation is available. However, the only available source of observations for the linear dynamic system in this group is estimated discharge by altimetry. Therefore, Kalman filter adapts the estimation to the directly estimated discharge from the statistical rating curves and in case of missing values it estimates the discharge with the help of the stochastic process model. The estimated discharge using Kalman filter can be compared with the available cyclostationary mean of discharge as depicted in

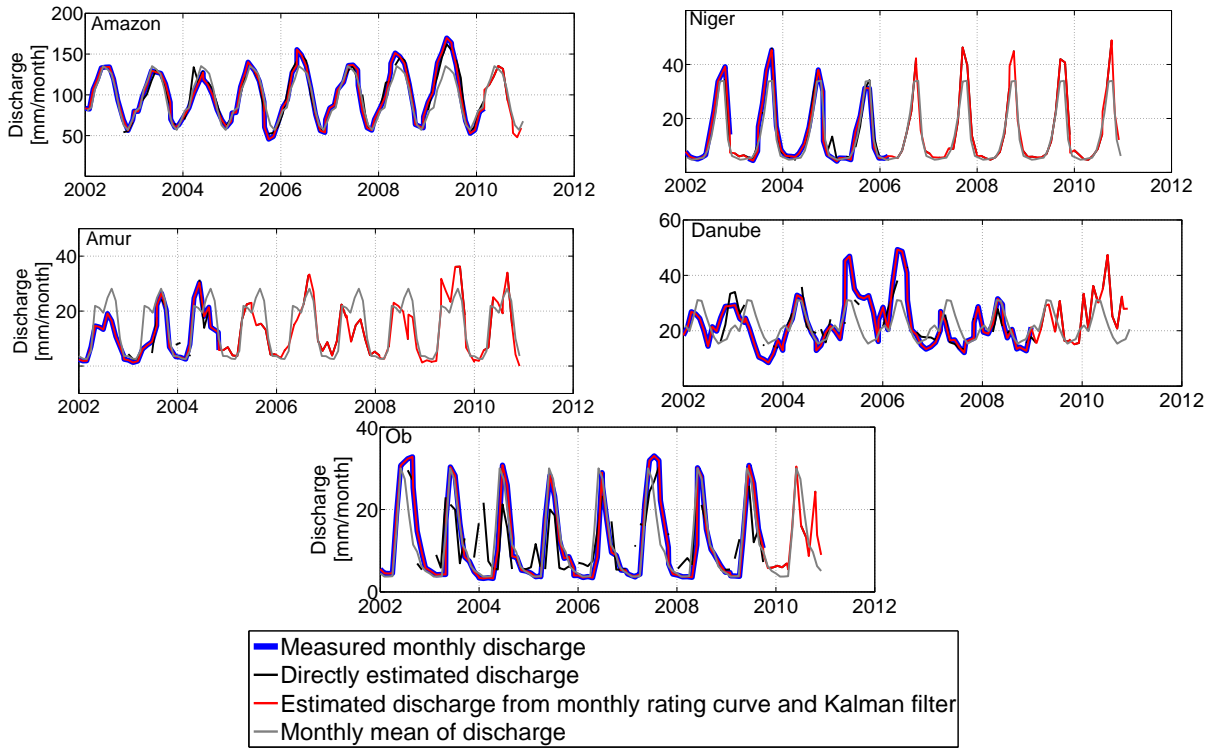


**Figure 3.17:** Estimated discharge using Kalman filter over the performed linear dynamic systems for rivers in group 1

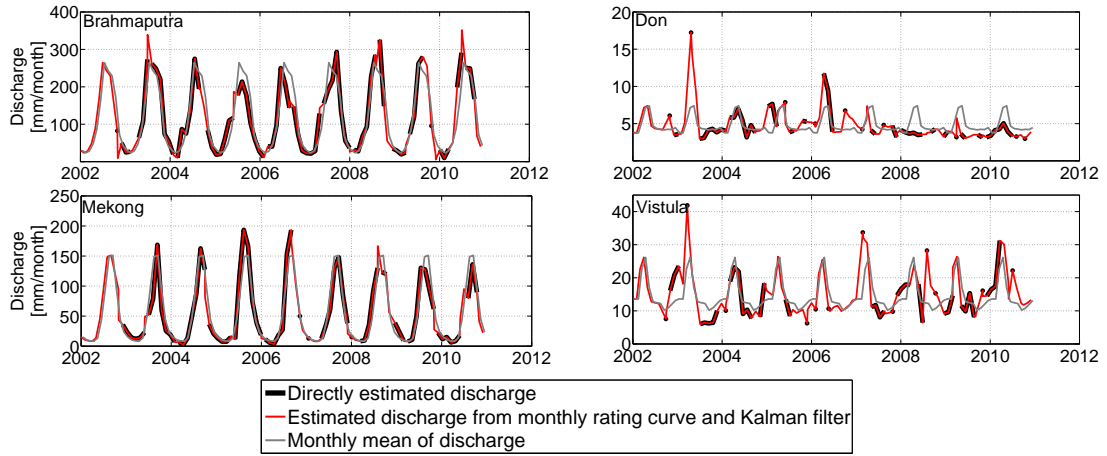


**Figure 3.18:** Estimated discharge using Kalman filter over the performed linear dynamic systems for rivers in group 2

figures 3.17 and 3.18. A high deviation from the mean (e.g. in Don River year 2008) reveals either wrong altimetric discharge or non-stationary behaviour of discharge.

**Table 3.10:** Computed RMSE values and their average for estimated discharge and errors using different excluded discharge data

| River  |               | Error of estimation (mm/month) |      |      |      |             | Average Error % |
|--------|---------------|--------------------------------|------|------|------|-------------|-----------------|
|        |               | 80%                            | 60%  | 40%  | 20%  |             |                 |
| Amazon | monthly       | 7.27                           | 6.03 | 5.49 | 3.73 | <b>5.64</b> | ~ 4%            |
|        | quasi-monthly | 6.70                           | 5.02 | 4.48 | 3.00 | <b>4.80</b> |                 |
| Niger  | monthly       | 1.19                           | 1.05 | 1.01 | 0.64 | <b>0.97</b> | ~ 5%            |
|        | quasi-monthly | 1.83                           | 1.77 | 1.72 | 0.44 | <b>1.44</b> |                 |
| Danube | monthly       | 5.04                           | 4.55 | 3.04 | 1.78 | <b>3.60</b> | ~ 8%            |
|        | quasi-monthly | 5.30                           | 4.74 | 3.14 | 1.99 | <b>3.79</b> |                 |
| Amur   | monthly       | 4.53                           | 3.87 | 2.83 | 2.30 | <b>3.38</b> | ~ 8%            |
|        | quasi-monthly | 4.02                           | 4.02 | 1.95 | 1.06 | <b>2.76</b> |                 |
| Ob     | monthly       | 5.46                           | 4.27 | 3.59 | 2.75 | <b>4.01</b> | ~ 13%           |
|        | quasi-monthly | 5.83                           | 4.26 | 3.61 | 2.74 | <b>4.11</b> |                 |

### 3.5.1 Validation of estimated discharge using Kalman filter

As mentioned above the estimated discharge using the Kalman filter method for rivers in group 1 matches perfectly with the available *in situ* measurements, because the uncertainty of *in situ* measurements was fixed to 0 in the observation model. Therefore, the obtained error out of the validation of estimated discharge against *in situ* measurements as ground truth is 0. In order to assess the error level of the performed Kalman filter method, a cross validation procedure is employed. For each river in group 1, different arbitrary *in situ* discharge measurements are constructed by excluding 20%, 40%, 60% and 80% of the original available measurements. Then, rating curves are established using the arbitrary discharge data set. Afterwards, the discharge is estimated applying the Kalman filter method to each of the discharge data sets. Finally, the estimated discharge is validated against the original available discharge measurements, and the computed RMS of difference is nominated as the corresponding error budget.

Table 3.10 shows the computed errors and their average from the estimation of discharge using different rate of excluded discharge data for rivers in group 1. The average RMSE of 0.97–5.64 mm/month is compatible with the RMSE from empirical and statistical approaches. The only river with higher average RMSE in cross validation is the Amur. For this river, the RMSE increases from 2.97 to 3.38 and 2.37 to 2.76 mm/month for monthly and quasi monthly discharge data, respectively. This result is explained by the difference of *in situ* discharge measurements and the monthly mean of discharge for Amur River (Figure 3.17). As in the absence of *in situ* measurement, Kalman filter follows the cyclostationarity of the discharge time series, the more close the measurements to the cyclostationary mean, the better the result of the Kalman filter.

In general, the validation shows that the Kalman filter method can solve the defined linear dynamic system appropriately. This result means that the problems of missing and noisy altimetry values can

be tackled by forming the stochastic process model and combining it with observation model. This promising results open rooms for further investigations on the stochastic process model and Kalman filter estimation, which can be defined as future works. For instance, two other choices of stochastic process model can be constructed.

**Choice 2** Unlike the proposed stochastic process model in 3.5, the model can be built on the cyclostationary signal of river discharge itself and not on residual. This means

$$X_t = \hat{A}X_{t-1}, \text{ where } \hat{A} = \Sigma x_\Delta \Sigma x^{-1}, \quad (3.40)$$

and

$$\Sigma x = C\{X_t, X_t\} = E\{X_t X_t^T\} = M\{X_t^T X_t\} = \frac{1}{N}\{X_t^T X_t\} \quad (3.41)$$

$$\Sigma x_\Delta = C\{X_t, X_{t-1}\} = E\{X_t X_{t-1}^T\} = M\{X_{t-1}^T X_t\} = \frac{1}{N-1}\{X_{t-1}^T X_t\}. \quad (3.42)$$

Such  $\Sigma x$  and  $\Sigma x_\Delta$  would lead to a different process noise level  $Ce_x$ .

**Choice 3** Another form of stochastic process model can be proposed as defining twelve state transition models  $\hat{A}_j$  belonging to different months  $j$ . In fact the  $X_{t_{i,j}}$  at month  $j$  and year  $i$  can be estimated by state transition model of that specific month  $\hat{A}_j$ .

$$X_{t_{i,j}} = \hat{A}_j X_{t_{i,j-1}}, \text{ where } \hat{A}_j = \Sigma_{\Delta j} \Sigma_j^{-1}. \quad (3.43)$$

The  $\Sigma_j$  and  $\Sigma_{\Delta j}$  are computed by forming the  $X_j$ , that contains the river discharge values at month  $j$  of all years  $i$

$$\Sigma_j = C\{X_j, X_j\} = E\{X_j X_j^T\} = M\{X_j^T X_j\} = \frac{1}{N}\{X_j^T X_j\} \quad (3.44)$$

$$\Sigma_{\Delta j} = C\{X_j, X_{j-1}\} = E\{X_j X_{j-1}^T\} = M\{X_{j-1}^T X_j\} = \frac{1}{N-1}\{X_{j-1}^T X_j\} \quad (3.45)$$

The two aforementioned choices for stochastic process model would definitely lead to different results than those obtained in this study. Which model performs the best? Which model is less sensitive to the uncertainty of observations? These are the questions that should be addressed within future works of this study.

Another issue that remains open in this study is solving the linear dynamic system for more than one time series. This means that the process model  $\hat{A}$  is not scalar value anymore and contains the covariance and cross-covariance information of river discharge belonging to different gauges or catchments. With the help of such setting for process model, estimation of river discharge for an ungauged catchment is feasible

through its cross-covariance information with gauged catchments. This cross-covariance information can be derived from available models or old data sets.

Moreover, it is expected that various noise level of observations  $Qx_t$  in the linear observation equation would lead to different estimation of Kalman filter. Therefore, the effect of observation noise level on the estimated river discharge by Kalman filter should be also addressed in future works of this study.

## Chapter 4

### Water storage changes by GRACE

Over the past several years, the quality of GRACE data processing in general has improved (Förste et al., 2008). However, the weaknesses of GRACE as a sensor, despite the overall success of the mission, are being acknowledged (Sneeuw, 2007; Wiese et al., 2011). As discussed in Chapter 1, the utility of GRACE solutions as representative of hydrological water storage changes is limited by the challenges: resolution, separability, consistency and uncertainty.

The aim of this chapter is to develop algorithms to cope with these challenges, so that the noise level of GRACE is reduced and reliable time series for water storage changes are obtained. In fact, this has been the aim of research from the beginning of the GRACE era. Optimal filtering of the GRACE products is an ongoing issue in the geodetic literature to tackle the North-South streaks (Kusche, 2007; Klees et al., 2008; Kusche et al., 2009; Wouters and Schrama, 2007). Several other attempts have been made for an evaluation of GRACE versus external models or data sets to quantify the noise in GRACE solutions. Global GPS deformations (Kusche and Schrama, 2005), ground-based superconducting gravimeters (SG) (Hinderer et al., 2006; Neumeyer et al., 2008; Weise et al., 2009), ocean bottom pressure (OBP) sounders (Rietbroek et al., 2007; Bingham and Hughes, 2007; Macrander et al., 2010) and hydrological models (Rangelova et al., 2007; Chen et al., 2008b; Virtanen et al., 2007; Syed et al., 2008) have been used as external constraints. However, inconsistency of the constraints in spatial and temporal scale makes improving GRACE solutions difficult. For instance, neither SG nor OBP provide point measurement, and their spatial resolution is not clearly known (Rieger et al., 2012). Hydrological models as external constraints also bring about a number of problems, one being the poor accuracy of evapotranspiration ( $ET_a$ ) estimates in the models, which leads to considerable variations between the different modelling approaches and also shows systematic deviations from observations (PILPS, 1996; Gates, 1997). The other problem being the coarse description of local runoff by means of a parameterization (Rieger et al., 2012).

Apart from the aforementioned constraints, the discussed triangle relationship (1.9) in Chapter 1 can be also introduced as a way to constrain GRACE temporal derivatives aggregated over catchments. In fact, comparing GRACE mass derivatives  $dM/dt$  with water storage changes from hydrological and also from hydro-meteorological water balances for gauged catchments can help to deal with the mentioned challenges and limitations. However, this method adds its own challenges since numerical inconsistencies

and inseparabilities are inevitable. This chapter aims to cope with this and the inherent GRACE challenges to reduce the noise level of GRACE monthly solutions and obtain an appropriate data set for hydrological studies.

## 4.1 Consistency challenge

The consistency challenge of GRACE comes about in two steps: 1) during the de-aliasing procedure and 2) within validation against external constraints. In the de-aliasing procedure, to cope with the inconsistency of atmospheric/oceanic pressure and GRACE data, a spherical harmonic analysis is performed. This is carried out through a numerical integration of the combined residual atmospheric and oceanic pressure for each degree separately (Zenner et al.; Flechtner, 2007). This integration provides numerical errors, which will be combined with input model errors and appear in different forms of uncertainties in the GRACE monthly solutions. As this study deals with the processed GRACE solutions after de-aliasing, the inconsistencies during de-aliasing will not be touched and their resulting uncertainty will be investigated in Section 4.4.

Besides that, for evaluation of GRACE monthly solutions against external constraints consistent data sets are needed. According to the equation (1.9), hydrological and hydro-meteorological signals can be used as constraints for the GRACE monthly solutions. However, they are comparable with the derivative of the aggregated equivalent water height over a catchment. The aggregated equivalent water height derived from GRACE  $M(\chi; t)$  over a catchment, see equation (1.7), can be written in complex exponential notation form

$$M(\chi; t) = \sum_{\omega=-\infty}^{\infty} c_{\omega} e^{i\omega t}. \quad (4.1)$$

Assuming only one harmonic,

$$M(\chi; t) = e^{i\omega t} \quad (4.2)$$

from which the derivative of the equivalent water height is

$$\frac{dM(\chi; t)}{dt} = i\omega e^{i\omega t}. \quad (4.3)$$

In fact  $dM/dt = i\omega e^{i\omega t}$  from GRACE is the term that is comparable with hydrological and hydro-meteorological signals. However, computing the derivative of a time series is only possible via numerical approaches. Among the numerical methods, due to less truncation error the central difference approach brings better results compared to backward and forward differences. In the central difference the  $dM(\chi; t)/dt$  is computed as

$$\frac{dM(\chi; t)}{dt} \approx \frac{M(\chi; t + \Delta t) - M(\chi; t - \Delta t)}{2\Delta t} \quad (4.4)$$

where for the monthly solution  $\Delta t$  is equal to one month. In complex exponential notation the central difference derivation can be written as

$$\begin{aligned} \frac{M(\chi; t+1) - M(\chi; t-1)}{2} &= \frac{e^{i\omega(t+1)} - e^{i\omega(t-1)}}{2} \\ &= \frac{e^{i\omega t}(e^{i\omega} - e^{-i\omega})}{2} \\ &= \frac{e^{i\omega t}(2i \sin \omega)}{2} \\ &= i \sin \omega e^{i\omega t} \end{aligned} \quad (4.5)$$

The difference between the central difference scheme and derivative is distinguished by comparing the equations (4.3) and (4.5)

$$\frac{M(\chi; t+1) - M(\chi; t-1)}{2} = \frac{dM(\chi; t)}{dt} \times \frac{\sin(\omega)}{\omega}, \quad (4.6)$$

which reveals that the difference is a sinc function  $\text{sinc}(\omega)$  (Figure 4.1). This means, for the known annual behaviour of the water storage changes with a 12 month period ( $\omega = \pi/6$ ), central difference scheme underestimates the amplitude of annual signal by  $\text{sinc}(\pi/6) = 0.95$ . This value would be even less, ca. 0.41 for a three month period. In fact, the underestimation of the derivative value occurs for all the frequencies in the Nyquist interval (Hamming, 1998). Therefore, what is computed by the cen-

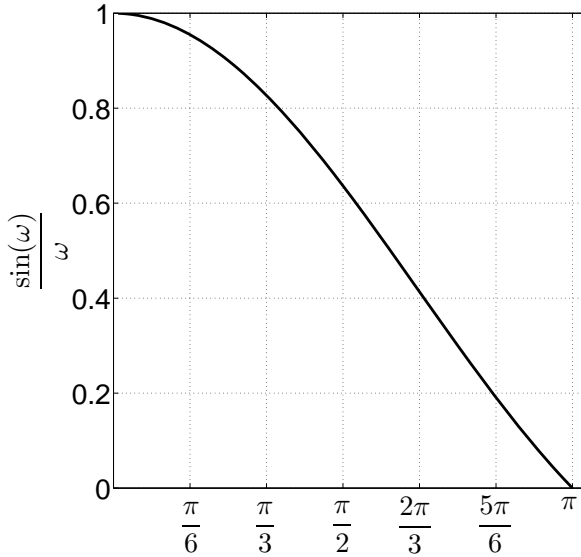


**Figure 4.1:** The behaviour of sinc function between 0 and  $\pi$ , which represents the difference between true derivative and central difference in frequency domain

tral difference scheme is different from what should be compared with the hydrological and hydro-meteorological signals. This inconsistency prevents analysing the noise level of GRACE by validation against corresponding signals, thoroughly.

A possible method to cope with this inconsistency is an inverse approach, in which a spectral estimate is multiplied by the inverse of the sinc function. Yet, this method can be only followed if a long time series of GRACE is available, for which an accurate spectral analysis can be performed. The sensitivity of spectral analysis to a short data set and its length is highlighted in Figure 4.2, where the spectrum of data from 2005–2008 differs from the one belonging to 2005–2010.

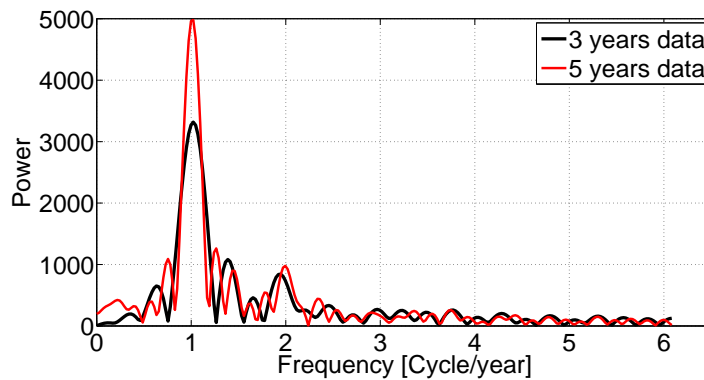


**Figure 4.2:** Spectral analysis on the two data sets of computed mass derivative via central difference scheme from GFZ solution release 5 over Amazon catchment with different length of 2005–2008 (black) and 2005–2010 (red)

As the inverse approach seems to be problematic, the consistency should be implemented by changing the right hand side of the equation. This means that the hydrological and hydro-meteorological signals should be filtered by a filter that acts similar to the sinc function in frequency domain. Therefore, the transfer function of filter in the relevant frequency domain should be defined having minimum difference with the sinc function. Two transfer functions are tested here

$$H_1(\omega) = \frac{\cos(\omega) + 1}{2} \quad (4.7)$$

$$H_2(\omega) = \frac{2\cos(\omega) + 3}{5}, \quad (4.8)$$

which are considered as filters 1 and 2. Figure 4.3 shows  $H_1(\omega)$  and  $H_2(\omega)$  together with the sinc function showing that the  $H_2(\omega)$  matches the sinc function well except for high frequencies.  $H_1(\omega)$  attains similar values at zero and  $\pi$ , but diverges from sinc function in comparison to the  $H_2(\omega)$ . The RMS values of residuals for  $H_1(\omega)$  and  $H_2(\omega)$  with respect to the sinc functions are 0.11 and 0.6, respectively. Filters 1 and 2 can be written in complex exponential notation as

$$H_1(\omega) = \frac{\cos(\omega) + 1}{2} = \frac{2\cos(\omega) + 2}{4} = \frac{e^{i\omega} + e^{-i\omega} + 2}{4} \quad (4.9)$$

$$H_2(\omega) = \frac{2\cos(\omega) + 3}{5} = \frac{e^{i\omega} + e^{-i\omega} + 3}{5} \quad (4.10)$$

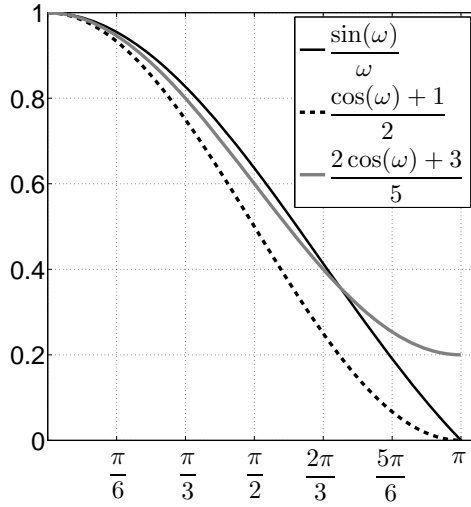


**Figure 4.3:**  $H_1(\omega)$  and  $H_2(\omega)$  together with the sinc function.  $H_1(\omega)$  fits with RMSE of 0.11 on sinc while  $H_1(\omega)$  has an RMSE of 0.6, yet with high deviation in high frequencies

Supposing that the input function is an harmonic  $e^{i\omega t}$  of frequency  $\omega$ , the above equations turn into

$$e^{i\omega t} H_1(\omega) = e^{i\omega t} \left( \frac{e^{i\omega} + e^{-i\omega} + 2}{4} \right) = \frac{e^{i\omega(t+1)} + 2e^{i\omega t} + e^{i\omega(t-1)}}{4} \quad (4.11)$$

$$e^{i\omega t} H_2(\omega) = e^{i\omega t} \left( \frac{e^{i\omega} + e^{-i\omega} + 3}{5} \right) = \frac{e^{i\omega(t+1)} + 3e^{i\omega t} + e^{i\omega(t-1)}}{5} \quad (4.12)$$

which corresponds to the convolution windows that operate on the data in the time domain

$$h_1 = \begin{bmatrix} 1 & 1 & 1 \\ \frac{1}{4} & 2 & \frac{1}{4} \end{bmatrix}$$

$$h_2 = \begin{bmatrix} 1 & 3 & 1 \\ \frac{1}{5} & 5 & \frac{1}{5} \end{bmatrix},$$

for filters 1 and 2, respectively. This means that the filtered hydrological or hydro-meteorological water storage change,  $dS_F/dt$  is obtained as

$$\frac{dS_{F1}}{dt}(t) = \frac{1}{4} \frac{dS}{dt}(t-1) + \frac{1}{2} \frac{dS}{dt}(t) + \frac{1}{4} \frac{dS}{dt}(t+1) \quad (4.13)$$

$$\frac{dS_{F2}}{dt}(t) = \frac{1}{5} \frac{dS}{dt}(t-1) + \frac{3}{5} \frac{dS}{dt}(t) + \frac{1}{5} \frac{dS}{dt}(t+1) \quad (4.14)$$

Figure 4.4 depicts the filtered hydro-meteorological water storage change together with the computed derivative of mass change using central difference scheme over the Amazon catchment. The time series of  $dM/dt$  and  $dS/dt$  have the correlation of 0.89, which is expected to increase by filtering the  $dS/dt$ . Correlations of 0.91 are achieved for time series of  $dS_{F1}/dt$  and  $dS_{F2}/dt$  with  $dM/dt$ . Increasing the correlation implies more consistency between GRACE and hydro-meteorological signals. Improving the consistency can be also checked by looking at the amplitude of the signals on the both sides of equa-

tion (1.9). The ratio of RMS of  $dS/dt$  and  $dS_F/dt$  to the RMS of  $dM/dt$ , expresses the consistency of signals in terms of amplitude. The ratio decreases from 1.17 to 1.05 and 1.07 for  $dS_{F1}/dt$  and  $dS_{F2}/dt$ , respectively. Figure 4.5 shows a polar diagram indicating the correlation and ratio of RMS of  $dM/dt$

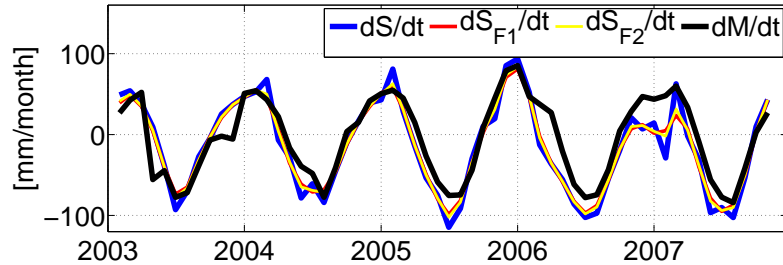


**Figure 4.4:** Comparison of water storage change from GRACE and un/filtered hydro-meteorological signals over Amazon catchment

and  $dS/dt$  together with the correlation and ratio of RMS of  $dM/dt$  and  $dS_F/dt$  for catchments with available river discharge data (each dot represents one catchment). The ideal scattering for the dots in

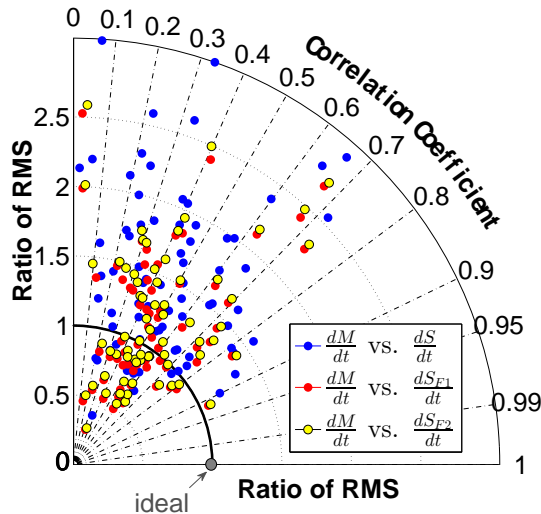


**Figure 4.5:** Polar diagram of correlation and ratio of RMS between GRACE and hydro-meteorological rate of water storage change before and after making the data consistent by filtering with filters  $H_1$  and  $H_2$

the Figure 4.5 occurs when the dots are scattered toward high correlation radial lines around the circle line with ratio of RMS equal to one. However, this is not the case for most of the catchment, although the ratio of RMS and correlation coefficients value are getting better after filtering the hydro-meteorological signal. The results show that both filters  $H_1$  and  $H_2$  lead to similar ratio of RMS values and correlation coefficients. Therefore, a general conclusion about comparison of  $H_1$  and  $H_2$  can not be drawn. In fact, performance of each filter depends on behaviour of the water storage change of each catchment. It can be expected that for a water storage change with dominant high frequencies  $H_1$  performs better, while  $H_2$  should lead to better result for those without dominant high frequencies.

The low correlation and the difference in ratio of RMS between GRACE and hydro-meteorological rate of water storage change after making the data sets consistent by filtering might be explained by existence of other issues.

## 4.2 Challenge of resolution

The ca. 400km spatial resolution of GRACE limits its application for small basins, where closing continental water balance is hindered by erroneous signals with high uncertainty. However, regional modeling and improving the resolution is an ongoing issue in the geodetic literature (Eicker et al., 2008; Kuroishi, 2009). Indeed, these studies can not fully address the resolution challenge as it is mainly driven by orbit configuration. As our current study focuses on catchments representation of water storage changes, to avoid misinterpretation the 255 largest catchments around the world are chosen for investigation. In particular, due to the aggregation, the GRACE error level reduces by increasing to area of the catchments. Henceforth, in this study for many of the analysis only the catchments with area greater than 250 000 km<sup>2</sup> are selected.

## 4.3 Challenge of separability

The water storage variations estimated by GRACE represents the integral of all storage components on the continents including atmosphere. Therefore, to obtain continental water storage changes, different sources of water storage changes like atmospheric and non-tidal oceanic variations should be separated, estimated and excluded from the GRACE observation (Flechtner et al., 2006). This is challenging because any mis-modeling would lead to an error in the GRACE monthly solutions. This study does not look at any refinement for separating continental water storage change from GRACE observation, yet the resulting uncertainty of mis-modeling in the de-aliasing procedure will be extensively scrutinized in Section 4.4.

Apart from that, as this study aims to evaluate the GRACE monthly solutions against the hydrological and hydro-meteorological signals, separability becomes more critical as the data from GRACE should be comparable with these respective constraints. In this respect, the de-aliased GRACE solutions over a catchment represent the water storage changes in different layers of vegetation, land surface, soil water and ground water (Figure 1.1). This makes closing of the water balance more difficult as models and *in situ* measurements often represent parts of these compartments (Güntner, 2008). As discussed in Chapter 1, the only input is the precipitation over the catchments and the outputs are discharge to the oceans and evapotranspiration. Among these input and outputs, discharge is the only process that occurs over different storage components. Hence, it is important to employ the whole river discharge for closing the water balance and not the overland, soil water or ground water flows. Therefore, in this study the river

discharge time series at the outlet of catchments is taken into the consideration for all of the investigations. It is highly expected that the river discharge at the outlet comprises the overland, soil water or ground water flows.

## 4.4 Challenge of uncertainty

The uncertainty challenge occurs at different steps within the GRACE processing chain. In fact, the uncertainty of GRACE is the result of errors, inconsistencies, mis-modeling and lack of modeling in the different stages of data processing. The errors in de-aliasing models, intrinsic instrumental error, the errors in precise orbit determination, lack of proper error propagation, limitation of GRACE to the modeling of  $C_{20}$  and invisibility of the degree 1 term are examples of sources for uncertainty in GRACE solutions. Indeed, separating the different types of errors in GRACE based on their sources has been a difficult task (Wahr et al., 2006). This becomes more problematic as the uncertainties in GRACE solutions will appear in different forms e.g. outliers (Tourian et al., 2011) or North-South streaks (Schrama et al., 2007; Wouters and Schrama, 2007).

Moreover, one can identify the uncertainties and improve the GRACE observations by comparing with hydrological and hydro-meteorological signals. Analysing the temporal inter-correlation between water storage change from each source should help in quantifying their common information content that has been deteriorated by noise (Rieger et al., 2012). Furthermore, if the analysis enables a reduction in the errors, then it must lead to an increased correlation. Therefore, the inter-correlation within the triangle, shown in equation (1.9), can be used for the assessment of noise levels. This means that the inter-correlations of time series from each part of the triangle, reveal the effect of reducing uncertainty. As mentioned before, a typical way to cope with the uncertainty in the GRACE data is filtering, which is mainly used to remove the North-South streaks. However, the inter-correlation of  $dS_F/dt$  and the filtered  $dM/dt$  by Gaussian filter with different radius (300, 350, 400, 450 and 500km) over catchments with area larger than 250 000 km<sup>2</sup>, reveal that the correlation changes differently for different catchments when increasing the radius (Figure 4.6). For a large catchment like Amazon, increasing the filter radius does not influence the correlation, while for Nelson River, St Lawrence River and Northern Dvina the correlation decreases by increasing the filter radius. On the other hand, for catchments like Western Sahara, and Helmand the correlation improves with higher filter radius. These results together with the interesting behaviour of correlation coefficients of catchments like Tarim and Gobi (Figure 4.6) imply that filtering the whole globe with a fixed filter does not cope with all the sources of uncertainties. Moreover, different catchments in different locations (close or not close to the coast) and with different size, shape and extension (North-South or West-East) behave differently to a certain filter. Similar results have been also obtained by Werth et al..

Therefore, in order to cope with the uncertainties in the GRACE data, each catchment should be assessed individually with respect to the corresponding hydrological and hydro-meteorological signals. In line with, a number of large peaks show up in the GRACE mass derivative aggregated  $dM/dt$  over

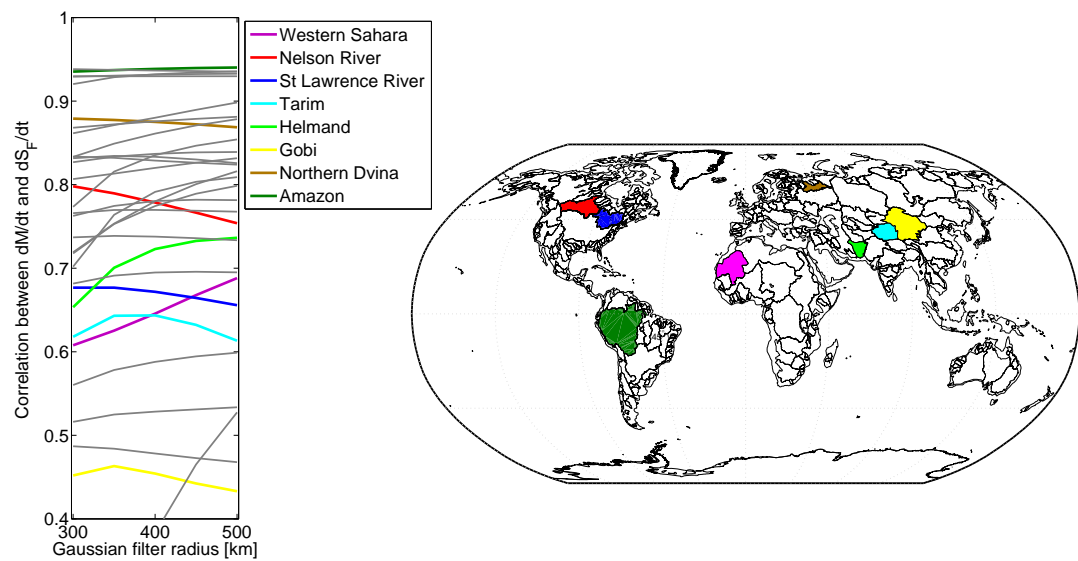


**Figure 4.6:** Correlation coefficients of  $dS_F/dt$  and the filtered  $dM/dt$  by different radius of Gaussian filter (300, 350, 400, 450 and 500km) over catchments with area larger than  $250\,000\text{km}^2$ . The Western Sahara, Nelson River, St Lawrence River, Tarim, Helmand, Gobi, Northern Dvina and Amazon catchments are highlighted among other catchments (gray lines)

the catchments, which do not correspond to the respective hydrological and hydro-meteorological data (Figure 4.7). These peaks must be interpreted as outliers, which carry the danger of signal degradation. Outliers are defined loosely as inconsistent observations in a data set (Barnett and Lewis, 1994). Basically, inconsistent observations in a data set are not necessarily erroneous values but can be nominated as outliers if they are 1) extreme values relative to their neighbouring measurements and 2) inconsistent with the rest of the data set (Kern et al., 2005). These two characteristics are crucial for detecting and defining outliers in a given time series. However, for the time series of GRACE, additional characteristics can be also employed, by which an outlier can be verified through validation against hydrological ground truth.

#### 4.4.1 Outlier identification algorithm

Several strategies to identify outliers have been suggested and performed, which in general can be categorized as follow

1. **Statistical methods:** In these methods the search for the outlier is carried out in the entire data set statistically. In other words, a statistical testing tool is employed, where the rejection of the hypothesis leads to identification of outliers. Baarda's data snooping method (Baarda, 1968), the Grubbs method (Grubbs, 1950), Mahalanobis distance method (Rousseeuw and Leroy, 1987) and the Dixon method (Dixon, 1951) are examples of methods which follow a statistical approach to identify outliers.

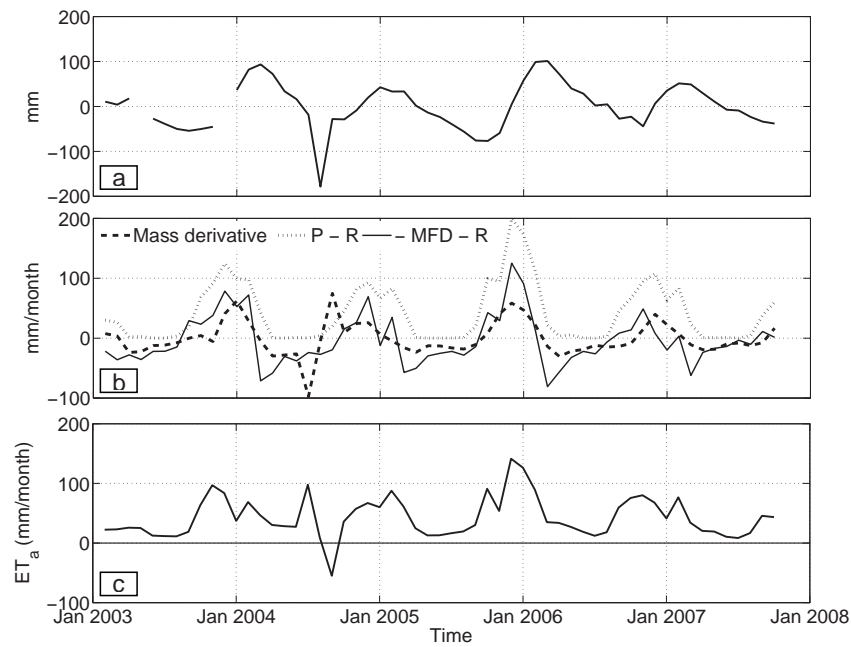


**Figure 4.7:** a) Mass deviation on Okavango catchment derived from GFZ solution. b)  $dM/dt$  (mass derivative) from GFZ,  $P - R$  and  $-\nabla \cdot \vec{Q} - R$ , over Okavango catchment. c) Computed  $ET_a$  by  $P - R - dM/dt$  over the Okavango catchment.

**2. Adaptation methods:** In these methods an adaptation technique is followed to detect the outliers. Nonparametric regression, robust methods, smoothers, kernel regression estimation, splines, wavelet and filter techniques can be used to identify outliers and achieve a smooth estimate of the data set (Kern et al., 2005).

In order to identify an outlier in the aggregated mass deviation time series over the catchments, the data snooping method seems to be suitable. In fact, the data snooping procedure does not just look for large values, but for values that are large in comparison to their own standard deviations (Baarda, 1968). To this end, the normalized value is used rather than the value itself. Supposing the statistical distribution of the normalized value to be known, statistical hypothesis testing with a specific probability level can be used to detect the outliers. Since the distribution of residual is known, the data snooping procedure is normally applied to residuals (Baarda, 1968).

For a cyclostationary signal, the residual is computed by subtracting the estimated monthly mean (cyclostationary mean) from the monthly values. In other words, as shown in Figure 4.8 (inset), for computing residuals in the  $j^{\text{th}}$  month (Jan. – Dec.) of the  $i^{\text{th}}$  year ( $r_{i,j}$ ), the estimated monthly mean ( $\bar{x}_j$ ) has to be removed from the signal ( $x_{i,j}$ ):

$$r_{i,j} = x_{i,j} - \bar{x}_j \quad \text{with} \quad \bar{x}_j = \frac{1}{N} \sum_{i=1}^N x_{i,j} \quad , \quad (4.15)$$

where  $N$  is the number of years. The residual is more sensitive to the errors because it does not contain the seasonal behaviour (Figure 4.8). Hence, the RMS of the residual can be interpreted as an upper error bound for the GRACE monthly solutions. K-S test is employed to compare normalized residual (divided

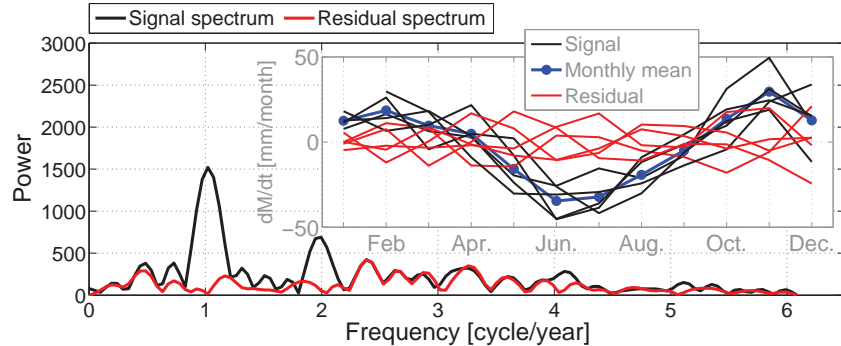


**Figure 4.8:** Spectra of monthly GRACE derivatives (signal) and residual of monthly GRACE derivatives. Inset: GRACE derivatives ( $dM/dt$ ) (signal), monthly mean and residual ( $dM/dt - \text{monthly mean}$ ) sorted for individual years over the Ob catchment

by  $\sigma$ ) to a standard normal distribution. For the test, the null hypothesis is defined as the normalized residual follows standard normal distribution. The null hypothesis is accepted for all catchments at the 5% significant level. The corresponding test statistics for different catchments vary between 0.04–0.15, which are smaller than the critical value, 0.22. This means that that residuals of mass deviation over catchments follow a normal distribution, which allows data snooping for detecting outliers (Figure 4.9).

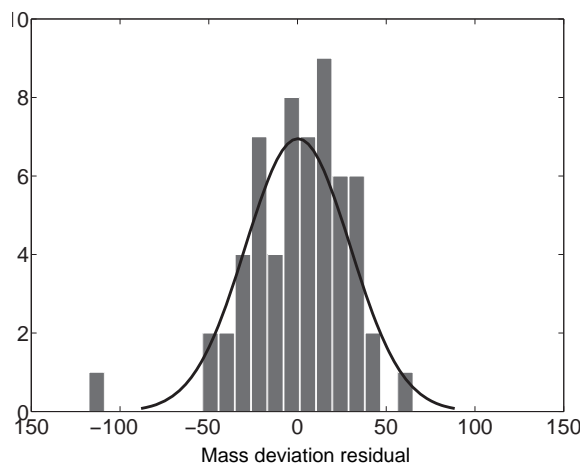


**Figure 4.9:** Histogram of mass deviation residual over the Okavango catchment

However, huge outliers in the data lead to a contaminated computing monthly mean  $\bar{x}_j$ . Thus, the desired algorithm for identifying outliers must contain a procedure to remove large outliers before computing the residual  $r_{i,j}$ . That means data snooping on  $x_{i,j}$  is needed.

The algorithm of identifying outliers in GRACE mass deviation is defined such that the data snooping procedure is applied on each year of mass deviation signal  $x_{i,j}$ , separately. The algorithm consists of the following steps and Figure 4.10 visualizes the implementation of the algorithm over the Colorado river catchment, step by step.

1. Data gaps in mass deviation signal are filled by interpolated values (Figure 4.10b).
2. The mean ( $\mu_i$ ) and the standard deviation ( $\sigma_i$ ) of each year  $i$  are computed. Subsequently, the annual centered normalized value of each month ( $z_{i,j}$ ) is computed by:

$$z_{i,j} = \frac{x_{i,j} - \mu_i}{\sigma_i}, \quad j = 1, 2, \dots, 12 , \quad (4.16)$$

By defining a suitable confidence level ( $\alpha_1$ ), the appropriate critical value ( $k_{\alpha_1/2}$ ) is attained under the null hypothesis  $H_0$  that no outlier exists in the time series (Figure 4.10c). So it will be accepted if:

$$-k_{\alpha_1/2} < z_{i,j} < k_{\alpha_1/2} . \quad (4.17)$$

3. By rejecting the null hypothesis  $H_0$ , outliers are identified iteratively. If  $H_0$  is rejected, the detected outliers ( $i = i_o, j = j_o, o = 1, \dots, d$ ) are removed and filled with the monthly mean of other years  $x_{j_o}$ , which represents a hydrologically plausible number:

$$x_{j_o} = \frac{1}{N-d} \sum_{\substack{i=1, \\ i \neq i_o}}^N x_{i,j} , \quad (4.18)$$

where  $d$  is the number of detected outliers (Figure 4.10d). After replacing the removed value the second step should start again to compute the new mean and standard deviation for each year. This procedure is done until  $H_0$  is accepted. Statistically, replacing the outliers with the monthly mean of other years, avoids the occurrence of high peaks in the residual and leads to a normal distribution for residual.

4. Based on (4.15) the uncontaminated monthly mean is computed through the corrected mass deviation signal (Figure 4.10e).
5. The mass deviation residual ( $r_{i,j}$ ) is computed from (4.15) to search for any possible outlier on the residual (Figure 4.10e). The null hypothesis is accepted if:

$$-k_{\alpha_2/2} < \frac{r_{i,j}}{\sigma} < k_{\alpha_2/2} , \quad (4.19)$$

where  $k_{\alpha_2/2}$  is the critical value based on the confidence level ( $\alpha_2$ ),  $\sigma$  is the standard deviation of the whole residual time series. Data snooping can be performed on the whole time series of residuals (Figure 4.10f). The rejected values are removed and filled with the monthly mean of other years (like for signal (4.18)), after which the fourth step should start again to compute

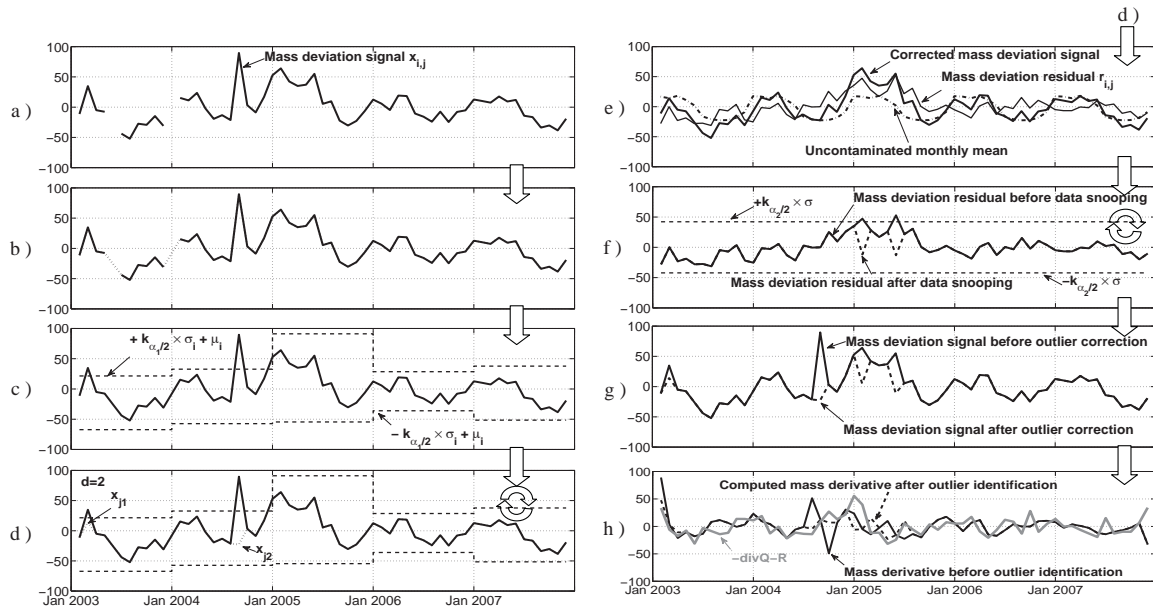


**Figure 4.10:** Implementing the outlier identification and correction algorithm over the Colorado river basin, step by step: **a)** mass deviation monthly time series derived from GFZ aggregated over the Colorado river catchment, **b)** mass deviation monthly time series with filled interpolated value for the gaps, **c)** mass deviation monthly time series with confidence limits for each individual year, **d)** data snooping on mass deviation time series identified 2 outliers ( $d = 2$ ): March 2003 and September 2004, which were replaced by the revised inter-annual mean via (4.18), **e)** corrected mass deviation signal ( $x_{i,j}$ ), computed monthly mean ( $\bar{x}_j$ ) via (4.15) and computed mass deviation residual (4.15), **f)** mass deviation residual monthly time series with confidence limits, data snooping identified 2 outliers in residual time series: February 2005 and June 2005 which were replaced by revised inter-annual mean, **g)** derived mass deviation monthly time series after performing the outlier correction algorithm and original time series, **h)** computed mass derivative  $\dot{x}_{i,j}$  from aggregated monthly time series of mass deviation  $x_{i,j}$  before and after outlier correction together with hydro-meteorological time series aggregated over the Colorado river catchment. Visual inspection on the four months which were identified as outliers: March 2003, September 2004, February 2005 and June 2005, reveals the improved agreement of corrected mass derivative and hydro-meteorological signal.

the new inter-annual monthly mean. This procedure is iterated until there is no further rejection (Figure 4.10g).

6. Finally, the mass derivatives are computed by central difference scheme, the derivatives at the beginning or the end of an interval, where no left and right value exist, were omitted. The computed derivative is cross-checked for compatibility with the hydrological and hydro-meteorological signals (1.9) (Figure 4.10h). In case of incompatibility, i.e. low correlation between GRACE and both hydrological and hydro-meteorological time series, the confidence levels ( $\alpha_1$  and  $\alpha_2$ ) are changed in the range 95%–99% until attaining optimal correlation.

As an example, detected outliers in the monthly time series of aggregated mass deviation over the Colorado river catchment are March 2003, September 2004, February 2005 and June 2005 (Figure 4.10g). While computing the derivative, these outliers in the mass deviation signals affect the months before and after (Figure 4.10h). Based on (1.9), the computed mass derivative after outlier correction should

provide a better correlation with hydrological and hydro-meteorological signals which is the case for the Colorado river catchment (Figure 4.10h).

By applying the algorithm for different available GRACE products (GFZ, JPL, CSR, ITG) aggregated over catchments and by cross checking with the hydro-meteorological signals, confidence levels of 97% ( $k_{\alpha_1/2} = 2.17$ ) for data snooping on the signal and of 98% ( $k_{\alpha_2/2} = 2.32$ ) for data snooping on the residual have been found as optimal confidence levels. Figure 4.11 shows the detected outliers from release 4 of GFZ, JPL, CSR and ITG mass deviation for the 255 catchments. The considered time series for each product is between Feb. 2003 and Dec. 2007 and the catchments were sorted in terms of area, in descending order (sorted from biggest catchment to smallest catchment, left to right). The detected outliers show specific months with high number of outliers for GFZ and ITG and less prominent features for JPL and CSR products (e.g. Sept. 2004).

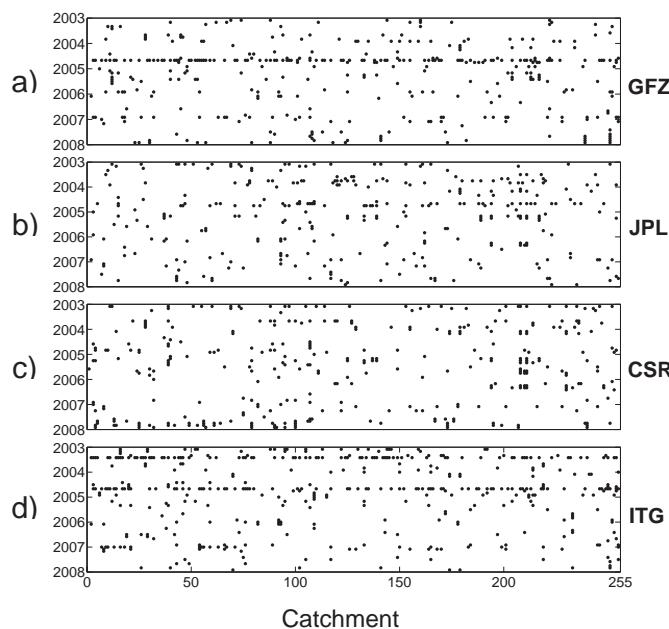


**Figure 4.11:** a, b , c and d show 372 (2.5%), 316 (2.1%), 339 (2.2%) and 426 (2.8%) detected outliers from GFZ, JPL, CSR and ITG catchment based aggregated monthly solutions, respectively.  $\alpha_1 = 97\%$  for data snooping on signal and  $\alpha_2 = 98\%$  for data snooping on residual have been used to identify above outliers.

A careful look at Figure 4.11 will reveal many outliers for particular months in all the solutions, except for those from CSR. These outliers occur in the months in which the GRACE spatial data coverage was insufficient due to repeat orbit mode (around September 2004) or problems with the position data from GPS (December 2006) (cf. release notes for GRACE L2 data products). For example, when GRACE was in repeat orbit mode during the months from July 2004 to October 2004, the resulting spherical harmonic solutions are not accurate enough and this is reflected in the outlier detection results. For the same reason a disproportionate amount of outliers are seen in particular months of the ITG solutions: June 2003, September 2004, and December 2006. The ITG solutions are provided for every month irrespective of the nature of the GRACE L1b data, and hence there are no data gaps in their time series. For instance, none

of the data centres, apart from ITG, provide spherical harmonic solutions for the month of June 2003. In order to counter the spatial coverage and GPS problems, GFZ provides regularized datasets for the troublesome months mentioned above (is not used in this study). It is not known how these problematic months are handled by CSR and JPL, but the outlier analysis suggests that, multi-month solutions are used to bridge the weak months.

Apart from the troublesome months, no spatial dependence on latitude, longitude or catchment area can be recognized. As a result for any combination of two products simultaneous outliers appear in  $\sim 10\%$  and for all four products in only  $\sim 2\%$  of all occurrences.

The impact of outlier correction on the consistency of GRACE with ground truth can be investigated by computing the correlation and RMS ratio of water storage changes from GRACE and hydro-meteorological signals. Figure 4.12 shows the polar diagram containing the correlation and RMS ratio of  $dM/dt$  and  $dS_{F2}/dt$ . The tendency of arrows toward higher correlation imply an improved consistency between GRACE and hydro-meteorological signal after outlier correction. On average ca. 14%, 8%, 2% and 13%

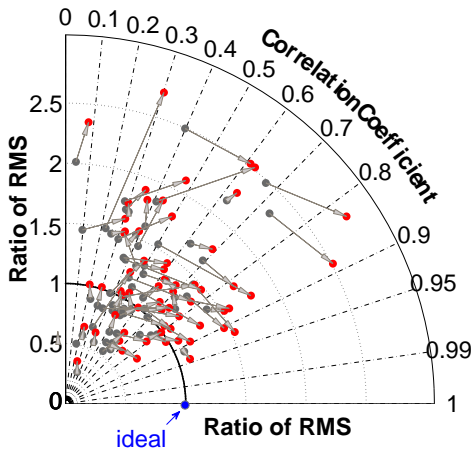


**Figure 4.12:** Polar diagram of correlation and ratio of RMS between GRACE and hydro-meteorological rate of water storage change before (gray) and after (red) outlier correction

increase in correlation for GFZ, JPL, CSR and ITG solution is achieved, respectively. Moreover, the RMS of the residual as a representative of upper error bound for the GRACE monthly solutions can be compared before and after outlier correction. Figure 4.13 shows the scatter plot of RMS of mass derivative residual  $dM/dt R$ , derived from GFZ solution, after outlier correction versus before outlier correction. On average ca. 26%, 3%, 4% and 12% reduction in RMS of residual are obtained for GFZ, JPL, CSR and ITG solutions, respectively.

In order to assess the reduction of noise level with respect to the signal amplitude of the GRACE aggregated solution, a Monthly Mean Signal to Noise Ratio (MMSNR) is defined as follow

$$\text{MMSNR} = \frac{1}{12} \sum_{j=\text{Jan}}^{\text{Dec}} \left| \frac{\bar{x}_j}{\sigma_j} \right| , \quad (4.20)$$

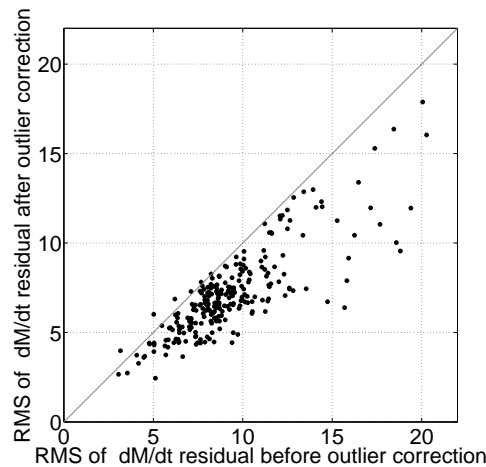


**Figure 4.13:** Scatter plot of RMS of mass derivative residual after versus before outlier correction for different catchments (Each dot represents one catchment). On average  $\sim 26\%$  reduction in RMS of residual is obtained

By comparing the MMSNR value before and after outlier correction, the reduction of noise can be quantified. Table 4.1 shows the average of MMSNR over 255 catchments before and after outlier correction for different products.

**Table 4.1:** Average of MMSNR before and after outlier correction for different products

| Products | MMSNR<br>before | MMSNR<br>after | %   |
|----------|-----------------|----------------|-----|
| GFZ      | 1.38            | 1.63           | 18% |
| JPL      | 1.71            | 1.81           | 6%  |
| CSR      | 1.51            | 1.66           | 10% |
| ITG      | 1.30            | 1.62           | 25% |

The impact of outlier correction in terms of improving correlation with hydro-meteorological signal and reduction of noise emphasizes that the outlier identification and correction must be performed before further assimilation of GRACE products into hydrological or hydro-meteorological analysis.

#### 4.4.2 Long-range correlations

As discussed in Chapter 1, the only input for the hydrological cycle is the precipitation. Therefore, it is expected that any pattern in the global precipitation leads to a pattern in any of the other hydrological phenomena e.g. change in the storage, evapotranspiration, etc.

Global air circulation pattern is responsible for precipitation behaviour by producing both the systematic and the air mass-controlled winds on the surface and aloft (Garrison, 2008). Figure 4.14 shows the global circulation pattern, which indicates reversal of flow patterns at  $30^\circ$  and  $60^\circ$  N & S latitude. The warm

air raises and diverges aloft toward each hemisphere's poles at the equator. Then it cools sufficiently to begin sinking around latitudes of 30° N & S. *Hadley Cells* are formed in both northern and southern hemispheres, as the colder air reaches the surface and spreads out such that the flow returns to the equatorial zone (Satoh, 2004). A reversed flow pattern occurs between 30° and 60° latitudes. Warm and moist air around 60° latitude rises and draws in the cooler 30° air to replace it. The warm air moves towards the equator, cooling as it goes, and then sinks were it encounters air from the *Hadley Cell*. At 30° latitude the air from both cells move downward but split at the surface, which cause maintaining each cell's circulation. The 60° zone is known as the *Subpolar Low*, since the converging surface air from both cells is warm and hence expanded to be in the low pressure state (Satoh, 2004). Some of the *Subpolar Low* air moves northward at altitude and cools progressively. It sinks around the poles, which leads to a *Polar Cell* circulation similar to the Subtropical pattern (Garrison, 2008).

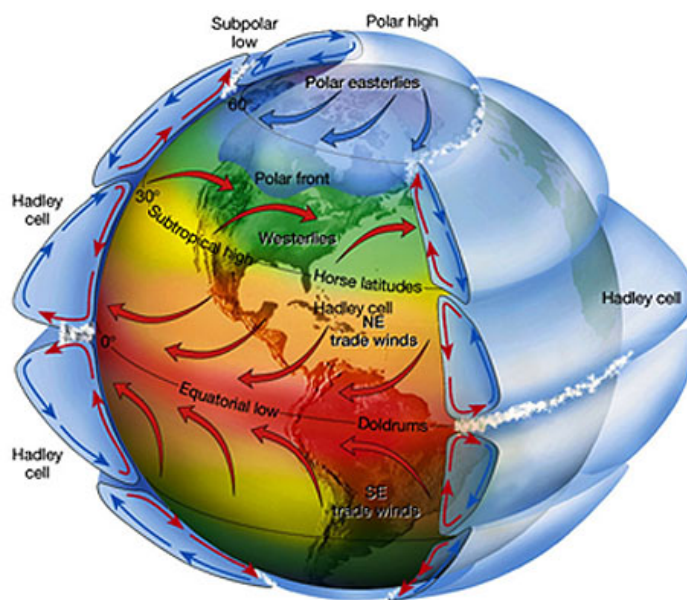


**Figure 4.14:** Global circulation pattern, from <http://www.fas.org>

From such a global circulation pattern, one can expect a correlated hydrological behaviour in *Hadley* and *Polar* cells and anti-correlated behaviour for hydrological phenomena in northern and southern hemisphere. The correlations can be investigated by computing the Inter Zonal Correlations (IZC) of hydrological phenomena. Figure 4.15 shows the IZC of spatially averaged signals and residuals of GRACE mass derivatives, precipitation  $P$  and moisture flux divergence  $\nabla \cdot \vec{Q}$  on 5° latitudinal zones.

As expected the IZC figures show patterns of high positive and negative correlations for the mass derivative signal  $dM/dt$  as well as for precipitation  $P$  and moisture flux divergence  $\nabla \cdot \vec{Q}$  signals.

For the respective residuals of  $dM/dt$ ,  $P$ ,  $\nabla \cdot \vec{Q}$ , which describe the deviations from the mean monthly behaviour introduced by annual variations of weather conditions, a different behaviour is expected. The local weather conditions are expected to be correlated within a limited correlation length i.e. by a neigh-

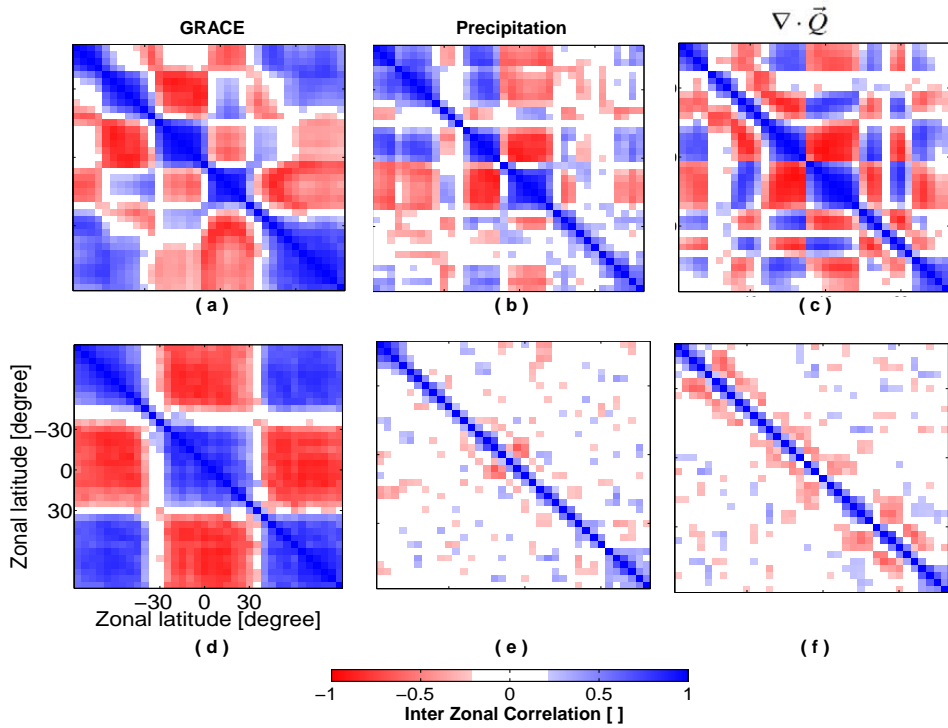


**Figure 4.15:** a) Inter Zonal Correlation (IZC) of GRACE mass derivative signal ( $dM/dt$ ) b) IZC of precipitation signal c) IZC of  $\nabla \cdot \vec{Q}$  signal d) IZC of GRACE mass derivative residual e) IZC of precipitation residual f) IZC of  $\nabla \cdot \vec{Q}$  residual

bourhood correlation. This is found to be true for the residuals of precipitation  $P$  and moisture flux divergence  $\nabla \cdot \vec{Q}$  (high correlations only in the diagonal). However, the residuals of GRACE mass derivatives (figure 4.16 bottom left) show a clear long-range correlation with a high positive correlation within the low latitude belt ( $|\varphi| < 30^\circ$ ) and a high negative correlation between low and high latitudes (Rieger et al., 2012).

Do the  $P$ ,  $\nabla \cdot \vec{Q}$  and  $dM/dt$  show the pattern because they are computed globally or is the pattern also valid over the landmasses? In order to investigate the pattern only over the landmasses, the matrices of Inter Basin Correlations (IBC) are formed displaying the temporal correlation for each catchment versus all other catchments. Figure 4.16 shows the IBC for the signal and residual time series of  $dM/dt$ ,  $P$  and  $\nabla \cdot \vec{Q}$  (the catchments have been sorted with respect to latitude of their center). The corresponding IBC matrices (figures 4.16) show very similar patterns as for IZC of signals and residuals. Again, the IBC of precipitation  $P$  and moisture flux divergence  $\nabla \cdot \vec{Q}$  residuals show a neighborhood correlation near the main diagonal, whereas the IBC of the mass derivative residual in addition shows a very clear latitudinal correlation pattern.

The individual cell by cell correlations or Inter Cell Correlations (ICC) on a ( $5^\circ \times 5^\circ$ ) grid of GRACE mass derivative residuals are determined. The spatial distribution of ICC with respect to a reference cell

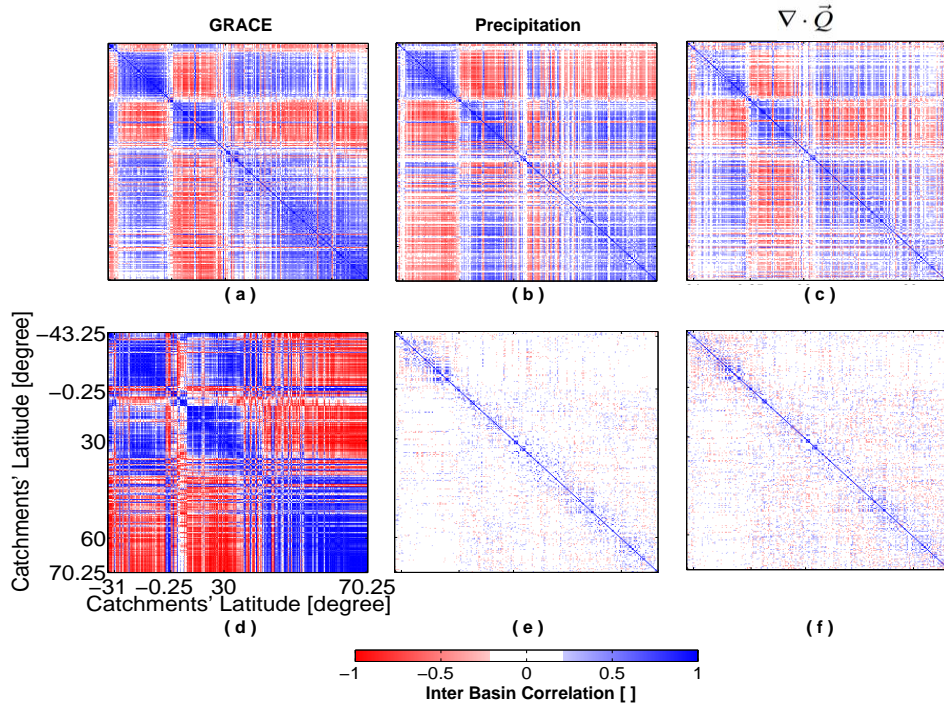


**Figure 4.16:** a) Inter Basin Correlation (IBC) of GRACE mass derivative signal ( $dM/dt$ ) b) IBC of precipitation signal c) IBC of  $\nabla \cdot \vec{Q}$  signal d) IBC of GRACE mass derivative residual e) IBC of precipitation residual f) IBC of  $\nabla \cdot \vec{Q}$  residual. The catchments have been sorted with respect to latitude of their center

at the North pole ( $\varphi = 87.5^\circ, \lambda = -177.5^\circ$ ) shows a long-range correlation over the globe independent from oceans and land masses (figures 4.17(a)).

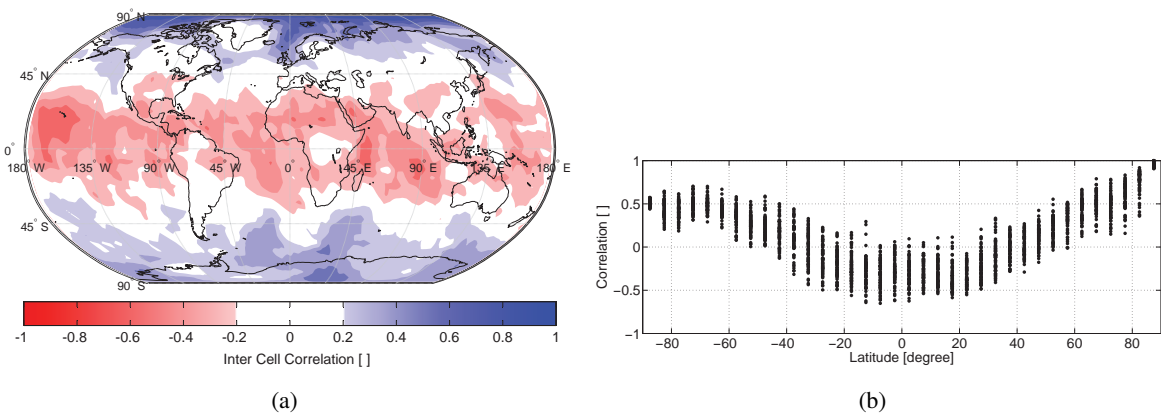


**Figure 4.17:** a) Spatial distribution of ICC b) Latitudinal dependence of ICC before reduction (both with respect to a reference cell at  $\varphi = 87.5^\circ, \lambda = -177.5^\circ$ )

The simultaneous occurrence of the ICC over oceans and land masses, for which mass change rates should have a totally different characteristic, confirms that the GRACE  $dM/dt$  residuals must contain a

signal component, which is independent from the hydrological driving forces of  $P$ ,  $R$ ,  $\nabla \cdot \vec{Q}$ ,  $ET_a$  and from ocean currents.

In order to identify the possible source responsible for the long-range correlation, an Empirical Orthogonal Functions (EOF) analysis is performed on a global ( $5^\circ \times 5^\circ$ ) grid of the GRACE mass derivative residuals.

$$\frac{dM_{\text{Res}}}{dt} = A = U\Sigma V^T = \sum_{j=1}^N \bar{u}_j \sigma_j \bar{v}_j^T \quad (4.21)$$

where  $U$  contains the eigenvectors of  $AA^T$ ,  $\Sigma$  is matrix showing the eigenvalues of matix  $AA^T$  in the diagonal and  $V$  consist of the eigenvectors of matix  $A^TA$ .

The singular value spectrum of the mass derivative residual  $\Sigma$  shows, that the mode number 1 is by far the most dominant contribution to  $dM/dt$  residual containing 8% of the whole variability (Figure 4.18). The principal component (PC) of EOF mode 1,  $U_{i,1}$ , shows a periodic variation. If the EOF analysis is

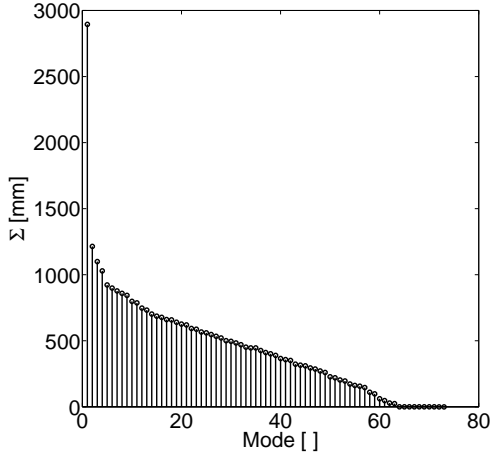


**Figure 4.18:** Singular value spectrum of mass derivative residual derived from EOF analysis

done for oceans and land masses separately, the resulting PCs are very similar to the PC of global EOF (Figure 4.19). This means, that EOF mode 1 represents a common signal component with no relation to hydrological and oceanographic driving forces, yet with long-range correlations over the globe.

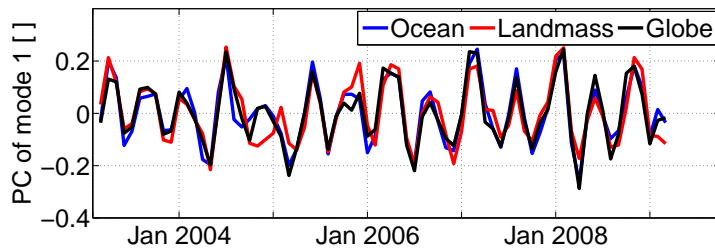


**Figure 4.19:** PCs of first mode of EOF analysis on Oceans (blue), landmasses (red) and global data set (black)

The spatial distribution of EOF mode 1,  $V_{i,1}$  (Figure 4.20) also shows an amplitude modulation by latitude as it is similarly found for the zonal averages.

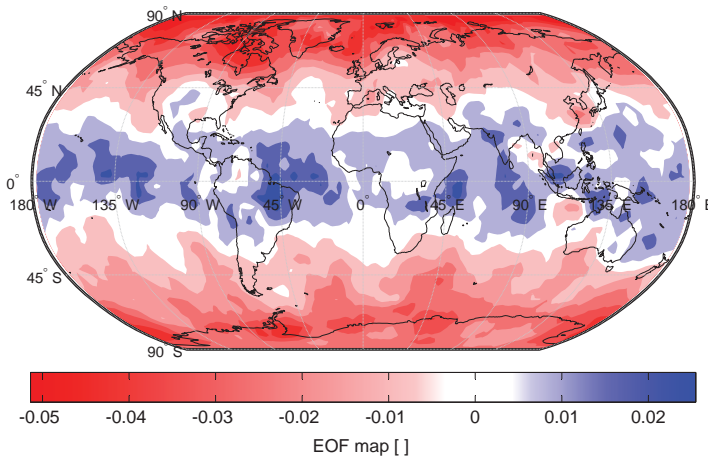


**Figure 4.20:** EOF map of mode number 1 derived from EOF analysis

The spatial distribution of EOF mode 1 does not show differences between ocean and land except for the Amazon, Congo, South-East Asia and Greenland. There EOF mode 1 and the ICC are close to zero, which means, that their residuals do not come from the common signal, but probably from climatic variations (not shown here).

If mode 1 of  $dM/dt$  residual is responsible for the ICC, its omission should remove the long-range correlation. Therefore, the new mass derivative residual can be constructed by

$$\frac{dM'_{\text{Res}}}{dt} = \sum_{j=2}^N \bar{u}_j \sigma_j \bar{v}_j^T \quad (4.22)$$

where  $N$  is the number of months and modes. Indeed, removing mode 1 leads to an IZC (Figure 4.21) and an ICC (Figure 4.22), for which the main long-range correlation structure is eliminated to a large extent.

Both IZC and ICC show, that neighborhood correlations have become dominant (for ICC round the reference point at  $85^\circ$  latitude). As there is still a kind of long-range correlation remaining for the IZC (in a very reduced form however), contributions from other EOF modes to the common signal cannot be excluded. However, cross checks with a selective removal of single EOF modes or their combinations did not lead to an improved reduction in IZC or ICC.

Therefore, EOF mode 1 of  $dM/dt$  residuals is the main contribution to ICC, and thus, mainly represents the correlated error, which effectively appears as error with respect to signals of hydrology, hydro-meteorology, oceanography and glaciology. The removal of the ICC mode leads to a decrease in long-range correlation, and thus, in total error (Figure 4.23). Especially for the high latitudes and the equatorial oceans a tremendous reduction in error amounting to 55% is achieved. The spatial distribution of the ratio of RMS in Figure 4.23 emphasizes the importance of ICC reduction with respect to noise especially for glaciology and oceanography.

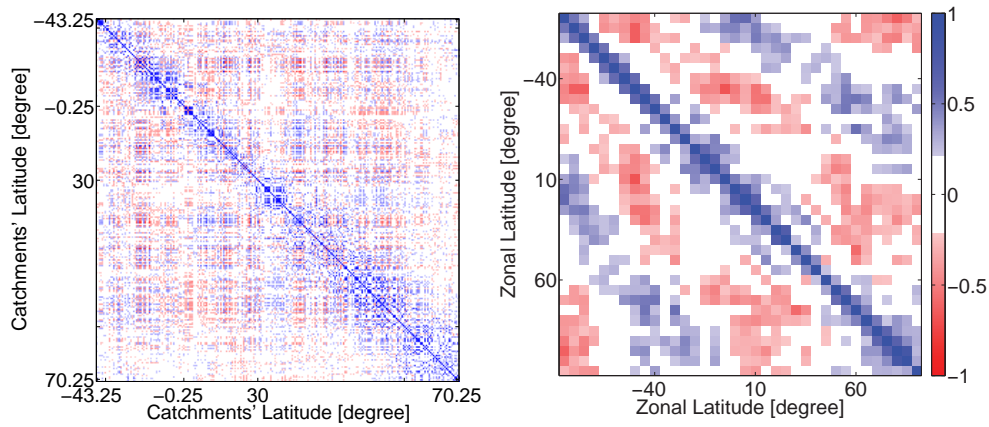


**Figure 4.21:** Left) IBC Right) IZC of  $dM/dt$  residual after reduction of mode 1 from the data set

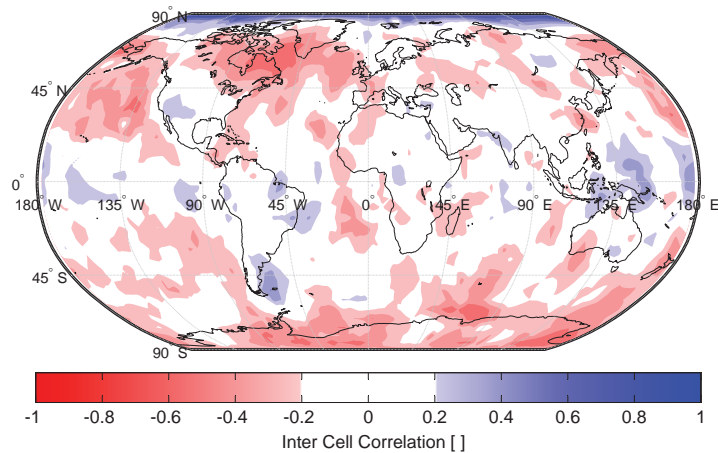


**Figure 4.22:** ICC of  $dM/dt$  residual with respect to a reference cell at  $\varphi = 87.5^\circ, \lambda = -177.5^\circ$  after reduction of mode 1 from the data set

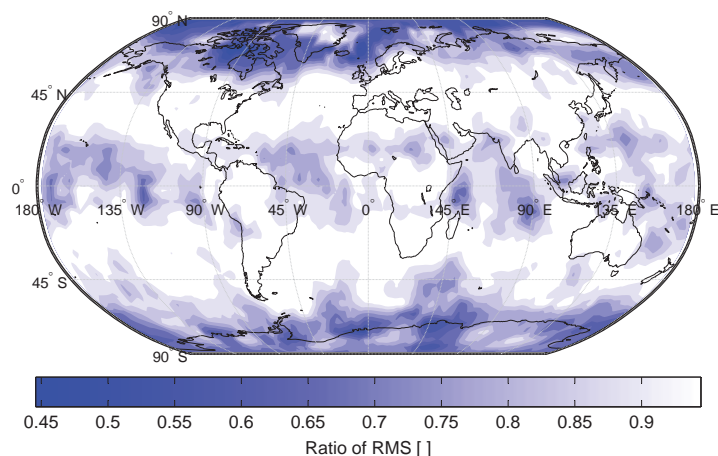


**Figure 4.23:** Ratio of RMS of monthly residuals before and after ICC reduction (after/before)

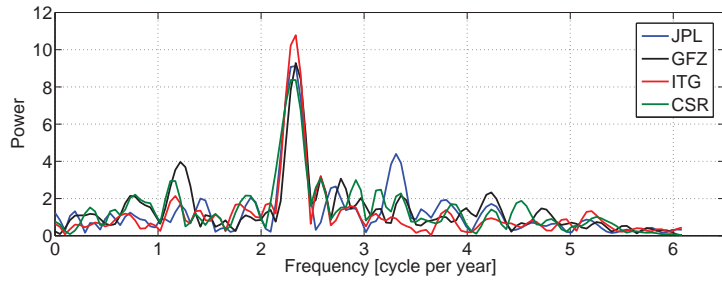


**Figure 4.24:** Estimated spectra of first  $m$  mode's PC from EOF analysis on GRACE residual for different GRACE data centers

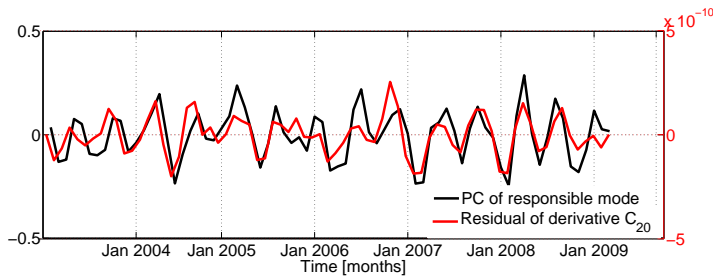


**Figure 4.25:** Comparison of PC of first mode from EOF analysis on  $dM/dt$  residual (GFZ) and a GRACE  $C_{20}$  time series

In order to find the dominant frequency in the obtained responsible PC, a spectral analysis using Fast Fourier Transform (FFT) method is performed. The resulting spectrum indicates a dominant frequency of 2.26 cycles per year (161 days). Figure 4.24 shows the spectra of responsible PCs of GRACE monthly solutions from different data centers. The dominant frequency of 2.26 cycles per year corresponds to the well known alias period of the S2 semi-diurnal solar tide (Chen et al., 2008a).

Many researches were devoted to scrutinize this frequency on the GRACE Level-1 & 2 data (Schrama et al., 2007; Seo et al., 2008; Han et al., 2005, 2007; Ray et al., 2003; Han et al., 2005; Ray and Luthcke, 2006; Seo et al., 2008). There, mainly low degree spherical harmonics and ocean tide models were targeted to cope with the S2 tidal aliasing error (Cheng and Ries, 2011). Chen and Wilson (2008) identified significant tidal alias errors, especially the S2 tide in the GRACE  $C_{20}$ .  $C_{20}$  is known to be one of the most problematic coefficients in GRACE monthly solutions. Therefore, the responsible PC obtained from EOF analysis is compared with the time derivative of GRACE  $C_{20}$ . Figure 4.25 shows this comparison, showing high correlation ( $r = 0.8$ ) between the first mode's PC and the derivative of  $C_{20}$ . This implies that the GRACE  $C_{20}$  is responsible for the long-range spatial correlation. This can also be demonstrated by looking at the computed ICC between mass derivative residuals on  $5^\circ \times 5^\circ$  grid with  $C_{20}$  excluded (Figure 4.26). In fact, what has been recognized as long-range spatial correlation error in the GRACE monthly residual is nothing else than the zonal behaviour of the GRACE  $C_{20}$  errors.

Looking at the GRACE and SLR  $C_{20}$  in the frequency domain expresses that the  $C_{20}$  of GRACE is considered as an error source because it contains tidal aliasing frequencies instead of white noise (flat spectrum).

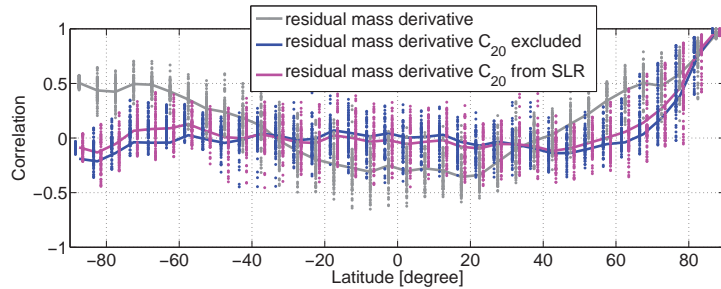


**Figure 4.26:** Inter Cell Correlation of GRACE residual mass derivative with respect to a reference cell at  $\phi = 87.5^\circ, \lambda = -177.5^\circ$

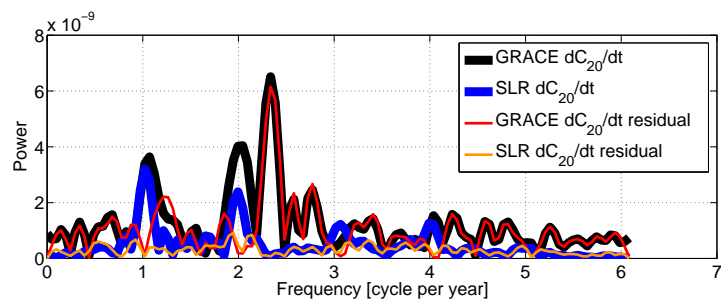


**Figure 4.27:** Comparison of derivative of  $C_{20}$  and its residual spectra from GRACE and SLR

Figure 4.27 shows the spectra of both the derivative of  $C_{20}$  time series  $dC_{20}/dt$  and its residual. As expected the spectrum of derivative of  $C_{20}$  residual does not show the seasonal behaviour as it is the case for derivative of the  $C_{20}$ . In other words, the residual highlights the long-range spatial correlation because the dominance of the seasonal behaviour has been taken out. This is better explained by comparing the mentioned spectra with the relevant spectra of  $C_{20}$  from SLR. The spectrum of GRACE  $C_{20}$  residual contains frequencies 1.13 and 2.26 cycles per year which are the tidal aliasing frequencies of P1 and S2, respectively. On the other hand, the derivative of the  $C_{20}$  from the SLR is mainly dominated by the annual behaviour which leads to a flat spectrum of its residual without any dominant tidal aliasing frequencies (Figure 4.27).

The long-range correlation reveals that the GRACE monthly solutions are contaminated by tidal aliasing error, although the de-aliasing procedure attempts to eliminate their effect. In fact, as other coefficients and not only  $C_{20}$  can be also contaminated by the aliasing error, simply replacing the GRACE  $C_{20}$  coefficient with the SLR coefficient does not address the full aliasing problem. Therefore, to reduce the uncertainties in GRACE monthly solutions, tidal aliasing errors should be extensively investigated and removed from the data set.

### 4.4.3 Tidal aliasing error

Aliasing derives from undersampling of the mass motions from GRACE's orbital configuration. Sampling of the tide is influenced by the ascending node rate of the orbit plane relative to the tide-generating body (Melachroinos et al., 2009). The ascending node precesses due to a secular perturbation from the zonal harmonics, mainly by  $C_{20}$  (Kaula, 2000; Brown, 2002) (Figure 4.28):

$$\dot{\Omega} = \frac{3nC_{20}a_E^2}{2(1-e^2)^2a^2} \cos I \quad (4.23)$$

where,  $n$  is the angular velocity,  $e$  is the eccentricity,  $a_E$  is the semi-major axis of ellipsoid,  $a$  is the semi major axis of the satellite orbit and  $I$  is the inclination of the satellite.

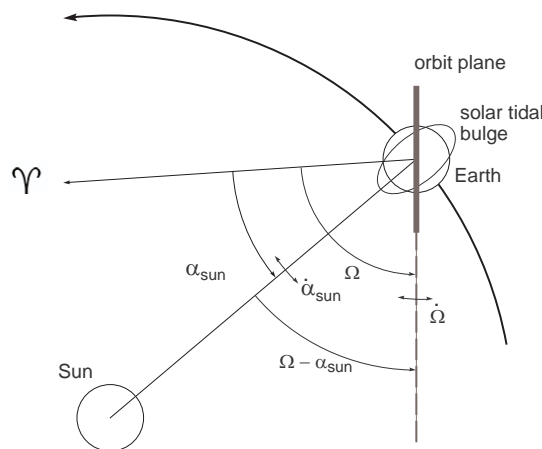


**Figure 4.28:** Two-dimensional geometry of the Earth, Sun and GRACE's orbit. The secular perturbation of the ascending node varies between  $1.115^\circ$ – $1.122^\circ$  per day

The secular perturbation of the ascending node with respect to the sun can then be estimated by computing the  $\dot{\alpha} - \dot{\Omega}$ .  $\dot{\alpha}$  for a day can be estimated by the  $360^\circ/(days\ of\ a\ sidereal\ year) = 360^\circ/365.256$ , which is equal to 0.985. In this study  $\dot{\Omega}$  is computed using equation (4.23) and observed orbital elements of the GRACE, i.e.  $a$ ,  $e$ ,  $I$ , which are available from <http://celestrak.com> (Kelso, 2000). As a second variant, the  $\dot{\Omega}$  can be also estimated by the observed  $\Omega$ , which is less accurate than first method. In both methods the  $C_{20}$  can be used from a Geodetic Reference System (GRS) or estimated from GRACE. However, as it is known that GRACE  $C_{20}$  is poorly estimated, this study uses the  $C_{20}$  from GRS80.

The estimated secular rate of the ascending node varies between  $1.115^\circ$ – $1.122^\circ$  per day (Figure 4.29) during GRACE's life time. This secular rate in the ascending node leads to a nodal day  $\simeq 23.92$  h. Figure 4.30 schematically demonstrates how a 23.92 h sampling of the S2 tidal wave leads to a long-period alias. Based on the nodal day, the aliasing frequency of the tidal constituents can be computed:

$$\Delta\Phi_{S_2} = \overbrace{\frac{24}{2}}^{\text{solar day}} - \overbrace{\frac{23.9256}{2}}^{\text{GRACE nodal day}} = 0.0371\text{ h} \quad (4.24)$$

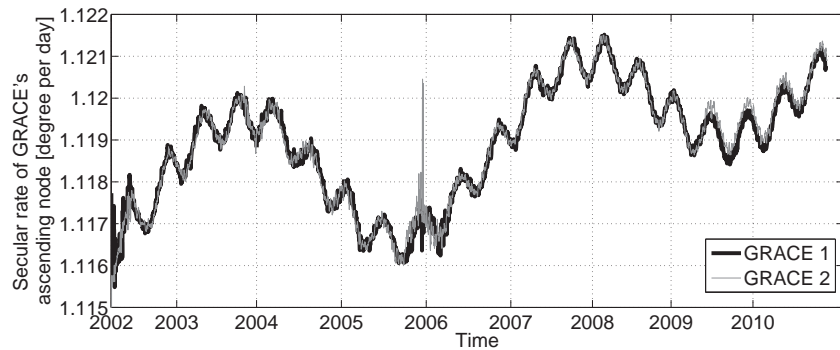


**Figure 4.29:** The secular rate of the ascending node of GRACE's orbit using the observed  $a, e, I$  of satellites and  $C_{20}$  from GRS80

$$\text{Required cycles to span} = \frac{\overbrace{T_{S2}}^{\text{period of S2 tide}}}{\Delta\Phi} = \frac{12 \text{ h}}{0.0371 \text{ h}} = 323.46 \quad (4.25)$$

$$\text{S2 tidal alias period} = 323.46 \times \frac{1}{2} \text{ day} = 161.8 \text{ days} \quad (4.26)$$

Following the formulation, the estimated primary tidal aliasing frequencies for the main tidal constituents are listed in Table 4.4.3. Among the main tidal constituents, S1, S2, P1, K1 and K2 have alias periods

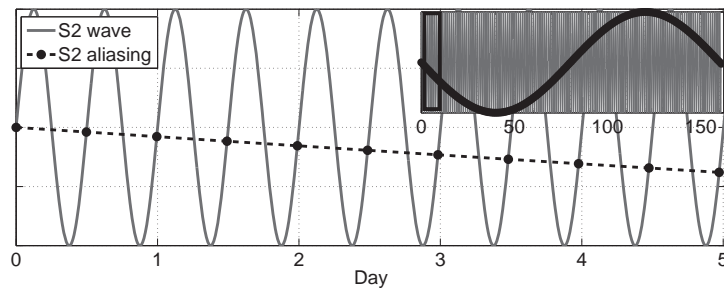


**Figure 4.30:** Sampling of S2 tide where the difference ( $\Delta\Phi$ ) between the satellite's nodal day  $\approx 23.92$  hour and one solar day 24 hour cause the aliasing error.

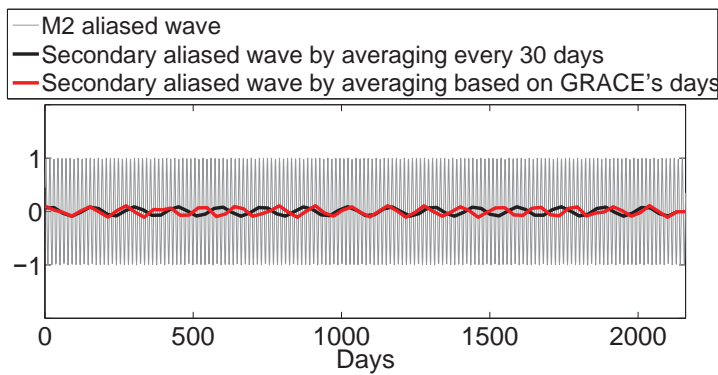
longer than 30 days and thus do not average out in the monthly solutions data. These aliases have to be removed from the GRACE monthly solutions.

As a secondary effect, the averaging procedure that provides the monthly solutions leads to a so-called secondary aliasing for the tidal constituents of M2, O2, O1 and Q1 with tidal aliasing error of less than 30. In fact, the secondary aliasing occurs by monthly sampling or averaging of the wave with the primary aliased frequency. Seo et al. (2008) investigated the effect of monthly sampling and concluded an aliased period of 140 days for the M2 tidal constituent. They assumed an exact 30 days sampling for monthly averaging. Actually, the monthly averaging of GRACE is an uneven sampling as it is carried out based on the availability of data within a calendar month. It varies between 27–31 days which leads to different behaviour for the secondary aliased wave. Figure 4.31 shows a simulated aliased wave of M2

**Table 4.2:** The estimated tidal aliasing period for the main tidal constituents

| Tidal constituent | Period [day] | Alias [day] |
|-------------------|--------------|-------------|
| M2                | 0.5175       | 13.6        |
| S1                | 1.0000       | 321.7       |
| S2                | 0.5000       | 160.8       |
| N2                | 0.5274       | 9.1         |
| K2                | 0.4986       | 1618.3      |
| K1                | 0.9973       | 2443.8      |
| O1                | 1.0758       | 13.6        |
| P1                | 1.0028       | 169.7       |
| Q1                | 1.1195       | 9.1         |

tide with period of 13.6 days, which will be aliased to a lower frequency wave with reduced amplitude after monthly averaging. The obtained secondary wave by assuming 30 days sampling is different than the one obtained by using GRACE's real averaging interval. For M2, the secondary wave's amplitude reduces by factor of ca. 0.09 of the M2 primary aliased wave's amplitude.

**Figure 4.31:** A simulated aliased wave of M2 tide with period of 13.6 days which is aliased to different waves by assuming 30 days sampling or using GRACE's days for averaging

In order to assess the effect of tidal aliasing error, first the frequency at which the secondary tidal aliasing occurs should be defined. As GRACE provides unevenly sampled data, the Lomb-Scargle method is employed to obtain the spectrum (Lomb, 1976). Figure 4.32 shows the spectra from the Lomb-Scargle method over the secondary aliased wave of M2. It indicates that the M2 secondary aliased period is 125.15 days, while in case of assuming equally sampled data the period is 146.37 days. Although within the monthly averaging the primary aliasing periods of S1, S2 and P1 do not change due to the Nyquist theorem, their amplitudes reduce by factors of ca. 0.99, 0.95 and 0.95, respectively.

Table 4.4.3 shows the secondary alias periods of M2, N2, O1 and Q1 together with the amplitude factor for each of the tidal constituents. The primary and secondary aliased periods of M2 and O1 are close to each other, similar for the N2 and Q1. The results express that the effect of the original tidal errors of M2, N2, O1 and Q1 are reduced by the factors of ca. 0.08 in the GRACE monthly solutions. However,

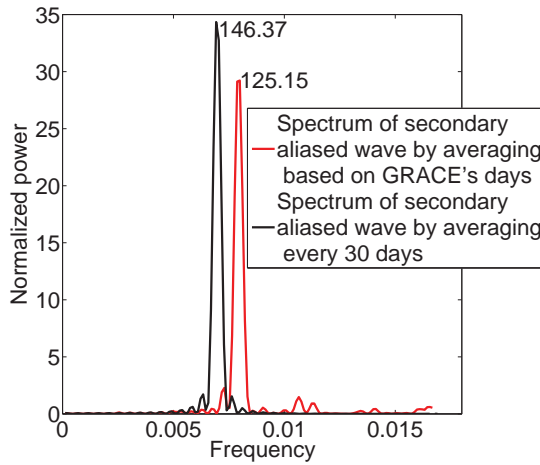


**Figure 4.32:** Spectra of the M2 secondary aliased wave. The red spectrum belongs to the aliased wave by averaging based on the GRACE's days and the black curve shows the spectrum of the secondary aliased wave by averaging on an even sampling of 30 days

**Table 4.3:** The secondary aliased period of the M2, N2, O1 and Q1 together with the amplitude factor for each of the tidal constituents

| Tidal constituent | Period [day] | Primary alias [day] | Secondary alias [day] | Amplitude factor |
|-------------------|--------------|---------------------|-----------------------|------------------|
| M2                | 0.5175       | 13.6                | 125.2                 | 0.09             |
| N2                | 0.5274       | 9.1                 | 89.03                 | 0.08             |
| O1                | 1.0758       | 13.6                | 130.8                 | 0.08             |
| Q1                | 1.1195       | 9.1                 | 90.9                  | 0.08             |

given large tidal errors in tide models one can expect that even the reduced effects in monthly solutions deteriorate the water storage changes provided by GRACE. Therefore, all the effects of remaining tidal aliasing errors should be quantified and removed from the GRACE monthly solutions.

#### 4.4.3.1 Removing the effect of tidal aliasing error

As it has been shown in Figure 4.8, the residuals of GRACE monthly solutions do not contain any seasonal variation. This characteristic encourages removing the effect of tidal aliasing error from the residual instead of the signal of GRACE monthly solution, which particularly helps to avoid mixing the real seasonal variation with the tidal error.

Hence, a parametric model of  $y = Ax + e$  can be defined

$$\Delta M_{\text{Res}}(t) = a_1 t + \sum_{i \in \text{TA}} a_i \cos(\omega_i t) + b_i \sin(\omega_i t), \quad (4.27)$$

where  $\Delta M_{\text{Res}}(t)$  is the residual of mass change from GRACE monthly solution. Similar models can be defined for the residual time series of spherical harmonic coefficients  $\Delta C_{lm}(t)$ ,  $\Delta S_{lm}(t)$ .  $a_1$  is the coefficient of trend,  $\omega_i$  is the tidal aliasing angular frequency and  $a_i$  and  $b_i$  are the unknown coefficients of the model. By performing a least squares analysis over the spherical harmonics coefficients or  $0.5^\circ \times 0.5^\circ$  grid based data set of  $\Delta M_{\text{Res}}(t)$ , the unknown coefficients are obtained. The amplitude of each tidal aliasing error representing the error level is then calculated by

$$c_i = \sqrt{a_i^2 + b_i^2} . \quad (4.28)$$

Among the tidal constituents, the tidal aliasing periods of K1 and K2 are ca. 6.7 and 4.5 years, respectively. As the length of GRACE time series is not long enough for extracting the effect of K1 and K2, the model can be only performed for the primary aliasing frequencies of S1, S2 and P1 together with the secondary aliasing frequencies of M2, N2, O1 and Q1, then TA={S1, S2, P1, M2, N2, O1 and Q1}.

By solving the model using least squares estimation, the covariance matrix of estimator can be computed as  $Q_{\hat{x}} = (A^T A)^{-1}$ , which represents the variances of the estimated tidal error in the diagonal and covariances of them in non-diagonal elements. As expected the estimated coefficients for N2 and Q1 show strong covariance as their aliasing period are similar to each other. This means that the estimated coefficients for N2 smears with the tidal error effect from Q1 and vice versa (Figure 4.33). This also occurs for M2/O1 and P1/S2 with lower covariance.

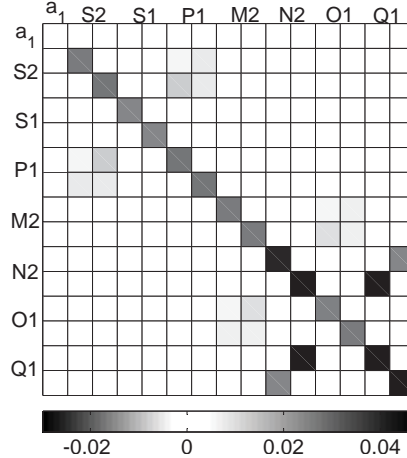


**Figure 4.33:** Covariance matrix of estimation of tidal aliasing coefficients for the primary aliasing frequencies of S1, S2 and P1 together with the secondary aliasing frequencies of M2, N2, O1 and Q1

Figure 4.34 shows the estimated amplitudes  $c$  of the tidal aliasing errors over the spherical harmonic coefficients of GRACE release 5. For all of the tidal aliasing errors the main contamination occurs on high (degree and) order coefficients. However, low degree coefficients are also contaminated by tidal aliasing errors mainly by primary aliasing errors of S2, S1 and P1. This is highlighted in the Figure 4.35, where the degree variance of three primary aliasing error of S2, S1 and P1 are higher than the degree variance of secondary aliasing errors of M2, N2, O1 and Q1. Also the degree variance for the RMS of

the residuals of spherical harmonic coefficients is depicted, which defines an upper bound for the GRACE error. The comparison between the degree variances show that the contribution of tidal aliasing errors

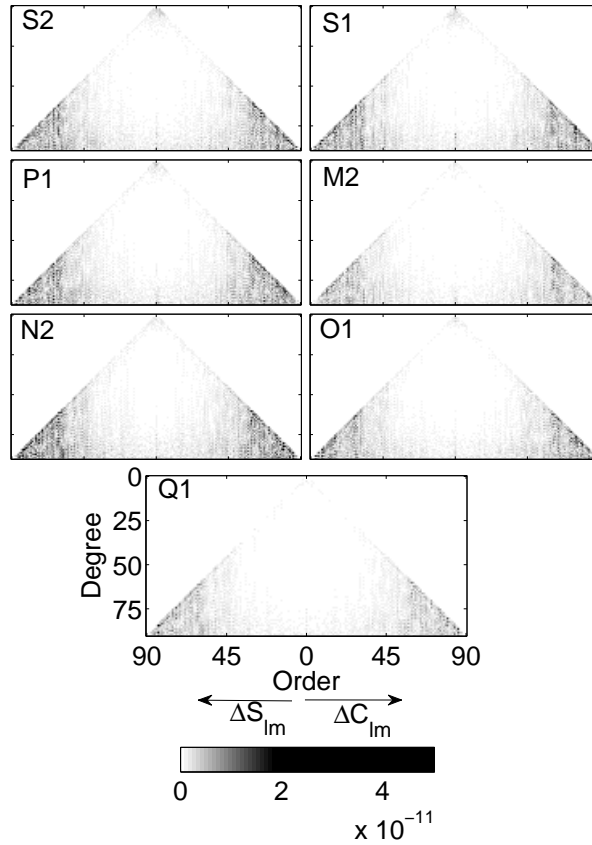


**Figure 4.34:** Estimated amplitude for primary aliasing errors of S2, S1 and P1 and secondary aliasing errors of M2, N2, O1 and Q1 over the spherical harmonic coefficients of GRACE RL05

for the total GRACE error varies between 3%–12%.

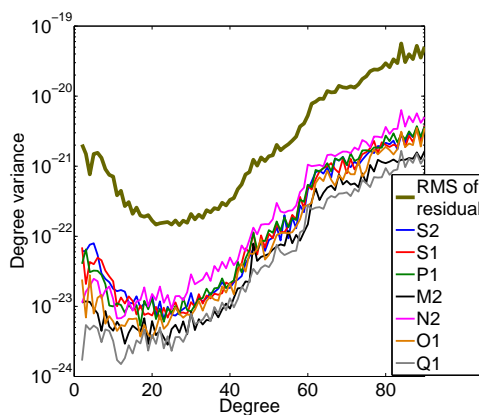


**Figure 4.35:** Degree variance of different tidal aliasing error in GRACE RL05 monthly solutions

The obtained spatial distributions of the S1, S2 and P1 primary aliasing in Figure 4.36 indicate amplitudes of up to 21.4, 13.8, and 14.8mm errors around the world, respectively. The obtained errors for S1 and P1 is similar to the errors of these tidal aliasing frequency in the GRACE release 4 monthly solutions. For S2, the comparison of errors in GRACE release 4 and 5 reveals that the error drastically decreased from the maximum amplitude of ca. 30mm to 13.8 mm due to the corrected  $C_{20}$  in GRACE release 5. The correction of  $C_{20}$  particularly led to removing the S2 tidal aliasing error in Northern part of Australia, which was addressed in previous studies e.g. (Melachroinos et al., 2009).

In general, the errors of the primary tidal aliasing of S1, S2 and P1 are mainly distributed at high northern and southern latitudes, where it is known that the ocean tide models are poorly determined. However, the errors also occur over the landmasses, which might be due to discretization error during de-aliasing procedure.

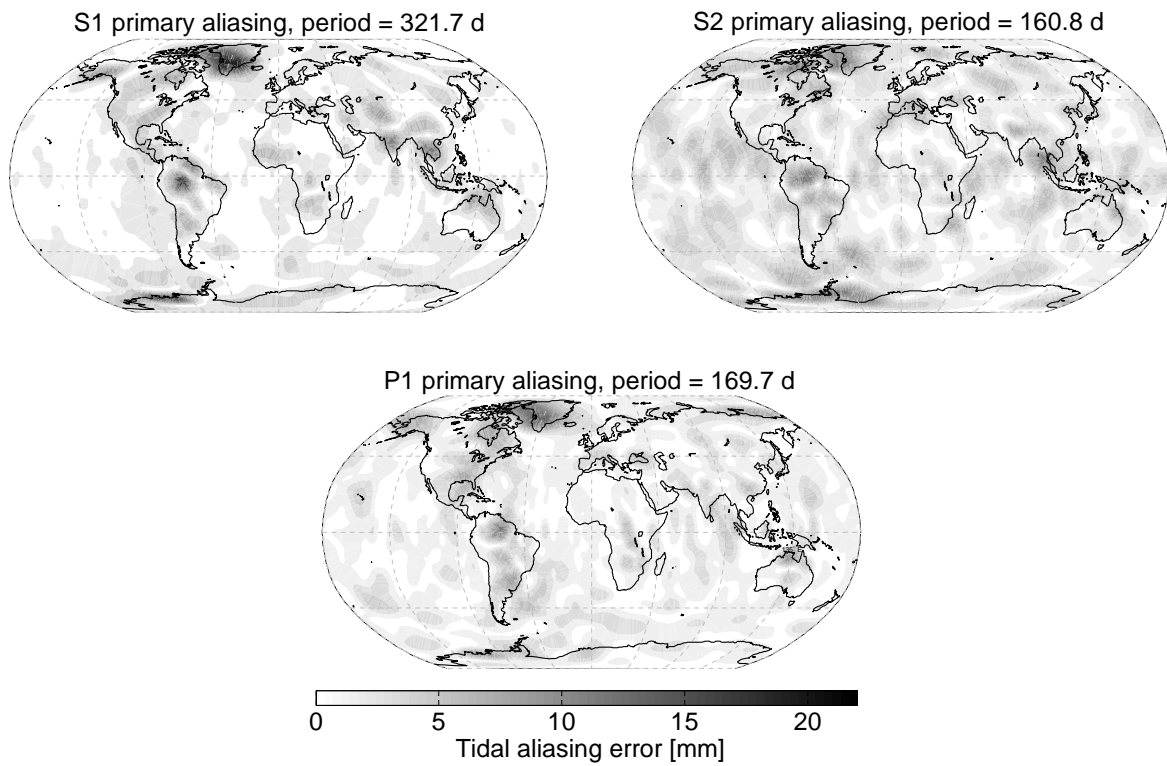


**Figure 4.36:** Amplitudes (mm) of the primary tidal aliasing frequencies S2, S1 and P1 from 72 GFZ RL05 monthly solutions

Similar to the primary tidal aliasing, the M2, N2, O1 and Q1 secondary tidal aliasing errors also show higher amplitudes in northern and southern regions (Figure 4.41). However, as expected their amplitudes are lower in comparison to the primary aliasing errors. The estimated error for the M2 tide, for instance, varies between 0–7.8 mm and is mainly distributed above and below the  $\pm 66^\circ$  latitude, in which the ocean tide is poorly modeled due to the lack of altimetry data. In fact, the estimated error for the secondary aliasing frequency corresponds to the reduced original tidal error of GRACE observations (Figure 4.31).

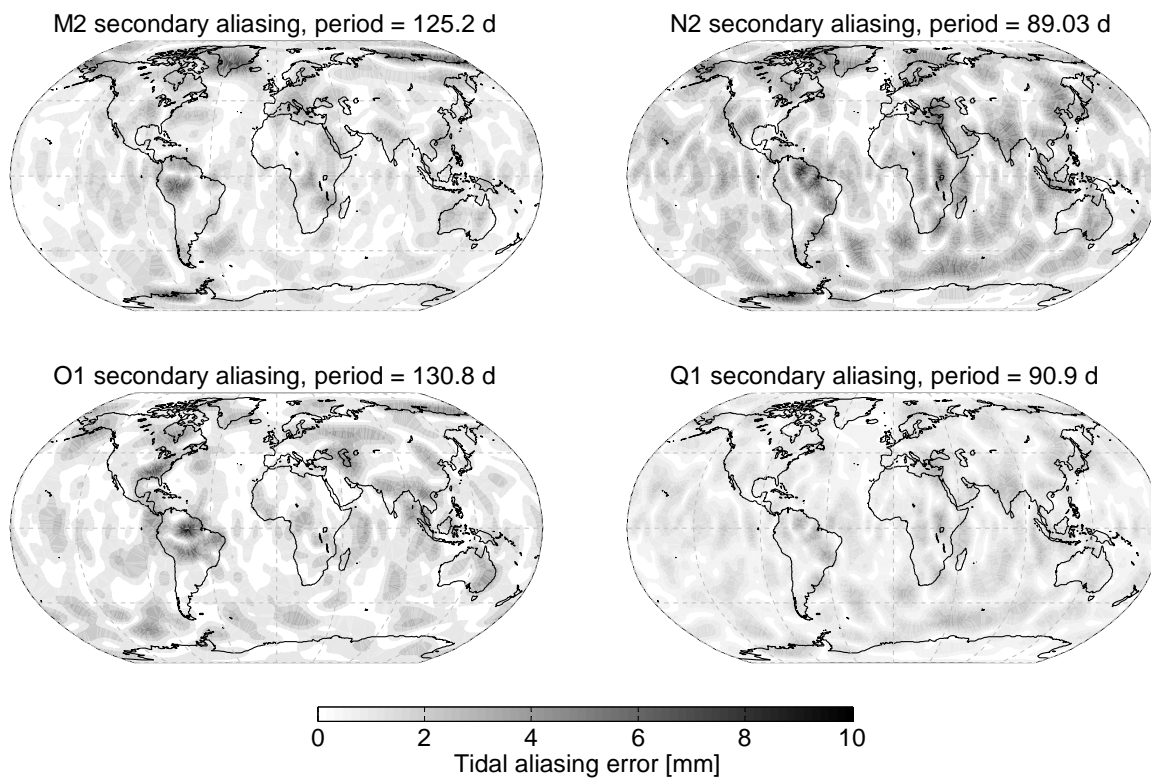


**Figure 4.37:** Amplitudes (mm) of the secondary tidal aliasing frequencies M2, N2, O1 and Q1 from 72 GFZ RL05 monthly solutions

In other words, the contribution of M2 tidal error in the GRACE observations before averaging is up to ca. 79 mm ( $\frac{7.8}{0.09}$ ), which reduces within the monthly averaging (Table 4.4). The errors of N2, O1 and Q1 reach up to levels of 9.4, 10 and 4 mm for GRACE monthly solutions, as listed in Table 4.4. The errors in monthly solutions imply maximum errors of 117, 125 and 50 mm in GRACE observations before monthly averaging.

**Table 4.4:** The results of estimation of the effects of primary and secondary tidal aliasing errors in GRACE monthly solutions and accordingly in GRACE solutions

|           | Tidal constituent | Aliasing period [day] | Extracted amplitude [mm] | Amplitude scale | Error in GRACE [mm] |
|-----------|-------------------|-----------------------|--------------------------|-----------------|---------------------|
| Primary   | S1                | 321.7                 | 0–21.4                   | 0.99            | 0–22                |
|           | S2                | 160.8                 | 0–13.8                   | 0.95            | 0–14                |
|           | P1                | 169.7                 | 0–14.8                   | 0.95            | 0–15                |
| Secondary | M2                | 125.2                 | 0–7.8                    | 0.09            | 0–79                |
|           | N2                | 89.03                 | 0–9.4                    | 0.08            | 0–117               |
|           | O1                | 130.8                 | 0–10.0                   | 0.08            | 0–125               |
|           | Q1                | 90.9                  | 0–4.0                    | 0.08            | 0–50                |

The relatively high contributions of tidal aliasing errors of M2, N2, O1 and Q1 in GRACE observations and their sources should be investigated. As in the de-aliasing procedure, attempts to remove the effects of ocean tides using the ocean tide models are made. The quality of the ocean tide model has a direct impact on the GRACE solutions and ocean tide model errors are a likely source for the remaining tidal aliasing error in GRACE solutions.

The ocean tide can be modeled in different ways and the result of modeling is not unique. For instance, for models like CSR and GOT (Ray, 1999), altimetric data is analyzed to extract various tidal signals. On the other hand, in models like FES95.2 (LeProvost et al., 1994) and ICOM hydrodynamic equations are used for tidal modeling. The ocean tide can be also modeled by assimilating the observed tidal data e.g. altimetry and coastal and pelagic tide gauges. NAO99 (Matsumoto et al., 2000), FES2004 (Lyard et al.), CSR4.0 (Eanes and Bettadpur, 1996), EOT08a and EOT10 (Bosch et al., 2009) are examples of assimilated models. Therefore, comparing different tide models can reveal potentially problematic regions for ocean tide modeling. The comparison also quantifies the level of possible errors, which directly lead to tidal aliasing error in GRACE solutions.

Here, the models of FES2004, CSR4.0 , NAO.99b and EOT10a are selected for comparison of different tidal constituents models. Figure 4.38 shows the differences between the M2 amplitude from four ocean models of FES2004, CSR.04 , NAO.99b and EOT10a above the 60° latitude in the range of -80 to 80 mm. As the EOT10a model was obtained by means of residual harmonic analysis of multi-mission altimeter data with respect to FES2004 (Bosch et al., 2009), its difference from CSR4.0 and NAO.99b models are similar to the respective differences from FES2004 and not shown here. The maps of differences indicate that the M2 tide models are mainly problematic in the Baffin Bay, Northwestern passages, Hudson Bay and southern parts of Arctic Ocean. On the other hand, the estimated M2 tidal aliasing error from GRACE monthly solution also shows ca. 8 mm of error over the southern parts of Arctic oceans and Greenland. As discussed before, this 8 mm corresponds to some larger error of 79 mm in the GRACE solutions before monthly averaging. The ocean tide model differences in Figure 4.38 does not follow similar pattern, yet the distributions of error in different models give rise to the belief that the ocean tide models in high latitudes are problematic. The problematic ocean tide models lead to the tidal error in GRACE, which is shown in Figure 4.38 for M2 tide. Although the spatial distribution of M2 tidal error does not match perfectly with the ocean tide model differences, similar range of error nominates the mis-modeling of ocean tide models as the reason for the tidal aliasing error in GRACE monthly solutions. Moreover, as within the de-aliasing procedure, the ocean tide model are used in the form of spherical harmonics. Contamination of landmasses by ocean tidal error is expected, which would explain the Greenland M2 tidal error.

Similar to the situation for the arctic region, the ocean tide models also show certain differences around the antarctic regions with the exception of the EOT10a and FES2004 models, which show ca. 0 mm difference in amplitude. The pattern of difference between models reveal that the coastal antarctic regions are problematic, which is also appeared to be deteriorated by M2 tidal error in GRACE monthly solutions.

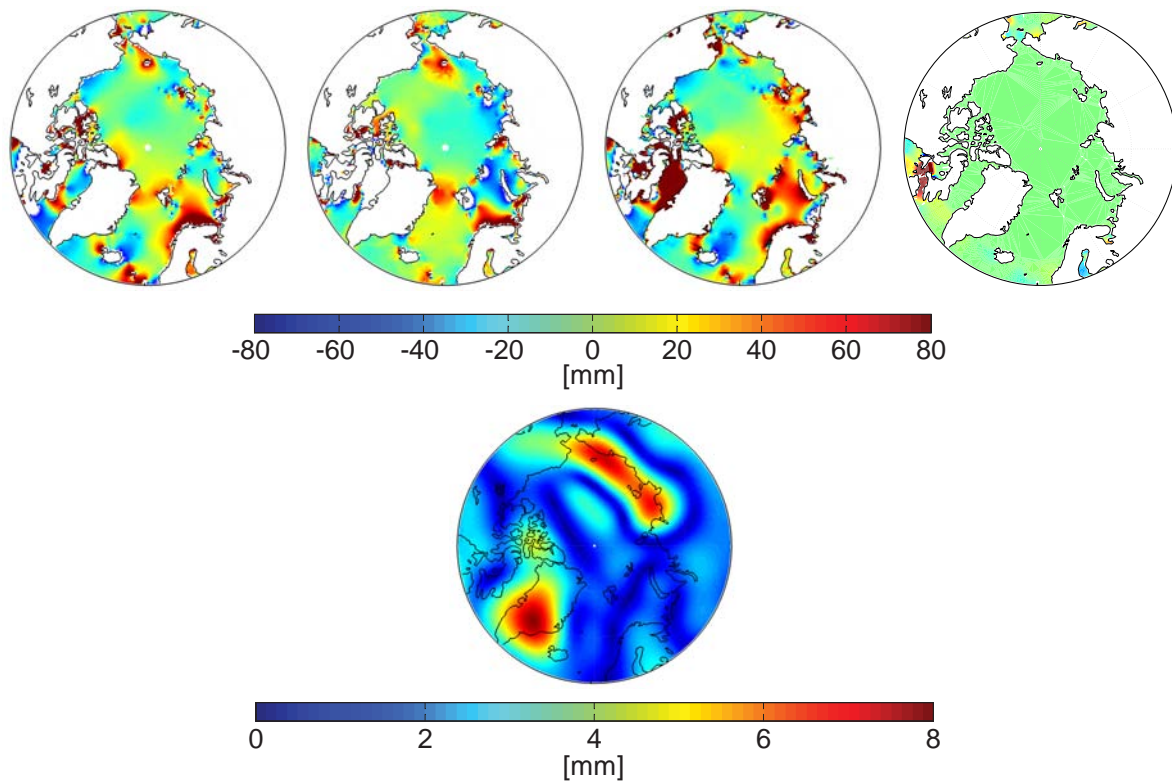


**Figure 4.38:** Top panel) M2 tidal model difference above  $60^{\circ}$  latitude. From left to right, FES2004–CSR.04, FES2004–NAO.99b, CSR.04–NAO.99b and EOT10a–FES2004. Bottom panel) The estimated secondary aliased M2 tide in GRACE monthly solutions, which corresponds up to ca. 79 mm of M2 tidal error in the GRACE solutions before averaging.

Again, similar ranges of tidal error in GRACE data and difference in ocean tide models highlight the ocean tide mis-modeling as a reason for the remaining tidal aliasing error in the GRACE monthly solutions.

#### 4.4.3.2 Impacts of removing tidal aliasing errors

Apart from the discussion of possible sources for the tidal aliasing errors and inaccuracy of the ocean tide models, the impact of removing the effect of tidal aliasing errors from the GRACE monthly solutions should be studied. The RMS value of the total tidal aliasing error represents the level of this error in the GRACE monthly solution. Figure 4.40 shows the RMS map of the total tidal aliasing errors including the errors of tidal constituents S1, S2, P1, M2, O2, O1 and Q1. The error contributes to the GRACE monthly solution up to 20 mm/month around the world. The relative high RMS values over Greenland, the Amazon, Congo, Mississippi, Hudson Bay, Kuskokwim River, Susitna River, Mekong River, Godavari, Ganges, Laptev and East Siberian sea emphasize the signature of tidal aliasing error in GRACE monthly solutions.

In order to quantify the impact and being sure that tidal aliasing error removal does not deteriorate signal, two quantities are computed: correlation and RMSE. The correlation of water storage changes

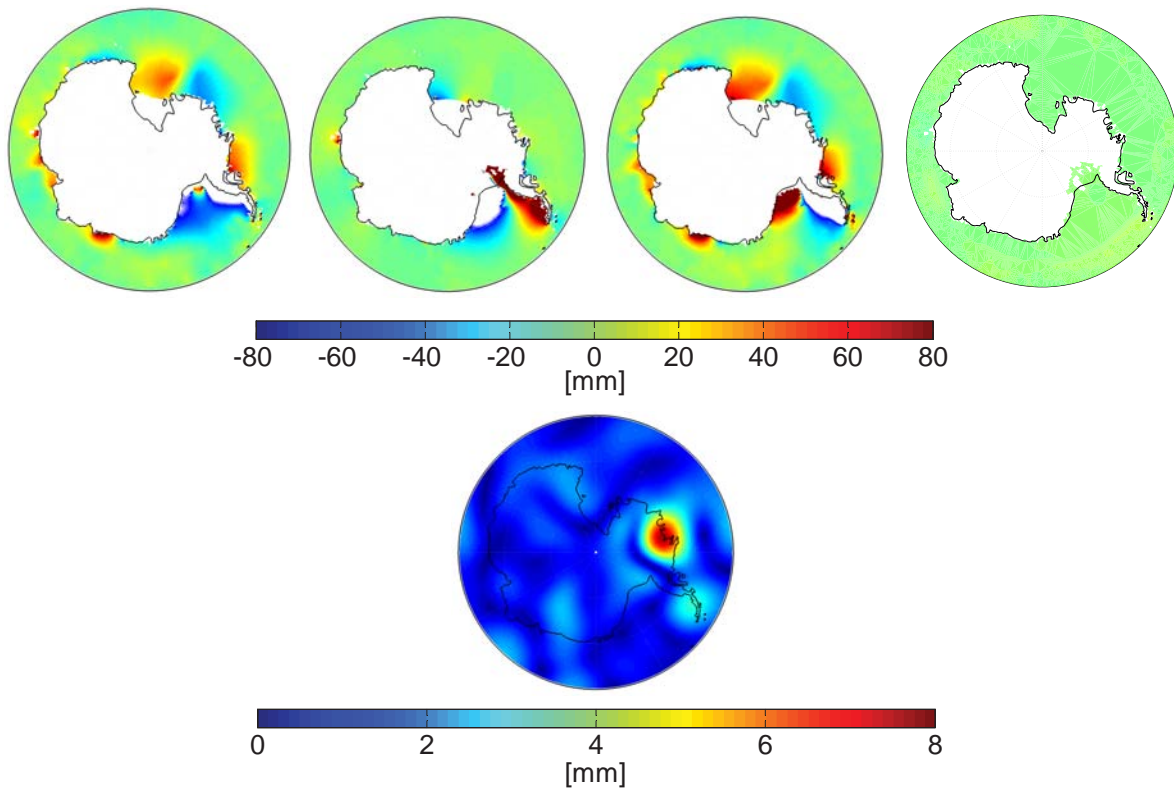


**Figure 4.39:** Top pannel) M2 tidal model differences below  $-60^{\circ}$  latitude. Top left) FES2004–CSR.04, top right) FES2004–NAO.99b bottom) CSR.04–NAO.99b. Bottom panel) The estimated secondary aliased M2 tide in GRACE monthly solution, which corresponds up to ca. 79 mm of M2 tidal error in the GRACE solutions before averaging.

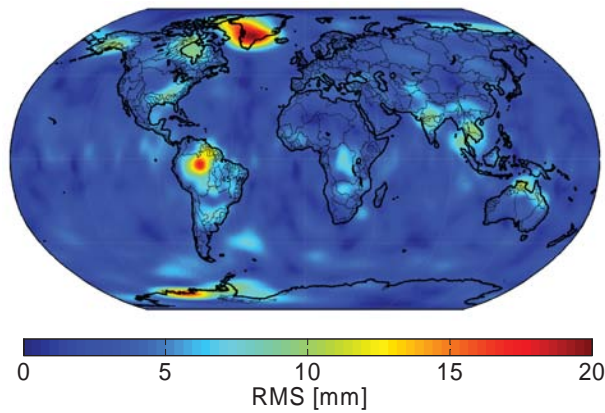


**Figure 4.40:** RMS of the total tidal aliasing errors including primary and secondary

from GRACE with hydro-meteorological water storage change is computed before and after removing the tidal aliasing error. Also, the RMSE of the hydro-meteorological and GRACE water storage change represent the error budget of GRACE before and after of removing the errors. In addition, the signal to

noise ratio (SNR) is computed by dividing the RMS of GRACE monthly time series to the RMS of residual of GRACE monthly time series

$$\text{SNR} = \frac{\text{RMS}(dM/dt)}{\text{RMS}(dM_{\text{Res}}/dt)} \quad (4.29)$$

Figure 4.41 shows the computed SNR after vs. before removing tidal aliasing error for the 255 largest catchments around the globe, indicating a systematic improvement in the SNR.

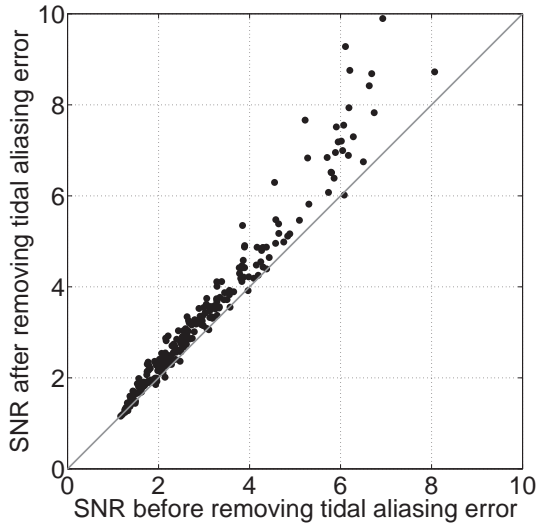


**Figure 4.41:** Signal to Noise Ratio (SNR) after removing tidal aliasing errors versus before removing over 255 largest catchments, in which each dot represents a catchment

Table 4.5 shows the computed correlation, RMSE and SNR for the catchments of the Amazon, Congo, Mississippi, Kuskokwim River and Western Australia, for which the tidal aliasing error is relatively high. The results indicate that removing tidal aliasing error from GRACE monthly solutions improves the solutions toward being more consistent with the hydro-meteorological water storage change. Indeed, as the water storage time series over a catchment are the results of aggregation over the whole catchment, the error is expected to be reduced. This is specially represented in the time series of water storage change (e.g. Western Australia in Figure 4.42), in which the time series of before and after are very similar to each other. However, even small changes in the time series have led to a better correlation, a lower RMSE and a better SNR.

As Figure 4.40 demonstrates, the maximum tidal aliasing error occurs over Greenland, where the investigation into its ice mass loss plays an important role for climatic studies (Sasgen et al., 2012; Liu et al., 2012). Therefore, it is important to study the impact of removing tidal aliasing error on the time series of equivalent water height. Figure 4.43 shows Greenland drainage divides developed by the Goddard Ice Altimetry Group from ICESat data. These drainage systems identify homogeneous regions in terms of surface slope orientation relative to atmosphere advection (Zwally et al., 2012).

The aggregated time series of equivalent water height over each of the drainage basins before and after removing the tidal aliasing error delineate the effect of the error. However, as the trend is known to be

**Table 4.5:** Quantification of impact of removing tidal aliasing error over the Amazon, Congo, Mississippi, Kuskokwim River and Western Australia catchment

| Catchment         |                 | Before<br>removing error | After<br>removing error |
|-------------------|-----------------|--------------------------|-------------------------|
| Amazon            | corr.           | 0.96                     | 0.96                    |
|                   | RMSE [mm/month] | 24.3                     | 23.7                    |
|                   | SNR             | 6.7                      | 7.8                     |
| Congo             | corr.           | 0.84                     | 0.86                    |
|                   | RMSE [mm/month] | 39.4                     | 39.0                    |
|                   | SNR             | 2.5                      | 3.0                     |
| Mississippi       | corr.           | 0.87                     | 0.89                    |
|                   | RMSE [mm/month] | 14.9                     | 14.5                    |
|                   | SNR             | 2.9                      | 3.5                     |
| Kuskokwim River   | corr.           | 0.74                     | 0.78                    |
|                   | RMSE [mm/month] | 18.4                     | 17.2                    |
|                   | SNR             | 3.1                      | 3.3                     |
| Western Australia | corr.           | 0.78                     | 0.82                    |
|                   | RMSE [mm/month] | 7.6                      | 7.3                     |
|                   | SNR             | 2.7                      | 3.3                     |

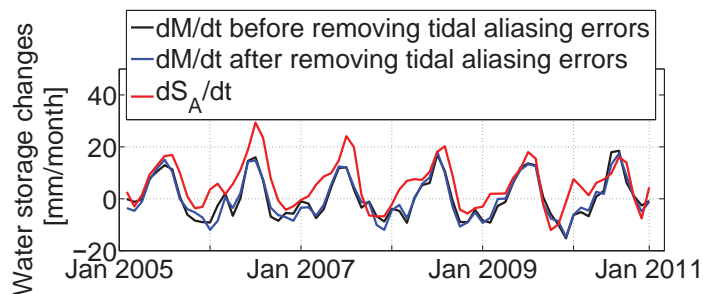


**Figure 4.42:** The water storage change  $dM/dt$  from GRACE before and after removing tidal aliasing error in comparison with the hydro-meteorological water storage change over Western Australia. The correlation improves after removing the tidal aliasing error from 0.78 to 0.82 and the RMSE decrease from 7.6 to 7.3 mm/month

the dominating component in Greenland for long-term analysis, GRACE data should be corrected for post glacial rebound. In essence, post glacial rebound produces long term trends in the Earth's gravity field as a result of the redistribution of lithospheric masses, rebounding from the glacial loading of the last ice age (Peltier, 1994). Therefore, the model developed by Paulson et al. (2007) is used to remove the effect of post glacial rebound. Figure 4.44 illustrates the post glacial rebound in mm/yr of equivalent water height, which varies between  $-20\text{--}64\text{ mm/yr}$  over the globe.

After correcting GRACE mass estimates for post glacial rebound the trend is computed using the real GRACE sampling intervals. The results of trend computation over drainage basins of Greenland for the time period of 2005–2011 reveal that the change in the trend is not significant after removing the tidal

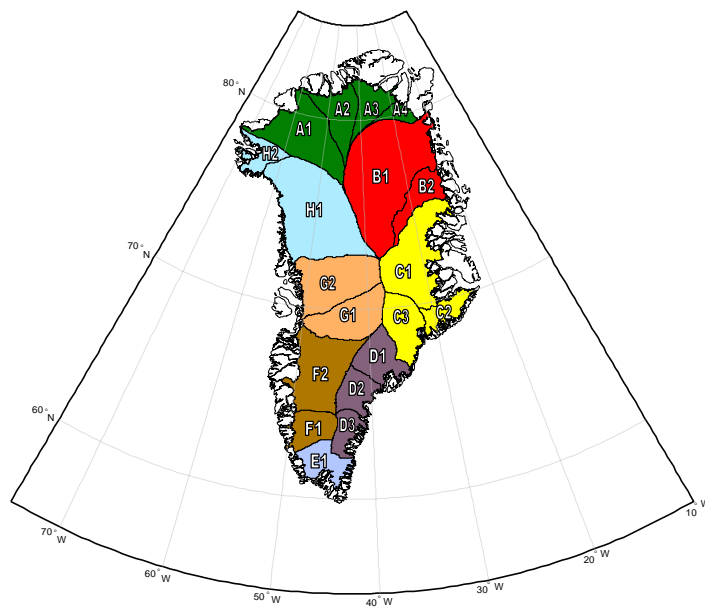


**Figure 4.43:** Greenland drainage divides developed by the Goddard Ice Altimetry Group from ICESat data

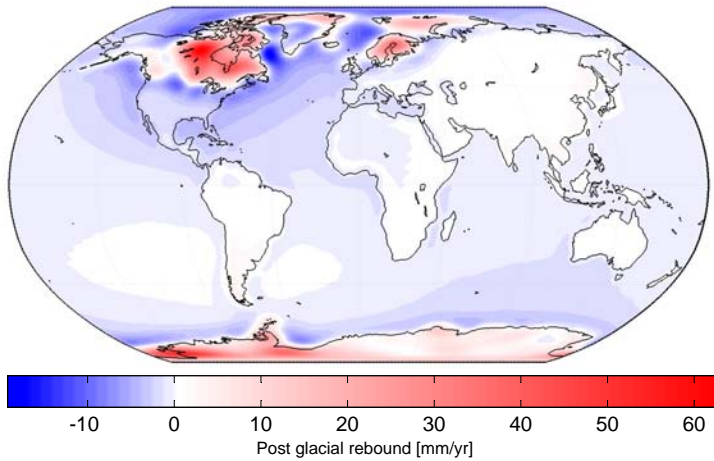


**Figure 4.44:** Post glacial rebound model developed by Paulson et al. (2007) in mm/yr of equivalent water

aliasing error (Figure 4.45). The trend of ice mass over the Greenland decreases from 202Gt/yr to 199Gt/yr, which seems to be not significant according to the given uncertainty in GRACE data. The low impact of tidal aliasing error on the estimated trend can be better represented in the frequency domain. The Lomb-Scargle spectral analysis of the time series over the whole Greenland before and after removing tidal aliasing error represents that the low frequencies belonging to the trend are not affected after removing the error (Figure 4.46). The estimated 199Gt/yr ice mass loss, however, is in good agreement within the error bars with the ensemble estimate of Schrama and Wouters (2011) based on different GRACE releases ( $-201 \pm 19$  Gt/yr), even though it was estimated from different time period of March 2003 to February 2010. As the trend is computed from the GRACE release 5 and for the time period of January 2005 to December 2011, any inconsistency with the results of previous studies like

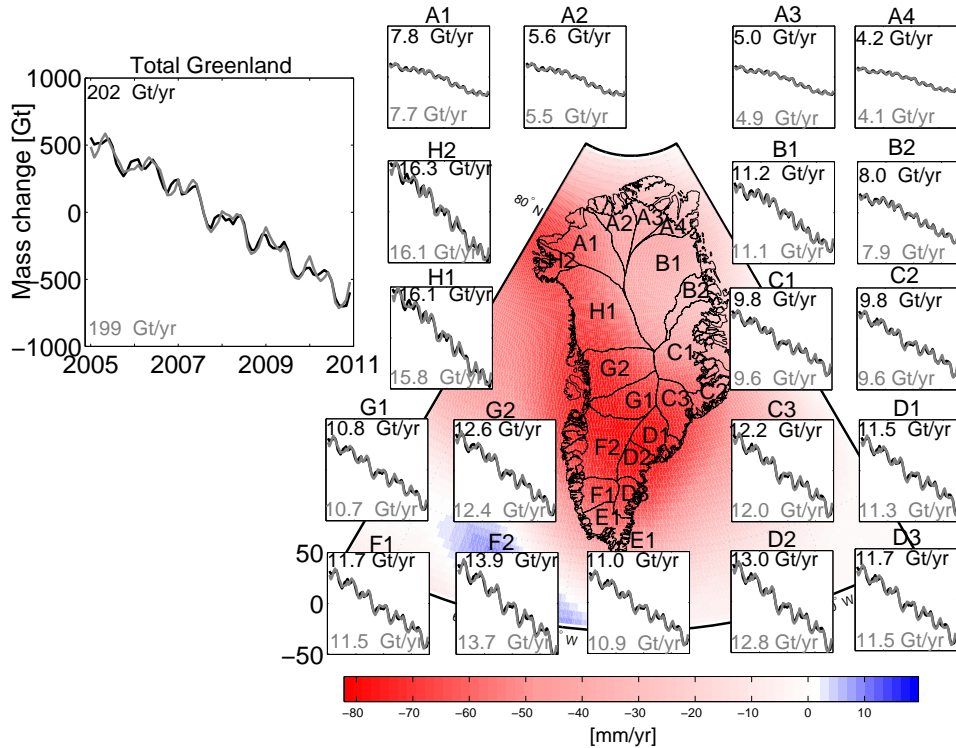


**Figure 4.45:** Mass changes over the drainage basins of Greenland before (black) and after (gray) removing tidal aliasing error. The map indicates the trend in mm/yr and the time series are in Gt. The ice mass loss in Gt/yr is shown beside each time series.

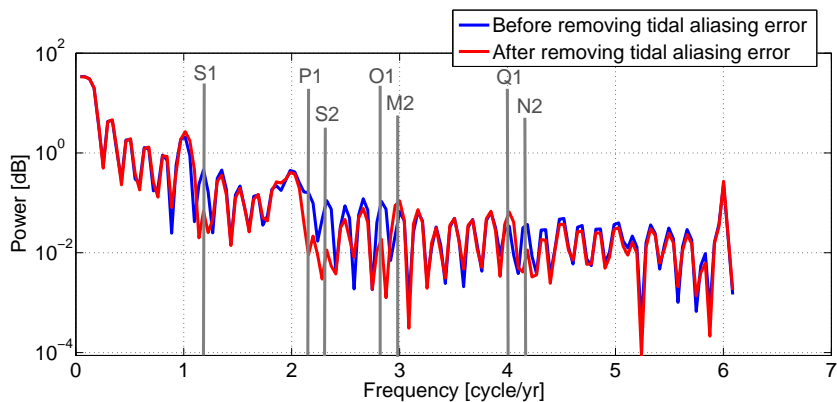


**Figure 4.46:** Spectra of the mass change time series over Greenland before and after removing tidal aliasing error

$-142 \pm 49$  Gt/yr (Shepherd et al., 2012),  $-238 \pm 29$  Gt/yr (Sasgen et al., 2012),  $-299 \pm 6$  km<sup>3</sup>/yr (Baur and Sneeuw, 2011),  $-219 \pm 38$  Gt/yr (Chen et al., 2011), are expected.

Table 4.6 summarizes the results of trend and acceleration estimation over the drainage basins of Greenland. Interestingly, unlike a linear trend, the acceleration increases after removing the tidal aliasing error. However, the estimated acceleration for both cases are different from  $-15$  Gt/yr<sup>2</sup> reported by Sasgen et al. (2012), which is derived from time interval August 2002–August 2010. The results are also in

**Table 4.6:** The estimated linear trend and acceleration from GRACE release 5 for the time period of Jan. 2005 to December 2011 for the 19 drainage basins (Figure 4.43)

| Drainage basin | Area<br>( $10^3 \text{ km}^2$ ) | Lin. Trend before<br>(Gt/yr) | Lin. Trend after<br>(Gt/yr) | Acc. before<br>(Gt/yr $^2$ ) | Acc. after<br>(Gt/yr $^2$ ) |
|----------------|---------------------------------|------------------------------|-----------------------------|------------------------------|-----------------------------|
| A1             | 130                             | -7.8                         | 7.7                         | -0.3                         | -0.4                        |
| A2             | 63                              | -5.6                         | -5.5                        | -0.3                         | -0.4                        |
| A3             | 46                              | -5.0                         | -4.9                        | -0.3                         | -0.4                        |
| A4             | 17                              | -4.2                         | -4.1                        | -0.3                         | -0.3                        |
| B1             | 273                             | -11.2                        | -11.1                       | -0.7                         | -0.7                        |
| B2             | 50                              | -8.0                         | -7.9                        | -0.5                         | -0.5                        |
| C1             | 148                             | -9.8                         | -9.6                        | -0.1                         | -0.1                        |
| C2             | 35                              | -9.8                         | -9.6                        | -0.0                         | -0.1                        |
| C3             | 72                              | -12.2                        | -12.0                       | 0.0                          | -0.0                        |
| D1             | 64                              | -11.5                        | -11.3                       | -0.1                         | -0.1                        |
| D2             | 47                              | -13.0                        | -12.8                       | -0.1                         | -0.1                        |
| D3             | 33                              | -11.7                        | -11.5                       | -0.1                         | -0.1                        |
| E1             | 49                              | -11.0                        | -10.9                       | -0.1                         | -0.1                        |
| F1             | 48                              | -11.6                        | -11.5                       | -0.1                         | -0.1                        |
| F2             | 135                             | -13.9                        | -13.7                       | -0.3                         | -0.3                        |
| G1             | 95                              | -10.8                        | -10.7                       | -0.2                         | -0.2                        |
| G2             | 129                             | -12.6                        | -12.4                       | -0.3                         | -0.3                        |
| H1             | 240                             | -16.1                        | -15.8                       | -0.4                         | -0.5                        |
| H2             | 34                              | -16.3                        | -16.1                       | -0.4                         | -0.5                        |
| Total          | 1718                            | -202                         | -199                        | -4.6                         | -5.4                        |

contradiction with the estimated acceleration of  $-17 \text{ Gt/yr}^2$  by Rignot et al. (2011), derived from April 2002 to June 2010. This discrepancy is due to the observation period and using different GRACE releases which heavily influence the computation of acceleration.

## 4.5 Noise level of GRACE

After dealing with the challenges and achieving a data set without outliers, long-range correlation and tidal aliasing errors, the noise level of GRACE monthly solutions can be finally quantified. To this aim, the RMS of monthly residuals are considered as representative of the upper bound of GRACE noise level. The results indicate that the noise level varies between 2–20 mm/month over different parts of the globe (Figure 4.47). In general, a higher noise level appears over the continents, which can be explained by a stronger interannual signal e.g. the Amazon, Congo. However, southern parts of the Arctic Ocean and Greenland also represent high noise levels of ca. 15 mm/month. The results show that among the continents, the higher contribution of noise level belong to the tropical regions, where the noise reaches up to 20 mm/month.

A latitudinal representation of RMS values over the globe clearly shows a high noise level in boreal and tropical regions (Figure 4.48). This cross section indicates an average noise level of 3–7 mm/month with higher levels over tropical and boreal regions.

The catchment noise level representation in Figure 4.48 also implies that small catchments in the tropics contain more contamination of noise in the GRACE monthly solutions. The results also show that a

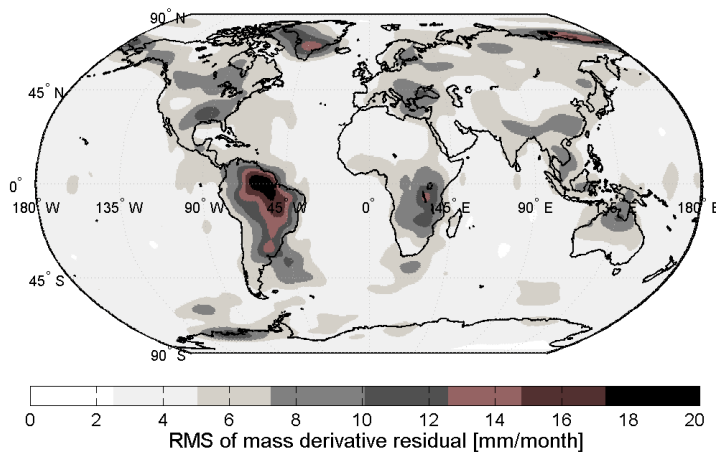


**Figure 4.47:** RMS of mass derivative residual representing an upper bound of GRACE noise level

lower noise level of a catchment does not necessarily lead to a better correlation of GRACE with hydro-meteorological signal e.g. Saudi Arabia. Moreover, a catchment with high RMS value for residual can be highly correlated with hydro-meteorological signal e.g. Lake Turkana, Copper River. This can be explained by an extreme value in mass derivative signal, which leads to a high RMS value for residual. Therefore, it is important to note again that RMS of residual can only represent the upper bound of GRACE noise level.

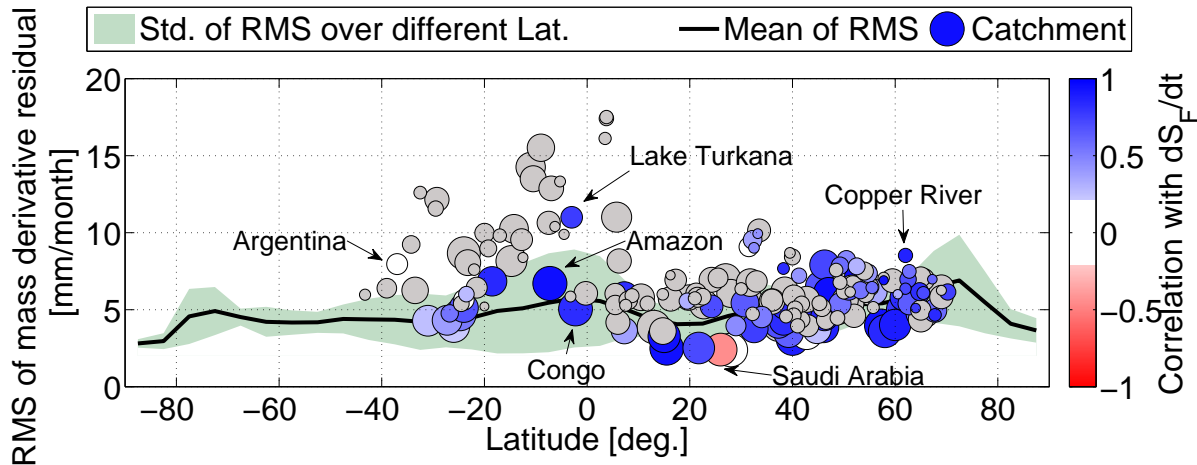


**Figure 4.48:** Latitudinal cross section of RMS of mass derivative residual of GRACE data after removing outliers and correcting for tidal aliasing and long-range correlation errors. The circles represent catchments and the size of each circle depicts the catchments' area. The color of the circles imply the correlation of  $dM/dt$  with  $dS_F/dt$  for each catchment. The gray circles belong to the catchments with no available discharge data



## Chapter 5

# Estimation of actual evapotranspiration using space-borne geodetic sensors

Earth's water, energy and carbon cycle are linked to each other through evapotranspiration (Rodell et al., 2004a). The extent to which water vapor is supplied by evapotranspiration is an indicator of the general climatic sensitivity to land-surface change (Brubaker et al., 1993). Hence, any trend in evapotranspiration may represent climate change and particularly acceleration of the hydrological cycle (Rodell et al., 2004a; Brutsaert and Parlange, 1993). As a consequence, for understanding the hydrological cycle and Earth system processes, quantification of evapotranspiration is essential. However, a precise point-wise measuring of  $ET_a$  at gauges seems to be difficult. A wide variety of model approaches exist at present from simple empirical to complex ones including radiative energy balance. Many researches have focused on remote sensing approaches, in which the observation of surface temperature and vegetation indices are used for estimation of evapotranspiration. However, the estimation from different approaches not only show considerable variations in monthly values, but also systematically underestimate the actual evapotranspiration in summer and overestimate in winter (PILPS, 1996; Gates, 1997). The inherent problem until present is, that the different approaches for short time  $ET_a$  can not be evaluated by independent measurements. As discussed in Chapter 1, over a river basin on monthly time scale, evapotranspiration can be indirectly estimated by GRACE data:

$$ET_a = P - R - \frac{dM}{dt} . \quad (5.1)$$

On monthly time scale and using the hydro-meteorological data,  $ET_a$  can be also estimated by:

$$ET_a = P + \nabla \cdot \vec{Q} . \quad (5.2)$$

In the first approach, hereafter called the *GRACE approach*, estimation of  $ET_a$  is feasible over catchments with available discharge data, while for the second approach, hereafter referred to as *hydro-meteorological approach*, only  $P$  and  $\nabla \cdot \vec{Q}$  are needed. In the first approach, the estimated discharge from satellite altimetry can be also used (*GRACE-altimetry approach*) to obtain an estimation based on two spaceborne geodetic sensors. In this chapter,  $ET_a$  over different catchments will be estimated using

mentioned approaches and statistically assessed. As  $ET_a$  is typically available from models only, the results will be compared with the available actual evapotranspiration models:

- GLEAM (Global Land-surface Evaporation: the Amsterdam Methodology) (Miralles et al., 2011)
- GLDAS (Global Land Data Assimilation System) (Rodell et al., 2004b)
- ECMWF (European Centre for Medium-Range Weather Forecasts) (Simmons et al., 2006; Berrisford and for Medium Range Weather Forecasts, 2009)
- MERRA (Modern Era-Retrospective Analysis for Research and Application) (Rienecker and Coauthors, 2011)
- MERRA Land (Reichle et al., 2011)

For most of the above models a wide range of remotely sensed observations are combined to derive evapotranspiration.

## 5.1 $ET_a$ from GRACE and hydro-meteorological approaches

In this section, the performance of the GRACE approach is assessed by comparing it with the hydro-meteorological approach and models. Figure 5.1 shows the estimated evapotranspiration from GRACE and hydro-meteorological approach together with the  $ET_a$  from different models over Mississippi, Amazon and Lake Chad catchments representing three different climate conditions. The Mississippi catchment is located in a region with warm temperate climatic conditions and a hot summer, which causes a high evapotranspiration in summer. This is also the case for Lake Chad catchment, which partly lies in an equatorial region with dry winter and partly in a hot desert. The estimated  $ET_a$  time series over Mississippi and Lake Chad agree with the models, yet with some large peaks indicating overestimation in summer or underestimation of models. On the other hand, over the fully humid equatorial Amazon,  $ET_a$  behaves almost constant, yet the estimation from GRACE and hydro-meteorological approaches are very dissimilar to the models.

Due to the existence of discrepancies between models, the average time series of different models in the overlapping time period of March 2003–Dec. 2007, is computed as an ensemble mean. In fact, the ensemble mean represents a fair representation of the models, for which the respective standard deviations imply the modeling discrepancies over time. The RMS of the ensemble standard deviations value over time can be interpreted as the absolute modeling discrepancy, which implies a larger modeling disagreement over tropical regions (Figure 5.2(top)). However, as this region has a high contribution to the global evapotranspiration, the relative modeling discrepancy, RMS of ensemble standard deviation divided by the RMS of ensemble mean, is not considerable (Figure 5.2(bottom)). For a catchment like Caspian Sea both absolute and relative modeling discrepancy show large values, which can be expected as the catchment lies in various climatic conditions making the modeling difficult.

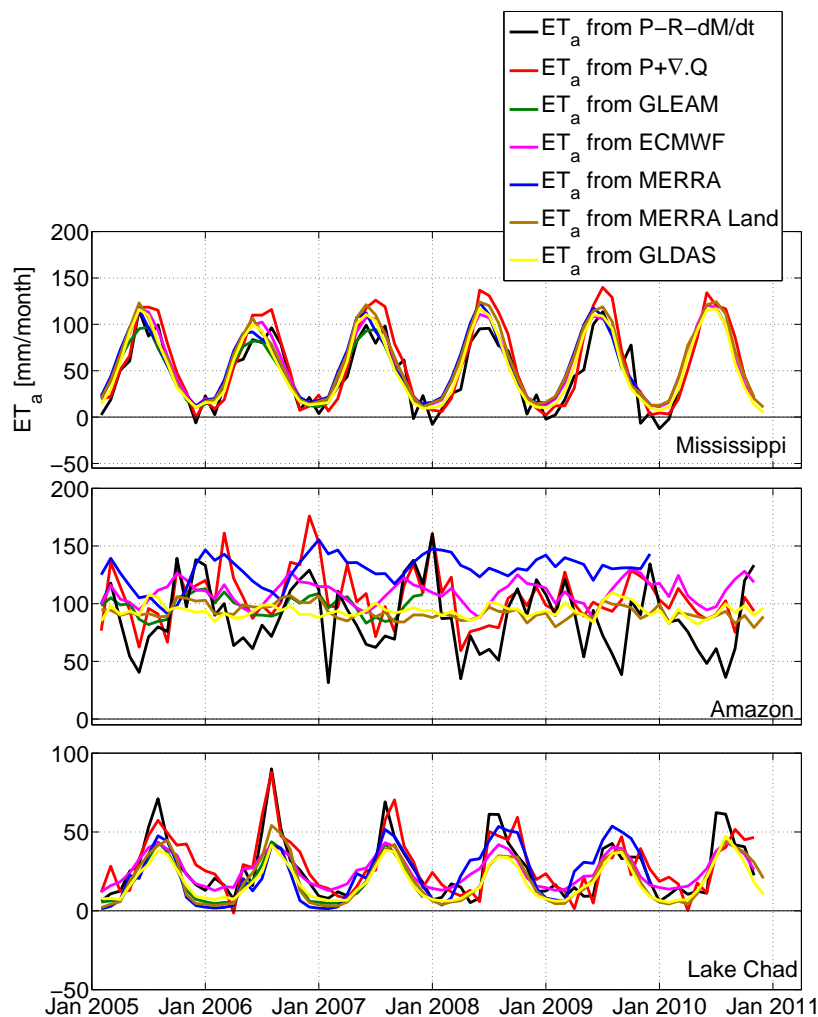


**Figure 5.1:** Estimated evapotranspiration from GRACE and hydro-meteorological approach together with the  $ET_a$  from different models over Mississippi, Amazon and Lake Chad catchments

In addition to the catchments in Figure 5.1, also Caspian Sea, Ob and West Australia catchments are assessed. They are representative of desert-cold plains, arctic and tropical dry climate conditions. Table 5.1 shows the statistical analysis of comparing the estimated  $ET_a$  from GRACE and hydro-meteorological approach with the ensemble mean.

The ensemble mean and the  $ET_a$  from GRACE approach show correlation of 0.91, 0.72, 0.90, 0.93, 0.66 and 0.74 over Mississippi, Amazon, Lake Chad, Caspian Sea, Ob and West Australia catchments, respectively (Figure 5.3). Despite the relatively high correlation, the over-estimated/underestimated  $ET_a$  is clearly depicted in the Figure 5.3 for the Mississippi, Amazon, Lake Chad and West Australia. In contrast, for an arctic tundra catchment of Ob with warm summer in its southern part, the  $ET_a$  is under-estimated in comparison to the other models.

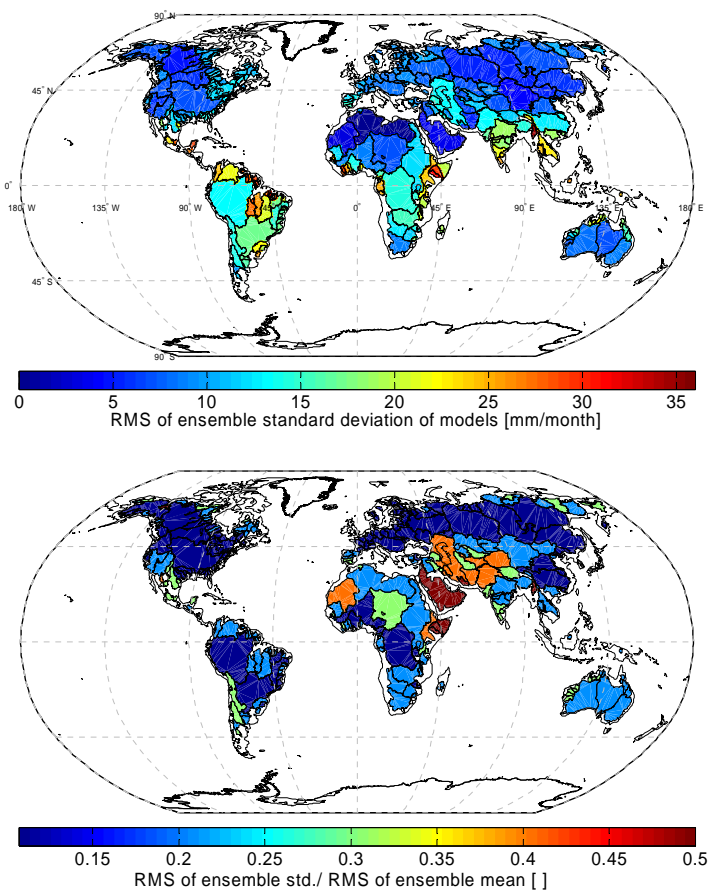


**Figure 5.2:** Top) RMS of ensemble standard deviations as representative of absolute modeling discrepancy, Bottom) RMS of ensemble standard deviations divided by the RMS of ensemble mean indicating the relative modeling discrepancy

**Table 5.1:** Statistical analysis of comparing the estimated  $ET_a$  from GRACE and hydro-meteorological approaches with ensemble mean

| Catchment      | Correlation |             | RMS of difference |      | Relative discrepancy |           |
|----------------|-------------|-------------|-------------------|------|----------------------|-----------|
|                | [ ]         |             | [mm/month]        |      | [%]                  |           |
|                | GRACE       | Hyd.        | GRACE             | Hyd. | GRACE                | Hyd.      |
| Mississippi    | 0.91        | <b>0.92</b> | 15.1              | 17.4 | <b>24</b>            | 27        |
| Amazon         | 0.72        | <b>0.80</b> | 27.8              | 22.1 | 26                   | <b>21</b> |
| Lake Chad      | <b>0.90</b> | 0.84        | 12.7              | 15.7 | <b>58</b>            | 72        |
| Caspian Sea    | <b>0.66</b> | 0.53        | 13.3              | 12.3 | 46                   | <b>43</b> |
| Ob             | 0.94        | <b>0.95</b> | 15.3              | 12.0 | 32                   | <b>25</b> |
| West Australia | 0.74        | <b>0.84</b> | 14.4              | 10.8 | 47                   | <b>35</b> |

The question of whether these under/over-estimation are valid, can only be assessed through comparison with *in situ* measurements. However, comparison of estimations against models for all catchments and months acknowledges a 47% and 58% underestimation of models or overestimation of  $ET_a$  from

GRACE and hydro-meteorological, respectively. The overall comparison also reveals biases of 22.8 and 29.7 mm/month and correlations of 0.66 and 0.65 (Figure 5.4).

It is expected that, by comparing the monthly mean of the estimated  $ET_a$  against the monthly mean of ensemble mean, the biases decrease and the correlations increase (Figure 5.5). The overestimation also decreases to the level of 34% and 42% for GRACE and hydro-meteorological approaches. These results imply noise in the different components of  $P$ ,  $R$ ,  $dM/dt$  and  $\nabla \cdot \vec{Q}$ , that are reduced by computing the monthly mean.

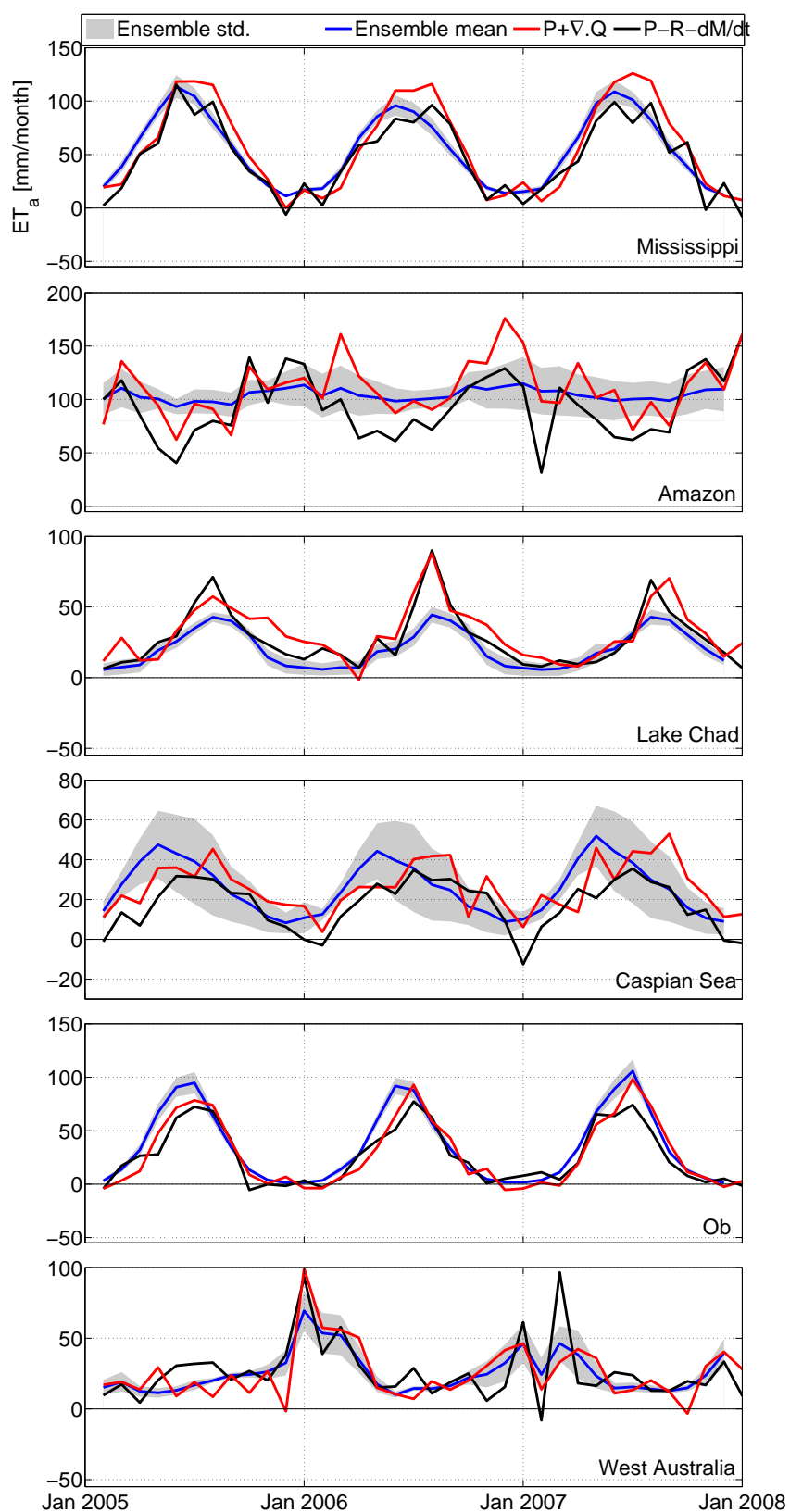


**Figure 5.3:** Estimated evapotranspiration from GRACE and hydro-meteorological approaches together with the ensemble mean and standard deviation

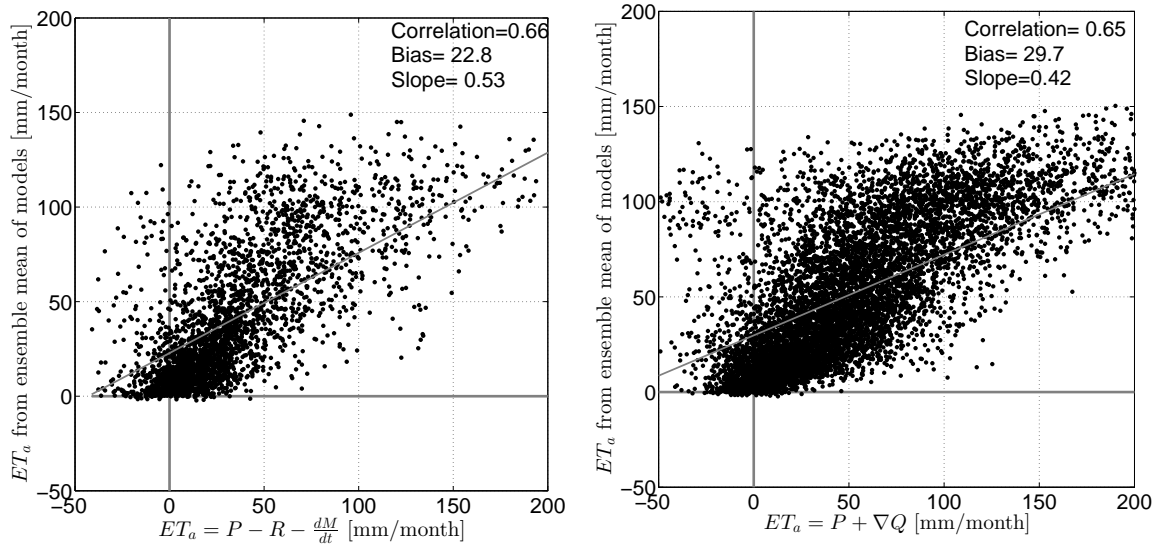


**Figure 5.4:** Left) scatter plot of monthly values of ensemble mean versus  $ET_a$  from GRACE approach, Right) scatter plot of monthly values of ensemble mean versus  $ET_a$  from hydro-meteorological approach for all catchments

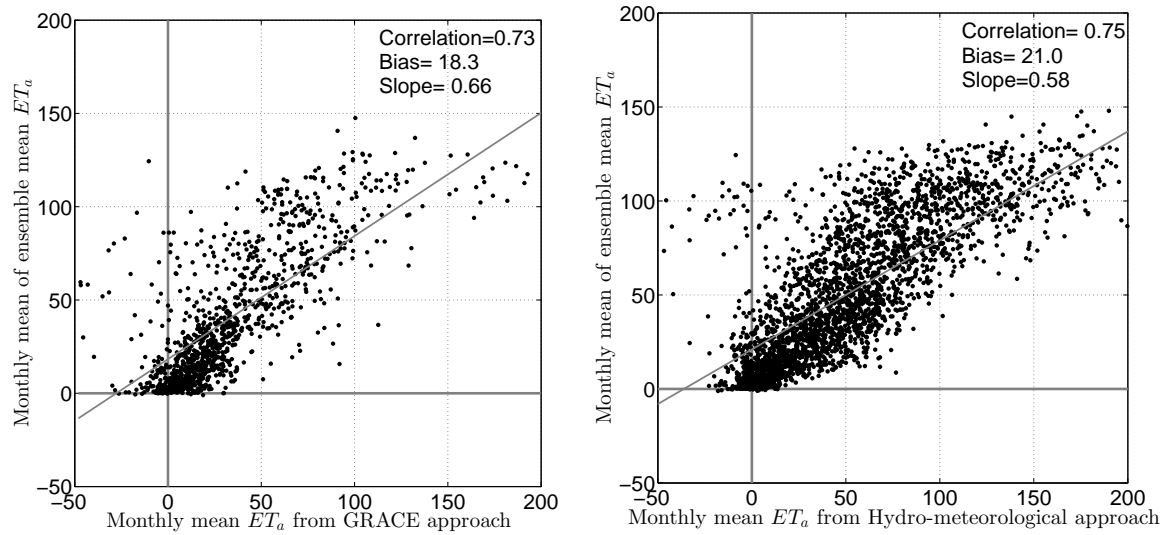


**Figure 5.5:** Left) scatter plot of monthly mean values of ensemble mean versus monthly mean of  $ET_a$  from GRACE approach, Right) scatter plot of monthly mean values of ensemble mean versus monthly mean of  $ET_a$  from hydro-meteorological approach

In general, the estimated  $ET_a$  from both GRACE and hydro-meteorological approaches are comparable and provide the same level of discrepancy from the ensemble mean. Both approaches provide ca. 20–30% relative discrepancy for catchments like the Amazon, Congo, Mississippi, Nelson River, Mackenzie River, Orange, Ob and North China. On the other hand, most of the catchments located in deserts show relative discrepancy larger than 50% (Figure 5.6). Given the relative discrepancy shown in Figure 5.6, GRACE approach as a spaceborne method seems to be a plausible way for determining  $ET_a$  for most non-desert catchments with hot and warm summers.

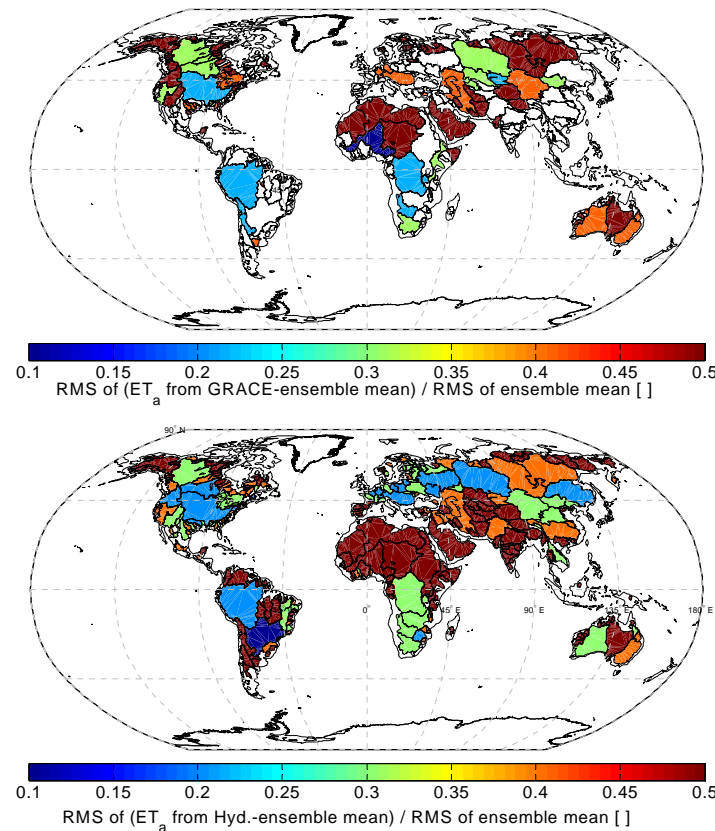


**Figure 5.6:** Relative discrepancy from the ensemble mean of estimated  $ET_a$  from the GRACE approach (top) and the hydro-meteorological approach (bottom)

## 5.2 $ET_a$ from GRACE-altimetry approach

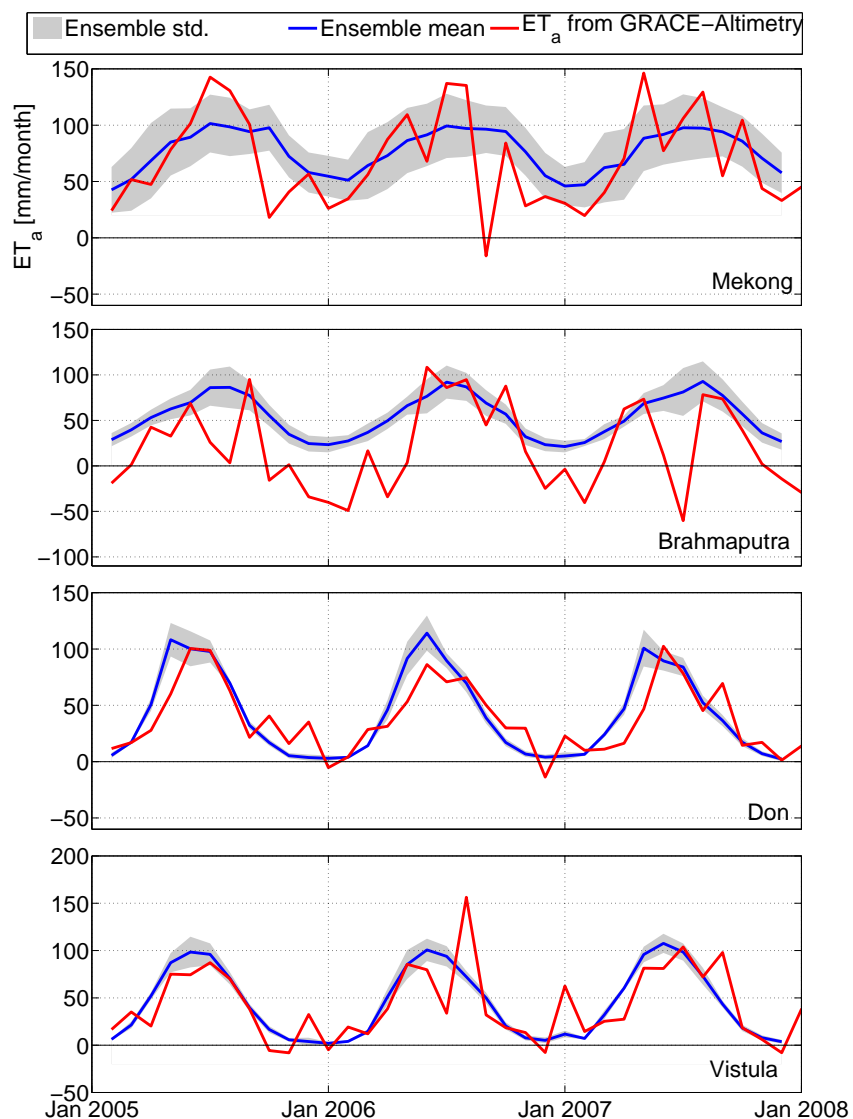
As discussed at the beginning of this chapter, for catchments with no available discharge data, estimation of discharge from satellite altimetry can be used as a way to derive evapotranspiration. To that end, river basins in group 2, discussed in Chapter 3, will be investigated for  $ET_a$  determination. Therefore, the altimetry based discharge values derived from Kalman filtered results from the quantile function approach of Mekong, Brahmaputra, Don and Vistula rivers are used for further investigation. Mekong and Brahmaputra are tropical catchments with a dry winter and hot summer, in which the models show relative discrepancies of 31% and 22%, respectively. On the other hand, the fully humid catchments of Don and Vistula, with almost no evapotranspiration during the winter, show ca. 12% relative discrepancy.

Figure 5.7 shows the estimated evapotranspiration from the GRACE-altimetry approach together with the ensemble mean over Mekong, Brahmaputra, Don and Vistula. The estimations for Mekong and Brahmaputra diverge from the ensemble mean with correlations of 0.62 and 0.64, respectively. In contrast, estimations for Don and Vistula catchments indicate a better fit to the ensemble mean with correlations of 0.84 and 0.76. Table 5.2 shows the statistical analysis of comparing the estimated  $ET_a$  from GRACE-altimetry approach with ensemble mean describing very high relative discrepancy from models for Brahmaputra.

**Table 5.2:** Statistical analysis of comparing the estimated  $ET_a$  from the GRACE-altimetry approach with ensemble mean

| Catchment   | Correlation<br>[ ] | RMS of difference<br>[mm/month] | Relative discrepancy<br>[%] |
|-------------|--------------------|---------------------------------|-----------------------------|
| Mekong      | 0.62               | 34.7                            | 43                          |
| Brahmaputra | 0.64               | 98.8                            | 165                         |
| Don         | 0.84               | 20.5                            | 36                          |
| Vistula     | 0.76               | 25.9                            | 44                          |

All in all, the spaceborne geodetic sensors as independent sources of measurement can contribute to the estimation of actual evapotranspiration. However, as results indicate,  $ET_a$  is overestimated in comparison to the models. This does not mean an overestimation against the true evapotranspiration, as it has been acknowledged that the models are underestimated (PILPS, 1996; Gates, 1997). In other words, the estimated  $ET_a$  from spaceborne geodetic sensors might be closer to the reality, which means that the models are underestimated. Apart from the systematic under/overestimation, an overall correlation of 0.66 for GRACE approach and correlations of ca. 0.6–0.8 for GRACE-altimetry approach at the monthly time scale justify a considerable variations in monthly values in comparison to the models. This is especially due to noise in water storage changes and discharge from GRACE and altimetry. However, in future the estimated evapotranspiration from spaceborne geodetic sensors can be turned into a favorable estimation by assimilation approaches. In this context, different types of stochastical process models together with the filtering and smoothing techniques can be employed to obtain a desirable estimation. There,



**Figure 5.7:** Estimated evapotranspiration from GRACE-altimetry approach together with the ensemble mean and standard deviation

the estimation from different sensors and *in situ* measurements can be assimilated with their respective uncertainties. It is expected that with improving the spaceborne geodetic sensors and their background models, the resulting  $ET_a$  from assimilation approach would be more helpful for hydrological applications.

# Chapter 6

## Summary, conclusion and recommendation

### 6.1 Summary and conclusion

Inspired by the evident limited knowledge of the spatial and temporal dynamics of the surface freshwater variations and discharges, this study motivates the monitoring of the hydrological cycle using spaceborne geodetic sensors. Among the current space geodetic sensors, GRACE and satellite altimetry are the two active mission concepts, which can capture and monitor part of the hydrological cycle. GRACE senses the variations in the gravity field at a spatial resolution of ca. 400km and at a monthly time scale. Satellite altimetry measures the surface water at a temporal resolution of 10 and 35 days (depending on mission) and spatial resolution of ca. 1 km along track and 80 km inter track. These temporal scales mostly cover the slow branch of the hydrological cycle, which are included by processes such as interception, stemflow, infiltration, percolation, capillary rise, groundwater flow, leakage and discharge. The main objective of this study is to monitor the hydrological cycle using spaceborne geodetic sensors. Given the capabilities of spaceborne geodetic sensors and the challenges of monitoring the hydrological cycle, the following tasks should be addressed for achieving the main goal of this study:

1. Developing an algorithm to derive inland water level time series from satellite altimetry with low uncertainty.
2. Developing an algorithm to derive river discharge from satellite altimetry.
3. Developing an algorithm to reduce the noise level of GRACE and achieve hydrologically meaningful time series for water storage changes over river basins.
4. Assessing the the limitations of actual evapotranspiration estimation from water balance equation and spaceborne geodetic sensors.

Initially, satellite altimetry has been investigated for being an independent spaceborne sensor to provide the water level and discharge time series. Therefore, developing a concrete algorithm to improve the quality of water level time series over inland water surfaces has been defined as the goal of Chapter 2. There, particularly the challenges of resolution and uncertainty of altimetry have been investigated. For the resolution challenge, footprint size, location and the problem of off-nadir measurements have been

studied. The uncertainty challenge has been tackled by developing an algorithm containing following steps:

- Outlier identification and elimination on the water level time series
- Off-nadir correction
- Excluding noisy waveforms
- Unsupervised classification of waveforms based on the modal and median waveforms in each data set and computing the heterogeneity index
- Retracking the waveforms by an appropriate algorithm

After employing the algorithms, the obtained LLH time series have been validated against *in situ* measurements, which showed a ca. 10% improvement in accuracy of the time series. The validation also reveals that the results of retracking after classifying the waveforms contain lower errors than those obtained without classification. This result proves and emphasizes the necessity of applying a classification procedure before retracking the waveforms.

Besides that, this study has proposed an algorithm to reduce the random noise of pre-retracked data. This algorithm relies on the fact that one specific retracker does not always provide the inland water level time series with the lowest noise level. Hence, a method has been developed, which combines the results of different retrackers and provides water level time series with reduced noise level. Although this algorithm does not take the biases between retrackers into account, the validation shows a significant reduction of noise level and a clear improvement in correlation with *in situ* measurements.

Further in Chapter 3, the study aimed to extract river discharge from satellite altimetry by establishing a rating curve using available discharge measurements and altimetry water level time series. The extraction of discharge is only achievable through having consistent data sets. Data availability and temporal resolution have been recognized as sources of inconsistency between water level time series from altimetry and available discharge measurements. From data availability, different rivers have been categorized into three groups. Group 1: rivers with available *in situ* discharge simultaneous with altimetry. Group 2: rivers with available *in situ* discharge non-simultaneous with altimetry. Group 3: rivers with no available discharge measurements at all, which have not been further investigated as it is not possible to establish a rating curve for these rivers. For rivers in group 1, river discharge can be estimated through a functional relationship, that is conventionally established via a rating curve computed using simultaneous data. Yet, having rivers in the group 2 raise the question of how to establish a rating curve without simultaneous data sets.

In order to answer the question, this study has proposed a statistical approach to derive discharge from height through a rating curve based on the quantile functions. This method is based on a scatter diagram of quantile functions, in which the probability-coordinate is eliminated. In contrast, the conventional methods operate directly on time series and eliminate the time-coordinate. The results show that the statistical approach based on the quantile functions of water level and discharge provides the same range of

error as the common conventional empirical method. The usefulness of the discharge database generated by satellite altimetry is supported by comparing the altimetric discharge and available annual cycles. It has been demonstrated that the statistical approach provides better discharge estimation than the annual cycle. The good performance of the statistical approach supports the usage of altimetry to salvage pre-satellite altimetry discharge data and turn them into active use for the satellite altimetry time frame. As the number of gauging station with this situation is ca. 4680 (ca. 60% of total gauges)—according to GRDC database—the statistical approach can be used as a tool to augment the discharge database around the world.

In general, the statistical approach based on quantile functions has its own limitations despite the good performance. The main limitation of this approach is that it leads to erroneous discharge when discharge behaviour of the river drastically varies over time. This is specially demonstrated where the changes in discharge behaviour of e.g. the Amur River over time causes different estimations of discharge from the empirical and statistical methods. On the other hand, similar to the empirical approach, the statistical approach is restricted to applying the model to the correspondent data set. This is highlighted in the Ob River where the noisy ice contaminated water level time series of altimetry close to the gauging station of discharge forces a choice of virtual station far from the gauge leading to an erroneous model out of non correspondent water level and discharge values. Besides that, discharge estimation from the obtained rating curve based on either empirical/statistical method is only possible at the time of altimetry, thus any missing value in altimetry leads to a gap in the estimation. In addition, noisy altimetry causes incorrect estimation of discharge. Therefore, it would be desirable to have an algorithm that covers the missing values and combines all available measurements with their uncertainties to provide an acceptable estimation. Hence, in this study a stochastic process model has been developed to cope with this problem and to improve the estimation.

The stochastic process model has been implemented in a way that benefits from the cyclostationary behaviour of the discharge. The model has been combined with the estimated discharge from altimetry and available *in situ* measurements to form a linear dynamic system. This dynamic system helps to estimate the discharge using the available measurements and monthly mean of discharge. The dynamic system has been solved using the Kalman filter, that provides an unbiased discharge with minimum variance. The results of the Kalman filter estimation have been then validated against the *in situ* measurements using a leave-out validation procedure. Average error levels of 0.9–5.6 mm/month, corresponding to the error of 4–17%, are achieved for different rivers. These results indicate comparable range of error with the RMSE from empirical and statistical approaches. As a conclusion, it can be stated that the problems of missing and noisy altimetry values can be tackled by forming the stochastic process model and solving it with the Kalman filter.

In general, it can be stated that the estimated river discharge using satellite altimetry would be appropriate for further hydrological investigation if

1. the altimetric water level is derived with sufficient quality

2. altimetry can appropriately sample the river's water level variations
3. the distance between virtual station and gauge is small enough to be geomorphologically similar
4. the river discharge is stationary (does not show significant trend or variation)
5. the heritage discharge data is lengthy enough to be statistically representative

In Chapter 3 the capability of satellite altimetry to monitor part of hydrological cycle by extracting river discharge has been discussed. However, for a comprehensive monitoring of the hydrological cycle, water storage changes are needed. GRACE gravity data allows to determine continental water storage changes and close the water budget on short time scales. However, the utility of GRACE data as representative of hydrological water storage changes is limited by the following challenges: consistency, resolution, separability and uncertainty. Hence, one of the goals of this study has been to develop algorithms to cope with these challenges, so that the noise level of GRACE is reduced and appropriate time series for water storage changes are obtained. The comparison of GRACE mass derivatives  $dM/dt$  with water storage changes from hydrological and hydro-meteorological water balances for catchments with available discharge measurements has been introduced as a way to tackle parts of the mentioned challenges and limitations.

In order to cope with the inconsistency challenge, in particular the inconsistency in discretization, two filters have been designed in Chapter 4. These filters have been implemented on hydrological and hydro-meteorological water storage changes, which lead to a better correlation with GRACE mass derivative. The challenges of separability and resolution have not been specifically investigated in this study, yet their consequences, which appear in different forms of uncertainties have been investigated. In fact, the uncertainty of GRACE is the result of errors, inconsistencies, miss-modeling and the lack of modeling in the different stages of data processing. The errors in de-aliasing models, intrinsic instrumental error, the errors in precise orbit determination, lack of proper error propagation, limitation of GRACE to the modeling of  $C_{20}$  and invisibility of the degree 1 term are examples of sources for uncertainty in GRACE solutions.

To deal with the GRACE uncertainties, first an algorithm has been developed to detect outliers in monthly solutions. The algorithm has been employed for GRACE solutions of different analysis centers (GFZ, JPL, CSR and ITG). The outliers have been corrected by replacing them by an inter-annual monthly mean of the respective month. The replaced values seem to be in most cases hydrologically plausible. However, as the algorithm is automatic and based on a statistical approach, error in outlier detection is inevitable. Nevertheless, outlier correction improves the correlation of hydrological and hydro-meteorological signals with GRACE observations. Although the percentage of detected outliers from the different centers is  $\sim 2\%$ , the correction of outliers show on average 2–14% improvement in correlation of GRACE observation versus hydrological and hydro-meteorological signals. Moreover, outlier correction leads to noise level reduction in the range of 3–26% (averaged over catchments) for the different data centers. Further, the occurrence of outliers has been compared for different combinations of the different centers. The small number of common outlier occurrences between the products is explained by the different data

processing algorithm used by the different data centers. This research has conclusively demonstrated that outlier identification and correction must be performed before further assimilation of GRACE products into hydrological or hydro-meteorological analysis.

Further, a long-range correlation has been identified as another source of uncertainty in GRACE monthly solutions. Unlike hydrological and hydro-meteorological residuals, GRACE residual are correlated spatially over the globe independent from oceans or land masses. In order to identify the possible responsible source for the long-range correlation, an Empirical Orthogonal Functions (EOF) analysis has been performed on the mass derivative residuals. The results allow us to identify the corresponding signal's PC time series with a periodic behaviour constant over the globe. The responsible signal contribution is modulated as a sine function over latitude, and appears as an error with respect to signals of hydrology, hydro-meteorology, oceanography and glaciology. The removal of the responsible mode leads to a decrease in long-range correlation, and thus, in total error. Especially for the high latitudes and the equatorial oceans, a tremendous error reduction amounting to 55% is achieved. In order to find out the dominant frequency in the obtained responsible PC, a spectral analysis was performed. The spectrum indicates a dominant frequency of 2.26 cycles per year (161 days), which is the well known alias period of the S2 semi-diurnal solar tide. Previous studies had revealed the contamination of low degree spherical harmonics with S2 tidal aliasing error. Therefore, in this study the responsible PC has been compared with the corresponding low spherical harmonics' variation in time and frequency domain. The comparison concluded that what has been recognized as long-range spatial correlation error is nothing else than the zonal behaviour of the GRACE  $C_{20}$  errors. In fact, it is considered as an error source because its residual contains tidal aliasing errors instead of white noise (flat spectrum).

The long-range correlation revealed that the GRACE monthly solutions are contaminated by the tidal aliasing error, although attempts to eliminate in the de-aliasing procedure are made. As other coefficients and not only  $C_{20}$  can be also contaminated by the aliasing error, simply replacing the GRACE  $C_{20}$  coefficient with the SLR coefficient does not address the full aliasing problem. Therefore, to reduce the uncertainties in GRACE monthly solutions, tidal aliasing errors have been investigated.

Among the main tidal constituents, S1, S2, P1, K1 and K2 alias into longer than 30 days period in GRACE and thus do not average out in the monthly solutions data. The effect of these alias periods have to be removed from the GRACE monthly solutions. On the other hand, monthly averaging procedure leads to a so-called secondary aliasing for the tidal constituents of M2, O2, O1, Q1 with primary aliasing periods of less than a month. The secondary aliasing effects contribute to GRACE error and degrade monthly solutions. This issue becomes more critical as the monthly averaging of GRACE is an uneven sampling given that it is carried out based on the availability of data within a calendar month. Therefore, the sampling interval can vary between 27–31 days which leads to a peculiar behaviour for the secondary aliased wave. A spectral analysis based on the Lomb-Scargle method is employed to define the dominant frequency of secondary wave. The Lomb-Scargle method is specifically appropriate for spectral analysis of unevenly sampled data. Interestingly, the results indicate that the dominant frequencies are different from those obtained when equally sampled data is considered. For instance, for the M2 tide, the main

secondary aliased period is 125.15 days, while in case of assuming equally sampled data the period is 146.37.

In order to remove the remaining effect of tidal aliasing error a least squares Fourier analysis has been performed over the spherical harmonics' time series. The obtained spatial distributions of the S1, S2, P1, M2, N2, O1 and Q1 aliasing indicate amplitude up to 21.4, 13.8, 14.8, 7.8, 9.4, 10.0 and 4.0 mm errors over the globe, respectively. In general, the errors of the tidal aliasing are mainly distributed in northern and southern regions, where it is known that the ocean tide models are poorly determined. To assess this point, a comparison has been made between four different ocean tide models and GRACE tidal errors. Similar ranges of tidal error in GRACE and differences in ocean tide models highlight the ocean tide mis-modeling as a possible reason for the remaining tidal aliasing error in the GRACE monthly solutions.

Furthermore, the high tidal aliasing error contribution (7–20 mm/month) over Greenland, the Amazon, Congo, Mississippi, Hudson Bay, Kuskokwim River, Susitna River, Mekong River, Godavari, Ganges, Laptev and East Siberian sea emphasize the impact of tidal aliasing error in GRACE monthly solutions. Therefore, the impact of removing tidal aliasing errors has been investigated. The results show that removing tidal aliasing error improves the solutions toward being more consistent with the hydro-meteorological water storage changes. Moreover, the trend and acceleration have been estimated over Greenland after correction of mass estimation of GRACE for post glacial rebound. The results over drainage basins of Greenland for the time period of 2005–2011 reveal that the changes in the trend and acceleration are not significant after removing the tidal aliasing error.

In general, after dealing with GRACE's challenges and achieving a data set without outliers, long-range correlation and tidal aliasing errors, the noise level of GRACE has been quantified. The quantification shows a variation between 2–20 mm/month over different parts of the globe, with higher values over tropical and boreal regions. The results specifically confirm that small catchments in the tropics contain more noise contamination. It has also been shown that a lower noise level of a catchment does not necessarily lead to a better correlation of GRACE with hydro-meteorological signal.

Finally, in Chapter 5, the performance of spaceborne geodetic sensors for estimating the actual evapotranspiration has been assessed. There, two approaches have been introduced to estimate evapotranspiration using the results of GRACE and satellite altimetry. The results of both approaches have been compared with different models and their ensemble mean. All in all, spaceborne geodetic sensors as independent sources of measurement can contribute to the estimation of actual evapotranspiration. Given the obtained relative discrepancy, the methods seem to be a plausible way for determining  $ET_a$  for most of non-desert catchments with hot and warm summers. However, as results indicate,  $ET_a$  is overestimated in comparison to the models. This does not mean an overestimation against the true evapotranspiration, as it has been acknowledged that the models are underestimated (PILPS, 1996; Gates, 1997). In other words, the estimated  $ET_a$  from spaceborne geodetic sensors might be closer to the reality, which means that the models are underestimated.

Overall, given the obtained results in this study, spaceborne geodetic sensors, designed for altogether different purposes, can be introduced as valuable hydrological monitoring tools. Satellite altimetry has demonstrated its potential to act as virtual lake and river gauges. GRACE has established a fundamentally new remote sensing tool for hydrological applications. It strongly constrains the hydrological cycle at continental scales and large catchments. Despite the overall success, some challenges like spatial and temporal resolution for both altimetry and GRACE, separability of GRACE solutions remain open, which promote number of proposals and ideas for future works and missions.

## 6.2 Perspective of future work

Some of the remaining challenges e.g. spatial and temporal resolution can only be addressed completely with the help of future altimetry technology and GRACE-Follow On (Flechtner et al., 2012). However, the results of this study show that employing new algorithms, techniques and approaches, help the usage of current spaceborne geodetic sensors for monitoring the hydrological cycle. Nevertheless, the remaining limitations enlighten future works, which can be dealt with improving current methodologies and/or developing new algorithms.

For the inland water application of satellite altimetry, the issue of possible systematic discrepancy e.g bias between retrackers remain open to investigate. As discussed in Chapter 2, waveform shape can vary due to effect of wind, vegetation canopy, water height and neighboring topography. Therefore, the bias between retrackers can be various from pass to pass over a virtual station. This makes a challenge as estimating a single bias value for two specific retrackers over a virtual station and applying it would not lead to better results. A possible way to go is to remove any bias between retrackers by investigating the bias at the waveform level and over each pass, individually. In such investigation one can classify the waveforms of each pass into classes of waveforms with similar sensitivity to the algorithm of retracking and find out the biases of them.

In order to derive river discharge from altimetric water level, this study built the rating curve using simple quadratic estimation. Indeed, as of future work different rating curves can be tested using different numerical and physically based approximation methods like polynomial regression, power type equation, etc. Moreover, the rating curve can be established via a look-up table from the obtained relationship between water level and river discharge either from empirical or from statistical approach.

As discussed extensively at the end of Chapter 3, the promising results of using stochastic process model and Kalman filter estimation open rooms for further investigations. In this context, other stochastic process models than the one used in this study can be constructed. For instance the model can be built on the river discharge itself rather than its residual or as other alternative the model can be developed by designing twelve state transition models belonging to different months. The question, therefore, is: Which model performs the best? Which model is less sensitive to the uncertainty of observations? These questions can be answered within future works of this study.

Apart from setting of the stochastic process model, the linear dynamic system comprising process model and observation equation can be solved for more than one discharge gauge. This means that the process model can be included by the covariance and cross-covariance information of river discharge belonging to different gauges or catchments. With this approach, one can estimate river discharge of an ungauged catchment through its cross-covariance information with gauged catchments. This cross-covariance information can be derived from the old data sets or from available models. Moreover, it is expected that various noise level of observations in the linear observation equation would lead to different estimation of Kalman filter. Therefore, the effect of observation noise level on the estimated river discharge by Kalman filter should be also addressed in future works of this study.

This study has used GRACE satellites for investigation on the hydrological water storage changes. However, it is known that GRACE has already outlived its predicted lifetime by more than five years. It is attempting to keep GRACE running until the GRACE Follow-On mission is fully operational. Nevertheless, in reality GRACE can fail at any time causing an outage in water storage changes data. Therefore, in future work alternative approach must be sought to provide backup plan dealing with any gap in the data.

This study showed the potential of spaceborne geodetic sensors for estimation of the actual evapotranspiration. The results concluded that geodetic sensors are useful tools for determining  $ET_a$  for most non-desert catchments with hot and warm summers. However, the  $ET_a$  from spaceborne geodetic sensors can be even improved by assimilation approaches. This means in future works, different types of stochastical process models together with the filtering and smoothing techniques can be employed to obtain a desirable evapotranspiration. In such approach one can assimilate the estimation from different sensors and *in situ* measurements with their respective uncertainties to obtain more meaningful results for hydrology. It is also expected that with future speceborn geodetic sensors and improved background models, the resulting  $ET_a$  would be more practical for hydrological applications.

## Bibliography

- Aeronautics & Space Engineering Board, N. R. C.: The Global Positioning System: A Shared National Asset, The National Academies Press, [http://www.nap.edu/openbook.php?record\\_id=4920](http://www.nap.edu/openbook.php?record_id=4920), 1995.
- Alsdorf, D. and Lettenmaier, D. P.: Tracking Fresh Water from Space, *Science*, 301, 1491–1494, doi:10.1126/science.1089802, 2003.
- Alsdorf, D., Rodriguez, E., and Lettenmaier, D. P.: Measuring surface water from space, *Reviews of Geophysics*, 45, RG2002, doi:10.1029/2006RG000197, 2002.
- Anderberg, M.: Cluster Analysis and Applications, Academic Press, New York, 1973.
- Anzenhofer, M., Shum, C. K., and Rentsh, M.: Coastal Altimetry and Applications, Tech. Rep. 464, Geodetic and GeoInformation Science, Department of Civil and Environmental Engineering and Geodetic Science, The Ohio State University, Columbus, Ohio 43210-1275, 1999.
- Baarda, W.: A testing procedure for use in geodetic networks, Netherlands Geodetic Commission, Delft, Publ 2(5), 1968.
- Badekas, J.: Investigation related to the establishment of a world geodetic system, Tech. Rep. AD0697163, Ohio State university, Department of geodetic science, Columbus, Ohio, 1969.
- Barlier, F. and Lefebvre, M.: A new look at planet Earth: Satellite geodesy and geosciences, *The Century of Space Science*, pp. 1623–1651, 2001.
- Barnett, V. and Lewis, T.: Outliers in statistical data, John Wiley & Sons, Chichester, 1994.
- Baur, O. and Sneeuw, N.: Assessing Greenland ice mass loss by means of point-mass modeling: a viable methodology, *Journal of Geodesy*, 85, doi:10.1007/s00190-011-0463-1, 2011.
- Berrisford, P. and for Medium Range Weather Forecasts, E. C.: The ERA-interim Archive: Version 1.0, ERA report series, European Centre for Medium Range Weather Forecasts, <http://books.google.de/books?id=cHyWQQAACAAJ>, 2009.
- Berry, P., Hoogerboord, J., and Pinnock, R.: Identification of common error signatures in global digital elevation models based on satellite altimeter reference data, *Physics and Chemistry of the Earth, Part A: Solid Earth and Geodesy*, 25, 95–99, doi:10.1016/S1464-1895(00)00016-8, <http://www.sciencedirect.com/science/article/pii/S1464189500000168>, 2000.
- Berry, P. A. M., Garlick, J. D., Freeman, J. A., , and Mathers, E. L.: Global inland water monitoring from multi-mission altimetry, *Geophysical Research Letter*, 32, L16401, doi:10.1029/2005GL022814, 2005.
- Bettadpur, S.: Gravity Recovery and Climate Experiment, Level-2 Gravity Field Product User Handbook, Center for Space Research, The University of Texas at Austin, GRACE 327-734, CSR-GR-03-01, 2007.

- Bingham, R. and Hughes, C.: Observing seasonal bottom pressure variability in the North Pacific with GRACE, *Geophysical Research Letters*, 33, L08 607, doi:10.1029/2005GL025489, 2007.
- Birkett, C. M.: The global remote sensing of lakes, wetlands and rivers for hydrological and climate research, in: *Geoscience and Remote Sensing Symposium, 1995. IGARSS '95. 'Quantitative Remote Sensing for Science and Applications'*, International, vol. 3, pp. 1979–1981 vol.3, doi:10.1109/IGARSS.1995.524084, 1995.
- Bosch, W., Savcenko, R., Flechtner, F., Dahle, C., Mayer-Gürr, T., Stammer, D., Taguchi, E., and Ilk, K.-H.: Residual ocean tide signals from satellite altimetry, GRACE gravity fields, and hydrodynamic modelling, *Geophysical Journal International*, 178(3), 1185–1192, doi:10.1111/j.1365-246X.2009.04281.x, 2009.
- Brown, C. D.: Elements of spacecraft design, American Inst. of Aeronautics and Astronautics, Reston, VA, 2002.
- Brown, G. S.: The Average Impulse Response of a Rough Surface and Its Applications, *IEEE TRANSACTIONS ON ANTENNAS AND PROPAGATION*, AP-25, 1977.
- Brubaker, K. L., Entekhabi, D., and Eagleson, P. S.: Estimation of continental precipitation recycling, *J. Climate*, 6, 1077–1089, doi:[http://dx.doi.org/10.1175/1520-0442\(1993\)006<1077:EOCPR>2.0.CO;2](http://dx.doi.org/10.1175/1520-0442(1993)006<1077:EOCPR>2.0.CO;2), 1993.
- Brutsaert, W. and Parlange, M. B.: Hydrologic cycle explains the evaporation paradox, *Nature*, 396, doi:10.1038/23 845, 1993.
- Burkard, R. K.: Geodesy for the Layman, National Oceanic and Atmospheric Administration, 1983.
- Calmant, S. and Seyler, F.: Continental surface waters from satellite altimetry, *Comptes Rendus Geoscience*, 338, 1113–1122, doi:10.1016/j.crte.2006.05.012, 2006.
- Calmant, S., da Silva, J. S., Moreira, D. M., Seyler, F., Shum, C., Crétaux, J.-F., and Gabalda, G.: Detection of Envisat RA2/ICE-1 retracked radar altimetry bias over the Amazon basin rivers using GPS, *Advances in Space Research*, pp. –, doi:10.1016/j.asr.2012.07.033, <http://www.sciencedirect.com/science/article/pii/S0273117712005091>, 2012.
- Cazenave, A., Bonnefond, P., Dominh, K., and Schaeffer, P.: Caspian sea level from Topex-Poseidon altimetry: Level now falling, *Geophysical Research Letters*, 24(8), 881–884, doi:10.1029/97GL00809, 1997.
- Chelton, D. B., Ries, J. C., Haines, B. J., Fu, L.-L., and Callahan, P. S.: Satellite Altimetry, in: *Satellite Altimetry and Earth Sciences: A Handbook of Techniques and Applications*, Fu, L.-L. and Cazenave, A. (eds.), pp. 1–132, 2001.
- Chen, J. L. and Wilson, C. R.: Low degree gravitational changes from GRACE, Earth Rotation, geophysical models, and satellite laser ranging, *Journal of Geophysical Research*, 113, B06 402, doi:10.1029/2007JB005397, 2008.
- Chen, J. L., Wilson, C. R., and Seo, K.-W.: S2 tide aliasing in GRACE time-variable gravity solutions, *Journal of Geodesy*, 83, 679–687, doi:10.1007/s00190-008-0282-1, 2008a.
- Chen, J. L., Wilson, C. R., and Tapley, B. D.: Interannual variability of Greenland ice losses from satellite gravimetry, *Journal of Geophysical Research*, 116, doi:10.1029/2010JB007789, 2011.
- Chen, Y., Schaffrin, B., and Shum, C. K.: Continental Water Storage Changes from GRACE Line-of-Sight Range Acceleration Measurements, VI Hotine-Marussi Symposium on Theoretical and Computational Geodesy,

- International Association of Geodesy Symposia, 132, 62–66, doi:10.1007/978-3-540-74584-6-10, 2008b.
- Cheng, M. and Ries, J.: GRACE Technical Note 05: Monthly estimates of C20 from 5 SLR satellites, 2011.
- Chow, V.-T.: Handbook of applied hydrology : a compendium of water-resources technology, New York: McGraw-Hill, 1964.
- Coe, M. T. and Brikett, C. M.: Calculation of river discharge and prediction of lake height from satellite radar altimetry: Example for the Lake Chad basin, Water Resource Research, 70, W102205, doi:10.1029/2003WR002543, 2004.
- Crétaux, J.-F. and Birkett, C.: Lake studies from satellite radar altimetry, Comptes Rendus Geoscience, 338, 1098–1112, doi:10.1016/j.crte.2006.08.002, <http://www.sciencedirect.com/science/article/pii/S1631071306002318>, 2006.
- Crétaux, J.-F., Calmant, S., Romanovski, V., Shabunin, A., Lyard, F., Bergé-Nguyen, M., Cazenave, A., Hernandez, F., and Perosanz, F.: An absolute calibration site for radar altimeters in the continental domain: Lake Issykkul in Central Asia, Journal of Geodesy, 83, 723–735, doi:10.1007/s00190-008-0289-7, 2009.
- Crétaux, J.-F., Jelinski, W., Calmant, S., Kouraev, A., Vuglinski, V., Bergé-Nguyen, M., Gennero, M., Nino, F., Rio, R. A. D., Cazenave, A., and Maisongrande, P.: SOLS: A lake database to monitor in the Near Real Time water level and storage variations from remote sensing data, Advances in Space Research, 47, 1497–1507, doi:10.1016/j.asr.2011.01.004, 2011.
- da Silva, J. S., Calmant, S., Seyler, F., Filho, O. C. R., Cochonneau, G., and Mansur, W. J.: Water levels in the Amazon basin derived from the ERS 2 and ENVISAT radar altimetry missions, Remote Sensing of Environment, 114, 2160–2181, doi:10.1016/j.rse.2010.04.020, <http://www.sciencedirect.com/science/article/pii/S0034425710001331>, 2010.
- Dabo-Niang, S., Ferraty, F., and Vieu, P.: On the using of modal curves for radar waveforms classification, Computational Statistics & Data Analysis, 51, 4878–4890, doi:10.1016/j.csda.2006.07.012, 2007.
- Davis, C. H.: A Surface and Volume Scattering Retracking Algorithm for Ice Sheet Satellite Altimetry, Geoscience and Remote Sensing, IEEE Transactions on, 31, 811–818, doi:10.1109/36.239903, 1993.
- Davis, C. H.: Growth of the Greenland Ice Sheet: A Performance Assessment of Altimeter Retracking Algorithms, Geoscience and Remote Sensing, IEEE Transactions on, 33, 1108–1116, doi:10.1109/36.469474, 1995.
- Davis, C. H.: A Robust Threshold Retracking Algorithm for Measuring Ice-Sheet Surface Elevation Change from Satellite Radar Altimeters, Geoscience and Remote Sensing, IEEE Transactions on, 35, 974–979, doi:10.1109/36.602540, 1997.
- Deng, X.: Improvement of Geodetic Parameter Estimation in Coastal Regions from Satellite Radar Altimetry, Ph.D. thesis, Curtin University of Technology, 2003.
- Deng, X. and Featherstone, W. E.: A coastal retracking system for satellite radar altimeter waveforms: Application to ERS-2 around Australia, Journal of Geophysical Research, 111, C06012, doi:10.1029/2005JC003039, 2006.
- Dickey, J., Bentley, C., Bilham, R., Carton, J., Eanes, R., Herring, T., Kaula, W., Lagerloef, G., Rojstaczer, S., Smith, W., van den Dool, H., Wahr, J., and Zuber, M.: Gravity and the hydrosphere: new frontier., Hydrological Science, 44(3), 407–415, doi:10.1080/0262669909492236, 1999.

- Dixon, W. J.: Ratios Involving Extreme Values, *The Annals of Mathematical Statistics*, 22, pp. 68–78, <http://www.jstor.org/stable/2236702>, 1951.
- Döll, P., Kaspar, F., and Lehner, B.: A global hydrological model for deriving water availability indicators: model tuning and validation, *Journal of Hydrology*, 270, 105–134, doi:10.1016/S0022-1694(02)00283-4, <http://www.sciencedirect.com/science/article/pii/S0022169402002834>, 2003.
- Douglas, B., Klosko, S., Marsh, J., and Williamson, R.: Tidal parameters from the variation of inclination of GEOS-1 and GEOS-2, *Celestial mechanics*, 10, 165–178, doi:10.1007/BF01227616, 1974.
- Drinkwater, M. R., Floberghagen, R., Haagmans, R., Muzi, D., and Popescu, A.: GOCE: ESA's first Earth Explorer core mission, in: *Earth gravity field from space – from sensors to Earth sciences*, edited by Beutler, G. B., Drinkwater, M. R., Rummel, R., and von Steiger, R., vol. 18 of *Space Sciences Series*, pp. 419–432, Kluwer academic publishers, 2003.
- Eanes, R. and Bettadpur, S.: The CSR3.0 global ocean tide model: Diurnal and semi-diurnal ocean tides from TOPEX/POSEIDON altimetry, *Tech. Rep. CRS-TM-96-05*, Centre for Space Research, University of Texas, Austin, Texas, 1996.
- Eicker, A., Mayer-Guerr, T., and Ilk, K.: Improved Resolution of a GRACE Gravity Field Model by Regional Refinements, in: *Observing our Changing Earth*, edited by Sideris, M., vol. 133 of *International Association of Geodesy Symposia*, doi:10.1007/978-3-540-85426-5\_12, 2008.
- Fekete, B. M. and Vörösmarty, C. J.: The current status of global river discharge monitoring and potential new technologies complementing traditional discharge measurements, *Predictions in Ungauged Basins: PUB Kick-off (Proceedings of the PUB Kick-off meeting held in Brasilia, 20-22 November 2002)*, IAHS Publ. 309, 2007.
- Fekete, B. M., Vörösmarty, C. J., Roads, J. O., and Willmott, C. J.: Uncertainties in Precipitation and Their Impacts on Runoff Estimates, *Journal of Climate*, 17, 294–304, 2004.
- Fersch, B.: Large scale water balance estimation from downscaled atmospheric moisture budgets and evaluation with global climatological data sets and the GRACE spaceborne gravimetry, Ph.D. thesis, University of Augsburg, 2011.
- Flechtner, F.: GFZ Level-2 processing standards document for Level-2 product Release 0004, *Tech. Rep. GR-GFZ-STD-001*, Deutsches GeoForschungsZentrum (GFZ), Potsdam , Germany, 2007.
- Flechtner, F., Schmidt, R., and Meyer, U.: De-aliasing of short-term atmospheric and oceanic mass variations for GRACE, *Observation of the Earth System from Space, Part II*, 83–97, doi: 10.1007/3-540-29522-4-7, 2006.
- Flechtner, F., Watkins, M., Morton, P., and Webb, F.: Status of the GRACE Follow-on Mission, in: *Joint GST-M/SPP Final Colloquium*, Potsdam, Germany, 2012.
- Förste, C., Stubenvoll, R., Flechtner, F., Meyer, U., König, R., Neumayer, H., Biancale, R., Lemoine, J. M., Bruinsma, S., Loyer, S., Barthelmes, F., and Esselborn, S.: The GeoForschungsZentrum Potsdam/Groupe de Recherche de Géodésie Spatiale satellite-only and combined gravity field models: EIGEN-GL04S1 and EIGEN-GL04C, *Journal of Geodesy*, 82, 331–346, doi: 10.1007/s00190-007-0183-8, 2008.

- Frappart, F., Cazenave, A., Seyler, F., , and Calmant, S.: Comparison of the ENVISAT waveform retrackers over inland waters, in: Proceeding of the 2004 Envisat & ERS Symposium, 2004.
- Frappart, F., Calmant, S., Cauhopé, M., Seyler, F., and Cazenave, A.: Preliminary results of ENVISAT RA-2-derived water levels validation over the Amazon basin, *Remote Sensing of Environment*, 100, 252–264, doi:10.1016/j.rse.2005.10.027, <http://www.sciencedirect.com/science/article/pii/S0034425705003585>, 2006a.
- Frappart, F., Minh, K. D., L'Hermitte, J., Cazenave, A., Ramillien, G., Le Toan, T., and Mognard-Campbell, N.: Water volume change in the lower Mekong from satellite altimetry and imagery data, *Geophysical Journal International*, 167, 570–584, doi:10.1111/j.1365-246X.2006.03184.x, 2006b.
- Frappart, F., Papa, F., Famiglietti, J. S., Prigent, C., Rossow, W. B., and Seyler, F.: Interannual variations of river water storage from a multiple satellite approach: A case study for the Rio Negro River basin, *Journal of Geophysical Research*, 113, D21 104, doi:10.1029/2007JD009438, 2008.
- Fu, L.-L. and Cazenave, A.: *Satellite Altimetry and Earth Sciences: A Handbook of Techniques and Applications*, International Geophysical series, 2001.
- Fu, L.-L., Christensen, E., and Yamarone, C. A.: TOPEX/POSEIDON mission overview, *Journal of Geophysical Research*, 99, 1994.
- Garrison, T.: *Essentials of oceanography*, BROOKS COLE PUB CO, 2008.
- Gates, W. L.: AMIP: The Atmospheric Model Intercomparison Project, Program for Climate Model Diagnosis and Intercomparison (PCMDI), PCMDI Report, No. 7, 1997.
- Gelb, A.: *Applied optimal estimation*, The M. I. T. Press, 1974.
- Getirana, A. C. V. and Peters-Lidard, C.: Water discharge estimates from large radar altimetry datasets in the Amazon basin, *Hydrology and Earth System Sciences Discussions*, 9, 7591–7611, doi:10.5194/hessd-9-7591-2012, <http://www.hydrol-earth-syst-sci-discuss.net/9/7591/2012/>, 2012.
- Gilchrist, W. G.: *Statistical modelling with quantile functions*, London: Chapman & Hall, 2000.
- Güntner, A.: Improvement of Global Hydrological Models Using GRACE Data, *Surveys in Geophysics*, 29, 375–397, doi:10.1007/s10712-008-9038-y, 2008.
- Gommenginger, C., Thibaut, P., Fenoglio-Marc, L., Quartly, G., Deng, X., Gomez-Enri, J., Challenor, P., and Gao, Y.: Retracking altimeter waveforms near the coasts, in: *Coastal Altimetry*, edited by Vignudelli, S., Kostianoy, A. G., Cipollini, P., and Benveniste, J., pp. 61–102, Springer, <http://eprints.soton.ac.uk/174869/>, 2011.
- Grubbs, F. E.: Sample criteria for testing outlying observations, *Ann. Math. Statistics*, 21, 27–58, 1950.
- Habib, E., Krajewski, W. F., and Kruger, A.: Sampling Errors of Tipping-Bucket Rain Gauge Measurements, *Journal of Hydrologic Engineering*, 6, doi:10.1061/(ASCE)1084-0699(2001)6:2(159), 2001.
- Haines, B. J., Desai, S. D., and Born, G. H.: The Harvest Experiment: Calibration of the Climate Data Record from TOPEX/Poseidon, Jason-1 and the Ocean Surface Topography Mission, *Marine Geodesy*, 33, 91–113, doi:10.1080/01490419.2010.491028, 2010.

- Hamming, R. W.: Digital filters, Wiley, New York, 1998.
- Han, S. C., Jekelli, C., and Shum, C. K.: Time-variable aliasing effects of ocean tides, atmosphere, and continental water mass on monthly mean GRACE gravity field, *Journal of Geophysical Research*, 109, B04403, doi:10.1016/j.jog.2004.08.002, 2004.
- Han, S. C., Shum, C. K., and Masumoto, K.: GRACE observations of M2 and S2 ocean tides underneath the Filchner-Ronne and Larsen ice shelves, Antarctica, *Geophysical Research Letters*, 32, L20311, doi:10.1029/2005GL024296, 2005.
- Han, S. C., Shum, C. K., and Masumoto, K.: Ocean tidal solutions in Antarctica from GRACE inter-satellite tracking data, *Geophysical Research Letters*, 34, L21607, doi:10.1029/2007GL031540, 2007.
- Hartigan, J.: Cluster Algorithms, WDover publications, Inc., New York, 1975.
- Hayne, G. S., Hancock, D. W., and Purdy, C. L.: The corrections for significant wave height and attitude effects in the TOPEX radar altimeter, *Journal of Geophysical Research*, 99, 24 941–24 955, doi:10.1029/94JC01777, 1994.
- Hendriks, M. R.: Introduction to Physical Hydrology, Oxford University Press Inc., 2010.
- Hinderer, J., Andersen, O., Lemoine, F., Crossley, D., and Boy, J. P.: Seasonal changes in the European gravity field from GRACE: A comparison with superconducting gravimeters and hydrology model predictions, *Journal of Geodynamics*, 41, doi:10.1016/j.jog.2005.08.037, 2006.
- Hirschi, M., Viterbo, P., and Seneviratne, S. I.: Basin-scale water-balance estimates of terrestrial water storage variations from ECMWF operational forecast analysis, *Geophysical Research Letters*, 33, L21401, doi:10.1029/2006GL027659, 2005.
- ITG-GRACE: ITG-Grace2010, Unconstrained monthly solutions, <http://www.igg.uni-bonn.de/apmg/index.php?id=itg-grace2010>, 2010.
- Kalman, R. E.: A new approach to linear filtering and prediction problems, *Transactions of the ASME, Series D, Journal of Basic Engineering*, 82, 35–45, 1960.
- Kalman, R. E. and Bucy, R. S.: New results in linear filtering and prediction theory, *Transactions of the ASME, Series D, Journal of Basic Engineering*, 83, 95–107, 1961.
- Kaula, W. M.: Theory of satellite geodesy: applications of satellites to geodesy, Dover Publications, Mineola, NY, dover ed. edn., 2000.
- Kececioglu, D.: Reliability and life testing handbook, no. Bd. 2 in Reliability and Life Testing Handbook, PTR Prentice Hall, <http://books.google.de/books?id=hRsFAQAAIAAJ>, 1993.
- Kelso, T. S.: CelesTrak, <http://celesttrak.com/>, 2000.
- Kern, M., Preimesberger, T., Allesch, M., Pail, R., Bouman, J., and Koop, R.: Outlier detection algorithms and their performance in GOCE gravity field processing, *Journal of Geodesy*, 78, 509–519, doi:10.1007/s00190-004-0419-9, 2005.
- Klees, R., Revtova, E. A., Gunter, B. C., Ditmar, P., Oudman, E., Winsemius, H. C., and Savenije, H. H. G.: The design of an optimal filter for monthly GRACE gravity model, *Geophysical Journal International*, 175, 417–432, doi:10.1111/j.1365–246X.2008.03922.x, 2008.

- Kouraev, A. V., Zakharova, E. A., Samain, O., Mognard, N. M., and Cazenave, A.: Ob' river discharge from TOPEX/Poseidon satellite altimetry (1992-2002), *Remote Sensing of Environment*, 93, 238–245, doi:10.1016/j.rse.2004.07.007, <http://www.sciencedirect.com/science/article/pii/S0034425704002184>, 2004.
- Krassovsk, V.: Exploration of the Upper Atmosphere with the Help of the Third Soviet Sputnik, *Proceedings of the IRE*, 47, 289–296, doi:10.1109/JRPROC.1959.287296, 1959.
- Kuroishi, Y.: Improved geoid model determination for Japan from GRACE and a regional gravity field model, *Earth Planets Space*, 61, 807–813, 2009.
- Kurtenbach, E.: Entwicklung eines Kalman-Filters zur Bestimmung kurzzeitiger Variationen des Erdschwerefeldes aus Daten der Satellitenmission GRACE, Ph.D. thesis, University of Bonn, 2011.
- Kusche, J.: Approximate decorrelation and non-isotropic smoothing of time-variable GRACE-type gravity field models, *Journal of Geodesy*, 81, 733–749, doi:10.1007/s00190-007-0143-3, 2007.
- Kusche, J. and Schrama, E. J. O.: Surface mass redistribution inversion from global GPS deformation and Gravity Recovery and Climate Experiment (GRACE), *Journal of Geophysical Research*, 110, B09 409, doi:10.1029/2004JB003556, 2005.
- Kusche, J., Schmidt, R., Petrovic, S., and Rietbroek, R.: Decorrelated GRACE time-variable gravity solutions by GFZ, and their validation using a hydrological model, *Journal of Geodesy*, 83, 903–913, doi:10.1007/s00190-009-0308-3, 2009.
- Launius, R. D.: What Are Turning Points in History, and What Were They for the Space Age?, in: *Societal Impact of Space flight*, edited by Dick, S. J. and Launius, R. D., The NASA history series, NASA SP-2007-4801, pp. 19–39, National Aeronautics and Space Administration, 2009.
- Laxon, S.: Sea ice altimeter processing scheme at the EODC, *International Journal of Remote Sensing*, 15, 915–924, doi:10.1080/01431169408954124, 1994.
- Lee, H. K.: Radar Altimetry methods for Solid earth Geodynamic Studies, Master's thesis, University of Ohio, 2008.
- Legrésy, B. and Rémy, F.: Surface characteristics of the Antarctic ice sheet and altimetric observations, *Journal of Glaciology*, 43(144), 265–275, 1997.
- Leon, J., Calmant, S., Seyler, F., Bonnet, M.-P., Cauhopé, M., Frappart, F., Filizola, N., and Fraizy, P.: Rating curves and estimation of average water depth at the upper Negro River based on satellite altimeter data and modeled discharges, *Journal of Hydrology*, 328, 481–496, 2006.
- LeProvost, C., Genco, M. L., Lyard, F., Vincent, P., and Canceli, P.: Spectroscopy of the ocean tides from a finite element hydrodynamic model, *Journal of Geophysical Research*, 99(C12), 24 777–24 797, 1994.
- Liu, L., Wahr, J., Howat, I., Khan, S. A., Joughin, I., and Furuya, M.: Constraining ice mass loss from Jakobshavn Isbræ (Greenland) using InSAR-measured crustal uplift, *Geophysical Journal International*, 188, 994–1006, doi:10.1111/j.1365-246X.2011.05317.x, 2012.
- Lomb, N. R.: Least squares frequency analysis of unequally spaced data, *Astrophysics and Space Science*, 39, 447–462, 1976.

- Lorenz, C. and Kunstmann, H.: The hydrological cycle in three state-of-the-art reanalyses: intercomparison and performance analysis, *Journal of Hydrometeorology*, 13, 1397–1420, doi:10.1175/JHM-D-11-088.1, 2012.
- Lyard, F., Lefevre, F., Letellier, T., and Francis, O.: Modelling the global ocean tides: modern insights from FES2004, *Ocean Dynamics*, 56, 394–415.
- Macrander, A., Böning, C., Boebel, O., and Schröter, J.: Validation of GRACE Gravity Fields by In-Situ Data of Ocean Bottom Pressure, *Advanced Technologies in Earth Sciences*, part 2, 169–185, doi: 10.1007/978-3-642-10228-8-14, 2010.
- Maidment, D. R.: *Handbook of hydrology*, McGraw-Hill, 1993.
- Markowitz, W.: Photographic determination of the moon's position, and applications to the measure of time, rotation of the earth, and geodesy, *The Century of Space Science*, 59, 69, 1954.
- Marth, P. C., Jensen, J. R., Kilgus, C. C., Perschy, J. A., MacArthur, J. L., Hancock, D. W., Hayne, G. S., Purdy, C. L., Rossi, L. C., and Koblinsky, C. J.: Prelaunch Performance of the NASA Altimeter for the TOPEX/POSEIDON Project, *Geoscience and Remote Sensing, IEEE Transactions on*, 31, 315 –332, doi: 10.1109/36.214909, 1993.
- Martin, T. V., Zwally, H., Brenner, A. C., and Bindschadler, R. A.: Analysis and Retracking of Continental Ice Sheet Radar Altimeter Waveforms, *Journal of Geophysical Research*, 88, 1608–1616, doi: 10.1029/JC088iC03p01608, 1983.
- Massey, F. J.: The Kolmogorov-Smirnov Test for Goodness of Fit, *Journal of the American Statistical Association*, 46, 68–78, 1951.
- Matsumoto, K., Takanezawa, T., and Ooe, M.: Ocean Tide Models Developed by Assimilating TOPEX/POSEIDON Altimeter Data into Hydrodynamical Model: A Global Model and a Regional Model around Japan, *Journal of Oceanography*, 56, doi:10.1023/A:1011157212596, 2000.
- Melachroinos, S. A., Lemoine, J. M., Tregoning, P., and Biancale, R.: Quantifying FES2004 S2 tidal model from multiple space-geodesy techniques, GPS and GRACE, over NorthWest Australia, *Journal of Geodesy*, 83, 915–923, doi:10.1007/s00190-009-0309-2, 2009.
- Milzow, C., Krogh, P. E., and Bauer-Gottwein, P.: Combining satellite radar altimetry, SAR surface soil moisture and GRACE total storage changes for hydrological model calibration in a large poorly gauged catchment, *Hydrol. Earth Syst. Sci.*, 15, 1729–1743, doi:10.5194/hess-15-1729-2011, 2011.
- Miralles, D. G., De Jeu, R. A. M., Gash, J. H., Holmes, T. R. H., and Dolman, A. J.: An application of GLEAM to estimating global evaporation, *Hydrology and Earth System Sciences Discussions*, 8, 1–27, doi:10.5194/hessd-8-1-2011, <http://www.hydrol-earth-syst-sci-discuss.net/8/1/2011/>, 2011.
- Moritz, H.: Advanced physical geodesy, Wichmann, Karlsruhe, 2. ed., repr. from the 1. ed. edn., <http://digitoool.hbz-nrw.de:1801/webclient/DeliveryManager?pid=3114130>, 1989.
- Neumeyer, J., Barthelmes, F., Kroner, C., Petrovic, S., Schmidt, R., Virtanen, H., and Wilmes, H.: Analysis of gravity field variations derived from Superconducting Gravimeter recordings, the GRACE satellite and hydrological models at selected European sites, *Earth, Planets and Space*, 60, 505–518, 2008.
- Papa, F., Prigent, C., Durand, F., and Rossow, W. B.: Wetland dynamics using a suite of satellite observations: A case study of application and evaluation for the Indian Subcontinent, *Geophysical Research Letters*, 33,

- L08 401, doi:10.1029/2006GL025767, 2006.
- Papa, F., Durand, F., Rossow, W. B., Rahman, A., and Bala, S. K.: Satellite altimeter-derived monthly discharge of the Ganga-Brahmaputra River and its seasonal to interannual variations from 1993 to 2008, *Journal of Geophysical Research*, 115, C12 013, doi:10.1029/2009JC006075, 2010.
- Papa, F., Biancamaria, S., Lion, C., and Rossow, W.: Uncertainties in Mean River Discharge Estimates Associated With Satellite Altimeter Temporal Sampling Intervals: A Case Study for the Annual Peak Flow in the Context of the Future SWOT Hydrology Mission, *Geoscience and Remote Sensing Letters*, IEEE, 9, 569–573, doi:10.1109/LGRS.2011.2174958, 2012.
- Partington, K. C., Cudlip, W., and Rapley, C. G.: An Assessment of the Capability of the Satellite Radar Altimeter for Measuring Ice Sheet Topographic Change, *International Journal of Remote Sensing*, 12, No. 3, 585–609, doi:10.1080/01431169108929674, 1991.
- Paulson, A., Zhong, S., and Wahr, J.: Inference of mantle viscosity from GRACE and relative sea level data, *Geophysical Journal International*, 171, 497–508, doi:10.1111/j.1365-246X.2007.03556.x, 2007.
- Peltier, W. R.: Ice Age Paleotopography, 265, 195–201, doi:10.1126/science.265.5169.195, 1994.
- PILPS: PILPS Special Issues, *Global and Planetary Change*, Elsevier Science, 13, Issues 1-4, 3-223. 1998, 19, Issues 1-3, 1-276. 2003, 38, Issues 1-2, 1-222, 1996.
- Quarry, G. D., Srokosz, M. A., and McMillan, A. C.: Analyzing Altimeter Artifacts: Statistical Properties of Ocean Waveforms, *Journal of Atmospheric and Oceanic Technology*, 18, 2074–2091, doi:10.1175/1520-0426(2001)018<2074:AAASPO>2.0.CO;2, 2001.
- Rangelova, E., van der Wal, W., Braun, A., Sideris, M., and Wu, P.: Analysis of Gravity Recovery and Climate Experiment time-variable mass redistribution signals over North America by means of principal component analysis, *Journal of Geophysical Research*, 112, F03 002, doi:10.1029/2006JF000615, 2007.
- Ray, R.: A global ocean tide model from TOPEX/POSEIDON altimetry: GOT99, Tech. Rep. NASA Tech. Mem. 209478, Goddard Space Flight Centre, Greenbelt, MD, USA, 1999.
- Ray, R. D. and Luthcke, S. B.: Tide model errors and GRACE gravimetry: towards a more realistic assessment, *Geophysical Journal International*, 167(3), 1055–1059, doi:10.1111/j.1365-246X.2006.03229.x, 2006.
- Ray, R. D., Rowlands, D. D., and Egbert, G. D.: Tidal models in a new era of satellite gravimetry, *Space Science Reviews*, 108, 271–282, doi:10.1023/A:1026223308107, 2003.
- Reichle, R. H., Koster, R. D., Lannoy, G. J. M. D., Forman, B. A., Liu, Q., Mahanama, S. P. P., and Toure, A.: Assessment and enhancement of MERRA land surface hydrology estimates, *Journal of Climate*, 24, 6322–6338, doi:10.1175/JCLI-D-10-05033.1., 2011.
- Ridley, J. K. and Partington, K. C.: A Model of Satellite Radar Altimeter Return from Ice Sheets, *International Journal of Remote Sensing*, 9, 601–624, doi:10.1080/01431168808954881, 1988.
- Rieger, J. and Güntner, A.: Time Variation In Hydrology and Gravity, *Earth, Moon, and Planets*, 94(1), 41–55, doi:10.1007/s11038-005-1831-8, 2005.
- Rieger, J., Tourian, M., Devaraju, B., and Sneeuw, N.: Analysis of grace uncertainties by hydrological and hydro-meteorological observations, *Journal of Geodynamics*, 59, 16–27, doi:10.1016/j.jog.2012.02.001, 2012.

- Rienecker, M. M. and Coauthors: MERRA: NASA's modern-era retrospective analysis for research and applications, *J. Climate*, 24, 3624–3648, doi:<http://dx.doi.org/10.1175/JCLI-D-11-00015.1>, 2011.
- Rietbroek, R., Legrand, P., Wouters, B., Lemoine, J. M., Ramillien, G., and Hughes, C. W.: Comparison of in situ bottom pressure data with GRACE gravimetry in the Crozet-Kerguelen region, *Geophysical Research Letters*, 33, L21 601, doi:10.1029/2006GL027452, 2007.
- Rignot, E., Velicogna, I., van den Broeke, M. R., Monaghan, A., and Lenaerts, J.: Acceleration of the contribution of the Greenland and Antarctic ice sheets to sea level rise, *Geophysical Research Letters*, 38, doi:10.1029/2011GL046583, 2011.
- Rodell, M. and Famiglietti, J.: Detectability of variations in continental water storage from satellite observation of time dependent gravity field, *Water Resource Research*, 35, 2705–2723, doi:10.1029/1999WR900141, 1999.
- Rodell, M., Famiglietti, J., Chen, J., Seneviratne, S., Viterbo, P., Holl, S., and Wilson, C.: Basin scale estimates of evapotranspiration using GRACE and other observations, *Geophysical Research Letters*, 31, L20 504, doi:10.1029/2004GL020873, 2004a.
- Rodell, M., Houser, P., Jambor, U., Gottschalck, J., Mitchell, K., Meng, C.-J., Arsenault, K., Cosgrove, B., Radakovich, J., Bosilovich, M., Entin, J., Walker, J., Lohmann, D., and Toll, D.: The Global Land Data Assimilation System, *Bull. Amer. Meteor. Soc.*, 85, 381–394, 2004b.
- Rodell, M., Chen, J., Kato, H., Famiglietti, J., Nigro, J., and Wilson, C.: Estimating groundwater storage changes in the Mississippi River basin (USA) using GRACE, *Hydrogeology Journal*, 15, 159–166, doi:10.1007/s10040-006-0103-7, 2006.
- Rodriguez, E. and Martin, J. M.: Assessment of the TOPEX altimeter performance using waveform retracking, *JOURNAL OF GEOPHYSICAL RESEARCH*, 99, 24 957–24 969, 1994.
- Rousseeuw, P. J. and Leroy, A. M.: Robust regression and outlier detection, John Wiley & Sons, Inc., New York, NY, USA, 1987.
- Sasgen, I., van den Broeke, M., Bamber, J. L., Rignot, E., SÃyrensen, L. S., Wouters, B., Martinec, Z., Velicogna, I., and Simonsen, S. B.: Timing and origin of recent regional ice-mass loss in Greenland, *Earth and Planetary Science Letters*, 333-334, 293–303, doi:10.1016/j.epsl.2012.03.033, 2012.
- Satoh, M.: Atmospheric Circulation Dynamics and Circulation Models, Springer, 2004.
- Schrama, E. J. O. and Wouters, B.: Revisiting Greenland ice sheet mass loss observed by GRACE, *Journal of Geophysical Research*, 116, doi:10.1029/2009JB006847, 2011.
- Schrama, E. J. O., Wouters, B., and Lavallée, D.: Signal and noise in Gravity Recovery and Climate Experiment (GRACE) observed surface mass variations, *Journal of Geophysical Research*, 112, B08 407, doi:10.1029/2006JB004882, 2007.
- Seeber, G.: Satellite geodesy, Berlin New York: Walter de Gruyter, 2003.
- Segall, P. and Davis, J.: GPS applications for geodynamics and earthquake studies, *Annual Reviews of Earth and Planetary Science*, 25, 301–336, 1997.

- Seo, K. W., Wilson, C. R., Han, S. C., and Waliser, D. E.: Gravity recovery and climate experiment (GRACE) alias error from ocean tides, *Journal of Geophysical Research*, 113, B03 405, doi:10.1029/2006JB004747, 2008.
- Shepherd, A., Ivins, E. R., A, G., Barletta, V. R., Bentley, M. J., Bettadpur, S., Briggs, K. H., Bromwich, D. H., Forsberg, R., Galin, N., Horwath, M., Jacobs, S., Joughin, I., King, M. A., Lenaerts, J. T. M., Li, J., Ligtenberg, S. R. M., Luckman, A., Luthcke, S. B., McMillan, M., Meister, R., Milne, G., Mouginot, J., Muir, A., Nicolas, J. P., Paden, J., Payne, A. J., Pritchard, H., Rignot, E., Rott, H., Sandberg Sorensen, L., Scambos, T. A., Scheuchl, B., Schrama, E. J. O., Smith, B., Sundal, A. V., van Angelen, J. H., van de Berg, W. J., van den Broeke, M. R., Vaughan, D. G., Velicogna, I., Wahr, J., Whitehouse, P. L., Wingham, D. J., Yi, D., Young, D., and Zwally, H. J.: A Reconciled Estimate of Ice-Sheet Mass Balance, *Science*, 338, 1183–1189, doi:10.1126/science.1228102, 2012.
- Simmons, A., Uppala, S., Dee, D., and Kobayashi, S.: ERA-Interim: New ECMWF reanalysis products, *ECMWF Newsletter*, 110, 25–35, 2006.
- Sneeuw, N.: A Semi-Analytical Approach to Gravity Field Analysis from Satellite Observations, Ph.D. thesis, Technische Universität München, 2000.
- Sneeuw, N.: Future Mission Concepts, in: R. Koop and R. Rummel (eds.) *The Future of Satellite Gravimetry, Report from the Workshop on the Future of Satellite Gravimetry, 12-13 April 2007, ESTEC, Noordwijk, The Netherlands*, 175, 417–432, doi:10.1111/j.1365-246X.2008.03922.x, 2007.
- Stanev, E. V., Peneva, E. L., and Mercier, F.: Temporal and spatial patterns of sea level in inland basins: Recent events in the Aral Sea, *Geophysical Research Letters*, 31, L15 505, doi:10.1029/2004GL020478, 2004.
- Strassberg, G., Scanlon, B., and Rodell, M.: Comparison of seasonal terrestrial water storage variations from GRACE with groundwater-level measurements from the High Plains Aquifer (USA), *Geophysical Research Letters*, 34, L14 402, doi:10.1029/2007GL030139, 2007.
- Swenson, S. and Wahr, J.: Estimated accuracies of regional water storage variations inferred from the Gravity Recovery and Climate Experiment (GRACE), *Water Resources Research*, 39(8), 1223, doi:10.1029/2002WR001808, 2003.
- Syed, T., Famiglietti, J., and Chambers, D.: GRACE-Based Estimates of Terrestrial Freshwater Discharge from Basin to Continental Scales, *Journal of Hydrometeorology*, 10, 22–40, doi:10.1175/2008JHM993.1, 2008.
- Tapley, B. D., Bettadpur, S., Ries, J. C., Thompson, P. F., and Watkins, M. M.: The Gravity Recovery and Climate Experiment: Mission overview and early results, *Geophysical Research Letters*, 31, L09 607, doi:10.1029/2004GL019920, 2004.
- Tourian, M. J., Rieger, J., Sneeuw, N., and Devaraju, B.: Outlier identification and correction for GRACE aggregated data, *Studia Geophysica et Geodaetica*, 55, No. 4, 627–640, doi:10.1007/s11200-009-9007-z, 2011.
- Tourian, M. J., Sneeuw, N., and Bárdossy, A.: A quantile function approach to discharge estimation from satellite altimetry (ENVISAT), *Water Resources Research*, 49, 4174–4186, doi:10.1002/wrcr.20348, 2013.
- Velicogna, I., Wahr, J., and den Dool, H. V.: Can surface pressure be used to remove atmospheric contributions from grace data with sufficient accuracy to recover hydrological signals?, *Journal of Geophysical Research*, 106(B8), 415–16 434, doi:10.1029/2001JB000228, 2001.

- Virtanen, J., Makinen, J., Bilker-Koivula, M., Shum, C., Lee, H., Thomas, M., Kangas, A., Vehviläinen, B., and Nordman, M.: GRACE Water Storage Estimates in Finland and the Effect of Baltic Sea Level Variation, *Eos Trans. AGU*, 88(52), Fall Meet. Suppl., Abstract U21C-0621, 2007.
- Wahr, J., Molenaar, M., and Bryan, F.: The Time-Variability of the Earth's gravity field: Hydrological and oceanic effects and their possible detection using GRACE, *Journal of Geophysical Research*, 103, 30 205–30 230, doi:10.1029/98JB02 844, 1998.
- Wahr, J., Swenson, S., and Velicogna, I.: Accuracy of GRACE mass estimates, *Geophysical Research Letters*, 33, L06 401, doi:10.1029/2005GL025305, 2006.
- Weise, A., Kröner, C., Abe, M., Ihde, J., Jentzsch, G., Naujoks, M., and Wziontek, H. W. H.: Gravity field variations from superconducting gravimeters for GRACE validation, *Journal of Geodynamics*, 48, 325–330, doi:10.1016/j.jog.2009.09.034, 2009.
- Werth, S., Güntner, A., Schmidt, R., and Kusche, J.: Evaluation of GRACE filter tools from a hydrological perspective, *Geophysical Journal International*, 179.
- Wiese, D. N., Visser, P., and Nerem, R. S.: Estimating low resolution gravity fields at short time intervals to reduce temporal aliasing errors, *Advances in Space Research*, 48, 1094 – 1107, doi:10.1016/j.asr.2011.05.027, <http://www.sciencedirect.com/science/article/pii/S0273117711003929>, 2011.
- Wingham, D. J., Rapley, C. G., and Griffiths, H.: New techniques in satellite altimeter tracking systems, in: *ESA Proceedings of the 1986 International Geoscience and Remote Sensing Symposium (IGARSS '86) on Remote Sensing: Today's Solutions for Tomorrow's Information Needs*, vol. 3, pp. 1339–1344, 1986.
- Wouters, B. and Schrama, E. J. O.: Improved accuracy of GRACE gravity solutions through empirical orthogonal function filtering of spherical harmonics, *Geophysical Research Letters*, 34, L23 711, doi:10.1029/2007GL032 098, 2007.
- Yeh, P., Swenson, S., Famiglietti, J., and Rodell, M.: Remote sensing of groundwater storage changes in Illinois using the Gravity Recovery and Climate Experiment (GRACE), *Water Resources Research*, 42, W12 203, doi:10.1029/2006WR005374, 2006.
- Zakharova, E. A., Kouraev, A. V., Cazenave, A., and Seyler, F.: Amazon River Discharge estimated from TOPEX/Poseidon altimetry, *Comptes Rendus Geoscience*, 338, 188–196, doi:10.1016/j.crte.2005.10.003, 2006.
- Zenner, L., Gruber, T., Jäggi, A., and Beutler, G.: Propagation of atmospheric model errors to gravity potential harmonics-impact on GRACE de-aliasing, *Geophysical Journal International*, 182.
- Zieger, A., Hancock, D., Hayne, G., and Purdy, C.: NASA radar altimeter for the TOPEX/POSEIDON Project, *Proceedings of the IEEE*, 79, 810 –826, doi:10.1109/5.90160, 1991.
- Zwally, H. J.: GSFC Retracking Algorithms, <http://icesat4.gsfc.nasa.gov>, 1996.
- Zwally, H. J., Giovinetto, M. B., Beckley, M. A., and Saba, J. L.: Antarctic and Greenland Drainage Systems, GSFC Cryospheric Sciences Laboratory, [http://icesat4.gsfc.nasa.gov/cryo\\_data/ant\\_grn\\_drainage\\_systems.php](http://icesat4.gsfc.nasa.gov/cryo_data/ant_grn_drainage_systems.php), 2012.

# Abbreviations

**CDF** Cumulative Distribution Function

**CHAMP** CHAllenging Minisatellite Payload

**CRU** Climatic Research Unit

**CSR** Center for Space Research

**DLR** Deutsche Zentrum für Luft- und Raumfahrt

**ECMWF** European Centre for Medium-Range Weather Forecasts

**ENVISAT** ENVIronmental SATellite

**EOF** Empirical Orthogonal Function

**EOT** Earth Ocean Tide model

**ERS** European Remote Sensing satellite

**ESA** European Space Agency

**FES** Finite Element Solution

**FFT** Fast Fourier transform

**GDR** Geophysical Data Record

**GEOS** Geodetic Earth Orbiting Satellite

**GFZ** GeoForschungsZentrum

**GLDAS** Global Land Data Assimilation System

**GLEAM** Global Land-surface Evaporation: the Amsterdam Methodology

**GOCE** Gravity Field and Steady-State Ocean Circulation Explorer

**GOT** Global Ocean Tide model

**GPCC** Global Precipitation Climatology Center

**GPCP** Global Precipitation Climatology Project

**GPS** Global Positioning System

**GRACE** Gravity Recovery And Climate Experiment

**GRDC** Global Runoff Data Centre

**IBC** Inter Basin Correlation

**ICC** Inter Cell Correlation

**IZC** Inter Zonal Correlation

**JPL** Jet Propulsion Laboratory

**K-S** Kolmogorov-Smirnov

**LLH** Lake Level Height

**MERRA** Modern Era-Retrospective Analysis for Research and Application

**MMSNR** Monthly Mean Signal to Noise Ratio

**NASA** National Aeronautics and Space Administration

**NCAR** National Center for Atmospheric Research

**NCEP** National Centers for Environmental Prediction

**OBP** Ocean Bottom Pressure

**OCOG** Off Centre Of Gravity

**PC** Principal Component

**RMS** Root Mean Square

**RMSE** Root Mean Square Error

**RSH** River Surface Height

**SDR** Sensor Data Record

**SG** Superconducting Gravimeter

**SLR** Satellite Laser Ranging

**SNR** Signal to Noise Ratio

**SWH** Significant Wave Height

**TRMM** Tropical Rainfall Measuring Mission

**USACE** United States Army Corps of Engineers

**USGS** United States Geological Survey

**WGS** World Geodetic System

# List of Figures

|      |   |    |
|------|---|----|
| 1.1  | Schematic illustration of the hydrological cycle . . . . .  | 11 |
| 1.2  | Spatial and temporal scales of hydrological cycle and spaceborne geodetic sensors . . . . .   | 13 |
| 1.3  | Comparison of different precipitation products for the Amazon catchment . . . . .   | 14 |
| 1.4  | Evolution of available stations with discharge data according to GRDC database . . . . .  | 15 |
| 1.5  | Number of catchments with area larger than 30000 km <sup>2</sup> with discharge data covering different time periods within the period of 1980–2010 . . . . .                           | 15 |
| 1.6  | Spatial distribution for number of available months within the period of 1980–2010 for catchment with area larger than 30000 km <sup>2</sup> . . . . .                                  | 16 |
| 1.7  | Challenges of deriving river discharge from satellite altimetry . . . . .   | 17 |
| 1.8  | Grid-based and catchment based equivalent water height . . . . .  | 19 |
| 1.9  | Challenges of utility of GRACE signals as representative of hydrological water storage changes . .  | 20 |
| 2.1  | Interaction of a pulse and scattering surface, and the procedure of constructing the returned waveform  | 26 |
| 2.2  | Schematic altimeter mean return waveform over ocean surface . . . . .   | 27 |
| 2.3  | 25 randomly selected TOPEX/Poseidon waveforms over Lake Balaton showing various shapes of waveforms, a sample from each type of waveform is shown . . . . .                             | 28 |
| 2.4  | The oval footprint characteristics for flat area belong to 1 sec averages of altimetry at nadir . . . .   | 29 |
| 2.5  | Schematic oval footprint and sub-satellite point, Lake Balaton (Hungary), TOPEX/Poseidon . . . .  | 29 |
| 2.6  | 10 Hz waveforms of altimetry over Balaton Lake belonging to cycle 25 of TOPEX/Poseidon . . . .  | 30 |
| 2.7  | Google Earth imagery over Brahmaputra River at the location of a virtual station . . . . .  | 31 |
| 2.8  | Diagram of the off-nadir effect in along-track height profiles . . . . .  | 31 |
| 2.9  | Off-nadir effect in narrow rivers . . . . .   | 33 |
| 2.10 | Off-nadir effect in large lakes . . . . .   | 34 |
| 2.11 | Outlier elimination procedure using fitting the inter-annual monthly mean variation . . . . .   | 35 |
| 2.12 | A sample of off-nadir affected along-track water level profile from 20Hz measurements over the Don River together with fitted degree two polynomial and the corrected profile . . . . . | 36 |
| 2.13 | Water level profiles over the Don River belong to different passes over the time . . . . .  | 36 |
| 2.14 | The concept of waveform retracking . . . . .  | 37 |
| 2.15 | Two sample waveform from group 1 and 2 of Balaton Lake and the defined tracing gate from different retracking methods . . . . .   | 38 |
| 2.16 | Fitting algorithm for ice-sheet waveform retracking . . . . .   | 40 |
| 2.17 | A sample waveform belongs to cycle 32 over Lake Balaton with its moving average and derivative  | 40 |
| 2.18 | Cross correlation of fitted waveform and a sample of original waveform together with the fitted waveform and shifted fitting waveform . . . . .   | 41 |
| 2.19 | Diagram of detecting the noisy waveforms . . . . .  | 42 |
| 2.20 | 25 randomly selected waveforms over Balaton Lake . . . . .  | 43 |
| 2.21 | Histograms of returned power of waveforms of TOPEX/Poseidon over Lake Balaton at different bins   | 44 |

|   |    |
|---|----|
| 2.22 Smoothing Kernel function . . . . .  | 45 |
| 2.23 The estimated entropy for a range of bandwidth (300–1000) for TOPEX/Poseidon waveforms over lake Balaton . . . . .   | 46 |
| 2.24 Obtained mean, median and modal waveforms over Lake Urmia . . . . .  | 47 |
| 2.25 Result of unsupervised classification over Urmia Lake . . . . .  | 48 |
| 2.26 Modal and median waveforms in the Urmia lakes . . . . .  | 48 |
| 2.27 Water level time series of Urmia Lake before and after retracking . . . . .  | 50 |
| 2.28 Water level time series for Niger River after geophysical and outlier corrections from different retrackers . . . . .  | 52 |
| 2.29 Water level variations over Obidos virtual station at Amazon River belonging to <i>Ocean and Ice-1</i> retrackers for November 2003 and 2005 . . . . .   | 54 |
| 2.30 Water level time series from different retracking methods . . . . .  | 55 |
| <br>  |    |
| 3.1 The discharge gauging stations and the crossing tracks of ENVISAT for different rivers . . . . .  | 58 |
| 3.2 Time series of daily discharge measurements and the river surface height over Niger River from ENVISAT . . . . .  | 59 |
| 3.3 Daily discharge of Niger River in April 2004 . . . . .  | 60 |
| 3.4 Scatter plot of quasi-monthly discharge versus the true monthly discharge value of Niger and Danube rivers for 2002–2012 . . . . .  | 60 |
| 3.5 Comparison of empirical cumulative distribution functions of whole available monthly/daily discharge and monthly/daily discharge at the time of altimetry . . . . .   | 62 |
| 3.6 Scatter plot of simultaneous measurements of discharge versus water level from altimetry with the fitted quadratic empirical rating curve models for the quasi-monthly and monthly discharge data of rivers in group 1 . . . . .  | 65 |
| 3.7 Rating curve from quantile functions over Mekong River . . . . .  | 67 |
| 3.8 Quantile functions from monthly and quasi-monthly discharge of the Mekong River . . . . .   | 68 |
| 3.9 Quantile functions from quasi-monthly discharge of the Mekong River constructed for each year separately . . . . .  | 68 |
| 3.10 Scatter plots of discharge versus the water levels from altimetry for rivers in group 2, produced from the respective quantile functions . . . . .   | 69 |
| 3.11 Scatter plot of simultaneous measurements of discharge versus water level from altimetry with the fitted quadratic empirical rating curve models for the quasi-monthly and monthly discharge data of rivers in group 1 . . . . .   | 70 |
| 3.12 Estimated discharge from the empirical rating curves of simultaneous measurements of discharge and water level from altimetry for rivers in group 1 together with the achieved residual by subtracting the estimated discharge from the <i>in situ</i> measurements . . . . .  | 71 |
| 3.13 Scatter plots of estimated discharge from the statistical method versus estimated discharge from the empirical method of constructed rating curves . . . . .   | 73 |
| 3.14 Estimated discharge in mm/month from the statistical rating curves obtained from the statistical method of performing rating curves out of asynchronous measurements of water level and discharge for different rivers in group 2. Inter-comparison of monthly and quasi-monthly discharge leads to RMSE of 2.3, 1.7 and 1.2 mm/month for the Mekong, Brahmaputra and Don, which correspond to 1%, 1% and 8% error, respectively . . . . . | 73 |
| 3.15 Estimated discharge from the rating curves obtained from the statistical methods of performing rating curve for rivers in group 1 . . . . .  | 75 |

---

|   |     |
|---|-----|
| 3.16 Comparison of estimated discharge by altimetry and the annual cycle computed by excluding data of different years . . . . .  | 77  |
| 3.17 Estimated discharge using Kalman filter over the performed linear dynamic systems for rivers in group 1 . . . . .  | 83  |
| 3.18 Estimated discharge using Kalman filter over the performed linear dynamic systems for rivers in group 2 . . . . .  | 83  |
| 4.1 The behaviour of sinc function between 0 and $\pi$ , which represents the difference between true derivative and central difference in frequency domain . . . . .                                       | 89  |
| 4.2 Spectral analysis on the two data sets of computed mass derivative via central difference scheme . .  | 90  |
| 4.3 $H_1(\omega)$ and $H_2(\omega)$ together with the sinc function . . . . .   | 91  |
| 4.4 Comparison of water storage change from GRACE and un/filtered hydro-meteorological signals over Amazon catchment . . . . .  | 92  |
| 4.5 Polar diagram of correlation and ratio of RMS between GRACE and hydro-meteorological rate of water storage change before and after making the data consistent by filtering with filters $H_1$ and $H_2$ | 92  |
| 4.6 Correlation coefficients of hydro-meteorological signals and the filtered mass derivative signal of GRACE by different radius of Gaussian filter over catchments . . . . .                              | 95  |
| 4.7 Mass deviation, derivative and computed $ET_a$ over the Okavango catchment . . . . .  | 96  |
| 4.8 Spectra of monthly GRACE derivatives (signal) and residual of monthly GRACE derivatives . . . .   | 97  |
| 4.9 Histogram of mass deviation residual over the Okavango catchment . . . . .  | 97  |
| 4.10 Implementing the outlier identification and correction algorithm over the Colorado river basin . .   | 99  |
| 4.11 Detected outliers from GFZ, JPL, CSR and ITG catchment based aggregated monthly solutions . .  | 100 |
| 4.12 Polar diagram of correlation and ratio of RMS between GRACE and hydro-meteorological rate of water storage change before (gray) and after (red) outlier correction . . . . .                           | 101 |
| 4.13 Scatter plot of RMS of mass derivative residual after versus before outlier correction for different catchments . . . . .  | 101 |
| 4.14 Global circulation pattern, from <a href="http://www.fas.org">http://www.fas.org</a> . . . . .   | 103 |
| 4.15 Inter Zonal Correlation of GRACE mass derivative, precipitation and $\nabla \cdot \vec{Q}$ . . . . .   | 104 |
| 4.16 Inter Basin Correlation of GRACE mass derivative, precipitation and $\nabla \cdot \vec{Q}$ . . . . .   | 105 |
| 4.17 Spatial distribution of ICC and its latitudinal dependence . . . . .   | 105 |
| 4.18 Singular value spectrum of mass derivative residual derived from EOF analysis . . . . .  | 106 |
| 4.19 PCs of first mode of EOF analysis on Oceans, land masses and global data set . . . . .   | 106 |
| 4.20 EOF map of mode number 1 derived from EOF analysis . . . . .   | 106 |
| 4.21 Left) IBC Right) IZC of $dM/dt$ residual after reduction of mode 1 from the data set . . . . .   | 107 |
| 4.22 ICC of $dM/dt$ residual with respect to a reference cell at $\phi = 87.5^\circ, \lambda = -177.5^\circ$ after reduction of mode 1 from the data set . . . . .  | 108 |
| 4.23 Ratio of RMS of monthly residuals before and after ICC reduction (after/before) . . . . .  | 108 |
| 4.24 Estimated spectra of first mode's PC from EOF analysis on GRACE residual for different GRACE data centers . . . . .  | 109 |
| 4.25 Comparison of PC of first mode from EOF analysis on $dM/dt$ residual (GFZ) and a GRACE $C_{20}$ time series . . . . .  | 109 |
| 4.26 Inter Cell Correlation of GRACE residual mass derivative with respect to a reference cell at $\phi = 87.5^\circ, \lambda = -177.5^\circ$ . . . . .   | 109 |
| 4.27 Comparison of derivative of $C_{20}$ and its residual spectra from GRACE and SLR . . . . .   | 110 |
| 4.28 Two-dimensional geometry of the Earth, Sun and GRACE's orbit . . . . .   | 111 |

|  |     |
|--|-----|
| 4.29 The secular rate of the ascending node of GRACE's orbit using the observed $a$ , $e$ , $I$ of satellites and $C_{20}$ from GRS80 . . . . .  | 111 |
| 4.30 Sampling of S2 tide where the difference ( $\Delta\Phi$ ) between the satellite's nodal day $\simeq 23.92$ hour and one solar day 24 hour cause the aliasing error. . . . .   | 112 |
| 4.31 A simulated aliased wave of M2 tide with period of 13.6 days which is aliased to different waves by assuming 30 days sampling or using GRACE's days for averaging . . . . .   | 113 |
| 4.32 Spectra of the M2 secondary aliased wave . . . . .  | 113 |
| 4.33 Covariance matrix of estimation of tidal aliasing coefficients for the primary aliasing frequencies of S1, S2 and P1 together with the secondary aliasing frequencies of M2, N2, O1 and Q1 . . . . .                    | 115 |
| 4.34 Estimated amplitude for primary aliasing errors of S2, S1 and P1 and secondary aliasing errors of M2, N2, O1 and Q1 over the spherical harmonic coefficients of GRACE RL05 . . . . .                                    | 116 |
| 4.35 Degree variance of different tidal aliasing error in GRACE RL05 monthly solutions . . . . .   | 116 |
| 4.36 Amplitudes (mm) of the primary tidal aliasing frequencies S2, S1 and P1 from 72 GFZ RL05 monthly solutions . . . . .  | 117 |
| 4.37 Amplitudes (mm) of the secondary tidal aliasing frequencies M2, N2, O1 and Q1 from 72 GFZ RL05 monthly solutions . . . . .  | 118 |
| 4.38 The difference between the amplitude of M2 tide model from three ocean models and the estimated secondary aliased M2 tide in GRACE monthly solutions above the $60^\circ$ latitude . . . . .                            | 119 |
| 4.39 The difference between the amplitude of M2 tide model from three ocean models and the estimated secondary aliased M2 tide in GRACE monthly solutions below the $-60^\circ$ latitude . . . . .                           | 120 |
| 4.40 RMS of the total tidal aliasing errors including primary and secondary . . . . .  | 121 |
| 4.41 Signal to Noise Ratio (SNR) after removing tidal aliasing errors versus before removing over 255 largest catchments . . . . .   | 122 |
| 4.42 The water storage change $dM/dt$ from GRACE before and after removing tidal aliasing error in comparison with the hydro-meteorological water storage change over Western Australia . . . . .                            | 123 |
| 4.43 Greenland drainage divides developed by the Goddard Ice Altimetry Group from ICESat data . . . . .  | 123 |
| 4.44 Post glacial rebound model developed by Paulson et al. (2007) in mm/yr of equivalent water . . . . .  | 124 |
| 4.45 Mass changes over the drainage basins of Greenland before and after removing tidal aliasing error . . . . .   | 124 |
| 4.46 Spectra of the mass change time series over Greenland before and after removing tidal aliasing error . . . . .  | 125 |
| 4.47 RMS of mass derivative residual representing an upper bound of GRACE noise level . . . . .  | 126 |
| 4.48 Latitudinal profile of RMS of mass derivative residual of GRACE data . . . . .  | 127 |
| <br>   |     |
| 5.1 Estimated evapotranspiration from GRACE and hydro-meteorological approach together with the $ET_a$ from different models over Mississippi, Amazon and Lake Chad catchments . . . . .                                     | 131 |
| 5.2 RMS of ensemble standard deviations as representative of absolute modeling discrepancy and RMS of ensemble standard deviation divided by the RMS of ensemble mean indicating the relative modeling discrepancy . . . . . | 132 |
| 5.3 Estimated evapotranspiration from GRACE and hydro-meteorological approaches together with the ensemble mean and standard deviation . . . . .   | 134 |
| 5.4 Scatter plots of monthly values of ensemble mean versus $ET_a$ from GRACE and hydro-meteorological approaches . . . . .  | 135 |
| 5.5 Scatter plot of monthly mean values of ensemble mean versus monthly mean of $ET_a$ from GRACE and hydro-meteorological approaches . . . . .  | 135 |
| 5.6 Relative discrepancy from the ensemble mean of estimated $ET_a$ from GRACE and hydro-meteorological approaches . . . . .   | 136 |

|     |   |     |
|-----|---|-----|
| 5.7 | Estimated evapotranspiration from GRACE-altimetry approach together with the ensemble mean and standard deviation . . . . . | 138 |
| A.1 | Fitting algorithm for ice-sheet waveform retracking . . . . .   | 166 |
| A.2 | Schematic description of the OCOG retracker . . . . .   | 167 |
| A.3 | A sample waveform includes DC bias level . . . . .  | 168 |



# List of Tables

|      |   |    |
|------|---|----|
| 1.1  | Mean annual precipitation of different products averaged over all catchments . . . . .  | 14 |
| 1.2  | Monitoring the hydrological cycle by spaceborne geodetic sensors: capabilities, challenges and possibilities . . . . .  | 22 |
| 2.1  | TOPEX telemetry sample to waveform sample relationship . . . . .  | 30 |
| 2.2  | Selected virtual stations and <i>in situ</i> gauge over the Lake Urmia for validation . . . . .   | 49 |
| 2.3  | Results of retracking of waveforms belonging to virtual stations 1, 2 and 3 over Urmia Lake using different scenarios . . . . .   | 50 |
| 2.4  | Virtual Stations over different rivers with their characteristics together with estimated average error $\bar{\sigma}$ of each retracker for the obtained water level time series . . . . .   | 52 |
| 2.5  | Estimated average error $\bar{\sigma}$ of each retracker together with the estimated error for the obtained water level time series before and after outlier correction for different rivers . . . . .  | 53 |
| 2.6  | Correlation and $\sigma$ of residual of obtained water level time series from different retracking methods and the combination approach with <i>in situ</i> measurements together with percentage of contribution of different retrackers for creating RSH for three virtual stations in Amazon, Congo and Mississippi rivers . . . . . | 56 |
| 3.1  | Discharge gauging stations of five rivers in group 1 with the time period of available discharge measurements for each and their distance to the close by virtual stations. + means that the virtual station is located upstream and – stands for downstream. . . . .   | 61 |
| 3.2  | Kolmogorov-Smirnov test statistics with significance level of 0.05 group 1 rivers . . . . .   | 62 |
| 3.3  | Discharge gauging stations of group 2 rivers with the time period of available discharge and their distance to the virtual stations . . . . .   | 63 |
| 3.4  | Kolmogorov-Smirnov test statistics with significance level of 0.05 for group 2 rivers . . . . .   | 63 |
| 3.5  | Computed Pearson's correlation (corr.) and rank correlation (rank corr.) coefficient of simultaneous measurements of quasi-monthly/monthly discharge with water level from altimetry for the selected rivers in group 1 . . . . .   | 64 |
| 3.6  | Computed RMSE of estimated discharge from empirical and statistical approach in mm/month for rivers in group 1 . . . . .  | 72 |
| 3.7  | Statistical comparison of discharge time series from empirical and statistical approach for the selected rivers in group 1 . . . . .  | 72 |
| 3.8  | Computed RMSE values for estimated river discharge from empirical and statistical approach in mm/month for rivers in group 1 . . . . .  | 74 |
| 3.9  | Calculated auto-covariance $\Sigma$ , cross-covariance $\Sigma_{\Delta}$ , scalar value of $\hat{A}$ and $C\{e\}$ from the monthly residual of discharge of rivers under study . . . . .  | 80 |
| 3.10 | Computed RMSE values and their average for estimated discharge and errors using different excluded discharge data . . . . .   | 84 |

---

|     |   |     |
|-----|---|-----|
| 4.1 | Average of MMSNR before and after outlier correction for different products . . . . .   | 102 |
| 4.2 | The estimated tidal aliasing period for the main tidal constituents . . . . .   | 112 |
| 4.3 | The secondary aliased period of the M2, N2, O1 and Q1 together with the amplitude factor for each of the tidal constituents . . . . .                                 | 114 |
| 4.4 | The results of estimation of the effects of primary and secondary tidal aliasing errors in GRACE monthly solutions and accordingly in GRACE solutions . . . . .       | 118 |
| 4.5 | Quantification of impact of removing tidal aliasing error over the Amazon, Congo, Mississippi, Kuskokwim River and Western Australia catchment . . . . .              | 122 |
| 4.6 | The estimated linear trend and acceleration from GRACE release 5 for the time period of Jan. 2005 to December 2011 for the 19 drainage basins (Figure 4.43) . . . . . | 126 |
| 5.1 | Statistical analysis of comparing the estimated $ET_a$ from GRACE and hydro-meteorological approaches with ensemble mean . . . . .                                    | 132 |
| 5.2 | Statistical analysis of comparing the estimated $ET_a$ from the GRACE-altimetry approach with ensemble mean . . . . .   | 137 |

## Appendix A

### Waveform retracking algorithms

In general, waveform retracking algorithms can be categorized into four classes:

1. Fitting algorithm:  $\beta$ -parameter retracking
2. The Off Centre Of Gravity (OCOG) technique
3. Threshold retracking
4. Surface/volume scattering retracking

#### A.1 Fitting algorithm $\beta$ -parameter retracking

Fitting algorithm is the first retracking algorithm for processing altimeter waveforms over continental ice sheets which was developed by Martin et al. (1983). He used the algorithm to retrack all SEASAT radar altimeter waveforms to obtain corrected surface elevation estimates. Basically, a 5 or 9 parameters function can be developed from the fitting algorithm. This algorithm fits a function to the waveform and extract the geophysical parameters from the fitted function. The 5 parameter function is used to fit single-ramp returns (Figure A.1), while the 9 parameter function is used to fit double-ramp returns (the effect of the penetration of the surface by the radar pulses) (Martin et al., 1983). It is also known as  $\beta$ -parameter retracking or the NASA algorithm (e.g., Davis, 1995). The general function fitting of the radar waveform is given as (Martin et al., 1983; Zwally, 1996):

$$y(t) = \beta_1 + \sum_{i=0}^n \beta_{2i}(1 + \beta_{5i}Q_i)P\left(\frac{t - \beta_{3i}}{\beta_{4i}}\right) \quad (\text{A.1})$$

$$Q_i = \begin{cases} 0 & \text{for } t < \beta_{3i} + 0.5\beta_{4i} \\ t - (\beta_{3i} + 0.5\beta_{4i}) & \text{for } t > \beta_{3i} + 0.5\beta_{4i} \end{cases} \quad (\text{A.2})$$

$$p(x) = \int_{-\infty}^x \frac{1}{\sqrt{2\pi}} \exp\left(-\frac{q^2}{2}\right) dq \quad (\text{A.3})$$

where  $n$  in equation (A.1) can be 1 or 2, is the number of the ramp in the waveform range window (bins 9-40 for TP 64 bins waveform) (Figures A.1). The double ramps indicates two distinct, nearly equidistant surfaces, which are observed by the altimeter (Deng, 2003). This effect occurs mainly due to the penetration of the surface (e.g. snow) by radar pulses. The unknown parameters are as follows:

- $\beta_1$ : The thermal noise level of the return waveform

- $\beta_2$ : Return signal amplitude
- $\beta_3$ : The mid-point on the leading edge of the waveform.
- $\beta_4$ : The return waveform rise time
- $\beta_5$ : The slope of the trailing edge

For the both single and double ramp fitting algorithm, the trailing edge can be replaced by exponential decay term to fit the waveform with fast decaying trailing edge (Zwally, 1996). Therefore, the equation (A.1) can be rewritten as:

$$y(t) = \beta_1 + \sum_{i=0}^n \beta_{2i} \exp(-\beta_{5i} Q_i) P\left(\frac{t - \beta_{3i}}{\beta_{4i}}\right) \quad (\text{A.4})$$

$$Q_i = \begin{cases} 0 & \text{for } t < \beta_{3i} + 0.5\beta_{4i} \\ t - (\beta_{3i} + 0.5\beta_{4i}) & \text{for } t > \beta_{3i} + 0.5\beta_{4i} \end{cases} \quad (\text{A.5})$$

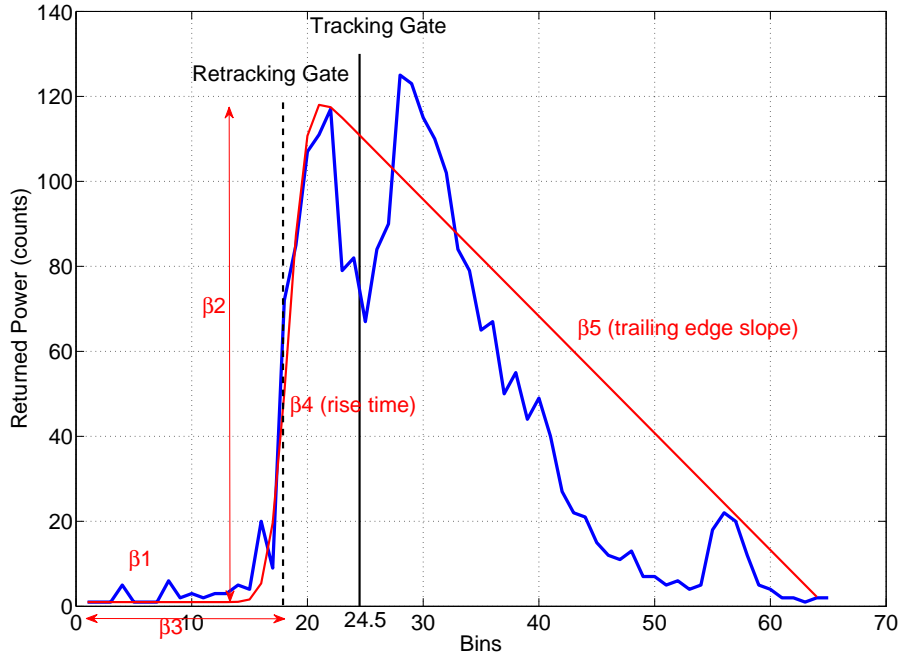


**Figure A.1:** 5 $\beta$  parameter model fitting algorithm, where  $\beta_1$  is the thermal noise level of the return waveform,  $\beta_2$  is the return signal amplitude,  $\beta_3$  is the mid-point on the leading edge of the waveform,  $\beta_4$  is the return waveform rise time and  $\beta_5$  is slope of the trailing edge

The 5/9 $\beta$ -parameter model is fitted on the waveform using least squares method to obtain  $\beta_1 - \beta_5$ . The range correction is then obtained by computing the offset between the estimated mid-point of the leading edge,  $\beta_3$ , and the on-board tracking gate (24.5 for TP and 32.5 for ERS-1/2 and Envisat). The offset is multiplied with sampling rate  $\tau$  (for TP it is 3.125 nsec) and half of light speed  $c/2$ :

$$\Delta R = (\beta_3 - \text{tracking gate}) \times \tau \times \frac{c}{2} \quad (\text{A.6})$$

## A.2 The Off Center Of Gravity (OCOG) retracker

The Off Center Of Gravity (OCOG) retracking algorithm was developed by Wingham et al. (1986) to produce ice sheet data products from ERS-1/2 radar altimetry. The method calculates the center of gravity (COG) of a rectangular box. The twice the height of the center of gravity is called amplitude  $A$  and determines the length of the box. The width ( $W$ ) of the box determines the retracking gate (Figure A.2). COG,  $A$  and  $W$  are given by following equations, in which the squares of the sample values are used to reduce the effect of low amplitude samples.

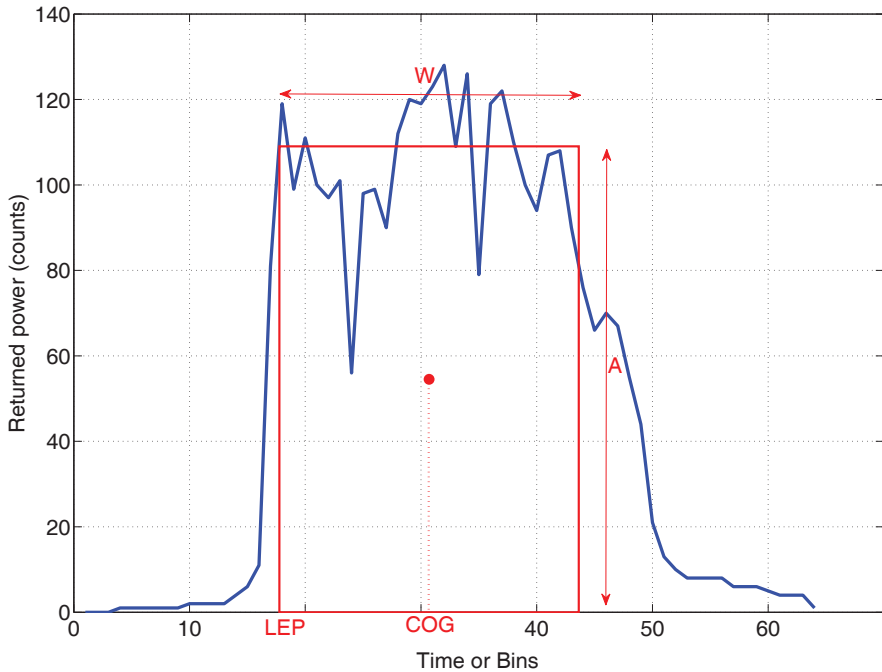


**Figure A.2:** Schematic description of the OCOG retracker.  $W$  is the width of the box,  $A$  is the length of the box that represents the amplitude of waveform and COG is the center of gravity of the box

$$\text{COG} = \frac{\sum_{i=1+n_a}^{64-n_a} iP^2(i)}{\sum_{i=1+n_a}^{64-n_a} P^2(i)} \quad (\text{A.7})$$

$$A = \sqrt{\sum_{i=1+n_a}^{64-n_a} P^4(i)} / \sqrt{\sum_{i=1+n_a}^{64-n_a} P^2(i)} \quad (\text{A.8})$$

$$W = \sqrt{\left(\sum_{i=1+n_a}^{64-n_a} P^2(i)\right)^2} / \sqrt{\sum_{i=1+n_a}^{64-n_a} P^4(i)} \quad (\text{A.9})$$

where  $P(i)$  is the waveform sample value at the  $i^{\text{th}}$  bin, and  $n_a$  is the number of aliased sample that is 4 for TP (Lee, 2008). In addition, the waveform samples 45–50 are excluded to avoid the leakage effects of TP waveforms (Hayne et al., 1994). The mid-point Leading Edge Position (LEP) is then given by:

$$\text{LEP} = \text{COG} - \frac{W}{2} \quad (\text{A.10})$$

Consequently, the range is estimated using the equation (A.6) by substituting of  $\beta_3$  by LEP.

The OCOG algorithm is an statistical algorithm that is simple to implement but it is sensitive to the shape of the waveform as it uses the full sample in waveform bins. A waveform shape affected by surface undulations and small slope in leading edge causes an erroneous estimate of LEP (Deng, 2003). The Ice-1 retracker which has been implemented in the ENVISAT GDR data is optimised for general continental ice sheets and it is based on OCOG retracking method.

### A.3 Threshold retracker

In the threshold retracking, the position on the leading edge is sought by locating the first range bin to exceed a percentage of the maximum waveform amplitude (Davis, 1997). This method could be complicated by the fact that a thermal noise (or DC bias) contaminates the range bins preceding the location of the actual return waveform (Figure A.3). The pre-leading edge DC bias is different for the two satellites and is also known to vary with

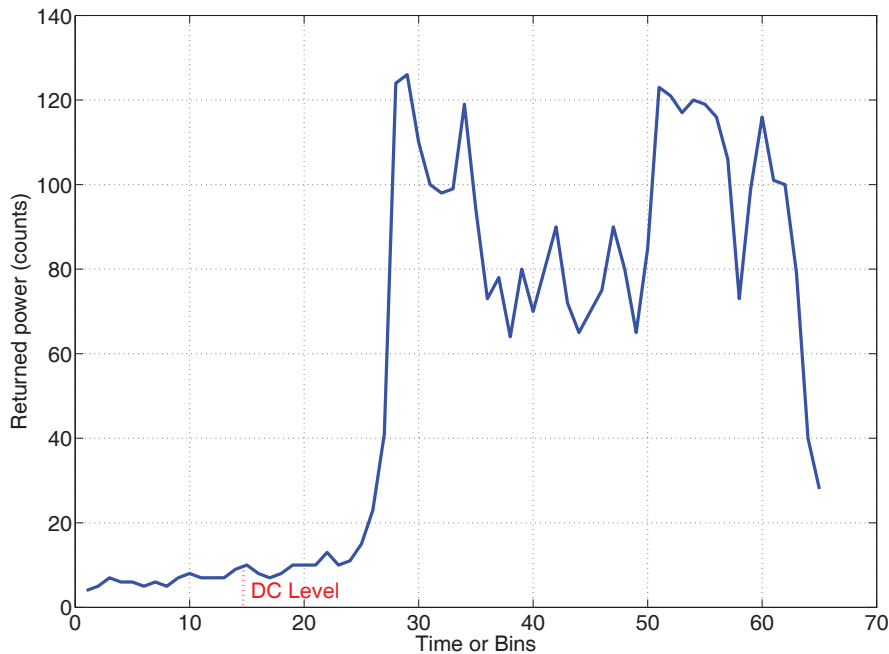


**Figure A.3:** A sample waveform includes DC bias level

location and time in a given satellite data set. The DC level is computed by averaging the waveform sample 5 to 7. The samples from 1 to 4, 45 to 50 and 61 to 64 are excluded for TOPEX Ku band waveform (Lee, 2008). Davis (1997) suggests the 50% threshold for surface-scattering dominated waveforms, and 10% or 20% threshold level for volume-scattering surface (See section A.4). The amplitude, DC level and retracked gate are computed as:

$$A_{\max} = \max(P(i)) \quad (\text{A.11})$$

$$\text{DC} = \frac{1}{3} \sum_{i=5}^7 P(i) \quad (\text{A.12})$$

$$\text{TL} = \text{DC} + T_{\text{coff}}(A_{\max} - \text{DC}) \quad (\text{A.13})$$

$A_{\max}$ : Maximum waveform amplitude

DC: Thermal noise or DC level

$T_{\text{coeff}}$ : Threshold

TL: Retracked gate

Again, the range is estimated using the equation (A.6) by substituting the  $\beta_3$  by TL. Davis (1995) developed an empirical method of threshold retracking to improve the estimation which was used by European Space Agency (ESA) to process the ERS satellite mission. The already implemented Sea-Ice retracker (Laxon, 1994) in the ENVISAT GDR data is optimized for specular returns from sea-ice and is based on threshold retracking scheme.

## A.4 Surface/volume scattering retracking

In most of the case, altimeter return waveforms from the ice sheets are influenced by subsurface volume scattering (Ridley and Partington, 1988). Ridley and Partington (1988) developed a model based upon the numerical evaluation of an integral to describe the volume scattered altimeter waveforms. Partington et al. (1991) applied their model to averaged altimeter waveforms which makes this conclusion that the shape of the altimeter waveforms from Greenland corresponds roughly to surface scattering in the low latitudes and volume scattering in the higher latitudes. Thousands of altimeter return waveforms were averaged together to prove the model because most of the individual waveforms from SEASAT and GEOSAT did not conform to their model's shape.

The combined surface and volume-scattering model are derived from the Gaussian approximations for the altimeter's antenna pattern and transmitted pulse shape (Davis, 1993) as below:

$$SV(n) = DC + \frac{A_m}{S_2} [S(n) + \frac{K}{S_1} V(n)] \quad (\text{A.14})$$

Where DC is the thermal noise,  $A_m$  is the maximum amplitude of the model waveform, and is an adjusted form of the Brown model given by:

$$S(n) = \frac{1}{2} [1 + \text{erf}(\frac{t - t_0}{\sqrt{2}\sigma})] \exp[-\frac{4c}{\gamma h}(t - t_0)] \quad (\text{A.15})$$

The volume-scattering model,  $V(n)$ , is given by

$$V(n) = \exp[-\frac{c^2 \beta_\tau^2}{4h^2 \beta_c^4} - \frac{c(t - t_0)}{h \beta_c^4}] - \exp(\beta_\tau^2 k_e^2 C_s^2 - 2k_e C_s(t - t_0)) \quad (\text{A.16})$$

$S_1$  and  $S_2$  are two values which are called normalizing factors that ensure the quantities  $V(n)$  and  $S(n) + V(n)$  range from zero to one,  $k$  represents the correct proportion of volume scattering,  $C_s$  is the speed of light in snow,  $\beta_c$  is a constant related to the antenna beamwidth,  $\beta_\tau$  is a constant that determines the 3 dB width of the transmitted pulse, and  $k_e$  is the extinction coefficient of snow (Davis, 1993). This is a fitting function, and there are six unknown parameters in the model. This algorithm can be combined with other retracking method to apply over inland water surfaces covered with snow.